MEASUREMENTS IN HIGHLY DISSIPATIVE REGIONS OF HYPERSONIC FLOWS

PART I. HOT-WIRE MEASUREMENTS IN LOW REYNOLDS NUMBER HYPERSONIC FLOWS

Thesis by

C. Forbes Dewey, Jr.

In Partial Fulfillment of the Requirements

For the Degree of

Doctor of Philosophy

California Institute of Technology

Pasadena, California

1963

ABSTRACT

Measurements were made of the heat loss and recovery temperature of a fine hot-wire at a nominal Mach number of 5.8. Data were obtained over an eight-fold range of Reynolds numbers in the transitional regime between continuum and free-molecule flow. At high Reynolds numbers, the heat transfer data agree well with the results of Laufer and McClellan, which were obtained at lower Mach numbers. At lower Reynolds numbers, the results indicate a monotonic transition between continuum and free molecule heat transfer laws. The slope of the heat transfer correlation also appears to vary monotonically, with $Nu \sim \sqrt{Re}$ at high Reynolds numbers and $Nu \sim Re$ for $Re << 1$.

Data on the wire recovery temperature (corresponding to zero net heat transfer) were obtained for free-stream Knudsen numbers between 0.4 and 3.0. Comparison with previous supersonic data suggests that for Mach numbers greater than about two the normalized variation of recovery temperature in the transitional regime is a unique function of the free-stream Knudsen number. The recent data of Vrebalovich (33) suggests that the relation between the normalized recovery temperature and Knudsen number found in this investigation also applies to subsonic and transonic flow.

The steady-state hot-wire may be used to obtain two thermodynamic measurements: the rate of heat transfer from the wire and the wire recovery temperature. An illustrative experiment was performed in the wake of a transverse cylinder, using both hot-wire and pressure instruments in a redundant system of measurements. It was shown that good accuracy may be obtained with a hot-wire even when the Reynolds number based on wire diameter is small.

ACKNOWLEDGMENTS

I would like to express my deep gratitude to Professor Lester Lees for suggesting this investigation and supervising the research program. His interest and broad understanding were a constant source of inspiration. Dr. Anthony Demetriades contributed to this investigation in many ways; his hot-wire experience provided a foundation for the present measurements. Professor Toshi Kubota contributed many suggestions, and was always ready to offer his constructive criticisms. An expression of appreciation is also due the staff of the hypersonic wind tunnel and the GALCIT machine shop for their many hours of expert assistance, Mrs. Elizabeth Fox for her assistance in preparing the manuscript, and Mrs. Truus van Harreveld for her careful and conscientious computational assistance. The cooperation of Dr. John Laufer and Dr. Thomas Vrebalovich of the Jet Propulsion Laboratory is also gratefully acknowledged.

I wish to express my gratitude to the California Institute of Technology for generous financial grants during the years 1959-61, and to the National Science Foundation for the award of a Graduate Fellowship during 1961-63.

Preliminary reports of this investigation may be found in GALCIT Hypersonic Research Project Memorandum No. 61, September 15, 1961, and in the American Rocket Society Journal, Vol. 31, No. 12, pp. 1709-1718, December 1961.

This thesis is dedicated to my parents, whose untiring devotion has always been my greatest resource.

TABLE OF CONTENTS

LIST OF FIGURES

LIST OF SYMBOLS

c_p	specific heat
d	hot-wire diameter
D	cylinder diameter
f	denotes a functional relation between two quantities
$f(s_1), g(s_1)$	functions of the molecular speed ratio s_1
h	convective heat transfer coefficient, $\frac{q}{T_w - T_{aw}}$
i	wire current
k	air thermal conductivity
k_w	wire thermal conductivity at temperature T_w
Kn	Knudsen number, $\sqrt{\pi\gamma/2}\ (M/Re_\infty)$
ℓ	wire length
M	Mach number
n	exponent in Nu_0 - Re_0 relation: $Nu_0 \sim Re_0^{\ n}$
Nu_m	Nusselt number measured with finite length wire, $h_m\, d/k_0$
Nu_0	Nusselt number for infinite length wire, hd/k_0
p	static pressure
p_{t_2}	pitot pressure
Pr_0	Prandtl number, $c_p \mu_0 / k_0$
q	heat transfer rate per unit area
R	wire resistance
Re	Reynolds number, $\frac{\rho_\infty U_\infty d}{\mu}$
s	resistance parameter, $\frac{\alpha_r T_0}{1+\alpha_r (T_{awm} - T_r)}$
s_1	molecular speed ratio $\sqrt{\gamma/2}\ M$

LIST OF SYMBOLS (Cont'd)

t	non-dimensional temperature, $\frac{T-T_{awm}}{T_0}$
T	temperature
U_∞	free-stream velocity
v	support temperature parameter (Eq. 12)
x	distance from cylinder axis in streamwise direction
y	distance from cylinder axis in transverse direction
α	accommodation coefficient
α_r	temperature-resistivity coefficient, $R_w/R_r = 1+\alpha_r(T_w-T_r)$
γ	ratio of specific heats
δ^*	boundary layer displacement thickness
ϵ	recovery ratio parameter, $\eta_*-\eta_m$
ζ	end loss correction parameter (Eq. 11)
η_c	experimental recovery ratio for continuum flow
η_f	theoretical recovery ratio for free molecule flow
η_m	measured recovery ratio, (T_{awm}/T_0)
η_s	non-dimensional support temperature, (T_s/T_0)
η_*	recovery ratio for infinite length wire, (T_*/T_0)
$\bar{\eta}$	normalized recovery ratio, $(\eta-\eta_c)/(\eta_f-\eta_c)$
μ	viscosity; also $(2/\sqrt{\pi})(1/Kn)\log(1/Kn)$ in near free molecule flow analysis
ν	dimensionless quantity (Eq. A-17)
ξ	measure of Nusselt number change with overheat (Eqs. 2 and 3)
ρ	density
τ	overheat, $(T_w-T_{aw})/T_{aw}$

LIST OF SYMBOLS (Cont'd)

χ	dimensionless quantity in near free molecule flow analysis, (Eq. 19)
ψ	dimensionless quantity in near free molecule flow analysis, (Eq. 20)
Ψ	end loss correction factor
ω	abbreviation for $(\tanh \nu/\nu)$

Subscripts

$( )_{aw}$	zero current
$( )_m$	measured
$( )_0$	evaluated at stagnation temperature
$( )_r$	evaluated at reference temperature T_r
$( )_s$	evaluated at support temperature T_s
$( )_w$	evaluated at wire temperature T_w
$( )_*$	refers to infinitely long wire
$( )_\infty$	free stream
$( )_2$	behind a normal shock
$( )_\ell$	evaluated at wake centerline

Superscripts

$(\tilde{\ })$	evaluated at zero overheat
$( )'$	local value at edge of wake mixing region
$( )^{(n)}$	the n^{th} approximation of an iterative solution
$(\bar{\ })$	length-average or normalized quantity

I. INTRODUCTION

Hot-wire probes have been used for a number of years to measure the mean properties of a fluid stream. The hot-wire is capable of providing two thermodynamic measurements: the rate at which heat is transferred from the wire to the stream and the wire recovery temperature for zero heat transfer. If sufficiently accurate relations are known for the heat loss and recovery temperature as a function of the properties of the flow, only one additional thermodynamic measurement is necessary to specify the flow field uniquely.

The present investigation was undertaken with two purposes in mind. First, it was desired to illustrate the use of the steady-state hot-wire as a quantitative tool in high-speed aerodynamic investigations. In order to use the hot-wire to measure mean quantities in low density compressible flow, it is necessary to have an accurate calibration of the wire heat loss and recovery temperature as a function of Mach number and Reynolds number. For high Reynolds number flows, these relations are well represented by the data of Laufer and McClellan (1).* Often, however, it is necessary to use the hot-wire in regions where the Reynolds number based on wire diameter is small. Previous investigations (3, 4, 6, 7) have illustrated the general qualitative features of the Nu-Re relation at small Reynolds numbers, but the experimental uncertainties were too large for calibration purposes. The first

* Numbers in parentheses denote references at the end of the text.

objective, therefore, was to obtain an accurate hot-wire calibration at high Mach number in the transition regime between continuum and free molecule flow.

The second purpose of this investigation was to provide further information on two features of low Reynolds number flow which are important from a theoretical point of view. One of these is the recovery temperature phenomenon which was theoretically and experimentally investigated by Stalder, Goodwin, and Creager (8). It was found by these authors that the equilibrium, or recovery, temperature of an unheated cylinder in free-molecule flow is greater than the stagnation temperature of the stream. Since the high Reynolds number equilibrium temperature is less than stagnation, the recovery ratio (T_{aw}/T_0) serves as one measure of the transition from continuum to free molecule flow. In the present investigation, measurements were made of the wire recovery temperature in the range of Knudsen numbers between 0.4 and 3.0. These and previous (1, 2) data provide an accurate high Mach number relation between the recovery ratio (T_{aw}/T_0) and Kn over the complete range from continuum to free molecule flow.

At high Reynolds numbers, the heat transfer to the stagnation point of a blunt body may be accurately predicted using boundary layer theory. Recently, a considerable amount of attention has been given to the problem of determining appropriate corrections to the high Reynolds number, high Mach number boundary layer solutions which would extend their validity to lower Reynolds numbers. Several alternative formulations of this problem have

been given in the literature, and more experimental evidence is needed to evaluate the results. The data obtained in this investigation, when combined with the results of Laufer and McClellan, show the departure of the Nu-Re relation from the high Reynolds number correlation and the approach to free-molecule flow for an infinite, conducting cylinder.

In many physical situations, it is difficult to obtain precise data using standard aerodynamic instruments such as static pressure probes. Particularly in regions of low density, instrumentation sufficiently large to obtain reliable results may introduce appreciable disturbances into the flow. The hot-wire is particularly suited to such investigations due to its small physical dimensions, lack of directional sensitivity, and ability to provide two thermodynamic measurements. Total temperature, mass flow, and velocity profiles in the far wake of a transverse cylinder were obtained to demonstrate the use of the hot-wire in high-speed flow. By using four measured quantities (two hot-wire measurements and static and pitot pressure), the flow field was over-determined, and this redundancy permitted an estimate of the accuracy of the hot-wire measurements. Further applications may be found in Part II of this thesis.

II. EXPERIMENTAL METHOD

II.1. Equipment

The measurements were performed in Leg 1 of the GALCIT hypersonic wind tunnel at a nominal Mach number of 5.8. This tunnel has a 3 in. by 3 in. core of uniform flow. Other features of this facility are described in Reference 9. The stagnation pressure was varied between 0 and 95 psig. at a nominal stagnation temperature of 226°F. Because of the tunnel wall boundary layer, the actual test section Mach number varied with stagnation pressure as shown in Figure 1. Figure 2 shows the variation of stagnation temperature with pressure which was introduced by the automatic temperature regulation system.

Under certain conditions, free-stream turbulence may effect the measured heat transfer rate. Demetriades (10) found that the free-stream integrated r.m.s. mass-flux and temperature fluctuations in Leg 1 were on the order of 0.4 per cent. The dominant turbulence scale, given by the velocity divided by the frequency, was on the order of 10^3 to 10^5 times the wire diameter, and by the criteria of Reference 12 should have caused no measurable effect on the heat loss. Additional quantitative turbulence measurements are necessary before a similar statement can be made about the wake results.

To determine the local Mach number, pitot pressure measurements were made within 0.5 in. of the hot-wire with the .063" I.D. stainless steel probe shown in Figure 3, and the local Mach

number computed assuming isentropic flow between the reservoir and test section. The stagnation pressure was measured by a total head tube directly upstream of the throat. Traverses normal to the flow direction showed that the local Mach number at the wire was identical to that measured by the probe within 0.5 per cent.

Stagnation temperatures were measured 1 inch ahead of the nozzle throat with a Pratt and Whitney type iron-constantan thermocouple, and all computations were made assuming isentropic, adiabatic expansion to the measured test section Mach number.

The detachable hot-wire holders consisted of a conical brass body, a thin double wedge brass support blade, and two sewing needles to hold the wire. The needles were attached to and electrically insulated from the brass blade by epoxy resin; Figure 3a illustrates the holder configuration. The complete hot-wire assembly, including holder, sting support, and total pressure tube is shown in Figure 3b. The hot-wire was soft-soldered to the needle supports within .002" of the tips; a typical installation is shown in Figure 4. Details of the electrical connectors and head assembly may be found in Reference 10.

Figure 5 is a drawing of the calibration oven used to determine the temperature-resistance relation of the wires. Heat was supplied by a helically wound nichrome ribbon, and sufficient thermal lagging was used to make the temperature gradients within the oven negligible. An iron-constantan thermocouple placed 0.25 inch from the wire gave the oven temperature. Measurements were made only when the oven had reached thermal

equilibrium (temperature change less than 0.2°F per minute).

The electrical instrumentation consisted of a precision Leeds and Northrup "K-2" potentiometer accurate to one part in 5,000, five-45 volt dry cells to supply the wire current, a variable series resistance for current control, and an auxiliary milliammeter and bridge as shown in Figure 6. Measurements of the potential drop across the wire and the standard one ohm resistor were made with the K-2 potentiometer, giving the wire current and resistance. All readings were corrected for the small line resistance between the hot-wire and the potentiometer. During each series of measurements, the current was constant within 0.02 per cent.

II.2. Measurements

To determine the Nusselt number and recovery temperature of the wire, the voltage drop across the wire and across a standard 1 ohm resistor were measured for several values of wire current. The resistance was then plotted against i^2 to determine the slope and intercept at zero current. Extreme care had to be exercised in achieving constant tunnel stagnation temperature, since a change of 1°F was easily detectable in the R vs. i^2 plot.

In performing the wake test, a continuous curve of wire temperature vs. position in the wake is desired for a fixed wire current, and a Moseley Autograph x-y plotter was used for this purpose. The traverse mechanism was geared to a linear resistance coil, and a small constant current through this resistance created a voltage drop proportional to the traverse position. This

signal and the voltage drop across the hot-wire were the two electrical inputs for the plotter. Scale factors were obtained by measuring the voltage drop across the wire with the K-2 potentiometer at two known values of (y/D).

II. 3. Wire Calibration and Annealing

The resistance of each wire was measured at several temperatures in the calibration oven. At the end of each series of runs, the wire resistance at room temperature was again measured; if the resistance had changed more than a few tenths of a per cent, the data were discarded. Several wires were calibrated both before and after prolonged testing to determine the effect of annealing and exposure on the temperature-resistivity coefficient.

All data were obtained using 0.00010 inch diameter Pt - 10 per cent Rh wire from a single spool. (Some preliminary tests using 0.00005 inch diameter wire are discussed in Appendix E.) No attempt was made to measure the wire diameter directly, since it was felt that the manufacturer's* drawing procedures were of greater accuracy than any available optical measurement technique. However, each wire was examined visually under a microscope to detect any macroscopic irregularities. The mounted wire resistance and length were also carefully measured and checked against the manufacturer's quoted resistance of 11,580 ohms/ft. at 68°F. The mean deviation of the unannealed, installed resistance from this reference value was less than 1 per cent, indicating high uniformity of the wire.

*Sigmund Cohn, Mt. Vernon, New York.

Through prolonged use, the wire resistance increased between 2 and 8 per cent. Since it was necessary to limit the increase between successive calibrations to a few tenths of a per cent, several special tests were conducted to determine the major factors involved. It was found that a large part of the resistance shift could be eliminated by heating the wire to a dull glow for several minutes prior to tunnel use. This result is in substantial agreement with the experience of Spangenberg (cf. Reference 18, Figure 9). To check the influence of starting loads, one wire ($\frac{\ell}{d}$ = 325) was subjected to seven consecutive tunnel starting cycles at 20 psig while immersed deep within the sidewall boundary layer. The resulting resistance change was less than 0.1 per cent.

It can be inferred that the primary causes of resistance change are associated with exposure to the free-stream pressure loads while the wire is at an elevated temperature. Further observation showed that the two primary factors were: (1) large step-wise increases in resistance if the previous maximum temperature and pressure of operation were exceeded ["deformation" phenomenon]; (2) a much smaller increase which was a function of time ["creep" phenomenon]. Since all wires were initially normal to the flow direction, a certain amount of stretching was to be expected. Figure 4 shows a typical deformation caused by an overheat of about 0.8 at 90 psig stagnation pressure. Higher overheats resulted in larger wire curvature and were not used in this investigation. The creep phenomenon was negligible after the first few hours of tunnel exposure.

Two factors limited the aspect ratio of the wires. First, it was found that wire curvature increased with aspect ratio. Second, for aspect ratios greater than 375, wires of 0.00010" diameter were easily broken during the tunnel starting process. Since it was desired to keep the end loss corrections as low as possible, the range $320 \leqq \frac{\ell}{d} \leqq 360$ was chosen as an acceptable compromise.

The temperature coefficient of resistivity α_r varied between 0.88 and 0.93×10^{-3} $(°F)^{-1}$ at 0°F, with a mean value of 0.91×10^{-3}, i.e. between 1.54 and 1.63×10^{-3} $(°C)^{-1}$ at 0°C, with a mean of 1.59×10^{-3}. Equilibrium wire temperatures were less than 270°F, and resistance varies linearly with temperature in this range. Calibration data were taken between 72 and 200°F, and the measured resistivity coefficient α_r was accurate to about 1.5 per cent for each wire. Several tests indicated that the resistivity coefficient was not affected by tunnel exposure, provided that the wire had been initially annealed to a dull glow in still air.

Under certain conditions, reversible strain gage effects may introduce systematic errors into the equilibrium temperature measurements. Using the relations of Morkovin (Reference 11, p. 24), the resistance error ΔR_w for this experiment caused by strain gauge effects would be $(\Delta R_w/R_w) \sim 10^{-4}$ to 10^{-5}, or considerably less than the uncertainty of the wire calibration. A more serious error could be introduced by differential thermal expansion between the wire and the support head. However, no evidence of this effect was present in the temperature calibrations, and

since tunnel operation was less severe from this standpoint than the oven calibration, it was assumed that thermal strain was negligible.

In Appendix A, the correction factors for heat loss to the wire supports are derived. This analysis is carried through with the support temperature as a free parameter, and shows that for large end loss correction the support temperature has an important effect on both the Nusselt number and recovery factor. Depending upon the tip shape, thermal conduction, and free-stream Reynolds number the effective value of $\eta_s = (T_s/T_0)$ should lie between .85 and 1.0, and should vary with the wire attachment location. Since the recovery temperature correction was quite sensitive to η_s, a special test (see Appendix C) was conducted to measure this parameter. The value of η_s was found to be constant over the complete range of tunnel conditions encountered, and equal to $0.903 \pm .005$. This value is approximately equal to the calculated laminar boundary layer recovery factor for flow along the needle downstream of the stagnation region.

III. DATA REDUCTION

The largest portion of heat transferred from a blunt body is in the vicinity of the forward stagnation point. At high Reynolds numbers and Mach numbers, the appropriate temperature for evaluating viscosity and thermal conductivity is that existing behind a normal shock at the free stream Mach number. At low Reynolds numbers, a distinct shock wave does not appear; under these conditions, the results of free molecule theory (8) may be conveniently expressed using fluid properties evaluated at the stagnation temperature. At high Mach numbers, the temperature behind a normal shock is close to the stagnation temperature and the two evaluations will give equivalent, but not identical, correlations. In this thesis, the heat transfer data are correlated using the Nusselt and Reynolds numbers

$$Nu_0 = (hd/k_0) \quad , \quad Re_0 = (\rho_\infty U_\infty d)/\mu_0 \quad , \qquad (1)$$

where μ_0 and k_0 are the air viscosity and thermal conductivity evaluated at stagnation temperature. This form offers distinct advantages when the hot-wire is used as a measuring instrument in non-uniform flow fields.*

All hot-wires of finite length lose a certain amount of heat to their supports. The quantity Nu_0 represents the heat transfer rate for a wire of infinite length, and is related to the measured Nusselt number Nu_m by the relation

* Morkovin (11) and Collis and Williams (13) discuss this problem in more detail.

$$Nu_0 = \Psi_N Nu_m = \Psi_N \left[\frac{i^2 R_m}{\pi \ell k_0 (T_w - T_{awm})} \right] \qquad (2)$$

where Ψ_N is the Nusselt number end loss correction factor, i^2R_m is the measured Joule heating, and $(T_w - T_{awm})$ is the measured temperature potential. Similarly, the recovery ratio η_* for an infinitely long wire may be written

$$\eta_* = (T_{aw*}/T_0) = \Psi_R \eta_m = \Psi_R (T_{awm}/T_0) \qquad (3)$$

where Ψ_R is the recovery ratio end loss factor. In Appendix A, the quantities Ψ_N and Ψ_R are derived in detail. They depend primarily on the wire aspect ratio and measured Nusselt number; for large aspect ratios and Nusselt numbers, Ψ_N and Ψ_R are close to unity.

The present measurements were conducted using very small heating currents. For $i \to 0$ and a linear temperature-resistance relation,

$$\frac{i^2 R_m}{(T_w - T_{aw})} = \alpha_r R_m R_r \left(\frac{i^2}{R_m - R_{awm}} \right) \cong \frac{\alpha_r R_{awm} R_r}{(dR/di^2)_{i=0}}$$

and Eq. 2 takes the simplified form

$$Nu_m = \left(\frac{\alpha_r}{\pi \ell k_0} \right) \frac{R_{awm} R_r}{(dR/di^2)_{i=0}} \quad . \qquad (2a)$$

A plot of R vs. i^2 (e.g. Figure 11) allows the quantity $(dr/di^2)_{i=0}$ to be determined accurately.

For high Reynolds numbers, the recovery ratio $\eta_c = (T_c/T_0)$

has been shown experimentally to be a function only of Mach number (11); η_c decreases from 1.0 at M = 0 to 0.95 for Mach numbers greater than about two. This behavior is explained by the well-known hypersonic "freeze" or Mach number independence principle, which recognizes that the viscous and inviscid flow fields become independent of Mach number if the Mach number is sufficiently large. For blunt bodies such as the cylindrical wire considered here, changes in the flow field are small beyond a Mach number of three.* A value $\eta_c = 0.950$ was used as a reference for the present experiments and the data of Laufer and McClellan (1) and Sherman (2). Stalder et al. (5) found $\eta_c = 0.96$, and this value was used in interpreting their results.

The high Reynolds number relations described above represent the limit of continuum flow. For free molecular flow, the heat loss and recovery temperature of an infinite, perfectly conducting cylinder with no radiative cooling are given in Reference 8:

$$Nu_0 = \frac{(\gamma-1)}{2(\pi)^{3/2}} \alpha \, Re_0 \, Pr_0 \, \left(\frac{g(s_1)}{s_1}\right) \tag{4}$$

$$\eta_f = (T_{aw}/T_0) = \left(1 + \frac{\gamma-1}{2} M^2\right)^{-1} \frac{f(s_1)}{g(s_1)} \tag{5}$$

$$s_1 = \sqrt{\gamma/2}\, M \tag{6}$$

*Tewfik and Geidt (14) have measured the angular variation of heat transfer coefficient and recovery temperature on a cylinder at Mach numbers of 1.3 and 6.0. These distributions, which are similar to those obtained at low speeds, may be used to calculate the temperature T_{aw} which a cylinder of infinite thermal conductivity would assume for no net heat transfer. As expected, the resulting values of $T_{aw}(M)$ agree well with the hot-wire measurements. Additional data reported in Part II of this thesis confirm the temperature distributions found by Tewfik and Geidt, and the conclusions given above.

where $f(s_1)$ and $g(s_1)$ depend only on the molecular speed ratio s_1 and the number of excited degrees of freedom of the medium. These functions are tabulated in Reference 8 for both monatomic and diatomic perfect gases. As $M \to \infty$, Eqs. 4 and 5 approach the limiting forms

$$Nu_0 = \left(\frac{\gamma + 1}{2\pi\gamma}\right) \alpha \, Re_0 \, Pr_0 \tag{4a}$$

and

$$\eta_f = \left(\frac{2\gamma}{\gamma+1}\right) \tag{5a}$$

As in the case of continuum flow, the Nusselt number and recovery ratio become independent of Mach number as the Mach number increases.*

The fact that the recovery ratio in continuum and free molecule flow obeys the Mach number independence principle suggests that the normalized recovery ratio

$$\eta_* = \frac{\eta_* - \eta_c}{\eta_f - \eta_c} \tag{7}$$

is a unique function of the Knudsen number for M sufficiently large. At lower Mach numbers, $\overline{\eta}_*$ might depend on additional parameters involving M and Re. Cybulski and Baldwin (7) report that for subsonic flow the continuum recovery ratio persists to quite high Knudsen numbers. However, the recent data of Vrebalovich (33) shows that $\eta_* (Kn_\infty)$ is independent of M_∞ for $M_\infty \geq 0.4$. This is discussed in Section IV.2.

* Reference 15 gives several additional examples of the Mach number independence principle for both continuum and free molecule flow.

All computations of flow properties were made using $\gamma = (7/5)$ and the Sutherland viscosity formula (with T expressed in °R)

$$\mu = 2.270 \frac{T^{3/2}}{198.6 + T} \times 10^{-8}, \frac{lb - sec}{ft^2} \tag{8}$$

Values of air thermal conductivity were obtained from Hilsenrath and Beckett (16), and the wire thermal conductivity was taken from Reference 17, with the data linearly extrapolated to the measured mean wire temperature.

A derivation of the end loss corrections appropriate to transitional flow is given in Appendix A. This analysis assumes that the wire temperature is radially uniform, wire resistance is a linear function of temperature, and the heat transfer coefficient $h = Nu_0 (k_0/d)$ is constant over the wire length. For convenience, the supports are taken to be equal in temperature, although this restriction is not essential. The relation between the measured Nusselt number Nu_m and the value Nu_0 for an infinite wire may be expressed as

$$\Psi_N = \left(\frac{\bar{t}}{t_* - \epsilon}\right) \frac{(1 + st_*)}{(1 + s\bar{t})} \tag{9}$$

while the recovery ratio end loss correction factor is given by

$$\Psi_R = \frac{\eta_*}{\eta_m} = \left[1 - \tilde{\omega}\left(\frac{\eta_s}{\eta_m}\right)\right](1 - \tilde{\omega})^{-1} \quad . \tag{10}$$

Here η_s is the normalized support temperature, η_m is the measured recovery ratio, $[\bar{t}/(t_* - \epsilon)]$ is the ratio of the measured wire overheat to the overheat of an infinitely long wire at the same current,

$s\bar{t}$ and st_* represent normalized resistances, and $\tilde{\omega}$ is a quantity which depends primarily on the wire aspect ratio and Nusselt number; $\tilde{\omega}$ represents the zero overheat value of ω. The quantities $[\bar{t}/(t_*-\epsilon)]$ and $[\omega/(1-\omega)]$ are given in Figures 13 and 14 as functions of the two parameters

$$\zeta = (\ell/d)\left[(k_0/k_w)\, Nu_m \frac{(1+\epsilon s)}{(1+s\bar{t})} \right]^{\frac{1}{2}} \tag{11}$$

and

$$v = -\tfrac{1}{2} t_s s \xi (\tilde{\omega}/\omega) \frac{(1-\omega)}{(1-\tilde{\omega})} \quad . \tag{12}$$

It is shown in Appendix A that the correction factor Ψ_N does not depend strongly on overheat; for $\tau \to 0$, Eqs. (9) - (12) assume the more tractable form

$$\Psi_N = \left(\frac{\bar{t}}{t_*-\epsilon}\right)(1+\epsilon s) \tag{9a}$$

$$\Psi_R = 1 + \left(1 - \frac{\eta_s}{\eta_m}\right)\left(\frac{\omega}{1-\omega}\right) \tag{10a}$$

$$\zeta = (\ell/d)\left[(k_0/k_w)\, Nu_m\, (1+\epsilon s)\right]^{\frac{1}{2}} \tag{11a}$$

$$v = -\tfrac{1}{2} t_s\, s \tag{12a}$$

where

$$\epsilon = (\eta_* - \eta_m) << 1$$

$$t_s = (\eta_s - \eta_m) << 1$$

and s is a constant of order one. As ζ decreases, both Ψ_N and Ψ_R depart from unity; the support temperature parameter v plays a

minor role in determining the end loss corrections, although it must be considered if the corrections are large.

These corrections were applied to the present data and to the recovery factor data of Laufer and McClellan (1) at the lower Reynolds numbers of their investigation. As discussed in the following section, this correction was primarily responsible for unifying the results of the several investigations of recovery temperature in supersonic flow.

For the present data, the measured value $\eta_s = 0.903$ was used with the measured values of η_m and Nu_m to compute the end loss correction. A slightly more complicated procedure was required in interpreting the results of Laufer and McClellan (1). In that investigation, measurements of the Nusselt number and recovery factor were made with different wires; the Nu_0 data were obtained with wires of aspect ratio between 400 and 550 and the recovery temperature data were obtained using aspect ratios of the order of 225. The Nusselt numbers reported in Reference 1 include a small (less than 5 per cent) end loss correction; for such small corrections the formulas used are essentially identical to those derived in Appendix A. The data given in Reference 1, therefore, represent Nu_0 in the present nomenclature.* The reported recovery ratio, however, represents η_m and requires a correction to account for support conduction.

The wire supports used by Laufer and McClellan (1) were

* The actual parameters used by Laufer and McClellan (1) were Nu_2 and Re_2, and conversion to Nu_0 and Re_0 follows directly.

equivalent to a two-dimensional wedge of 7° included angle. Using the observation (Appendix C) that the support temperature is equal to the laminar boundary layer adiabatic wall temperature, η_s could be calculated explicitly. Since Nu_m was not known, an iterative computation process was adopted which used as input the known quantities η_s, η_m and the wire Reynolds number Re_0. With Re_0 known, Nu_0 was taken from the heat loss correlation and the value of Nu_m was computed. The procedure for obtaining Nu_m and η_* with Nu_0 and η_m known is analogous to the determination of Nu_0 and η_* with Nu_m and η_m given.

The present free stream data were subject to end loss corrections in the ranges $.703 \leqq \Psi_N \leqq .833$ and $1.208 \leqq \Psi_R \leqq 1.633$. For the low Reynolds number wake tests, values $.59 \leqq \Psi_N \leqq .68$ and $1.70 \leqq \Psi_R \leqq 2.06$ were used. In view of the appreciable end losses encountered, it should be emphasized that the important thing is not the magnitude of the corrections per se, but the accuracy with which these corrections are known. The largest uncertainty lies in the actual end conditions of the wire, as characterized by η_s; for this reason, η_s was measured directly in the present investigation (Appendix B). This parameter is sensitive not only to the shape and material properties of the support but also to the flow field around the tips. In transonic or non-uniform flow fields, the determination of an effective value of η_s is a formidable problem, as Sherman (2) has pointed out.

No correction was made to the data for radiation effects since calculation showed that the error in both Nu_0 and $\overline{\eta}_s$ was less

than one tenth of one per cent. The correction is roughly proportional to (T_w^4/Nu), and may become appreciable for high overheats or extremely low Reynolds numbers. At low temperatures, say $T_w < 400°F$, it may easily be shown that the radiation correction will always be a minute fraction of the end loss correction.

The raw data from the wake traverse consisted of a series of continuous curves of wire voltage vs. voltage output from the traverse mechanism. The voltage scale was established by two calibration measurements with the K-2 potentiometer at known values of (y/D). Using this calibration and the measured value of wire current, the wire resistance was computed for several representative stations within the wake. Figure 11 shows the measured wire resistance as a function of wire current.

Two thermodynamic measurements were obtained with the hot-wire; these were $[dR/d(i^2)]_{i=0}$ and the zero current intercept R_{aw}, both of which were taken from Figure 11.* Pitot pressure and static pressure across the wake were also measured separately. Thus, the measured thermodynamic quantities were more than sufficient to specify the flow completely, and this redundancy permitted an estimate of the accuracy of the combined measurements. A description of the computation procedure is given below.

From the four quantities $[dR/d(i^2)]_{i=0}$ (i.e., Nu_m),

* The small error incurred in taking the slope of the R vs. i^2 curve rather than the correct slope of R vs. i^2R was neglected in this preliminary investigation. However, the refined measurement techniques used in Part II of this thesis justified the use of the R vs. i^2R slope for all data.

R_{aw} (i.e., T_{aw}), p_{t2}, and p, four groups of three independent quantities may be formed, and any one of these groups would provide sufficient data to determine the state of the flow uniquely. Any two groups would provide an independent, redundant calculation; in certain cases, the accuracy and convergence of the iterative solution may depend strongly on the choice of parameters.* For purposes of illustration, the following groups of variables were chosen**:

Group I: $[dR/di^2]_{i=0}$, R_{awm}, p

Group II: p_{t_2}, R_{awm}, p

The computation procedure is similar in principle to that which would be used for any two groups of three variables.

To interpret the local values $[dR/di^2]_{i=0}$ in the wake an empirical relation between Nu_0 and Re_0 was required for the range $.34 < Re_0 < .66$, only part of which was covered by the present free-stream measurements. For the lower Reynolds numbers, the calibration curve given in Figure 8 for $M >> 1$ was extrapolated to $Re_0 = .315$ using a smooth curve which asymptotically approached the free molecule heat transfer law (Eq. 4), with $\alpha = 1.0$. The justification for this choice of α is given in the following section. Interpretation of the measured recovery temperature was made

---

* Several examples are cited by Morkovin (11) to illustrate this point.

** Quantities without superscripts are functions of distance from the wake centerline, while ( )' signifies the measured value at the edge of the wake mixing region.

using values of $\overline{\eta}_*(Kn)$ given by the solid curve of Figure 10.

The static and pitot pressure measurements were obtained by John F. McCarthy, Jr. of this laboratory. Free stream conditions for the hot-wire and pressure traverses were

	M_∞	x/D	Re_∞
Hot-wire	5.74	9.0	1.75×10^4
Pressure	5.74	9.0	2.60×10^4

Hot-wire fluctuation measurements showed that the wake was laminar in both cases, and the assumption was made that the local pressure profiles were similar for the two tests. The Reynolds number effect is discussed more fully in Section V.

Data reduction was most conveniently carried out by assuming distributions of the unknown flow quantities across the wake, computing the end loss corrections based on these assumed values, and from the measured quantities and the end loss corrections obtaining improved guesses for the unknown quantities. For Group I, this iteration was performed using M and T_0 as the unknowns; the calculation for Group II used T_0 as the iterative quantity. In each case, only three hand iterations were required to obtain convergence.

Similar measurements in the "near" wake of a cylinder, covering the region between separation and (x/D) = 5.00, are reported in Part II of this thesis. For that investigation, the measured quantities were $(dR/di^2)_{i=0}$, R_{awm}, and p_{t2}. In order to check the assumption of constant pressure in the separated region, calculations were also made using $(dR/di^2)_{i=0}$, R_{awm}, and an assumed

value of p. Since about 1500 individual data points were involved in this investigation, it was found desirable to develop an IBM 7090 data reduction program. A description of this program is given in Appendix B.

IV. RESULTS AND DISCUSSION

IV.1. Heat Transfer Measurements

In attempting to compile an empirical correlation of hot-wire heat transfer data over an extended range of variables, the investigator is faced with two problems: the number of experimental papers on the subject is quite large, running well over fifty, and the results of investigations conducted under seemingly identical conditions differ by as much as 40 per cent. The effects of wire overheat and stagnation temperature (particularly in the transonic regime) have yet to be fully resolved (19).

Theoretical studies are of limited use in preparing a heat transfer correlation. The solution of Cole and Roshko (23) for continuum Oseen flow agrees well with the experiments of Collis and Williams (24) at low Reynolds numbers. Levy (25) has considered the Oseen flow problem with temperature-jump boundary conditions, and the results agree qualitatively with the experiments of Cybulski and Baldwin (7). However, the velocities and Reynolds numbers covered by Oseen theory are quite small.

Free molecule analysis has provided what appears from Eq. 4 to be a straightforward calibration for all flows where the Knudsen number is sufficiently high. The fact that the accommodation coefficient α is an unknown parameter has been a major weakness in all attempts to apply this theory to a given set of data*. It is not uncommon to find investigations with an experimental scatter

* An excellent appraisal of the problems of momentum and energy accommodation is given by Hurlbut (26).

greater than 30 per cent in which the authors infer a specific value of accommodation coefficient by comparing the asymptotic behavior of their Nu_0 - Re_0 curve to Eq. 4, and ascribing the difference to incomplete accommodation.

Figure 7 has been prepared as a guide to the experimental variation of Nusselt number as a function of Reynolds number and Mach number in the range $0.1 \leqq Re_0 \leqq 100$.

The figure was compiled from the data of References 1, 7, 20, 21, 22, and 33, and the present investigation. Particular weight was given to the correlation of McAdams (20) at M = 0, the data of Christiansen (22) and Vrebalovich (33) at transonic speeds, and the data of Laufer and McClellan (1) and the present investigation for M > 2. The data of Spangenberg (19) was used as a guide for the high Reynolds number transonic region. Within the Reynolds number range $1 \leqslant Re_0 \leqslant 100$, the data of Baldwin (21) and Cybulski and Baldwin (7) exhibit the same qualitative Nu_0 - Re_0 relation shown in Figure 7, but their data indicate an asymptotic approach to free-molecule theory based on an accommodation coefficient of about one half. For air, this result is not in agreement with the other experimental results cited above, and may be due to the large variations of Nu_0 with overheat that their data exhibit. The correlation given in Figure 7 is intended to represent Nu_0 (Re_0, M) at zero overheat ($\tau \to 0$); however, the effect of overheat is not large (see Appendix D). The curves shown in the figure were extrapolated to $Re_0 = 0.1$ by fairing a smooth monotonic curve between the available experiments and free-molecule theory with an accommodation

coefficient of unity. An analytic expression for the correlation may be found in Appendix B.

The heat transfer data obtained in this investigation are presented in Figure 8. These data agree well with the measurements of Laufer and McClellan (1) at Reynolds numbers Re_0 greater than three. One may infer from this agreement and the Mach number independence principle that the solid line shown in Figure 8 represents the Nu_0 - Re_0 relation for Mach numbers greater than about three.

For comparative purposes, the results of free molecule theory (Eq. 4) and the extrapolated slope of the high Reynolds number data are shown in Figure 8. At high Reynolds numbers, the Nusselt number becomes proportional to $(Re_0)^{\frac{1}{2}}$, while $Nu_0 \sim Re_0$ for $Re_0 << 1$. The present measurements asymptotically approach the free molecule result with an accommodation coefficient α near unity. For the heat transfer tests in air and argon by Christiansen (23), Weltman and Kuhns (6), and Wong (3), an accommodation coefficient of unity represents the data within the experimental error. Experimentally, it has been found that surface conditions are of primary importance in determining the degree of energy accommodation (26). The recent review of Wachman (34) indicates that α increases with an increase of adsorbed surface gas. It has also been pointed out in the literature that these surface effects may vary with the energy of the incident molecule and the body temperature.

All data shown in Figure 8 are based on the measured Nusselt number at zero overheat (the effects of overheat are discussed in detail in Appendix D). In free molecule flow, the surface temperature enters the heat transfer relation only through its effect on the accommodation coefficient. If the accommodation coefficient were unaffected by surface temperature, the cold wire results of Christiansen (22) and the present results should agree closely (except for the small Mach number variation given by $f(s_1)/s_1$ in Eq. 4). Figure 7 indicates that the hot wire and cold wire data agree well up to a Reynolds number Re_0 of about one.

For high Reynolds number flows, a large part of the heat transfer to the body occurs in the vicinity of the forward stagnation point. For a perfect gas, the heat transfer at the stagnation point of a cylinder in supersonic flow is closely represented by (27)

$$Nu_0 \cong 0.50 \sqrt{Re_0} \left(\frac{Pr_0}{Pr_w}\right) \left(\frac{T_0}{T_w} \frac{\mu_w}{\mu_0}\right)^{.06} . \qquad (13)$$

Equation 13 indicates that the effects of overheat at high Reynolds numbers should be small over the range of conditions encountered in the laboratory.

Although no complete solutions are available for a cylinder in high speed flow because of the lack of an adequate theory covering the region of separation, many analyses are available for heat transfer near the stagnation point of a blunt body. It has been pointed out that both the hot-wire data and the stagnation point boundary layer solutions exhibit heat transfer coefficients proportional to $\sqrt{Re_0}$ at high Reynolds numbers, and the behavior of the stagnation point

solutions with decreasing Reynolds number should agree well with the hot-wire measurements.

Two recent investigations by Probstein and Kemp (26) and Van Dyke (32) have used the Navier-Stokes equations to describe the flow field near the stagnation point of a blunt body in hypersonic flow. These analyses show that conventional high Reynolds number boundary layer theory must be modified as the body Reynolds number is decreased. First order corrections may be present due to external vorticity, boundary layer displacement, surface velocity and temperature jump, and body curvature. For a cylinder, the vorticity along the zero streamline is zero in the inviscid flow, so the vorticity effect on heat transfer is of second order. However, the boundary layer displacement and curvature effects both produce a first order decrease in surface heat transfer, compared with the conventional high Reynolds number value. Slip effects would also decrease the heat transfer rate. Probstein and Kemp (26) have proposed a merged layer analysis based on continuum relations for the range $30 \lesssim Re_0 \lesssim 100$. The results agree qualitatively with the present measurements. In view of the large body of experimental data now available for cylinder heat transfer, recovery temperature, and drag, an extension of existing theory for axisymmetric bodies to the case of a two-dimensional stagnation point should prove very enlightening.

The slope of the Nu_0 - Re_0 relation is a quantity of considerable interest. The exponent n in the relation

$$Nu_0 \sim Re_0^{\,n} \tag{14}$$

correlates the results of several independent investigations better than the absolute magnitudes of the observed quantities. In Figure 9, the exponent n is shown as a function of Reynolds number and Mach number for several investigations.* The present measurements and those of Laufer and McClellan (1) were used for $M > 2$, while selected results of Christiansen (22), Cybulski (7), and Baldwin (21) are shown for $M < 1$. At high Reynolds numbers, the exponent n is $\frac{1}{2}$; in the limit of $Kn \to 0$, the free molecule relation, Eq. 4, shows that $n = 1$. A third relation, derived from the Oseen solution of Cole and Roshko (23), is applicable when $M/Re \ll 1$ and $Re_0 \ll 1$; in this instance, the exponent is of the form

$$n = \frac{1}{\log\left(\frac{8}{Re_0\, Pr_0}\right)} \tag{15}$$

Collis and Williams' (24) experiments agree very well with Eq. 15 for $0.01 < Re_0 < 0.3$.

At high Mach numbers, the exponent n is seen to vary monotonically between the continuum and free molecule values of $\frac{1}{2}$ and 1. The measured slope begins to depart from the continuum value at a Reynolds number Re_0 of about 200 for an insulated wire. A comparison between Christiansen's (22) data and the present measurements indicate that the departure from the continuum heat transfer law occurs at a slightly lower value of Re_0 if the wall is highly cooled;

*An analytic expression for $n(Re_0, M)$ is given in Appendix B.

this may be explained by the fact that a cool wall decreases the boundary layer displacement effect at a given Reynolds number. For low Reynolds numbers, the approach to the free molecule heat transfer law does not appear to vary with wire overheat, although the data are not sufficient to resolve this question completely.

Willis (29) has treated several problems in the near free molecule regime using an iterative solution to the integral form of the Boltzmann equation. This approach is equivalent to the so-called first collision theory if only the first iterate is considered. Willis' results for a two-dimensional strip normal to a rarefied flow should be identical in form to the solution for a cylinder normal to the flow. By writing a heat balance for the body, the resulting equations may be solved for the departure of the Nusselt number and recovery temperature from the free molecule values as a function of the free stream Knudsen number. The results may be expressed as ($\alpha = 1$)

$$\frac{Nu_0}{(Nu_0)_{Free\ Molecule}} = 1 + \mu\chi \tag{16}$$

$$\frac{T_{aw}}{(T_{aw})_{Free\ Molecule}} = \frac{1 + \mu\psi}{1 + \mu\chi} \tag{17}$$

where

$$\mu = \frac{2}{\sqrt{\pi}} \frac{1}{Kn} \log\left(\frac{1}{Kn}\right) \tag{18}$$

$$\chi = \frac{N_i - N_{if}}{\mu N_{if}} \tag{19}$$

$$\psi = \frac{Q_i - Q_{if}}{\mu\, Q_{if}} \tag{20}$$

Here N_i is the incident molecular flux, Q_i is the incident energy flux, and $(\ )_f$ indicates the value for $\mu \to 0$.

Willis has evaluated the parameters ψ and χ for a two-dimensional strip, and finds that they depend on the molecular speed ratio, the body temperature, the molecular model, and the number of degrees of freedom of the gas. ψ and χ are weak functions of the body temperature if the overheat is small; the results are more sensitive to body temperature at higher values of the molecular speed ratio s_1. For $s_1 \to \infty$, Willis has computed ψ and χ as a function of body temperature for both the hard sphere and modified Krook molecular models. For an insulated body ($T_w = T_{aw}$), $\psi = .42$ and $\chi = .11$ for the modified Krook model while $\psi = .78$ and $\chi = .48$ if the hard sphere model is used. From equation 16, it may be seen that the departure of the Nusselt number from the free molecule result is a strong function of the molecular model employed. Eqs. 16 and 17 agree qualitatively with the present experiments if $\psi > \chi > 0$.

Several interesting conclusions may be drawn from the above analysis. First, the small parameter in near free molecule flow for a two-dimensional body is (1/Kn) log (1/Kn) rather than the quantity (1/Kn) which pertains to axisymmetric bodies. Thus, the range of validity of the two-dimensional analysis is restricted to higher Knudsen numbers than the axisymmetric counterpart. Second, for viscosity proportional to $(T)^{\frac{1}{2}}$, $Kn \sim (1/Re_0)$

at high Mach number and the analysis predicts that the Nu_0 - Re_0 relation at high Knudsen numbers should, as expected, become independent of Mach number.

Schaaf (35) has recently compared the numerical results of Willis' theory to the experimental data given here, and to the results of cylinder drag measurements at low Reynolds numbers (36). In both cases, the theory departs from the free-molecule values at Knudsen numbers on the order of 100, whereas the experimental data show no significant departures above a Knudsen number of about 10. Using a normalization similar to that employed in Figure 10, Sherman (37) has shown that the drag coefficient

$$\overline{C_D} = \frac{C_D - (C_D)_c}{(C_D)_f - (C_D)_c}$$

is a strong function of Mach number, in contrast to the results obtained for the recovery temperature parameter $\bar{\eta}_*$ (see Figure 10). Constant values of $\overline{C_D}$ are more closely associated with constant values of Re_0, a result which is not surprising in view of the intimate relation between cylinder drag and heat transfer.

IV.2. Recovery Temperature Measurements

Measurements of the recovery temperature of a cylinder placed normal to the flow have previously been made at high Reynolds numbers up to a Mach number of 4.5. The excellent work of Laufer and McClellan has shown that the recovery temperature is independent of Mach number above approximately 2. A justification of this effect has already been given.

In the transitional regime, the measurements reported in References 1 and 2 indicated that at Knudsen numbers of about 0.1 the recovery temperature begins to rise above the high Reynolds number value, while at Knudsen numbers greater than 10, the full temperature rise predicted by Eq. 5 is attained. However, at Knudsen numbers of about 1 and at roughly the same Mach number, the two investigations reported significant differences in the recovery factor.

The present investigation was undertaken in an attempt to resolve this apparent discrepancy and at the same time provide additional recovery temperature data for use in steady-state hot wire work. The results are shown in Figure 10, using the normalized recovery ratio $\overline{\eta}_*$ and the free-stream Knudsen number as parameters. Fortunately, the recovery temperature for a cylinder is independent of the accommodation coefficient (provided that the wire is infinitely long!) and rapidly approaches an asymptote as the Mach number increases. Therefore, since $\overline{\eta}_* = 0$ for $\eta_* = \eta_c$ and $\overline{\eta}_* = 1$ for $\eta_* = \eta_f$, all investigations should agree at least in these two limits.

The shaded area representing the data of Laufer and McClellan defines the limits of experimental scatter of nearly 100 separate measurements made over a large range of Mach and Reynolds numbers. Considering the range of parameters studied, the data are extremely consistent. However, the aspect ratios of the wires used in their recovery temperature study were on the order of 200, and at the higher Knudsen numbers these wires were

subject to significant end losses. Using the relations derived in Appendix A several representative data points were corrected for support conduction and plotted in Figure 10.

By combining the corrected data of Reference 1, the results of Sherman (2), and the present measurements, a continuous transition of the normalized recovery factor is obtained between continuum and free molecule flow. From a consideration of the Mach number independence principle, this curve should be valid for all Mach numbers above approximately two. Considering the sensitivity of the normalized recovery ratio to experimental error, the correlation appears to be very good.

Vrebalovich (33) has recently extended the available recovery temperature data to include the transonic regime. These data cover the range $0.4 < M < 1.2$, and are also shown in Figure 10. It may be seen that the variation of the normalized recovery ratio $\overline{\eta}_{*}$ is both qualitatively and quantitatively similar throughout the complete subsonic-supersonic-hypersonic regime which has been investigated. The single curve shown in Figure 10 agrees with the data within $\pm 10\%$ for all Mach numbers. Since the difference between η_f and η_c rapidly approaches zero as M decreases below one, this curve may be used as an empirical calibration relation for interpreting measured recovery temperatures in flow fields where the stagnation temperature is unknown (see Part II of this thesis for a typical application). The error in the final stagnation temperature due to Mach number effects should be less than $\pm 1.5\%$ over the complete range $0.4 < M < \infty$.

The behavior of the $\bar{\eta}_*(Kn)$ relation at small Knudsen numbers agrees qualitatively with the results of Probstein and Kemp (28). In the incipient merged layer analysis, they find that the gas temperature at the stagnation point of a blunt body becomes greater than the free stream stagnation temperature in the low Reynolds number continuum range. For large Knudsen numbers, Eq. 17 predicts that the recovery temperature will fall below the free molecule value if $\psi > \chi$; the experimental data shown in Figure 10 indicates that for a circular cylinder and a diatomic gas, ψ and χ are nearly equal. Schaaf (35) used the two-dimensional strip results of Willis (29) to evaluate ψ and χ; he found that the theory departed from $\bar{\eta}_* = 1$ at a Knudsen number of about 100, whereas the data of Figure 10 show that the departure is not significant above a Knudsen number of 10.

V. APPLICATION OF THE STEADY-STATE HOT-WIRE TO WAKE MEASUREMENTS

Several classic experiments have been made using the hot-wire as a steady-state measuring instrument. These have been well reported in the cited references, and it is pertinent only to emphasize that wire calibration is the primary problem in all quantitative measurements.

The number of investigations utilizing the hot-wire in a redundant measurement scheme is quite small, and consequently it was decided to perform an illustrative experiment involving four measured quantities, two of which were obtained from a hot-wire operated in the transitional regime. The far wake of a cylinder transverse to a hypersonic flow was chosen both because its flow field was amenable to hot-wire and pressure measurements and because of current interest in the thermal wakes of hypersonic blunt bodies.

The wire used in this experiment had an aspect ratio of 311 and $\alpha_r = 0.93 \times 10^{-3} \cdot F^{-1}$. The measured variation of wire resistance with i^2 is shown in Figure 11. One important conclusion which can be drawn is that the instrument sensitivity was quite sufficient to pick out small differences in the R vs. i^2 relation. This property is absolutely essential for quantitative interpretation.

The following groups of variables were chosen to represent the data*:

* See Section III for a discussion of the data reduction procedure.

Group I: $\left[\frac{dR}{d(i^2)}\right]_{i=0}$, R_{awm}, p

Group II: p_{t2}, p, R_{awm}.

The distributions of flow quantities across the wake were computed using the measurements of Group I and Group II in independent calculations. Thus, the agreement between the results of Group I and Group II provides a measure of the accuracy of the combined measurements.

Figure 12a shows the results of the stagnation temperature calculations. T_0' is the measured stagnation temperature at the outer edge of the mixing layer. Results for the several representative stations are shown first as "uncorrected" data. By "uncorrected" is meant the temperature one would calculate using only the zero current intercept of Figure 11 and the wire resistivity coefficient. The wire was subject to end loss effects, and by using Figures 8 and 10 and the derived end loss corrections, an iteration was performed to find the true value of T_0. Only three iterations were required to obtain convergence.

Qualitatively, the behavior of (T_0/T_0') is similar to that obtained in a high speed boundary layer (1) with Prandtl number less than one. Because of laminar shear and heat conduction processes, the centerline Mach number for this particular streamwise station was about 3/4 of M' and the centerline stagnation temperature was about 0.96 of the outer edge temperature T_0'. The two measured values of T_0' computed from Groups I and II agreed within 0.14 per cent, and were two per cent lower than the free stream stagnation

temperature. This result agrees well with the postulate of isoenergetic flow everywhere outside the viscous mixing region.

The local mass flow in the wake is shown in Figure 12b. For purposes of comparison, the "uncorrected" hot-wire data is also shown; the measured heat loss of the wire $R_{aw}\ (dR/di^2)^{-1}$ is directly proportional to the local mass flow (ρu) if end losses are negligible. Since the end loss correction increases with decreasing (ρu), the uncorrected mass flow is higher than the final corrected values based on the measurements of Group I.

The agreement between the two values of ($\rho u/\rho' u'$) computed using Group I and Group II is good. The differences between the two curves are primarily due to the different cylinder Reynolds numbers for the hot-wire and pressure tests (see page 21). Subsequent pitot pressure data have indicated that the higher value of ($\rho u/\rho' u'$) at the wake centerline obtained with Group II is caused by the higher values of $Re_{\infty,D}$ for the pressure measurements. At the edge of the wake, ($\rho' u'$) for Group I was 0.85 of ($\rho' u'$) for Group II. Taking this Reynolds number effect into account, the absolute values of (ρu) from Group I and Group II were found to agree within 7 per cent throughout the mixing region. The small differences between the two curves of (T_0/T_0') vs. (y/D) shown in Figure 12a are also attributable to the difference in $Re_{\infty,D}$.

The velocity defect in the wake mixing region is shown in Figure 12c. The agreement between the hot-wire and pressure measurements is seen to be excellent, and verifies the fact that the differences shown in Figures 12 and 12b are due to differences in $Re_{\infty,D}$;

for (x/D) = 9 and these Reynolds numbers, the wake is laminar and the velocity defect $[(u - u_{\infty})/(u' - u_{\infty})]$ should show little dependence on $Re_{\infty,D}$.

In summary, this wake survey has shown that the steady-state hot-wire may be used as an accurate quantitative instrument when operated at small wire Reynolds numbers, provided sufficiently accurate calibration relations are available. The hot-wire is capable of providing two thermodynamic measurements; only one additional measurement (such as total or static pressure) is required to determine the flow field uniquely.

Part II of this thesis is an application of the hot-wire techniques described above to the near wake of a cylinder in hypersonic flow. Point-by-point correlations between hot-wire and pitot pressure measurements obtained under identical flow conditions allowed the flow field to be mapped out in great detail and with considerably greater accuracy than the illustrative experiment given here.

REFERENCES

1. Laufer, J. and McClellan, R., "Measurements of Heat Transfer from Fine Wires in Supersonic Flows", J. Fluid Mech., Vol. 1, No. 3, pp. 276-289, 1956.

2. Sherman, F. S., "A Low-Density Wind-Tunnel Study of Shock-Wave Structure and Relaxation Phenomena in Gases", NACA TN 3298, 1955.

3. Wong, Howard, "Design and Development of a Free-Molecule Heat Transfer Probe", U. of Calif. (Berkeley) Report HE-150-143, 1956.

4. Laurman, J. A. and Ipsen, D. C., "Use of a Free-Molecule Probe in High Speed Rarefied Gas Flow Studies", U. of Calif. (Berkeley) Report HE-150-146, 1957.

5. Stalder, J. R., Goodwin, G., and Creager, M. O., "Heat Transfer to Bodies in a High-Speed Rarefied-Gas Stream", NACA Report 1093, 1952.

6. Weltmann, R. N. and Kuhns, P. W., "Heat Transfer to Cylinders in Crossflow in Hypersonic Rarefied Gas Streams", NASA TN D-267, 1960.

7. Cybulski, R. J. and Baldwin, L. V., "Heat Transfer from Cylinders in Transition from Slip Flow to Free-Molecule Flow", NASA Memorandum 4-27-59E, 1959.

8. Stalder, J. R., Goodwin, G., and Creager, M. O., "A Comparison of Theory and Experiment for High-Speed Free-Molecule Flow", NACA Report 1032, 1951.

9. Eimer, M., "Direct Measurements of Laminar Skin Friction at Hypersonic Speeds", GALCIT Hypersonic Wind Tunnel, Memorandum No. 16, 1953.

10. Demetriades, Anthony, "An Experimental Investigation of the Stability of the Hypersonic Laminar Boundary Layer", GALCIT Hypersonic Research Project, Memorandum No. 43, 1958. Also, J. Fluid Mechanics, Vol. 7, No. 3, pp. 385-396, 1960.

11. Morkovin, M. V., "Fluctuations and Hot-Wire Anemometry in Compressible Flows", AGARDograph 24, 1956.

12. Van Der Hegge Zijnen, B. G., "Heat Transfer from Horizontal Cylinders to a Turbulent Air Flow", App. Sci. Res., Vol. 7, Sect. A, pp. 205-223, 1958.

13. Collis, D. C. and Williams, M. J., "Molecular and Compressibility Effects on Forced Convection or Heat from Cylinders", Australian Aero. Res. Lab. Report ARL/A.110, 1958.

14. Tewfik, O. K. and Geidt, W. H., "Local Heat Transfer, Recovery Factor, Pressure Distribution around a Circular Cylinder Normal to a Rarefied Supersonic Air Stream", Proceedings of the 1959 Heat Transfer and Fluid Mechanics Institute.

15. Hayes, W. D. and Probstein, R. F., "Hypersonic Flow Theory", Academic Press, 1959.

16. Hilsenrath, J., Beckett, W. S., et al., "Tables of Thermal Properties of Gases", N.B.S. Circular 564, 1955.

17. "Handbook of Chemistry and Physics", 35th Edition, Chemical Rubber Publishing Co., Cleveland, Ohio (1953).

18. Kovasznay, L.S.G. and Tõrmarck, S.I.A., "Heat Loss of Hot-Wires in Supersonic Flow", Bumblebee Report No. 127, Johns Hopkins University, 1950.

19. Spangenberg, W. G., "Heat Loss Characteristics of Hot-Wire Anemometers at Various Densities in Transonic and Supersonic Flow", NACA TN 3381, 1955.

20. McAdams, "Heat Transmission", Third Ed., McGraw-Hill, New York, 1954.

21. Baldwin, L. V., "Slip-Flow Heat Transfer from Cylinders in Subsonic Airstreams", NACA TN 4369, 1958.

22. Christiansen, W. H., "Development and Calibration of a Cold Wire Probe for Use in Shock Tubes", GALCIT Hypersonic Research Project, Memorandum No. 62, July 1, 1961.

23. Cole, J. D. and Roshko, A., "Heat-Transfer from Wires at Reynolds Numbers in the Oseen Range", Proceedings of the 1954 Heat Transfer and Fluid Mechanics Institute.

24. Collis, D. C. and Williams, M. J., "Two-Dimensional Convection from Heated Wires at Low Reynolds Numbers", J. Fluid Mech., Vol. 6, pp. 357-384, 1959.

25. Levy, H. C., "Heat Transfer in Slip Flow at Low Reynolds Number", J. Fluid Mech., Vol. 6, pp. 385-391, 1959.

26. Hurlbut, F. C., "Notes on Surface Interaction and Satellite Drag", RAND Symposium on Aerodynamics of the Upper Atmosphere, June 1959.

27. Beckwith, I. E., "Similar Solutions for the Compressible Boundary Layer on a Yawed Cylinder with Transpiration Cooling", NASA TR R-42, 1959.

28. Probstein, R. F. and Kemp, N. H., "Viscous Aerodynamic Characteristics in Hypersonic Rarefied Gas Flow", J. Aerospace Sci., Vol. 27, No. 3, pp. 174-192, 1960.

29. Willis, D. R., "On the Flow of Gases under Nearly Free Molecular Conditions", Princeton University, Dept. of Aero. Eng., Report No. 442, December 1958.

30. McClellan, R., "Equilibrium Temperature and Heat Transfer Characteristics of Hot Wires in Supersonic Flow", Ae.E. Thesis, California Institute of Technology, Pasadena, 1955.

31. Winovich, W. and Stine, H. A., "Measurements of the Non-Linear Variation with Temperature of Heat-Transfer Rate from Hot Wires in Transonic and Supersonic Flow", NACA TN 3965, 1957.

32. Van Dyke, M., "Second-Order Boundary-Layer Theory for Blunt Bodies in Hypersonic Flow", ARS Paper No. 1966-61. Presented at the International Hypersonics Conference, Cambridge, Mass., August 1961.

33. Vrebalovich, T., "Heat Loss from Hot Wires in Transonic Flow", J.P.L. Research Summary No. 36-14, May 1, 1962.

34. Wachman, H. Y., "The Thermal Accommodation Coefficient: A Critical Survey", General Electric Space Sciences Laboratory Report R61SD197, Dec., 1962. See also ARS Journal, January 1962.

35. Schaaf, S. A., "A Comparison of Theory and Experiment at the Borders of Transition Flow of a Rarefied Gas", RAND Corporation Memorandum RM-3108-ARPA, May 1962.

36. Maslach, G. J., and Schaaf, S. A., "Cylinder Drag in the Transition from Continuum to Free Molecule Flow", U. of California (Berkeley) Report HE-150-194, March 20, 1962.

37. Sherman, F. S., "Transition Flow (A Survey of Experimental Results and Methods for the Transition Region of Rarefied Gas Dynamics)", U. of California (Berkeley) Report HE-150-201, Aug. 15, 1962.

38. McCarthy, J.F., Jr., "Hypersonic Wakes", Thesis, Calif. Inst. of Tech, 1962.

APPENDIX A

END LOSS CORRECTIONS FOR THE TRANSITIONAL REGIME

In interpreting hot-wire measurements in low density flows, it is imperative that the heat loss to the wire supports be accurately taken into account. For high Reynolds number flow where the convective heat transfer is large and end loss corrections are small, the derivation given by Kovasznay (18) is adequate. However, considerable care must be exercised when these corrections amount to 20 per cent or more of the measured quantity.

Formulation of the Problem

Neglecting radiation, we may write the following heat balance equation:

$$\pi d \ell h (T-T_{aw}) = (\frac{\pi d^2 \ell}{4}) (d/dz) (k_w \frac{dT}{dz}) + i^2 R \qquad (A-1)$$

where the left side of the equation represents the convective heat loss, the first term on the right hand side is the net heat added by conduction, and ($i^2 R$) is the electrical dissipation. Solution of this equation involves the following assumptions:

(a) h, the convective heat transfer coefficient, is a constant and is equal to the value which would be measured by an infinite wire at the same current. This implies that the external flow is uniform along the wire.

(b) The wire thermal conductivity, k_w, is constant.

(c) Wire resistance varies linearly with temperature:

$$\frac{R}{R_{awm}} = \frac{1 + \alpha_r(T-T_r)}{1 + \alpha_r(T_{awm}-T_r)} \equiv 1 + st$$

$$s = \frac{\alpha_r T_0}{1 + \alpha_r(T_{awm}-T_r)} \qquad \text{(A-2)}$$

$$t = (T - T_{awm})/T_0 \quad .$$

(d) Each cross-section of the wire is at uniform temperature (implicit in Eq. A-1).

(e) Both wire supports are maintained at a temperature $T_s = \eta_s T_0$.* The boundary conditions are thus

$$z = \pm \frac{\ell}{2}\ , \ t = t_w = (T_s - T_{awm})/T_0 \quad . \qquad \text{(A-3)}$$

With the above boundary conditions, Eq. A-1 may be integrated to give

$$t = \frac{1}{\nu^2 s}\left[\left(\frac{\ell}{d}\right)^2 \left(\frac{k_0}{k_w}\right) Nu_0 \ (1+\epsilon s) - \nu^2\right]\left[1 - \frac{\cosh 2\nu(z/\ell)}{\cosh\nu}\right] + t_s \frac{\cosh 2\nu(z/\ell)}{\cosh\nu} \qquad \text{(A-4)}$$

where

$$\nu^2 = \left(\frac{\ell}{d}\right)^2 \left(\frac{k_0}{k_w}\right) Nu_0 - \frac{i^2 R_{awm} \ell s}{\pi d^2 k_w T_0}\ ,$$

$$\epsilon = \eta_* - \eta_m \ .$$

The average wire temperature at any given current is

* This restriction is not essential although it simplifies the mathematics considerably. The effect of non-uniform flow near the supports may be partially accounted for by an appropriate choice of η_s.

$$t = \int_{-\ell/2}^{\ell/2} t\,dz = \frac{1}{\nu^2 s}\left[\left(\frac{\ell}{d}\right)^2 \left(\frac{k_0}{k_w}\right) Nu_0\ (1+\epsilon s) - \nu^2\right]\left[1 - \frac{\tan\nu}{\nu}\right] + t_s \frac{\tanh\nu}{\nu} \qquad (A\text{-}5)$$

For an infinitely long wire, $(\ell/d) \to \infty$, $\bar{t} \to t_*$, $[(\tanh\nu/\nu)] \to 0$ and

$$\lim_{(\ell/d)\to\infty} \bar{t} \equiv t_* = \frac{1}{\nu^2 s}\left[\left(\frac{\ell}{d}\right)^2 \left(\frac{k_0}{k_w}\right) Nu_0\ (1+\epsilon s) - \nu^2\right] .$$

Eq. A-5 may now be rewritten in the final form

$$\bar{t} = t_* \left(1 - \frac{\tanh\nu}{\nu}\right) + t_s \frac{\tanh\nu}{\nu} . \qquad (A\text{-}6)$$

This relation is identical to that derived by Kovasznay (18) if we let the support temperature be equal to the wire recovery temperature ($t_s = 0$) and $\epsilon = 0$. It is easily seen that the measured wire temperature $\bar{t}$ will always lie between the temperature t_* of an infinite wire and the support temperature t_s. For large end losses (ν small), the mean wire temperature approaches the temperature of the supports.

Nusselt Number Correction

In order to correct Nu_m to the value Nu_0 for an infinite wire, we must find the ratio of these two quantities at a given current. In the present nomenclature, this ratio is

$$\Psi_N = \frac{Nu_0}{Nu_m} = \left(\frac{\bar{t}}{t_* - \epsilon}\right) \frac{(1+st_*)}{(1+s\bar{t})} . \qquad (A\text{-}7)$$

Introducing the quantities

$$\xi^2 = \frac{\left[\left(\frac{\bar{t}}{t_* - \epsilon}\right) Nu_m\right]_{i=0}}{\left[\left(\frac{\bar{t}}{t_* - \epsilon}\right) Nu_m\right]}$$

$$\tilde{\nu} \equiv (\nu)_{i=0} = \nu(1 + s\bar{t})^{\frac{1}{2}} \xi$$

and defining

$$\omega = (\tanh\nu/\nu), \quad \tilde{\omega} = (\tanh\tilde{\nu}/\tilde{\nu})$$

we have

$$\epsilon = -t_s \left(\frac{\tilde{\omega}}{1-\tilde{\omega}}\right) . \tag{A-8}$$

Equations A-6 and A-8 must be solved simultaneously for t_* and in terms of the measured quantities of the experiment.

For low overheats τ, we may perform an expansion in the parameter $(s\bar{t})$. From Eqs. A-6 and A-8,

$$\left(\frac{\bar{t}}{t_* - \epsilon}\right) = (1 - \omega)\left[1 + G(\epsilon, \bar{t}, t_s)\right] \tag{A-9}$$

where

$$G = -\left(\frac{t_s}{t_* - \epsilon}\right) \frac{\omega - \tilde{\omega}}{(1-\omega)(1-\tilde{\omega})} . \tag{A-10}$$

Using the relations

$$(\tilde{\nu}/\nu) = \xi\left[1 + \tfrac{1}{2}\, s\bar{t} - \frac{1}{8}(s\bar{t})^2 + \ldots\ldots\right]$$

and

$$\tanh(\tilde{\nu} - \nu) = \frac{\tanh\tilde{\nu} - \tanh\nu}{1 - \tanh\tilde{\nu}\tanh\nu}$$

a certain amount of manipulation leads to the equation

$$G = \tfrac{1}{2} t_s \, s\xi \, \frac{\tilde{\omega}}{(1-\tilde{\omega})(1-\omega)} \left(\frac{\bar{t}}{t_* - \epsilon}\right) \left[1 - \tfrac{1}{4}(s\bar{t}) + \ldots + \frac{2}{5}\frac{(\xi - 1)}{(s\bar{t})}\right] \times$$

$$\times \left[1 - \frac{(1 - \tanh \nu \tanh \tilde{\nu})}{\tilde{\omega}} \left\{1 - \frac{\nu^2}{3}\left(\frac{\tilde{\nu}}{\nu} - 1\right)^2 + 0\left(\frac{\tilde{\nu}}{\nu} - 1\right)^5 \right\}\right] . \qquad \text{(A-11)}$$

At this point, we are able to make some definite arguments about the magnitudes of the terms appearing in Eq. A-9. The quantity s will in general be of order 1 and if the end loss is to be small, then $\tilde{\omega}$ must also be small and

$$\frac{\tilde{\omega}}{(1 - \tilde{\omega})(1 - \omega)} << 1.$$

Since $|t_s| = |(\eta_s - \eta_m)| << 1$, G will then be $0(\eta_m - \eta_s)$ if the bracketed quantities in Eq. A-11 are 0(1). The following approximations are now made:

(a) The quantity $(\xi-1)/(s\bar{t})$ is small, justified by the experimental fact that Nusselt number changes slowly with overheat.

(b) $(1 - \tanh \tilde{\nu} \tanh \nu) << 1$. This is strictly true only for large ν, but making this assumption places an upper bound on G and may be checked a posteriori.

Defining

$$v = -\tfrac{1}{2} t_s \, s\xi \, (\tilde{\omega}/\omega) \frac{(1-\omega)}{(1-\tilde{\omega})} \qquad \text{(A-12)}$$

we have the form

$$G = -\frac{v\omega}{(1-\omega)^2} \left(\frac{\bar{t}}{t_* - \epsilon}\right)\left[1 + \ldots + 0\left\{(s\bar{t}), \frac{(\xi-1)}{(s\bar{t})}, (1 - \tanh\nu \tanh\tilde{\nu})\right\}\right] \qquad \text{(A-13)}$$

Substituting Eq. A-13 into Eq. A-9 and noting that $v << 1$, we obtain the final relations

$$\Psi_N = \frac{Nu_0}{Nu_m} = \left(\frac{\bar{t}}{t_* - \epsilon}\right) \frac{(1 + st_*)}{(1 + s\bar{t})} \tag{A-14}$$

$$\left(\frac{\bar{t}}{t_* - \epsilon}\right) = (1-\omega)\left[1 - \frac{v\omega}{(1-\omega)^2}\left\{1 + \ldots 0\left(s\bar{t}, \frac{\xi - 1}{s\bar{t}}\right)\right.\right. \tag{A-15}$$

$$\left.\left. + 0\left(1 - \tanh\nu \tanh\tilde{\nu}\right)\right\} + 0(v^2\omega^2)\right]$$

$$v = -\tfrac{1}{2} t_s s\xi \left(\tilde{\omega}/\omega\right) \frac{(1-\omega)}{(1-\tilde{\omega})} \tag{A-16}$$

$$\nu = \left(\frac{\bar{t}}{t_* - \epsilon}\right)^{\frac{1}{2}} \zeta \tag{A-17}$$

$$\zeta = (\ell/d)\left[(k_0/k_w)\, Nu_m\right]^{\frac{1}{2}} \left[\frac{(1 + \epsilon s)}{(1 + s\bar{t})}\right]^{\frac{1}{2}} \tag{A-18}$$

$$\xi^2 = \left[\left(\frac{\bar{t}}{t_* - \epsilon}\right) Nu_m\right]_{i=0} \left[\left(\frac{\bar{t}}{t_* - \epsilon}\right) Nu_m\right]^{-1} . \tag{A-19}$$

For the special case of zero overheat, $\bar{t} = 0$, $t_* = \epsilon$, $\nu = \tilde{\nu}$, $\xi = 1$, and Eqs. A-6 and A-8 may be combined to give an explicit form for the Nusselt number correction factor:

$$(\Psi_N)_{i=0} = (1 - \omega)\left[1 - \tfrac{1}{2} t_s s \left(\frac{\omega}{1-\omega}\right) - \tfrac{1}{2}(t_s s)^2 \left(\frac{\omega}{1-\omega}\right)^2\right] . \tag{A-20}$$

Recovery Factor Correction

From Eq. A-8, we may easily find the recovery factor corrections to be

$$\Psi_R = \frac{\eta_*}{\eta_m} = \left[\frac{1 - (\eta_s/\eta_m)\tilde{\omega}}{(1 - \tilde{\omega})}\right] \tag{A-21}$$

$$\overline{\Psi}_R = \frac{\overline{\eta}_*}{\overline{\eta}_m} = 1 + \frac{\tilde{\omega}}{(1-\tilde{\omega})} \left[1 + \frac{\eta_c - \eta_s}{\eta_m - \eta_c} \right] . \qquad \text{(A-22)}$$

Computational Procedure

At this juncture, it seems advantageous to illustrate the computational advantages of Eq. A-15. Neglecting higher order terms, if v and ν are taken to be parameters we have the relations

$$\left(\frac{\overline{t}}{t_* - \epsilon}\right) = f(\nu, v)$$

$$\nu = f\left[\left(\frac{\overline{t}}{t_* - \epsilon}\right), \zeta\right]$$

and hence

$$\left(\frac{\overline{t}}{t_* - \epsilon}\right) = f(\zeta, v)$$

$$\nu = f(\zeta, v) .$$

In Figures 13 and 14, $[\overline{t}/(t_* - \epsilon)]$ and $[\omega/(1-\omega)]$ are shown as functions of $(1/\zeta)$, with v as a parameter. The quantity S used by Kovasznay is related to ζ by

$$S = \lim_{\epsilon \to 0} (1/\zeta) . \qquad \text{(A-23)}$$

The analysis of that reference further restricts the solution to cases where $\xi = 1$ and $t_s = 0$.

It may be readily seen from Figure 13 that the parameter v becomes important only in circumstances where the end loss correction is sizeable. To assess the relative magnitude of v and its effect on the solution we take a hypothetical case where the end loss may be expected to be large. Let

$(k_0/k_w)^{\frac{1}{2}} = .03125$, $Nu_m = 0.1600$, $\bar{t} = 0$, $\xi = 1$

$t_s = -0.120$, $s = \frac{1}{2}$, $(\ell/d) = 250$

$\eta_c = .950$, $\eta_m = 1.020$, $\eta_f - \eta_c = 0.210$.

To start the calculation, assume $\epsilon = 0$. Then from Eq. A-18

$$\zeta^{(0)} = .03125 \times 0.4 \times 250 = 3.125$$
$$1/\zeta^{(0)} = .3200$$

From Eq. A-16, we calculate

$$v = -\tfrac{1}{2}\,(-0.120) \cdot \tfrac{1}{2} = .030$$

and from Figures 13 and 14 we obtain

$$(\bar{t}/t_* - \epsilon)^{(0)} = 0.571\,, \left[\frac{\omega}{(1-\omega)}\right]^{(0)} = 0.710\ .$$

Using Eq. A-15 with $\bar{t} = 0$ and $t_* \equiv \epsilon = 0$,

$$\Psi_N^{(0)} = 0.571\ .$$

The first approximation to the correction factor for $\bar{\eta}_*$ is computed from Eq. A-22:

$$\bar{\Psi}_R^{(0)} = (\bar{\eta}_*/\bar{\eta}_m)^{(0)} = 1 + 0.710\left[1 + \frac{0.05}{0.07}\right] = 2.217$$

and

$$\epsilon^{(0)} = (\eta_f - \eta_c)\,\bar{\eta}_m\left(\frac{\bar{\eta}_*}{\bar{\eta}_m} - 1\right)$$
$$= 0.210 \times 0.333 \times 1.217$$
$$= .0852$$

The calculation may now be repeated and a second approximation obtained using $\epsilon^{(0)}$. The following results are obtained:

Quantity	Assumed Value	$(\ )^{(0)}$	$(\ )^{(1)}$	$(\ )^{(2)}$
ϵ	0	0.0852	0.0817	0.0817
$\overline{\Psi}_R$	-	2.217	2.167	2.167
Ψ_N	-	0.571	0.608	0.608

This hypothetical example illustrates several general properties of the solution. Even for large corrections, the iteration scheme rapidly converges to the true value, regardless of the initial choice of ϵ. Further, the magnitudes of the neglected terms in Eq. A-15 may be evaluated and suitable correction applied before the final iteration. For finite overheats, ξ will also enter the computation; since ξ appears only as a multiplier of v and is always close to one, its contribution to the computation should be negligible.

Summary

A rapidly convergent procedure for obtaining end loss corrections appropriate to transitional flow is given. Eq. A-22 indicates that the support temperature may contribute significantly to the correction of the normalized recovery ratio, and unless the end losses are small, it must be accurately known. The support temperature enters the Nusselt number correction only through the parameter v, and unless the parameter ζ is less than 5, it has a negligible effect on the corrected value Nu_0.

APPENDIX B

NUMERICAL PROCEDURES FOR DATA REDUCTION

The utility of a hot-wire in quantitative investigations depends on the inherent accuracy of the instrument and the ease with which the resulting measurements may be translated into the dynamic and thermodynamic quantities of interest. One of the most cumbersome parts of a hot-wire investigation is the data reduction procedure, since an iterative and rather tedious calculation is required to obtain the final quantities of interest.

An IBM 7090 data reduction program was developed to handle this phase of the investigation. A serious user of the hot-wire technique will find such a program of great utility, inasmuch as tables of constants may be used to represent thermodynamic variables such as $\mu(T)$ to any desired degree of accuracy, and a high degree of convergence may be obtained without significant computing costs. Using the present program, the average time to compute all quantities (ρ, u, ρu, Re_0, T_0, M, etc.) at a given point in the flow field to a convergence of one part in 10^4 was about one second on the 7090.

The present program is set up to handle two alternative computations involving three of the four variables p_{t_2}, p, R_{awm}, and $(dR/di^2)_{i=0}$. These combinations are:

PITOT Group: p_{t_2}, R_{awm}, $(dR/di^2)_{i=0}$

STATIC Group: p, R_{awm}, $(dR/di^2)_{i=0}$

In addition to the three measured flow properties, the following hot-wire constants must also be specified:

a. Wire length and diameter

b. Resistivity coefficient α_r

c. Wire resistance at reference temperature T_r

Tables of thermodynamic properties of the test gas must also be given. In this program, the values of $\mu(T)$ for air are those compiled by McCarthy (38) using a Lennard-Jones model at low temperatures and a Sutherland viscosity law at higher temperatures. The $\mu(T)$ relation is given in Table 3 of Subroutine CONST listed at the end of this Appendix. The ratio of specific heats γ was taken to be a constant, and equal to 7/5. The air thermal conductivity $k(T)$ was taken from Hilsenrath and Beckett (16) and is listed in Table 1 of Subroutine CONST. The wire thermal conductivity $k_w(T)$ was represented by the two-term formula

$$k_w(T) = C_1 + C_2\,(T-273),\ [T] = {}^\circ K\ .$$

Zero Current Relations

The effect of overheat on the measured heat transfer coefficient is shown to be small in Appendix D. Thus, the slope of the R vs i^2R relation is linear and is a direct measure of the heat transfer coefficient. Using careful instrumentation techniques, this slope may be determined with great accuracy even at overheats as low as 3-5%. The formulas for the end loss correction factors are greatly simplified for this case, and may be expressed as

$$\Psi_N = (1 - \omega)\left[1 - \tfrac{1}{2}\left(t_s s \frac{\omega}{1-\omega}\right) - \tfrac{1}{2}\left(t_s s \frac{\omega}{1-\omega}\right)^2\right] \qquad \text{(B-1)}$$

$$\Psi_R = 1 - \frac{\omega}{1-\omega}\frac{\eta_s}{\eta_m} \tag{B-2}$$

$$\overline{\Psi}_R = 1 + \frac{\omega}{1-\omega}\left[1 + \frac{\eta_c - \eta_s}{\eta_m - \eta_c}\right] \tag{B-3}$$

$$\omega = \tanh\nu/\nu \tag{B-4}$$

where ν is given by the implicit relation

$$\frac{\nu^2}{(1-\omega+\frac{1}{2}t_s\omega)(1+\epsilon s)} = \left(\frac{\ell}{d}\right)^2 \left(\frac{k_0}{k_w}\right) Nu_m \tag{B-5}$$

$$\epsilon = -\tfrac{1}{2}\, t_s \left(\frac{\omega}{1-\omega}\right) . \tag{B-6}$$

Nusselt Number Relation

For any quantitative investigation involving Mach numbers less than 3, the variation of Nu_0 with both Re_0 and M must be considered. Only a limited amount of experimental data exists in the subsonic range and in the very low Reynolds number supersonic regime; therefore, an extrapolation of available results was necessary. This was accomplished by fairing the best smooth curve through the existing data and extrapolating to (a) the theoretical free-molecule heat transfer law at low Reynolds numbers and (b) to the empirical continuum heat transfer law at high Reynolds numbers. Free molecule flow was assumed to be represented by an accommodation coefficient α of unity, a specific heat ratio γ of 7/5 and a Prandtl number Pr of 0.7. At high Reynolds numbers, the results of Spangenberg (19) were used to indicate the variation of Nu_0 with

M between M = 0 and M = 2, and the value of Nu_0 for M ≥ 2 was taken to be that found by Laufer and McClellan (1). All curves were therefore asymptotically correct in the limits $Re_0 \to 0$ and $Re_0 \to \infty$, both in slope and absolute value (assuming an accommodation coefficient of unity!).

A tabular representation of Nu_0 (Re_0, M) over the range $0.2 < M < \infty$ and $10^{-1} < Re_0 < 10^3$ would require an undue amount of data storage in the computer. It was decided to adopt the alternative procedure of finding an analytic expression which represented the master calibration curves to a high degree of accuracy. Although the resulting expression was algebraically complex, its solution offered little numerical difficulty using standard computing techniques.

The following expression was found to represent the empirical hot-wire heat loss data and free-molecule theory for Nu_0 (Re_0, M)*;

$$Nu_0 = ENTRM \cdot \left[.1400 + .2302 \left(\frac{Re_0^{.7114}}{15.44 + Re_0^{.7114}} \right) + \left(\frac{.01569}{.3077 + Re_0^{.7378}} \right) \left(\frac{15}{15 + Re_0^{3}} \right) \right] \cdot EMTRM \qquad (B\text{-}7)$$

where

$$ENTRM = Re_0^{n} \qquad (B\text{-}8)$$

* For those unfamiliar with FORTRAN notation, groups of algebraic characters are to be read as a single variable.

$$EMTRM = 1 + ATRM \cdot BTRM \cdot CTRM \tag{B-9}$$

$$ATRM = \frac{.6039}{M} + .5701\left[\left(\frac{M^{1.222}}{1+M^{1.222}}\right)^{1.569} - 1\right] \tag{B-10}$$

$$BTRM = 1 + \left(.300 - \frac{.0650}{M^{1.670}}\right)\left(\frac{Re_0}{4+Re_0}\right) \tag{B-11}$$

$$CTRM = 1.834 - 1.634\left(\frac{Re_0^{1.109}}{2.765 + Re_0^{1.109}}\right) \tag{B-12}$$

$$n = 1 - \tfrac{1}{2}\left(\frac{Re_0^{.6713}}{2.571 + Re_0^{.6713}}\right) \tag{B-13}$$

This formula is asymptotically correct for all M as $Re_0 \to 0$ (free-molecule limit with Pr = 0.7, $\alpha = 1$, and $\gamma = 1.4$) and is within ±7% of the measured values of Nu_0 for $10^{-1} < Re_0 < 10^3$ and $M > 0.2$. For the range $M > 0.6$ and $2 \times 10^{-1} < Re_0 < 10^2$, the formula is believed to be accurate to within about ±3%. For $M \to \infty$, $2 \times 10^{-1} < Re_0 < 10^2$, the formula represents the mean line through the present measurements and the data of Laufer and McClellan (1) to about ±0.75%.

In Equation B-7, the quantity EMTRM is the ratio $[Nu_0(M)/Nu_0(M \to \infty)]$ evaluated at a fixed Reynolds number. The quantity n given by Equation B-13 is an accurate representation of the slope n of the high Mach number Nu_0-Re_0 curve shown in Figure 9.

The results of free-molecule theory are available only in tabular form (8). However, the fact that the free-molecule heat transfer law possesses closed form solutions as $M \to 0$ and

$M \to \infty$ allows the following simple analytic representation to be written:

$$\frac{Nu_0(Re_0, M)}{Re_0} = \frac{.2023}{M} + .1910 \left(\frac{M^{1.222}}{1+M^{1.222}}\right)^{1.596} \qquad \text{(B-14)}$$

This quantity appears in the ATRM expression of Equation B-10. Again, the values $\alpha = 1$, $Pr = 0.7$, and $\gamma = 1.4$ have been used. This expression is in error by less than $\pm 3\%$ for all M, less than $\pm 0.5\%$ for $0.8 < M < \infty$, and approaches the exact values as $M \to 0$ and $M \to \infty$.

Recovery Temperature Relation

It was noted in Section IV.2 that the normalized recovery factor $\bar{\eta}_*(Kn_\infty)$ is independent of Mach number within the range and accuracy of present experimental evidence. Therefore, the solid curve of Figure 10 was used to interpret all measured wire recovery temperatures. This relation appears in the data reduction program as Table 5, Subroutine CONST. The two free-molecule functions $f(s_1)$ and $g(s_1)$ are listed in the same subroutine as Tables 6p and 6pp respectively.

Program Logic

The data reduction program was formulated as an iterative routine. For both the PITOT and STATIC computations, initial guesses are assigned to M and T_0, the end loss corrections computed, and new v alues for M and T_0 obtained. The iteration is repeated until the required convergence is obtained. A schematic

diagram of the program is given on the following page.

The detailed features of the program may be readily ascertained from an examination of the program listing given at the end of this Appendix. However, it is important to point out one serious and fundamental difficulty associated with the use of the three quantities p_{t_2}, R_{awm}, and $(dR/di^2)_{i=0}$ to specify the flow field. Suppose that initial guesses have been assigned to M and T_0. Then a trial value of Re_0 may be computed (Subroutines PRLCM and NUOREO) and a new guess for M may be found (Subroutine MF22) from the dimensionless quantity*

$$FI7 = \frac{Re_0 \mu_0}{\alpha p_{t_2}} \sqrt{(\frac{\gamma+1}{2\gamma}) R T_0} \qquad \text{(B-15)}$$

For $M < 1$, we have

$$(\frac{\gamma+1}{2} M^2)(1 + \frac{\gamma-1}{2} M^2)^{-(\frac{\gamma+1}{\gamma-1})} = (FI7)^2 \qquad \text{(B-16)}$$

and for $M > 1$,

$$(1 + \frac{\gamma-1}{2} M^2)(\frac{\gamma+1}{2} M^2)^{-(\frac{\gamma+1}{\gamma-1})} [\frac{2\gamma M^2 - (\gamma-1)}{\gamma+1}]^{\frac{2}{\gamma-1}} = (FI7)^2 \qquad \text{(B-17)}$$

* For STATIC calculations, p_{t_2} in Equation B-15 is replaced by p. The resulting function is monotonic, and proportional to M^2 as $M^2 \to \infty$.

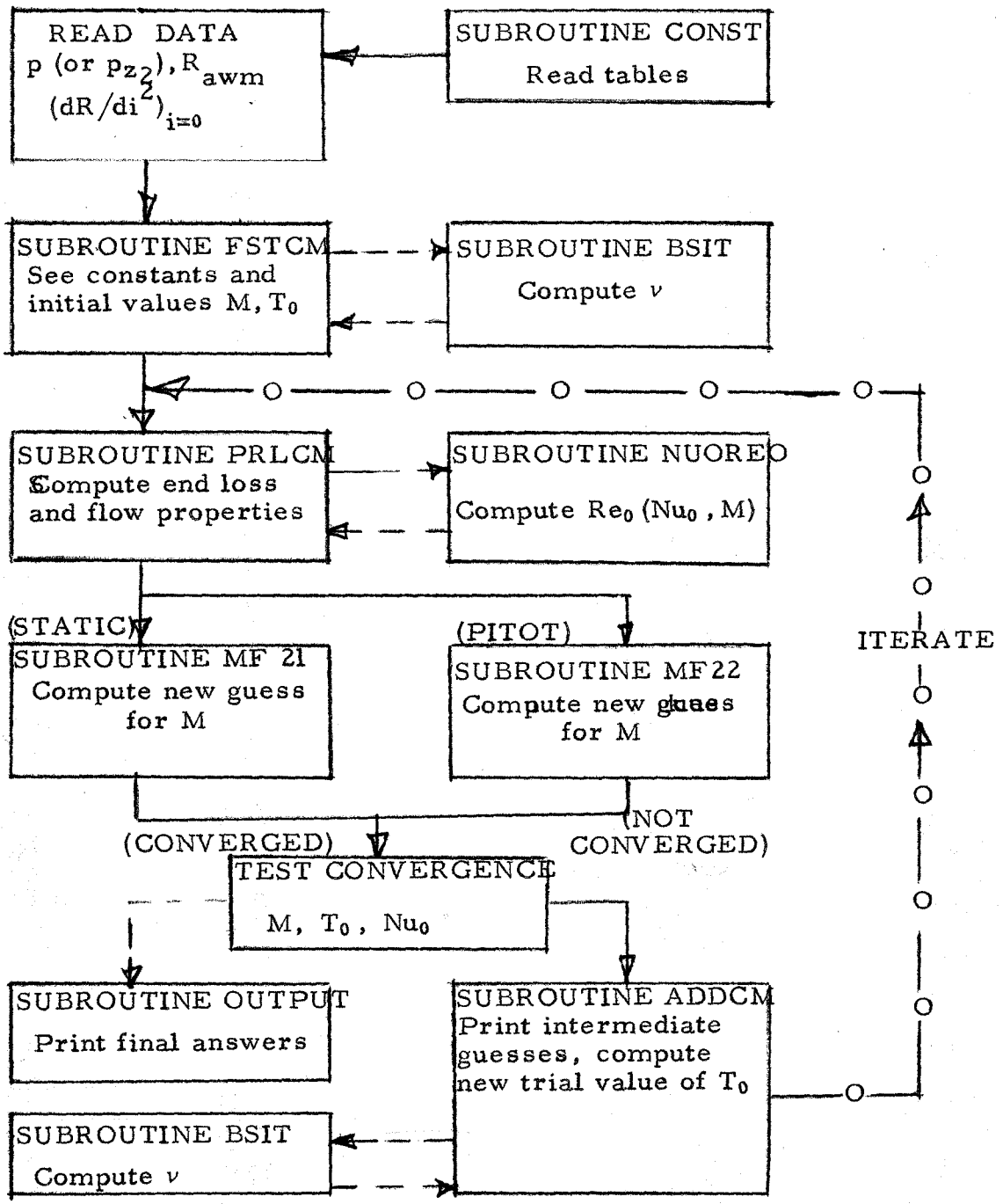
READ DATA
p (or p_{z_2}), R_{awm}
$(dR/di^2)_{i=0}$
SUBROUTINE CONST
Read tables
SUBROUTINE FSTCM
See constants and initial values M, T_0
SUBROUTINE BSIT
Compute ν
SUBROUTINE PRLCM
Compute end loss and flow properties
SUBROUTINE NUORE
Compute Re_0 (Nu_0, M)
(STATIC)
SUBROUTINE MF 21
Compute new guess for M
(PITOT)
SUBROUTINE MF22
Compute new guess for M
(CONVERGED)
(NOT CONVERGED)
TEST CONVERGENCE
M, T_0, Nu_0
SUBROUTINE OUTPUT
Print final answers
SUBROUTINE ADDCM
Print intermediate guesses, compute new trial value of T_0
SUBROUTINE BSIT
Compute ν
ITERATE

The behavior of FI7 as a function of M is shown in the sketch below.

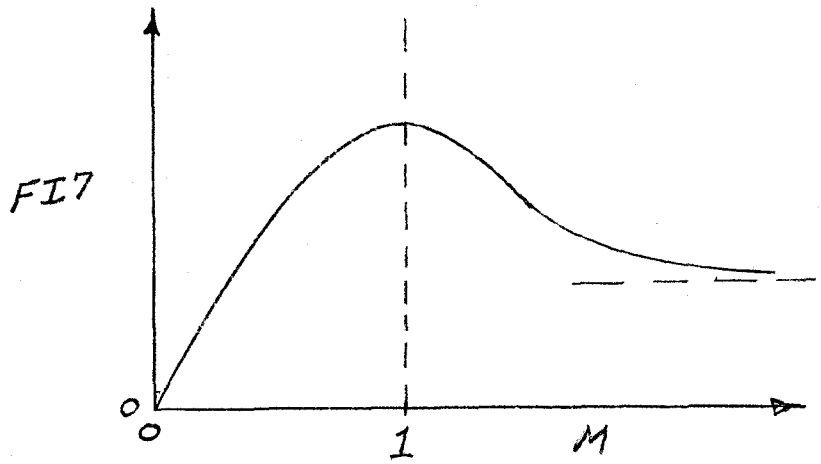

It is apparent that the function is double-valued, and that [dM/d(FI7)] becomes very large at higher Mach numbers. This means that any inaccuracy in the measured values of p_{t_2} or (dR/di^2) will lead to an extremely large error in the final calculated value of M if $M \gtrsim 4$. Now this error is not serious in determining the local value of Re_0, since the $Nu_0 (Re_0, M)$ relation is relatively insensitive to M at these values. On the other hand, the Knudsen number may be expressed as

$$Kn_\infty \sim Re_0 \left(\frac{\mu_0 (T_0)}{\mu_\infty (T_\infty)}\right) \cdot \frac{1}{M}$$

and is insensitive to errors in M ($M \gg 1$) only if $\mu \sim T$. For the present experiments and those reported in Part II of this thesis, μ_∞ is more nearly proportional to $T^{3/2}$, and in the transitional range where $Kn_\infty \sim O(1)$, the computed value of $\bar{\eta}_*$ may be seriously in error at the higher Mach numbers if a PITOT calculation is made.

Fortunately, the values of Kn_∞ were sufficiently large in the wake tests of Section V that no appreciable error was incurred; that is, Kn_∞ was large enough that its uncertainty did not cause a significant error in $\bar{\eta}_*$ or the computed value of T_0.

In summary, the use of the three measured quantities p_{t_2}, R_{awm}, and $(dR/di^2)_{i=0}$ may lead to sizeable uncertainties in the quantities M, p, and T if the Mach number is large. However, the local values of the ρu-product and the stagnation temperature T_0 may still be accurately determined if the local Knudsen number is not close to unity.

Program Listing

The following "dictionary" is used to interpret the program code:

Q1 = Q4, Q10, Q12, Q17 - Q20 = Case identification

Q5 = Group identification (PITOT/STATIC)

Q6 = Value of p or p_{t_2} (mm Hg.)

Q7 = $(dR/di^2)_{i=0}$ (Ω/amp^2)

Q8, Q13 = $R_{awm}(\Omega)$, $R_r(\Omega)$

Q9 = Initial guess for M

Q11 = η_s

Q14, Q15 = (ℓ/d), ℓ(cm)

Q16 = α_r ($^\circ C^{-1}$ at $0^\circ C$)

C1, C2 = Constants in k_w formula

C5 = Initial guess for η_m

C40 = Gas constant R = 2.87×10^6 (cm^2/sec^2-°K)

C41 = γ

C42 = T_r = 273°K

Z18 = Nu_0

Z19 = $\overline{\eta}_*$

Z20 = M

Z21 = T_0 (°K)

Z22 = ρu (g(M)/cm^2-sec)

Z23 = u (cm/sec.)

Z24 = T_∞ (°K)

Z25 = Re_0

Z26 = Re_∞

Z27 = T* (°K)

Z28 = Kn_∞

Z30 = Ψ_R

Z31 = $\overline{\Psi}_R$

Z32 = Ψ_N

Z34 = T_m (°K)

NZ35 = N (number of iterations)

Z37 = Convergence flag

Y1, Y1, Y3 = Storage locations for η_m, Nu_0, M

EPS = ϵ

ETAS = η_s

FKO = k_0 (cal/sec-cm-°K)

FKW = k_w (cal/sec-cm-°K)

FMUO = μ_0 (gm(m)/cm-sec)

FNBR = $\overline{\eta}_m$

FNU = γ

FNUC = η_c

FNUF = η_f

FNUM = Nu_m

FI7 = Defined by Eq. B-15

SO = s

SS = s_1

TAW = $f(s_1)$

TS = t_s

TSBZ = $g(s_1)$

VISIN = μ_∞ (gm(m)/cm-sec)

WO = ω

```
      COMMON Z18,Z19,Z20,Z21,Z22,Z23,Z24,Z25,Z26,Z27,Z28,Z30,Z31,Z32,Z33
     1,Z34,Z35,Z37
      COMMON C1,C2,C5,C40,C41,C42
      COMMON Q1,Q2,Q3,Q4,Q5,Q6,Q7,Q8,Q10,Q11,Q12,Q13,Q14,Q15,Q16,Q17,Q18
     1,Q19,Q20,Q9
      COMMON D,EPS,ETAS,FKD,FKW,FMUN,FMUO,FNBR,FNU,FNUC,FNUF,FNUM,FI7,NZ
     135,SO,SS,TAW,TS,TSBZ,VISIN,WO,Y1,Y2,Y3
      COMMON TBL1,TBL1P,TBL3,TBL3P,TBL4,TBL4P,TBL5,TBL5P,TBL6,TBL6P,TBL6
     1PP
      DIMENSION TBL1(41),TBL1P(41),TBL3(43),TBL3P(43),TBL4(13),TBL4P(13)
     1,TBL5(40),TBL5P(40),TBL6(28),TBL6P(28),TBL6PP(28)
      DIMENSION Z37(3)

            MAIN PROGRAM
      PITOT=(+6HPITOT )
      STATIC=(+6HSTATIC)
      PTOT=(+6HPTOT  )
      NZ35=1
      CALL CONST
   10 READ INPUT TAPE 5,11,Q1,Q2,Q18,Q19,Q3,Q5,Q6,Q7,Q8                    INPT
   11 FORMAT (6A6,3E11.4)                                                  INPT
      READ INPUT TAPE 5,12,Q9,Q2,Q18,Q12,Q10,Q20,Q16,Q14,Q13               INPT
   12 FORMAT (6A6,3E11.4)                                                  INPT
      IF (Q1-PTOT) 20,9000,20
   20 CALL FSTCM
   30 CALL PRLCM
   50 IF (Q5-PITOT) 55,70,55
   55 IF (Q5-STATIC) 9900,60,9900
   60 TEMP=SQRTF(1./((C41-1.)**2)+(4./(C41**2-1.))*((FI7)**2))             MF21
      Z20=SQRTF((-1./(C41-1.))+TEMP)                                       MF21
      GO TO 80
   70 CALL MF22
   80 DLT1=ABSF(Z20-Y3)-.001
      IF (DLT1) 150,150,100
  100 DLT4=NZ35-12
  110 IF (DLT4) 120,200,200
  120 NZ35=NZ35+1
      CALL ADDCM
      GO TO 30
  200 Z37(1)=(+6H DID N)
      Z37(2)=(+6HOT CON)
      Z37(3)=(+6HVERGE )
      CALL OUTPUT
      GO TO 10
  150 DLT2=ABSF(FMUN-Y1)-.0001
  160 IF (DLT2) 170,100,100
  170 DLT3=ABSF((Z18-Y2)/Y2)-.0001
      IF (DLT3) 190,190,100
  190 Z37(1)=(+6H CONVE)
      Z37(2)=(+6HRGED  )
      Z37(3)=(+6H      )
      CALL OUTPUT
      GO TO 10
 9600 CALL EXIT
 9900 WRITE OUTPUT TAPE 6,9901
 9901 FORMAT (31H Q5 IS NEITHER STATIC NOR PITOT)
      GO TO 10
      END
```

```
 SUBROUTINE FSTCM
 COMMON Z18,Z19,Z20,Z21,Z22,Z23,Z24,Z25,Z26,Z27,Z28,Z30,Z31,Z32,Z33
1,Z34,Z35,Z37
 COMMON C1,C2,C5,C40,C41,C42
 COMMON Q1,Q2,Q3,Q4,Q5,Q6,Q7,Q8,Q10,Q11,Q12,Q13,Q14,Q15,Q16,Q17,Q18
1,Q19,Q20,Q9
 COMMON D,EPS,ETAS,FKO,FKW,FMUN,FMUO,FNBR,FNU,FNUC,FNUF,FNUM,FI7,NZ
135,SO,SS,TAW,TS,TSBZ,VISIN,WO,Y1,Y2,Y3
 COMMON TBL1,TBL1P,TBL3,TBL3P,TBL4,TBL4P,TBL5,TBL5P,TBL6,TBL6P,TBL6
1PP
 DIMENSION TBL1(41),TBL1P(41),TBL3(43),TBL3P(43),TBL4(13),TBL4P(13)
1,TBL5(40),TBL5P(40),TBL6(28),TBL6P(28),TBL6PP(28)
 DIMENSION Z37(3)
                        SET CONSTANTS
 C1=0.072
 C2=0.0000077
 C5=1.025
 C40=2871000.0
 C41=1.4
 C42=273.0
 Q11=0.9030
                        SET INITIAL VALUES
 EPS=0.06
 FNU=2.5
 FMUN=C5
 NZ35=1
 Q9=2.00
 SO=0.5
 TS=.9030-1.025
 Y1=C5
 Y3=2.00
 Z20=2.0
                        COMPUTE
 Z34=C42+(Q8-Q13)/(Q13*Q16)
 FKW=C1+(Z34-C42)*C2
 Z21=Z34/FMUN
 Q15=Q14*.000254
 NO=41
 CALL TBLKP(Z21,TBL1,FKO,TBL1P,NO)
 FKO=FKO*(0.00001)
 FNUM=Q16*Q13*Q8/(3.1415927*Q15*FKO*Q7*4.187)
 CALL BSIT
 RETURN
 END
```

```
      SUBROUTINE PRLCM
      COMMON Z18,Z19,Z20,Z21,Z22,Z23,Z24,Z25,Z26,Z27,Z28,Z30,Z31,Z32,Z33
     1,Z34,Z35,Z37
      COMMON C1,C2,C5,C40,C41,C42
      COMMON Q1,Q2,Q3,Q4,Q5,Q6,Q7,Q8,Q10,Q11,Q12,Q13,Q14,Q15,Q16,Q17,Q18
     1,Q19,Q20,Q9
      COMMON D,EPS,ETAS,FKO,FKW,FMUN,FMUO,FNBR,FNU,FNUC,FNUF,FNUM,FI7,NZ
     135,SO,SS,TAW,TS,TS8Z,VISIN,WO,Y1,Y2,Y3
      COMMON TBL1,TBL1P,TBL3,TBL3P,TBL4,TBL4P,TBL5,TBL5P,TBL6,TBL6P,TBL6
     1PP
      DIMENSION TBL1(41),TBL1P(41),TBL3(43),TBL3P(43),TBL4(13),TBL4P(13)
     1,TBL5(40),TBL5P(40),TBL6(28),TBL6P(28),TBL6PP(28)
      DIMENSION Z37(3)
      WO =(EXPF(2.*FNU)-1.)/(FNU*(EXPF(FNU*2.)+1.))
      TS=Q11-Y1
      SO=(Q16*Z21)/(1.+Q16*(Z34-C42))
      Z32=(1.-WO)*(1.-0.5*TS*SO*(WO/(1.-WO))-0.5*(TS*SO*WO/(1.-NO))**2)
      Z18=Z32*FNUM
      Y2=Z18
      NO1=43
      CALL TBLKP(Z21,TBL3,FMUO,TBL3P,NO1)
      FMUO=FMUO*(0.0000001)
      Z24=Z21/(1.+0.5*(C41-1.)*(Z20**2))
      CALL TBLKP(Z24,TBL3,VISIN,TBL3P,NO1)
      VISIN=VISIN*(0.0000001)
      CALL NUOREO
      Z28=(VISIN*Z20/(Z25*FMUO))*SQRTF(0.5*C41*3.1415927)
      NO1=40
      CALL TBLKP(Z28,TBL5,Z19,TBL5P,NO1)
      NO1=40
      CALL TBLKP (Z20,TBL4,FNUC,TBL4P,NO1)
      Z31=1.+WO*(1.+(FNUC-Q11)/(Y1-FNUC))/(1.-WO)
      FI7=(Z25*FMUO*SQRTF(C40*Z21*(C41+1.)/(2.*C41)))/(0.3386*Q6)
      SS=Z20*SQRTF(0.5*C41)
      NO=28
      CALL TBLKP(SS,TBL6,TAW,TBL6P,NO)
      CALL TBLKP(SS,TBL6,TS8Z,TBL6PP,NO)
      FNUF=(TAW/TS8Z)/(1.+.5*(Z20**2)*(C41-1.))
      FNBR=Z19/Z31                                                    IMCM
      FMUN=FNUC+(FNUF-FNUC)*FNBR                                      IMCM
      RETURN
      END
```

```
      SUBROUTINE ADDCM
      COMMON Z18,Z19,Z20,Z21,Z22,Z23,Z24,Z25,Z26,Z27,Z28,Z30,Z31,Z32,Z33
     1,Z34,Z35,Z37
      COMMON C1,C2,C5,C40,C41,C42
      COMMON Q1,Q2,Q3,Q4,Q5,Q6,Q7,Q8,Q10,Q11,Q12,Q13,Q14,Q15,Q16,Q17,Q18
     1,Q19,Q20,Q9
      COMMON D,EPS,ETAS,FKO,FKW,FMUN,FMUO,FNBR,FNU,FNUC,FNUF,FNUM,FI7,NZ
     135,SO,SS,TAW,TS,TSBZ,VISIN,WO,Y1,Y2,Y3
      COMMON TBL1,TBL1P,TBL3,TBL3P,TBL4,TBL4P,TBL5,TBL5P,TBL6,TBL6P,TBL6
     1PP
      DIMENSION TBL1(41),TBL1P(41),TBL3(43),TBL3P(43),TBL4(13),TBL4P(13)
     1,TBL5(40),TBL5P(40),TBL6(28),TBL6P(28),TBL6PP(28)
      DIMENSION Z37(3)
      Z21=Z34/FMUN
      NO=41
      CALL TBLKP(Z21,TBL1,FKO,TBL1P,NO)
      FKO=FKO*(0.00001)
      FNUM=Q16*Q13*Q8/(3.1415927*Q15*FKO*Q7*4.187)
      Z22=Z25*FMUO*Q14/Q15
      Z23=Z20*SQRTF(C41*C40*Z24)
      Z26=Z25*FMUO/VISIN
      Z27=Z21*(FNUC+(FNUF-FNUC)*Z19)
      Z30=(1.-WO*(Q11/FMUN))/(1.-WO)
      ETAS=Z27/Z21
      EPS=ETAS-FMUN
      CALL OSIT
      Y3=Z20
      Y1=FMUN
      Y2=Z18
      PITOT=(+6HPITOT )
      STATIC=(+6HSTATIC)
      IF (Q5-STATIC) 10,30,10
   10 IF (Q5-PITOT) 20,40,20
   20 WRITE OUTPUT TAPE 6,21
   21 FORMAT (31H Q5 IS NEITHER STATIC NOR PITOT)
      GO TO 110
   30 IF (Z20-1.) 31,31,32
   31 Z99=(1.+.5*(C41-1.)*Z20*Z20)**(C41/(C41-1.))*Q6
      GO TO 50
   32 Z99=((.5*(C41+1.)*Z20*Z20)**(C41/(C41-1.))*((C41+1.)/(2.*C41*Z20*Z
     120-C41+1.))**(1./(C41-1.)))*Q6
      GO TO 50
   40 IF (Z20-1.) 41,41,42
   41 Z99=(1.+.5*(C41-1.)*Z20*Z20)**(C41/(C41-1.))**(-1.)*Q6
      GO TO 50
   42 Z99=((.5*(C41+1.)*Z20*Z20)**(C41/(C41-1.))*((C41+1.)/(2.*C41*Z20*Z
     120-C41+1.))**(1./(C41-1.)))**(-1.)*Q6
      GO TO 50
   50 WRITE OUTPUT TAPE 6,106,Z22,Z25,Z26,Z30
  106 FORMAT (6H RHOU=E11.4,5H REO=E11.4,7H REINF=E11.4,7H PSI R=E11.4)
      WRITE OUTPUT TAPE 6,107,Z23,Z18,Z27,Z31
  107 FORMAT (6H    U=E11.4,5H NUO=E11.4,7H TSTAR=E11.4,7H PSIBR=E11.4)
      WRITE OUTPUT TAPE 6,108,Z20,Z34,Z19,Z32
  108 FORMAT (6H    M=E11.4,5H  TM=E11.4,7H ETAB*=E11.4,7H PSI N=E11.4)
      WRITE OUTPUT TAPE 6,109,Z21,Z28,Z24,Z99
  109 FORMAT (6H   TO=E11.4,5H  KN=E11.4,7H  TINF=E11.4,7H   *P*=E11.4)
      WRITE OUTPUT TAPE 6,111
  111 FORMAT (1H )
      RETURN
      END
```

```
      SUBROUTINE OUTPUT
      COMMON Z18,Z19,Z20,Z21,Z22,Z23,Z24,Z25,Z26,Z27,Z28,Z30,Z31,Z32,Z33
     1,Z34,Z35,Z37
      COMMON C1,C2,C5,C40,C41,C42
      COMMON Q1,Q2,Q3,Q4,Q5,Q6,Q7,Q8,Q10,Q11,Q12,Q13,Q14,Q15,Q16,Q17,Q18
     1,Q19,Q20,Q9
      COMMON D,EPS,ETAS,FKO,FKW,FMUN,FMUO,FNBR,FNU,FNUC,FNUF,FNUM,FI7,NZ
     135,SO,SS,TAW,TS,TSBZ,VISIN,WO,Y1,Y2,Y3
      COMMON TBL1,TBL1P,TBL3,TBL3P,TBL4,TBL4P,TBL5,TBL5P,TBL6,TBL6P,TBL6
     1PP
      DIMENSION TBL1(41),TBL1P(41),TBL3(43),TBL3P(43),TBL4(13),TBL4P(13)
     1,TBL5(40),TBL5P(40),TBL6(28),TBL6P(28),TBL6PP(28)
      DIMENSION Z37(3)
      Z23=Z20*SQRTF(C41*C40*Z24)
      Z22=Z25*FMUO*Q14/Q15
      Z26=Z25*FMUO/VISIN
      Z27=Z21*(FNUC+(FNUF-FNUC)*Z19)
      Z30=(1.-WO*(Q11/FMUN))/(1.-WO)
      PITOT=(+6HPITOT )
      STATIC=(+6HSTATIC)
      IF (Q5-STATIC) 10,30,10
   10 IF (Q5-PITOT) 20,40,20
   20 WRITE OUTPUT TAPE 6,21
   21 FORMAT (31H Q5 IS NEITHER STATIC NOR PITOT)
      GO TO 110
   30 IF (Z20-1.) 31,31,32
   31 Z99=(1.+.5*(C41-1.)*Z20*Z20)**(C41/(C41-1.))*Q6
      GO TO 50
   32 Z99=((.5*(C41+1.)*Z20*Z20)**(C41/(C41-1.))*((C41+1.)/(2.*C41*Z20*Z
     120-C41+1.))**(1./(C41-1.)))*Q6
      GO TO 50
   40 IF (Z20-1.) 41,41,42
   41 Z99=(1.+.5*(C41-1.)*Z20*Z20)**(C41/(C41-1.))**(-1.)*Q6
      GO TO 50
   42 Z99=((.5*(C41+1.)*Z20*Z20)**(C41/(C41-1.))*((C41+1.)/(2.*C41*Z20*Z
     120-C41+1.))**(1./(C41-1.)))**(-1.)*Q6
      GO TO 50
   50 WRITE OUTPUT TAPE 6,100,Q1,Q3,Q5,Q6
  100 FORMAT (10H   RUN=63-A6,8H    Y/D=A6,22H * OPERATIONAL DATA   A6,1
     1H=F7.3,31H       *          WIRE PROPERTIES)
      WRITE OUTPUT TAPE 6,101,Q18,Q2,Q7,Q12
  101 FORMAT (10H PO(PSIG)=A6,8H    X/D=A6,29H * DIMEN.=CGS
     1  A=1PE11.4,11H  *  WIRE  A6)
      WRITE OUTPUT TAPE 6,102,Q19,Q20,Q5,Q8,Q13,Q16
  102 FORMAT (10H TO(DEGF)=A6,8H  RE(D)=A6,15H * VARIAB=A+RM+A6,8H      R
     1M=F7.3,12H       *  RR=F7.3,12H       ALPHA=1PE11.4)
      WRITE OUTPUT TAPE 6,103,Q4,Q10,Q17,Q9,Q14,Q11
  103 FORMAT (10H    THETA=A6,8H      D=A6,10H * EMISIV=E11.4,8H   M(O)=
     1F6.2,13H       * L/D=F6.1,13H       ETA S=F7.4)
      WRITE OUTPUT TAPE 6,104,Z37(1),Z37(2),Z37(3),NZ35
  104 FORMAT (57H                THE FOLLOWING QUANTITIES WERE COMPUTED AN
     1D 3A6,6H IN N=I2,11H ITERATIONS)
      WRITE OUTPUT TAPE 6,105,Q1,Q3,Q2
      WRITE OUTPUT TAPE 7,105,Q1,Q3,Q2
  105 FORMAT (18H            RUN=63-A6,9H     Y/D=A6,9H      X/D=A6)
      WRITE OUTPUT TAPE 6,106,Z22,Z25,Z26,Z30
      WRITE OUTPUT TAPE 7,106,Z22,Z25,Z26,Z30
  106 FORMAT (6H RHOU=E11.4,5H REO=E11.4,7H REINF=E11.4,7H PSI R=E11.4)
      WRITE OUTPUT TAPE 6,107,Z23,Z18,Z27,Z31
```

```
      WRITE OUTPUT TAPE 7,107,Z23,Z18,Z27,Z31
  107 FORMAT (6H     U=E11.4,5H NUO=E11.4,7H TSTAR=E11.4,7H PSIBR=E11.4)
      WRITE OUTPUT TAPE 6,108,Z20,Z34,Z19,Z32
      WRITE OUTPUT TAPE 7,108,Z20,Z34,Z19,Z32
  108 FORMAT (6H     N=E11.4,5H  TM=E11.4,7H ETAB*=E11.4,7H PSI N=E11.4)
      WRITE OUTPUT TAPE 6,109,Z21,Z28,Z24,Z99
      WRITE OUTPUT TAPE 7,109,Z21,Z28,Z24,Z99
  109 FORMAT (6H    TO=E11.4,5H  KN=E11.4,7H  TINF=E11.4,7H    *P*=E11.4)
  110 WRITE OUTPUT TAPE 6,111
      WRITE OUTPUT TAPE 7,111
  111 FORMAT (1H )
      WRITE OUTPUT TAPE 6,112
  112 FORMAT (1H )
      RETURN
      END
```

```
      SUBROUTINE BSIT
      COMMON Z18,Z19,Z20,Z21,Z22,Z23,Z24,Z25,Z26,Z27,Z28,Z30,Z31,Z32,Z33
     1,Z34,Z35,Z37
      COMMON C1,C2,C5,C40,C41,C42
      COMMON Q1,Q2,Q3,Q4,Q5,Q6,Q7,Q8,Q10,Q11,Q12,Q13,Q14,Q15,Q16,Q17,Q18
     1,Q19,Q20,Q9
      COMMON D,EPS,ETAS,FKO,FKW,FMUN,FMUO,FNBR,FNU,FNUC,FNUF,FNUM,FI7,NZ
     135,SO,SS,TAW,TS,TSBZ,VISIN,WO,Y1,Y2,Y3
      COMMON TBL1,TBL1P,TBL3,TBL3P,TBL4,TBL4P,TBL5,TBL5P,TBL6,TBL6P,TBL6
     1PP
      DIMENSION TBL1(41),TBL1P(41),TBL3(43),TBL3P(43),TBL4(13),TBL4P(13)
     1,TBL5(40),TBL5P(40),TBL6(28),TBL6P(28),TBL6PP(28)
      DIMENSION Z37(3)

               THIS IS A DIRECT BISECTION FOR FNU
 20   IF (FNU-8.0) 40,40,950
 40   IF (1.0-FNU) 60,60,960
 60   WO=((EXPF(2.*FNU)-1.)/(EXPF(2.*FNU)+1.))/FNU
      CON=(FKO/FKW)*FNUM*((Q14)**2)*(1.+EPS*SO)
      FTN=(FNU**2)/(1.-WO+.5*TS*SO*WO)
      X1=ABSF(FTN-CON)
      IF (X1-.0002) 990,990,80
 80   IF (FTN-CON) 100,990,200
100   TOP=8.
      BOTT=FNU
      GO TO 300
200   TOP=FNU
      BOTT=1.
      GO TO 300
300   V=.5*(TOP+BOTT)
301   IF (V-7.995) 302,302,950
302   IF (V-1.005) 960,303,303
303   FWO=((EXPF(2.*V)-1.)/(EXPF(2.*V)+1.))/V
      FV=(V**2)/(1.-FWO+.5*TS*SO*FWO)
      X2=ABSF(FV-CON)
      IF (X2-.0002) 900,900,310
310   IF (FV-CON) 400,900,500
400   BOTT=V
      GO TO 300
500   TOP=V
      GO TO 300
900   FNU=V
      GO TO 990
950   WRITE OUTPUT TAPE 6,951
951   FORMAT (15H NU EXCEEDS 8.0)
      FNU=7.99
      GO TO 990
960   WRITE OUTPUT TAPE 6,961
961   FORMAT (13H NU BELOW 1.0)
      FNU=1.01
      GO TO 990
990   WRITE OUTPUT TAPE 6,991,FNU,CON,WO,EPS,
991   FORMAT (6H  FNU=E11.4,6H  CON=E11.4,6H   WO=E11.4,6H  EPS=E11.4)
      RETURN
      END
```

```
      SUBROUTINE NUOREO
      COMMON Z18,Z19,Z20,Z21,Z22,Z23,Z24,Z25,Z26,Z27,Z28,Z30,Z31,Z32,Z33
     1,Z34,Z35,Z37
      COMMON C1,C2,C5,C40,C41,C42
      COMMON Q1,Q2,Q3,Q4,Q5,Q6,Q7,Q8,Q10,Q11,Q12,Q13,Q14,Q15,Q16,Q17,Q18
     1,Q19,Q20,Q9
      COMMON D,EPS,ETAS,FKO,FKW,FMUN,FMUO,FNBR,FNU,FNUC,FNUF,FNUM,FI7,NZ
     I35,SO,SS,TAW,TS,TSDZ,VISIN,WO,Y1,Y2,Y3
      COMMON TBL1,TBL1P,TBL3,TBL3P,TBL4,TBL4P,TBL5,TBL5P,TBL6,TBL6P,TBL6
     1PP
      DIMENSION TBL1(41),TBL1P(41),TBL3(43),TBL3P(43),TBL4(13),TBL4P(13)
     1,TBL5(40),TBL5P(40),TBL6(28),TBL6P(28),TBL6PP(28)
      DIMENSION Z37(3)
               THIS SUBROUTINE SOLVES FOR REO(NUO,M)
10    IF (Z18-.01) 950,950,20
20    IF (Z18-5.) 30,30,960
30    ENTRM=Z25**(1.-.5*(Z25**.6713/(2.571+Z25**.6713)))
      ATRM=0.6039/Z20+0.5701*((Z20**1.222/(1.+Z20**1.222))**1.596-1.)
      BTRM=1.+(0.300-0.0650/Z20**1.670)*(Z25/(4.+Z25))
      CTRM=1.834-1.634*(Z25**1.109/(2.765+Z25**1.109))
      EMTRM=1.+ATRM*BTRM*CTRM
      FC=ENTRM*(.1400+.2302*(Z25**.7114/(15.44+Z25**.7114))+.01569*15./(
     1(.3077+Z25**.7378)*(15.+Z25**3)))*EMTRM
      CON=Z18
      X1=ABSF((FC-CON)/CON)
40    IF (X1-.00005) 990,990,50
50    TR=(CON/.1478)**1.25
      ENTRM=TR**(1.-.5*(TR**.6713/(2.571+TR**.6713)))
      BTRM=1.+(0.300-0.0650/Z20**1.670)*(TR/(4.+TR))
      CTRM=1.834-1.634*(TR**1.109/(2.765+TR**1.109))
      EMTRM=1.+ATRM*BTRM*CTRM
      TFC=ENTRM*(.1400+.2302*(TR**.7114/(15.44+TR**.7114))+.01569*15./((
     1.3077+TR**.7378)*(15.+TR**3)))*EMTRM
      IF (TFC-CON) 60,910,70
60    TRA=TR
      TRB=1.2*TR
61    ENTRM=TRB**(1.-.5*(TRB**.6713/(2.571+TRB**.6713)))
      BTRM=1.+(0.300-0.0650/Z20**1.670)*(TRB/(4.+TRB))
      CTRM=1.834-1.634*(TRB**1.109/(2.765+TRB**1.109))
      EMTRM=1.+ATRM*BTRM*CTRM
      TFCB=ENTRM*(.1400+.2302*(TRB**.7114/(15.44+TRB**.7114))+.01569*15.
     1/((.3077+TRB**.7378)*(15.+TRB**3)))*EMTRM
62    IF (TFCB-CON) 63,920,64
63    TRA=TRB
      TRB=1.2*TRA
      IF (TRB-60.) 61,61,970
64    TOP=TRB
      BOTT=TRA
      GO TO 100
70    TRA=TR
      TRB=.833*TR
71    ENTRM=TRB**(1.-.5*(TRB**.6713/(2.571+TRB**.6713)))
      BTRM=1.+(0.300-0.0650/Z20**1.670)*(TRB/(4.+TRB))
      CTRM=1.834-1.634*(TRB**1.109/(2.765+TRB**1.109))
      EMTRM=1.+ATRM*BTRM*CTRM
      TFCB=ENTRM*(.1400+.2302*(TRB**.7114/(15.44+TRB**.7114))+.01569*15.
     1/((.3077+TRB**.7378)*(15.+TRB**3)))*EMTRM
72    IF (TFCB-CON) 73,920,74
73    TOP=TRA
```

NUO REO
-p2-

```
    BOTT=TRB
    GO TO 100
 74 TRA=TRB
    TRB=.833*TRA
    IF (TRB-.02) 980,71,71
 .0 P=.5*(TOP+BOTT)
101 IF (P-.02) 980,102,102
102 IF (P-60.) 120,120,970
120 ENTRM=P**(1.-.5*(P**.6713/(2.571+P**.6713)))
    BTRM=1.+(0.300-0.0650/Z20**1.670)*(P/(4.+P))
    CTRM=1.834-1.634*(P**1.109/(2.765+P**1.109))
    EMTRM=1.+ATRM*BTRM*CTRM
    FP=ENTRM*(.1400+.2302*(P**.7114/(15.44+P**.7114))+.01569*15./((.30
   177+P**.7378)*(15.+P**3)))*EMTRM
    X2=ABSF((FP-CON)/CON)
130 IF (X2-.00005) 900,900,200
200 IF (FP-CON) 300,900,400
300 BOTT=P
    GO TO 100
400 TOP=P
    GO TO 100
900 Z25=P
    GO TO 990
910 Z25=TR
    GO TO 990
920 Z25=TRB
    GO TO 990
950 WRITE OUTPUT TAPE 6,951
951 FORMAT (19H NUO LESS THAN 0.01)
    Z25=.05
    GO TO 990
960 WRITE OUTPUT TAPE 6,961
961 FORMAT (16H NUO EXCEEDS 5.0)
    Z25=20.
    GO TO 990
970 WRITE OUTPUT TAPE 6,971
971 FORMAT (15H REO EXCEEDS 60)
    Z25=20.
    GO TO 990
980 WRITE OUTPUT TAPE 6,981
981 FORMAT (15H REO BELOW 0.02)
    Z25=.05
    GO TO 990
990 RETURN
    END
```

```
      SUBROUTINE MF22
      COMMON Z18,Z19,Z20,Z21,Z22,Z23,Z24,Z25,Z26,Z27,Z28,Z30,Z31,Z32,Z33
     1,Z34,Z35,Z37
      COMMON C1,C2,C5,C40,C41,C42
      COMMON Q1,Q2,Q3,Q4,Q5,Q6,Q7,Q8,Q10,Q11,Q12,Q13,Q14,Q15,Q16,Q17,Q18
     1,Q19,Q20,Q9
      COMMON D,EPS,ETAS,FKO,FKW,FMUN,FMUO,FNBR,FNU,FNUC,FNUF,FNUM,FI7,NZ
     135,SO,SS,TAW,TS,TSBZ,VISIN,WO,Y1,Y2,Y3
      COMMON TBL1,TBL1P,TBL3,TBL3P,TBL4,TBL4P,TBL5,TBL5P,TBL6,TBL6P,TBL6
     1PP
      DIMENSION TBL1(41),TBL1P(41),TBL3(43),TBL3P(43),TBL4(13),TBL4P(13)
     1,TBL5(40),TBL5P(40),TBL6(28),TBL6P(28),TBL6PP(28)
      DIMENSION Z37(3)
C             THIS IS A DIRECT BISECTION FOR M GREATER THAN ONE.
C           IF M LESS THAN ONE, USE OTHER VERSION OF MF22.
      FM=Z20
   10 IF (FM-1.) 950,950,20
   20 IF (10.-FM) 960,960,30
   30 FC=(1.+.5*(C41-1.)*(FM**2))*(.5*(C41+1.)*(FM**2))**(-(C41+1.)/(C41
     1-1.))*((2.*C41*FM*FM-C41+1.)/(C41+1.))**(2./(C41-1.))
      CON=FI7**2
      X1=ABSF(FC-CON)
   40 IF (X1-.00002) 990,990,50
   50 IF (FC-CON) 60,990,70
   60 TOP=FM
      BOTT=1.
      GO TO 100
   70 TOP=10.
      BOTT=FM
      GO TO 100
   00 P=.5*(TOP+BOTT)
  101 IF (P-1.01) 950,950,102
  102 IF (9.99-P) 960,960,120
  120 FP=(1.+.5*(C41-1.)*P*P)*(.5*(C41+1.)*P*P)**(-(C41+1.)/(C41-1.))*((
     12.*C41*P*P-C41+1.)/(C41+1.))**(2./(C41-1.))
      X2=ABSF(FP-CON)
  130 IF (X2-.00002) 900,900,200
  200 IF (FP-CON) 300,900,400
  300 TOP=P
      GO TO 100
  400 BOTT=P
      GO TO 100
  900 Z20=P
      GO TO 990
  950 WRITE OUTPUT TAPE 6,951
  951 FORMAT (13H  M BELOW 1.0)
      Z20=1.1
      GO TO 990
  960 WRITE OUTPUT TAPE 6,961
  961 FORMAT (16H  M EXCEEDS 10.0)
      Z20=9.9
      GO TO 990
  990 WRITE OUTPUT TAPE 6,991,P,FP,CON,FC
  991 FORMAT (6H     M=E11.4,6H   FP=E11.4,6H  CON=E11.4,6H    FC=E11.4)
      RETURN
      END
```

```
      SUBROUTINE MF22
      COMMON Z18,Z19,Z20,Z21,Z22,Z23,Z24,Z25,Z26,Z27,Z28,Z30,Z31,Z32,Z33
     1,Z34,Z35,Z37
      COMMON C1,C2,C5,C40,C41,C42
      COMMON Q1,Q2,Q3,Q4,Q5,Q6,Q7,Q8,Q10,Q11,Q12,Q13,Q14,Q15,Q16,Q17,Q18
     1,Q19,Q20,Q9
      COMMON D,EPS,ETAS,FKO,FKW,FMUN,FMUO,FNBR,FNU,FNUC,FNUF,FNUM,FI7,NZ
     135,SO,SS,TAW,TS,TSBZ,VISIN,WO,Y1,Y2,Y3
      COMMON TBL1,TBL1P,TBL3,TBL3P,TBL4,TBL4P,TBL5,TBL5P,TBL6,TBL6P,TBL6
     1PP
      DIMENSION TBL1(41),TBL1P(41),TBL3(43),TBL3P(43),TBL4(13),TBL4P(13)
     1,TBL5(40),TBL5P(40),TBL6(28),TBL6P(28),TBL6PP(28)
      DIMENSION Z37(3)
                THIS IS A DIRECT BISECTION FOR M LESS THAN ONE.
                IF M GREATER THAN ONE, USE OTHER VERSION MF22.
      FM=Z20
   10 IF (FM-1.) 20,20,950
   20 IF (FM-.2) 960,30,30
   30 FC=(.5*(C41+1.)*FM*FM)*(1.+.5*(C41-1.)*FM*FM)**(-(C41+1.)/(C41-1.)
     1)
      CON=FI7**2
      X1=ABSF(FC-CON)
   40 IF (X1-.00005) 990,990,50
   50 IF (FC-CON) 60,990,70
   60 TOP=1.
      BOTT=FM
      GO TO 100
   70 TOP=FM
      BOTT=0.2
      GO TO 100
    0 P=.5*(TOP+BOTT)
  101 IF (P-.999) 102,102,950
  102 IF (P-0.2005) 960,120,120
  120 FP=(.5*(C41+1.)*P*P)*(1.+.5*(C41-1.)*P*P)**(-(C41+1.)/(C41-1.))
      X2=ABSF(FP-CON)
  130 IF (X2-.00005) 900,900,200
  200 IF (FP-CON) 300,900,400
  300 BOTT=P
      GO TO 100
  400 TOP=P
      GO TO 100
  900 Z20=P
      GO TO 990
  950 WRITE OUTPUT TAPE 6,951
  951 FORMAT (15H  M EXCEEDS 1.0)
      Z20=.99
      GO TO 990
  960 WRITE OUTPUT TAPE 6,961
  961 FORMAT (17H  M LESS THAN 0.2)
      Z20=0.201
      GO TO 990
  990 WRITE OUTPUT TAPE 6,991,P,FP,CON,FC
  991 FORMAT (6H    M=E11.4,6H   FP=E11.4,6H  CON=E11.4,6H   FC=E11.4)
      RETURN
      END
```

```
      SUBROUTINE TBLKP(VO,VAR,FO,FCN,NO)
      DIMENSION VAR(100),FCN(100)

            THIS SUBROUTINE PERFORMS TABLE LOOK-UP OPERATIONS.
      DO 100 I=1,NO
      VAR1=VAR(I)
      IF (VO-VAR1) 200,150,100
  100 CONTINUE
      WRITE OUTPUT TAPE 6,900,VO,NO
  900 FORMAT (34H VARIABLE EXCEEDS TABLE FOR VALUE E11.4,13H TABLE SIZE
     1=I5)
      FO =FCN(NO)
      GO TO 300
  150 FO=FCN(I)
      GO TO 300
  200 IF (I-1) 210,290,210
  210 I1=I-1
      TEMP=VO-VAR(I1)
      TEM1=VAR(I)-VAR(I1)
      RATIO=TEMP/TEM1
      FO=RATIO*(FCN(I)-FCN(I1))+FCN(I1)
      GO TO 300
  290 FO=FCN(I)
  300 RETURN
      END
```

```
      SUBROUTINE CONST
      COMMON Z18,Z19,Z20,Z21,Z22,Z23,Z24,Z25,Z26,Z27,Z28,Z30,Z31,Z32,Z33
     1,Z34,Z35,Z37
      COMMON C1,C2,C5,C40,C41,C42
      COMMON Q1,Q2,Q3,Q4,Q5,Q6,Q7,Q8,Q10,Q11,Q12,Q13,Q14,Q15,Q16,Q17,Q18
     1,Q19,Q20,Q9
      COMMON D,EPS,ETAS,FKO,FKW,FMUN,FMUO,FNRR,FNU,FNUC,FNUF,FNUM,FI7,NZ
     135,SO,SS,TAW,TS,TSBZ,VISIN,WO,Y1,Y2,Y3
      COMMON TBL1,TBL1P,TBL3,TBL3P,TBL4,TBL4P,TBL5,TBL5P,TBL6,TBL6P,TBL6
     1PP
      DIMENSION TBL1(41),TBL1P(41),TBL3(43),TBL3P(43),TBL4(13),TBL4P(13)
     1,TBL5(40),TBL5P(40),TBL6(28),TBL6P(28),TBL6PP(28)
      DIMENSION Z37(3)
      TBL1  (1 ) = 30.
      TBL1  (2 ) = 40.
      TBL1  (3 ) = 50.
      TBL1  (4 ) = 60.
      TBL1  (5 ) = 70.
      TBL1  (6 ) = 80.
      TBL1  (7 ) = 90.
      TBL1  (8 ) = 100.
      TBL1  (9 ) = 110.
      TBL1  (10) = 120.
      TBL1  (11) = 130.
      TBL1  (12) = 140.
      TBL1  (13) = 150.
      TBL1  (14) = 160.
      TBL1  (15) = 170.
      TBL1  (16) = 180.
      TBL1  (17) = 190.
      TBL1  (18) = 200.
      TBL1  (19) = 210.
      TBL1  (20) = 220.
      TBL1  (21) = 230.
      TBL1  (22) = 240.
      TBL1  (23) = 250.
      TBL1  (24) = 260.
      TBL1  (25) = 270.
      TBL1  (26) = 280.
      TBL1  (27) = 290.
      TBL1  (28) = 300.
      TBL1  (29) = 310.
      TBL1  (30) = 320.
      TBL1  (31) = 330.
      TBL1  (32) = 340.
      TBL1  (33) = 350.
      TBL1  (34) = 360.
      TBL1  (35) = 370.
      TBL1  (36) = 380.
      TBL1  (37) = 390.
      TBL1  (38) = 400.
      TBL1  (39) = 410.
      TBL1  (40) = 420.
      TBL1  (41) = 430.
      TBL1P (1 ) = 0.7039
      TBL1P (2 ) = 0.9117
      TBL1P (3 ) = 1.131
      TBL1P (4 ) = 1.350
      TBL1P (5 ) = 1.568
```

```
TBL1P (6 ) = 1.784
TBL1P (7 ) = 1.996
TBL1P (8 ) = 2.210
TBL1P (9 ) = 2.425
TBL1P (10) = 2.640
TBL1P (11) = 2.855
TBL1P (12) = 3.068
TBL1P (13) = 3.281
TBL1P (14) = 3.492
TBL1P (15) = 3.703
TBL1P (16) = 3.912
TBL1P (17) = 4.119
TBL1P (18) = 4.324
TBL1P (19) = 4.527
TBL1P (20) = 4.729
TBL1P (21) = 4.929
TBL1P (22) = 5.127
TBL1P (23) = 5.323
TBL1P (24) = 5.517
TBL1P (25) = 5.709
TBL1P (26) = 5.897
TBL1P (27) = 6.087
TBL1P (28) = 6.272
TBL1P (29) = 6.457
TBL1P (30) = 6.641
TBL1P (31) = 6.820
TBL1P (32) = 6.999
TBL1P (33) = 7.178
TBL1P (34) = 7.357
TBL1P (35) = 7.530
TBL1P (36) = 7.703
TBL1P (37) = 7.876
TBL1P (38) = 8.043
TBL1P (39) = 8.211
TBL1P (40) = 8.378
TBL1P (41) = 8.545
TBL3  (1 ) = 30.
TBL3  (2 ) = 40.
TBL3  (3 ) = 50.
TBL3  (4 ) = 60.
TBL3  (5 ) = 70.
TBL3  (6 ) = 80.
TBL3  (7 ) = 90.
TBL3  (8 ) = 100.
TBL3  (9 ) = 110.
TBL3  (10) = 120.
TBL3  (11) = 130.
TBL3  (12) = 140.
TBL3  (13) = 150.
TBL3  (14) = 160.
TBL3  (15) = 170.
TBL3  (16) = 180.
TBL3  (17) = 190.
TBL3  (18) = 200.
TBL3  (19) = 210.
TBL3  (20) = 220.
TBL3  (21) = 230.
TBL3  (22) = 240.
TBL3  (23) = 250.
TBL3  (24) = 260.
TBL3  (25) = 270.
TBL3  (26) = 280.
TBL3  (27) = 290.
TBL3  (28) = 300.
TBL3  (29) = 310.
TBL3  (30) = 320.
TBL3  (31) = 330.
TBL3  (32) = 340.
TBL3  (33) = 350.
TBL3  (34) = 360.
TBL3  (35) = 370.
TBL3  (36) = 380.
TBL3  (37) = 390.
TBL3  (38) = 400.
TBL3  (39) = 410.
TBL3  (40) = 420.
TBL3  (41) = 430.
TBL3  (42) = 440.
TBL3  (43) = 450.
TBL3P (1 ) = 215.7
TBL3P (2 ) = 281.1
TBL3P (3 ) = 347.3
TBL3P (4 ) = 416.3
TBL3P (5 ) = 485.6
TBL3P (6 ) = 555.1
TBL3P (7 ) = 622.9
TBL3P (8 ) = 692.9
TBL3P (9 ) = 763.3
TBL3P (10) = 831.9
TBL3P (11) = 899.0
TBL3P (12) = 964.6
TBL3P (13) = 1029.
TBL3P (14) = 1091.
TBL3P (15) = 1152.
TBL3P (16) = 1212.
TBL3P (17) = 1271.
TBL3P (18) = 1329.
TBL3P (19) = 1385.
TBL3P (20) = 1440.
TBL3P (21) = 1494.
TBL3P (22) = 1547.
TBL3P (23) = 1599.
TBL3P (24) = 1650.
TBL3P (25) = 1700.
TBL3P (26) = 1750.
TBL3P (27) = 1798.
TBL3P (28) = 1846.
TBL3P (29) = 1893.
TBL3P (30) = 1939.
TBL3P (31) = 1985.
TBL3P (32) = 2030.
TBL3P (33) = 2075.
TBL3P (34) = 2118.
TBL3P (35) = 2160.
TBL3P (36) = 2202.
TBL3P (37) = 2245.
TBL3P (38) = 2286.
TBL3P (39) = 2327.
TBL3P (40) = 2366.
TBL3P (41) = 2406.
TBL3P (42) = 2445.
TBL3P (43) = 2485.
TBL4  (1 ) = 0.
TBL4  (2 ) = 0.2
TBL4  (3 ) = 0.4
TBL4  (4 ) = 0.6
TBL4  (5 ) = 0.8
TBL4  (6 ) = 1.0
TBL4  (7 ) = 1.2
TBL4  (8 ) = 1.4
TBL4  (9 ) = 1.6
TBL4  (10) = 1.8
TBL4  (11) = 2.0
TBL4  (12) = 2.2
TBL4  (13) = 8.0
TBL4P (1 ) = 1.0
TBL4P (2 ) = 0.998
TBL4P (3 ) = 0.995
TBL4P (4 ) = 0.991
TBL4P (5 ) = 0.985
TBL4P (6 ) = 0.977
TBL4P (7 ) = 0.970
TBL4P (8 ) = 0.964
TBL4P (9 ) = 0.959
TBL4P (10) = 0.955
TBL4P (11) = 0.952
TBL4P (12) = 0.950
TBL4P (13) = 0.950
TBL5  (1 ) = 0.05
TBL5  (2 ) = 0.06
TBL5  (3 ) = 0.07
TBL5  (4 ) = 0.08
TBL5  (5 ) = 0.09
TBL5  (6 ) = 0.10
TBL5  (7 ) = 0.11
TBL5  (8 ) = 0.12
TBL5  (9 ) = 0.14
TBL5  (10) = 0.15
TBL5  (11) = 0.17
TBL5  (12) = 0.19
TBL5  (13) = 0.20
TBL5  (14) = 0.23
TBL5  (15) = 0.25
TBL5  (16) = 0.30
TBL5  (17) = 0.35
TBL5  (18) = 0.40
TBL5  (19) = 0.50
TBL5  (20) = 0.60
TBL5  (21) = 0.70
TBL5  (22) = 0.80
TBL5  (23) = 0.90
TBL5  (24) = 1.0
TBL5  (25) = 1.1
TBL5  (26) = 1.2
TBL5  (27) = 1.3
TBL5  (28) = 1.4
TBL5  (29) = 1.5
```

```
TBL5  (30) = 1.7
TBL5  (31) = 1.9
TBL5  (32) = 2.0
TBL5  (33) = 2.5
TBL5  (34) = 3.0
TBL5  (35) = 3.5
TBL5  (36) = 4.0
TBL5  (37) = 5.0
TBL5  (38) = 6.0
TBL5  (39) = 7.0
TBL5  (40) = 8.0
TBL5P (1 ) = 0.02
TBL5P (2 ) = 0.03
TBL5P (3 ) = 0.042
TBL5P (4 ) = 0.054
TBL5P (5 ) = 0.068
TBL5P (6 ) = 0.082
TBL5P (7 ) = 0.097
TBL5P (8 ) = 0.112
TBL5P (9 ) = 0.144
TBL5P (10) = 0.158
TBL5P (11) = 0.188
TBL5P (12) = 0.218
TBL5P (13) = 0.232
TBL5P (14) = 0.272
TBL5P (15) = 0.294
TBL5P (16) = 0.350
TBL5P (17) = 0.397
TBL5P (18) = 0.437
TBL5P (19) = 0.505
TBL5P (20) = 0.558
TBL5P (21) = 0.603
TBL5P (22) = 0.640
TBL5P (23) = 0.672
TBL5P (24) = 0.700
TBL5P (25) = 0.724
TBL5P (26) = 0.744
TBL5P (27) = 0.765
TBL5P (28) = 0.783
TBL5P (29) = 0.800
TBL5P (30) = 0.826
TBL5P (31) = 0.849
TBL5P (32) = 0.858
TBL5P (33) = 0.895
TBL5P (34) = 0.916
TBL5P (35) = 0.932
TBL5P (36) = 0.944
TBL5P (37) = 0.960
TBL5P (38) = 0.970
TBL5P (39) = 0.977
TBL5P (40) = 0.982
TBL6  (1 ) = 0.2
TBL6  (2 ) = 0.4
TBL6  (3 ) = 0.6
TBL6  (4 ) = 0.8
TBL6  (5 ) = 1.0
TBL6  (6 ) = 1.2
TBL6  (7 ) = 1.4
TBL6  (8 ) = 1.6
TBL6  (9 ) = 1.8
TBL6  (10) = 2.0
TBL6  (11) = 2.2
TBL6  (12) = 2.4
TBL6  (13) = 2.6
TBL6  (14) = 2.8
TBL6  (15) = 3.0
TBL6  (16) = 3.2
TBL6  (17) = 3.4
TBL6  (18) = 3.6
TBL6  (19) = 3.8
TBL6  (20) = 4.0
TBL6  (21) = 4.2
TBL6  (22) = 4.4
TBL6  (23) = 4.6
TBL6  (24) = 4.8
TBL6  (25) = 5.0
TBL6  (26) = 5.2
TBL6  (27) = 5.4
TBL6  (28) = 5.6
TBL6P (1 ) = 9.80271
TBL6P (2 ) = 10.94784
TBL6P (3 ) = 12.89399
TBL6P (4 ) = 15.69746
TBL6P (5 ) = 19.43609
TBL6P (6 ) = 24.20781
TBL6P (7 ) = 30.12863
TBL6P (8 ) = 37.32923
TBL6P (9 ) = 45.95230
TBL6P (10) = 56.14932
TBL6P (11) = 68.07771
TBL6P (12) = 81.89947
TBL6P (13) = 97.77902
TBL6P (14) = 115.88287
TBL6P (15) = 136.37821
TBL6P (16) = 159.43361
TBL6P (17) = 185.21769
TBL6P (18) = 213.89927
TBL6P (19) = 245.64801
TBL6P (20) = 280.63340
TBL6P (21) = 319.02474
TBL6P (22) = 360.99204
TBL6P (23) = 406.70528
TBL6P (24) = 456.33364
TBL6P (25) = 510.04756
TBL6P (26) = 568.01730
TBL6P (27) = 630.41182
TBL6P (28) = 697.40229
TBL6PP(1 ) = 9.61234
TBL6PP(2 ) = 10.16410
TBL6PP(3 ) = 11.04924
TBL6PP(4 ) = 12.22282
TBL6PP(5 ) = 13.63288
TBL6PP(6 ) = 15.22758
TBL6PP(7 ) = 16.96068
TBL6PP(8 ) = 18.79408
TBL6PP(9 ) = 20.69872
TBL6PP(10) = 22.65358
TBL6PP(11) = 24.64392
TBL6PP(12) = 26.65990
TBL6PP(13) = 28.69470
TBL6PP(14) = 30.74382
TBL6PP(15) = 32.80398
TBL6PP(16) = 34.87300
TBL6PP(17) = 36.94914
TBL6PP(18) = 39.03112
TBL6PP(19) = 41.11800
TBL6PP(20) = 43.20904
TBL6PP(21) = 45.30354
TBL6PP(22) = 47.40108
TBL6PP(23) = 49.50126
TBL6PP(24) = 51.60366
TBL6PP(25) = 53.70808
TBL6PP(26) = 55.81428
TBL6PP(27) = 57.92200
TBL6PP(28) = 60.03114
*RETURN
  END
```

APPENDIX C

MEASUREMENT OF THE WIRE SUPPORT TEMPERATURE

The analysis given in Appendix A shows clearly that the temperature of the hot-wire supports is an important parameter in the interpretation of recovery temperature data. This is particularly true when the normalized parameter $\overline{\eta}_*$ is used, since an error in the determination of the absolute wire temperature is magnified by a factor of five or more in the computation of $\overline{\eta}_*$. For this reason, a special test was conducted to determine the quantity η_s explicitly.

Two .001" diameter wires, one Pt - 10 per cent Rh and one Constantan, were soft-soldered to the tip of one of the hot-wire support needles to form a thermocouple junction. The complete assembly was then placed in the calibrating oven and a curve of e.m.f. vs. junction temperature obtained. The thermocouple wires were terminated in a constant-temperature junction box for both the oven and tunnel tests, thus eliminating spurious e.m.f. sources caused by thermocouple wire-lead wire temperature variation.

The hot-wire support and thermocouple combination was placed in the tunnel to reproduce, as closely as possible, the actual flow conditions encountered in the hot-wire measurements. Since the needle supports tapered from .02" diameter at several calibers to about .01" at the tip, the .001" thermocouple wire was small compared to body dimensions and should have had a small

effect on the surrounding flow field. No correction was made for heat loss by conduction along the thermocouple wire.

Measurements of the support temperature were made over the complete range of tunnel conditions for several positions of the thermocouple near the needle stagnation point. These data are shown in Figure 15. The needle tip was roughly ogival in shape (as shown in the insert) and the angle θ used to define the thermocouple location refers to the angle between the surface normal and the free-stream direction at that point. These data indicate that the support temperature was a constant and equal to $0.903\ T_0$ over the complete operating range.

This result can be corroborated by a simple dimensional argument. The rate at which heat is supplied to the probe by convection is proportional to $\left[\frac{k_0\ Nu_0\ (\Delta T_g)}{d}\right]$, where ΔT_g is the local difference between the actual support temperature and the adiabatic temperature. From point to point within the solid, the heat transfer rate is proportional to $\left[\frac{k_s(\Delta T_s)}{x}\right]$ where ΔT_s is the temperature difference between two points a distance x apart and k_s is the thermal conductivity of the support. The ratio of the two temperature differences is thus of order

$$(\Delta T_s/\Delta T_g) \sim (k_0/k_s)\ (x/d)\ Nu_0 \quad .$$

The ratio (k_0/k_s) for air and a steel needle is of order 10^{-4}; hence $\Delta T_s << \Delta T_g$, and the needle is very close to constant temperature throughout.

Let us carry the argument one step further. The free-stream Reynolds number based on support diameter is of the order of 10^3 and a laminar boundary layer will exist along the length of the support. If negligible heat is lost from the hot-wire support itself, then the net integrated heat transfer must be zero. This means that any heat transferred to the support near the stagnation point will rapidly be conducted away and returned to the flow somewhere downstream. By considering the expansion process around a blunt body in hypersonic flow and the size of the stagnation point surface relative to the downstream exposed surface, it is easily seen that the support temperature should be very close to the adiabatic temperature of a laminar boundary layer with local external Mach number M_n (see the insert of Figure 15). Expressed in mathematical terms,

$$(T_s/T_0) \cong \frac{1 + \sqrt{Pr}\,(\frac{\gamma-1}{2})\,M_n^2}{1 + (\frac{\gamma-1}{2})\,M_n^2} \quad ,$$

where M_n is of order 2.5 to 3 for a blunt ogival body in hypersonic flow. This result agrees with the experimental value to high precision.

APPENDIX D

THE EFFECT OF OVERHEAT ON NUSSELT NUMBER

During the course of this investigation, a few preliminary measurements were made to determine the effect of overheat on the measured Nusselt number. From the results of McClellan (30) and Spangenberg (19), it was not expected that at low overheats and Mach numbers outside the transonic range any significant effects would be found. However, in the region where slip effects become appreciable, it is not evident a priori that a variation of surface temperature may be neglected. I shall begin by discussing the data obtained, and conclude with a qualitative description of the results of this and several other investigations.

The present data for $\tau = \frac{T_w - T_{aw}}{T_{aw}} > 0$ were obtained by a procedure identical to that described in Section II. For finite overheat, the variation of wire resistance with heating current must be considered, and Equation 2 is the appropriate computational relation. Four tests were carried out for Reynolds numbers Re_0 between 0.5 and 2.0. As can be seen from Figures 8, 9, and 10, the effects (if any) of rarefaction should be very noticeable in this region.

The data of all four tests fell within the shaded region shown in Figure 16. Although the reproducibility of these measurements was not sufficient to discern the influence of Re_0 on the $[Nu_0(\tau)/Nu_0(\tau = 0)]$ relation, a comparison with the results of McClellan show that even in the slip flow regime, the effect cannot be large for Mach numbers above the transonic range. The difference between the $Re_0 \sim 4$ data of McClellan and the present

measurements is probably due to the limited amount of information available from both sources. (See McClellan's thesis, p. 19.)

Comparison of the data of Spangenberg at subsonic and transonic speeds with the supersonic and hypersonic data is facilitated by the insert shown in Figure 16. This insert (Figure 22a, Reference 19) is typical of the data available in this range. That the relation between Nusselt number and overheat is quite complex may be seen by comparing the effects of τ for various values of (M/Re). (See for example Figures 22a-ℓ, Reference 19.)

One fact which further complicates the question of the effect of overheat on Nu_0 is that none of the available experimental evidence in the transonic range (7, 19, 21, 31) includes the appropriate data for zero overheat. For example, the data of Spangenberg reproduced in Figure 16 is normalized about the value $\tau = 0.214$. As a comparison, Baldwin (21) often found as much as a 20 per cent change in the heat transfer coefficient between the values $\tau = 0.07$ and $\tau = 0.22$. Another rather surprising comparison between the works of Baldwin (21), Cybulski (7), and Spangenberg is the behavior found at overheats approaching one. As illustrated in Figure 16, Spangenberg found that the change in Nu_0 was close to linear with a change in overheat over a large range of Mach and Reynolds numbers. On the contrary, References 7 and 21 show a negligible change in Nu_0 when τ is increased beyond about 0.35.

In attempting to interpret these results, it is necessary to

distinguish between three separate types of phenomena which are in evidence in these various investigations. The first may be broadly classed as thermodynamic, which would include small changes in the local temperature of the fluid near the body and the subsequent effects on viscosity, density, Prandtl number and the like. These differences for the most part are small (at least for small overheats or changes in stagnation temperature) and may be accounted for at high Reynolds numbers by using any of the several available compressible boundary layer analyses. The second class may be broadly termed induced flow effects, wherein a change in body temperature is sufficient to alter the basic features of the flow field, and through this "interaction" change the measured heat transfer. Thirdly, the effect of surface temperature on molecular processes must also be considered.

From the above delineation, we may immediately imply several important generalizations. First, in the range of high Reynolds numbers, the effects of overheat should be of the thermodynamic type. Second, as the Reynolds number decreases, a given fractional change in the boundary layer thickness caused by fluid property variation would have an increasing effect on the flow field adjacent to the body. From boundary layer theory, $q \sim (d/2)^{-\frac{1}{2}}$ where d is the diameter of the cylinder. If the boundary layer displacement thickness is not negligibly small, then $q \sim [(d/2)(1+\frac{2\delta^*}{d})]^{-\frac{1}{2}}$, and an increase in the displacement thickness (i.e., an increase in the wire temperature) would tend to decrease the heat transfer rate to the body. This result agrees with the experimental results

given in Figure 16. The third conclusion is that this induced flow effect would be most pronounced in the transonic regime, where the flow field is extremely sensitive to the effective body shape. All of these statements are borne out by the present experiments and the data of Spangenberg (19) and Winovich and Stine (31). In cases where these different effects are of the same order, it becomes difficult to separate them by less than rigorous analysis.

Several investigations (2, 3, 6, 7, 8, 22) have been conducted under conditions approaching free molecule flow. Air, nitrogen, helium, and argon have all been used as test gases for these subsonic and supersonic experiments. In all cases, the test body (a hot-wire, unheated wire or butt-welded thermocouple) was maintained at a temperature differing significantly from the equilibrium recovery temperature. Several interesting but as yet unexplained results were obtained for various combinations of overheat (both positive and negative), test medium, and Mach number. The most important requirement at this time is a working model of the actual interaction process between a rapidly moving molecule and a surface of arbitrary roughness and temperature. As indicated earlier, in free molecule flow the body temperature will change the heat transfer rate only through its effect on the accommodation coefficient.

APPENDIX E

MEASUREMENTS AT REYNOLDS NUMBERS APPROACHING FREE MOLECULE FLOW

At the conclusion of this investigation, an attempt was made to extend the data to lower Reynolds numbers by using .00005" diameter Pt - 10 per cent Rh wires. These tests were not quantitatively repeatable because of possible non-uniformity of the wires, repeated breakage and consequent incomplete calibration, and other reasons which are not yet fully understood. However, each individual wire produced a self-consistent set of heat transfer data.

The accuracy of these measurements was considerably less than the accuracy obtained using .0001" diameter wire. Microscopic examination revealed that these small wires possessed a variety of small "kinks"; whether these non-uniformities were caused by installation, tunnel exposure, or the actual manufacturing process was not clear.

Figure 17 shows that the slope of the Nu_0 - Re_0 curve obtained with each individual wire was equal to unity within the experimental scatter. Although the slopes agreed quite well, the proportionality constant varied by as much as 40 per cent. Data obtained at high Mach numbers in air and nitrogen by Weltmann and Kuhns (6) and by Wong (3) are included in the figure for comparison. In each of these experiments, the slope of the Nu_0 - Re_0 curve is again nearly unity within the limits of the data. This

fact emphasizes several of the remarks made earlier with reference to Figure 9; between several independent investigations there appears to be better agreement in the slope of the Nu_0 - Re_0 relation than in the absolute magnitude of the correlation.

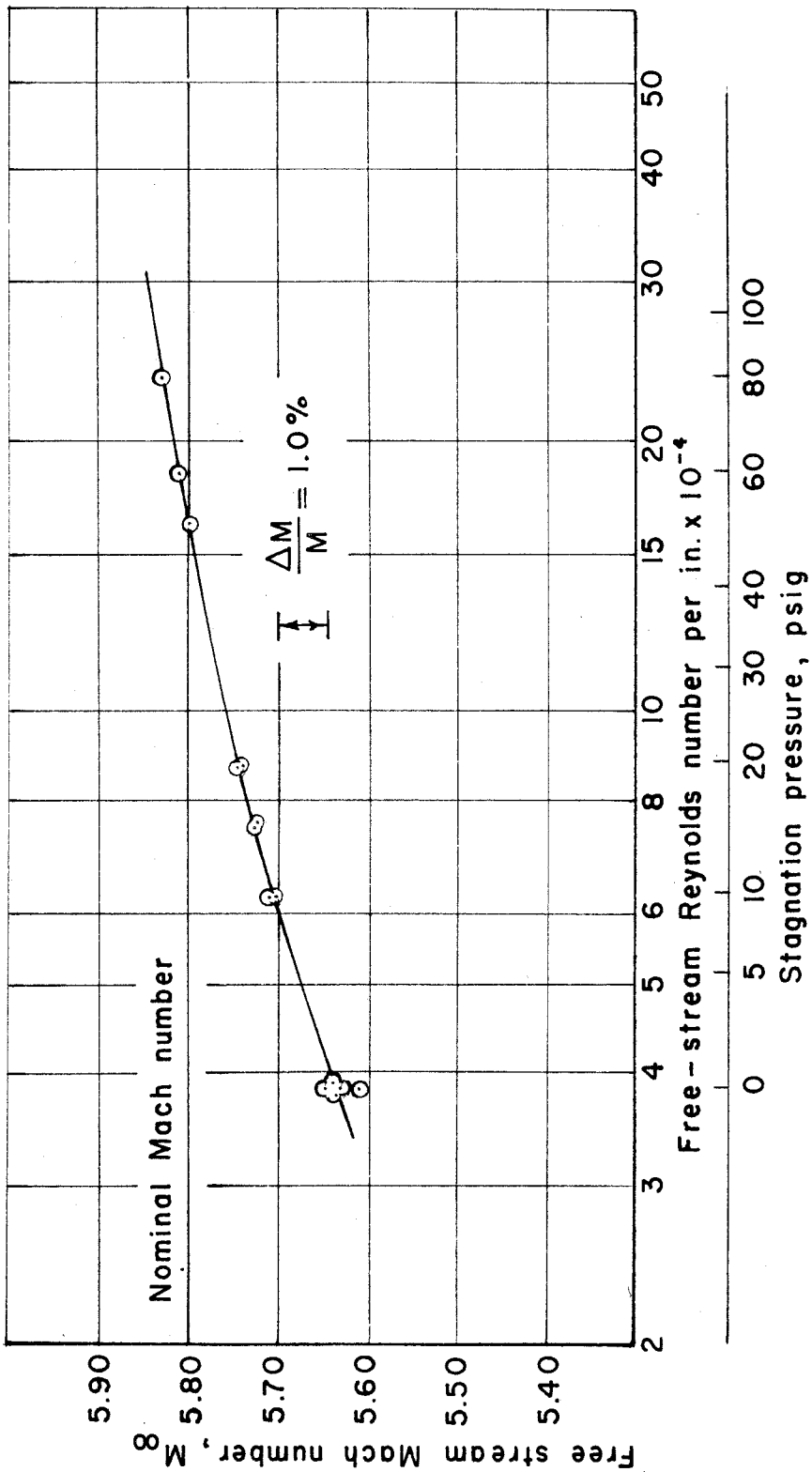

FIG. I VARIATION OF FREE STREAM MACH NUMBER WITH TUNNEL PRESSURE

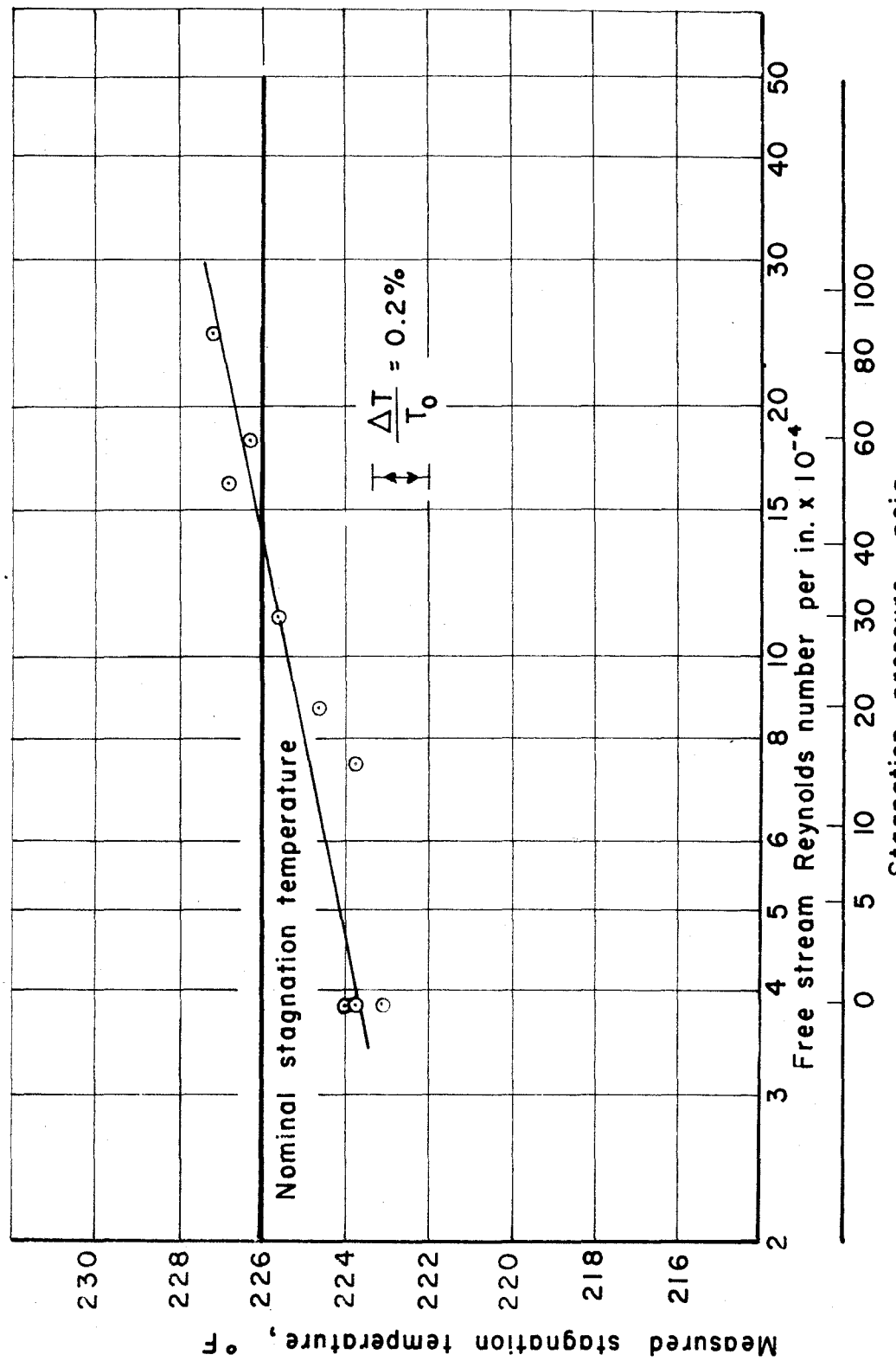

FIG. 2 VARIATION OF STAGNATION TEMPERATURE WITH TUNNEL PRESSURE

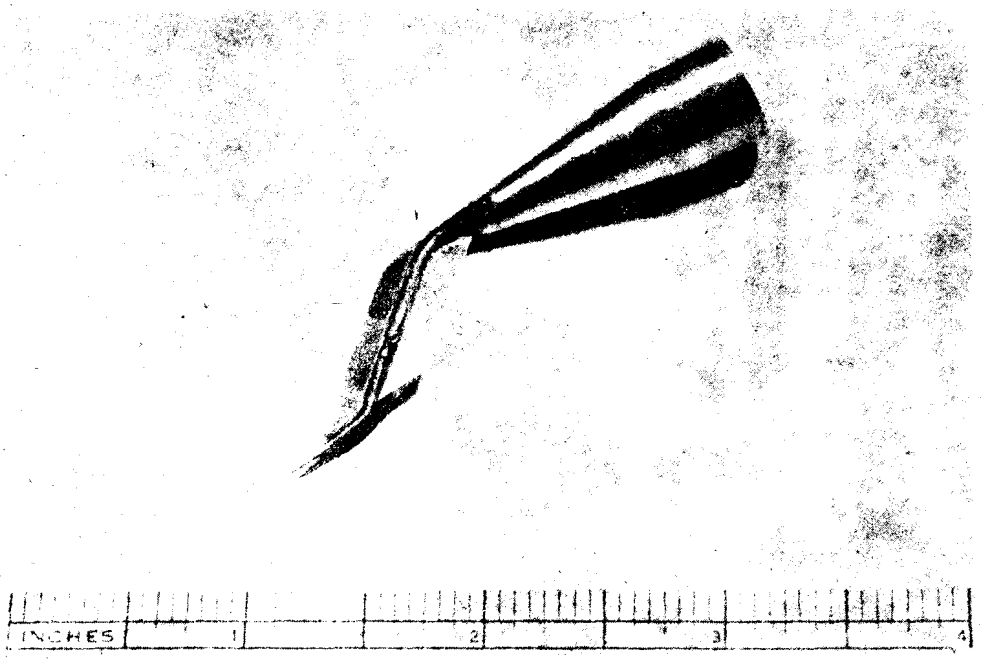

a) Hot – Wire Probe

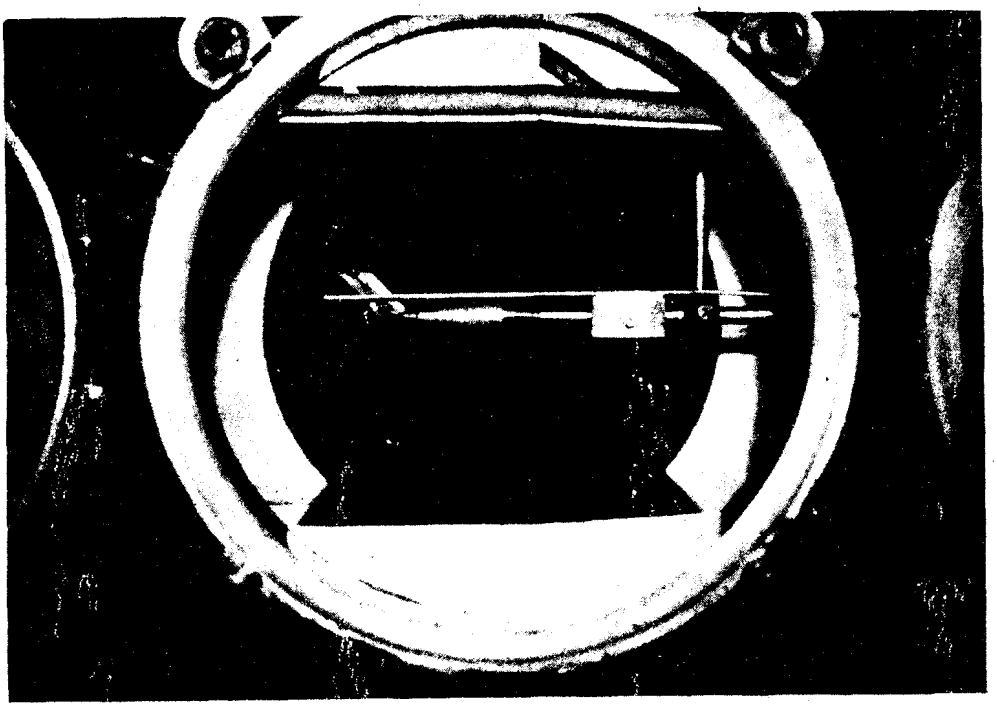

b) Hot-Wire Probe and Total Pressure Tube Installed in Tunnel

FIG. 3 HOT-WIRE PROBE AND TUNNEL INSTALLATION

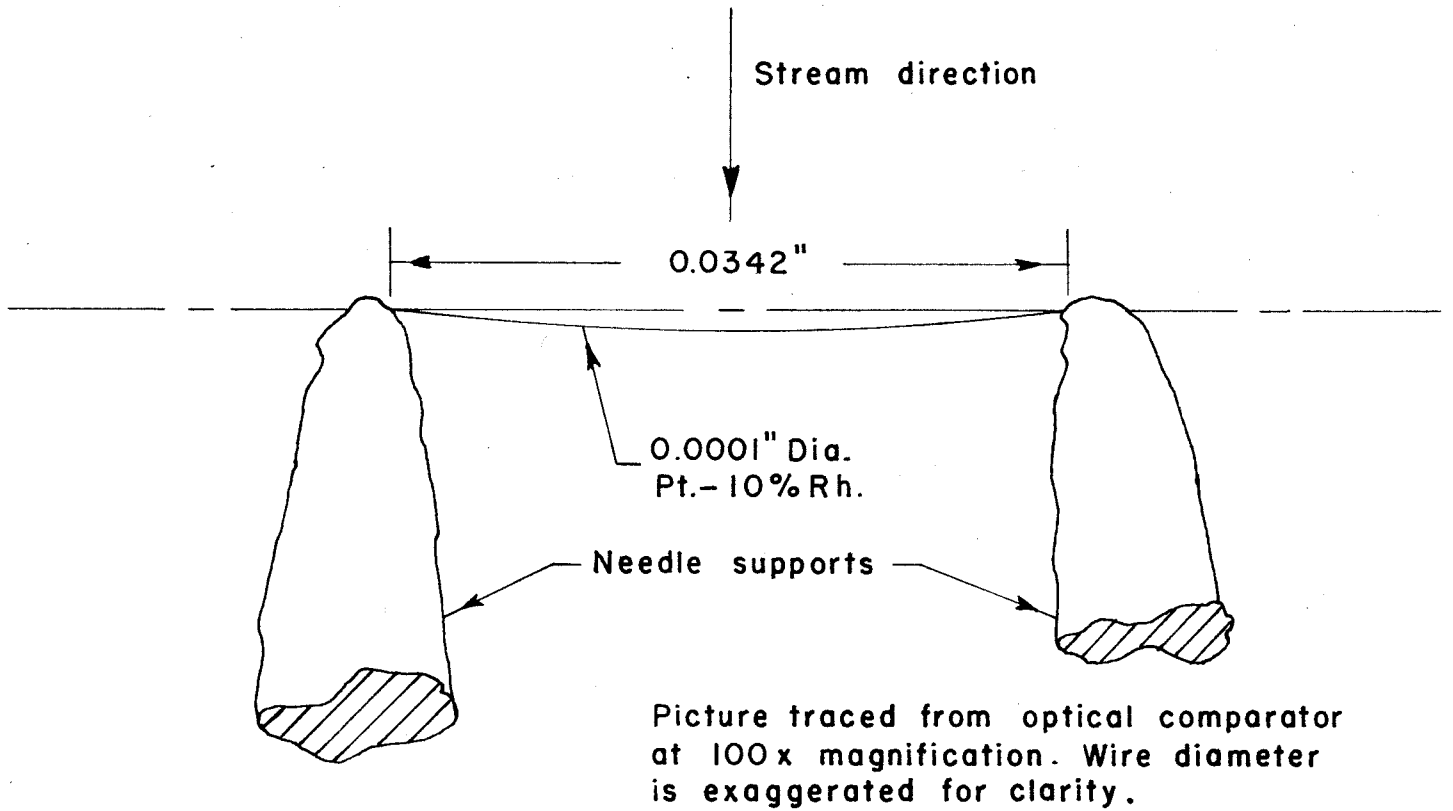

FIG. 4 TYPICAL HOT-WIRE INSTALLATION AFTER TUNNEL EXPOSURE

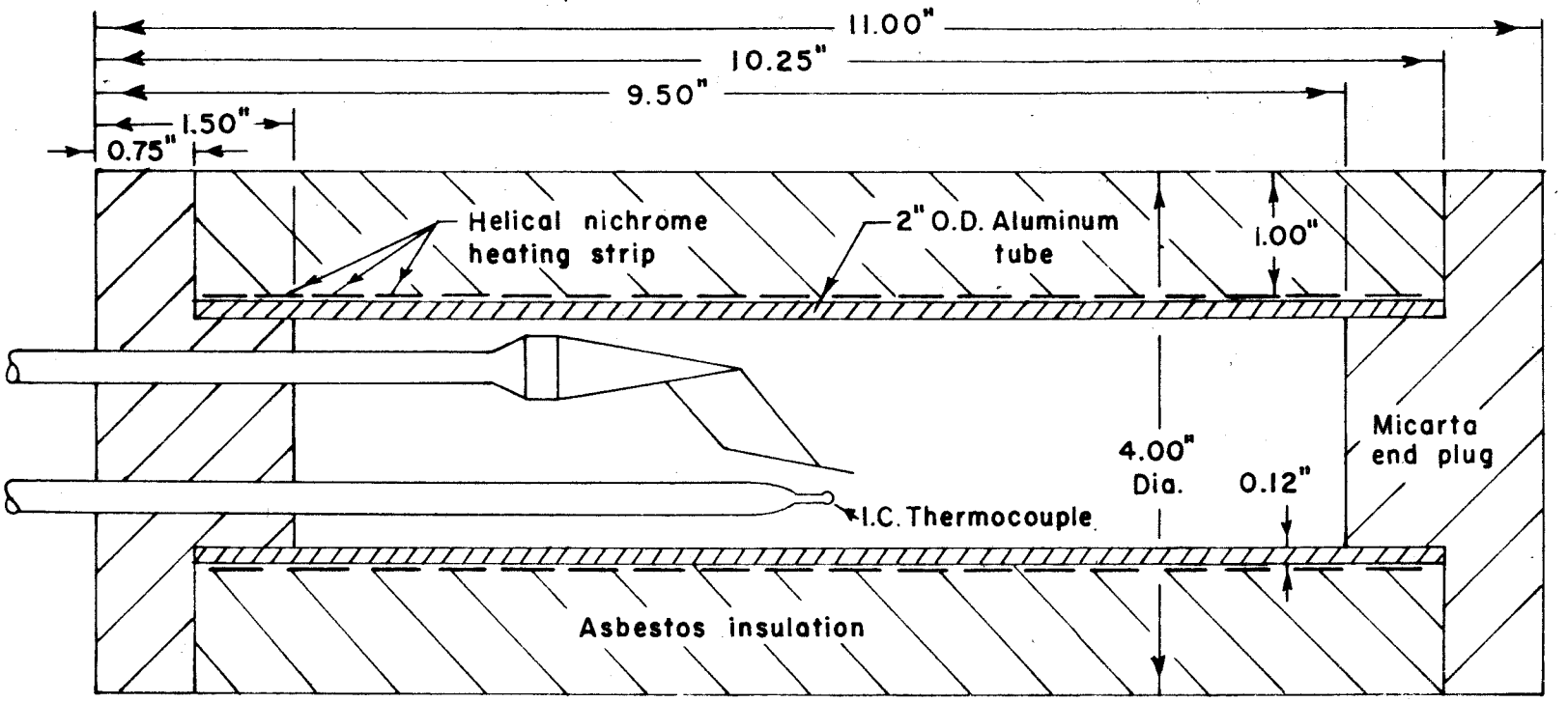

FIG. 5 DIAGRAM OF CALIBRATION OVEN

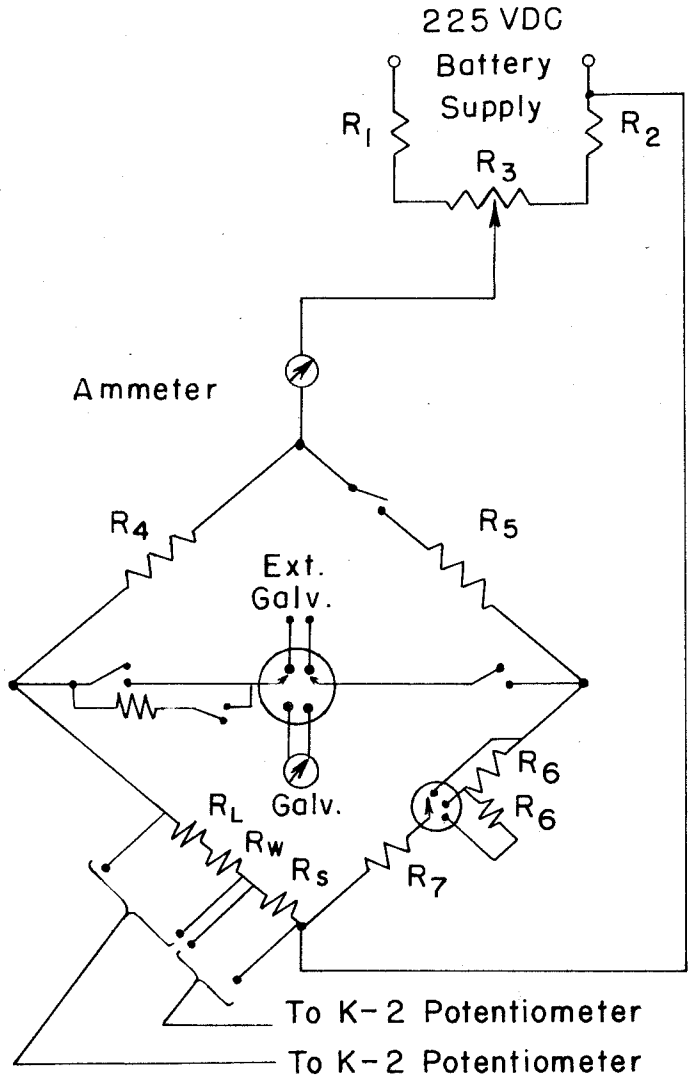

Resistance Table

	Setting I	II	III	IV
R_1	24K Ω	18K Ω	12K Ω	6K Ω
R_2	0	6.8K Ω	16K Ω	24K Ω

R_3	0-6K Ω 15-Turn Helipot (± 0.5% Linearity)
R_4	7.5 K Ω
R_5	75 K Ω
R_6	1K Ω
R_7	0-1 K Ω 10-Turn Helipot (± 0.5% Linearity)
R_W	Hot-Wire (~40 Ω)
R_L	Line (~ 0.6 Ω)
R_S	1.000 Ω ± 0.1% (Standard Resistor)

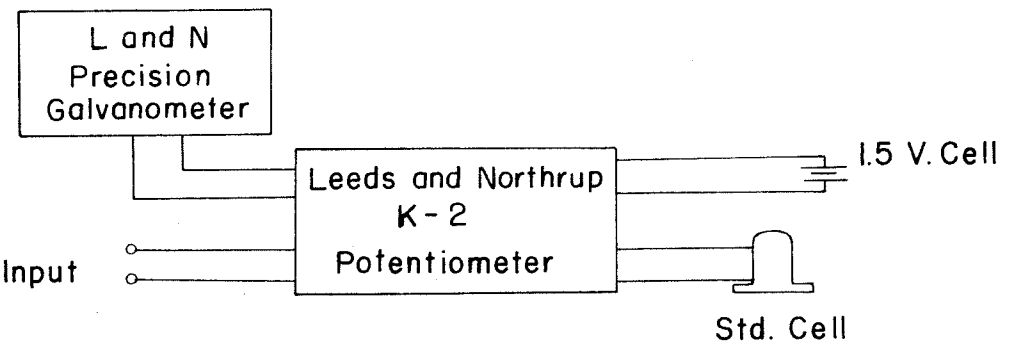

FIG. 6 ELECTRICAL CIRCUIT DIAGRAM

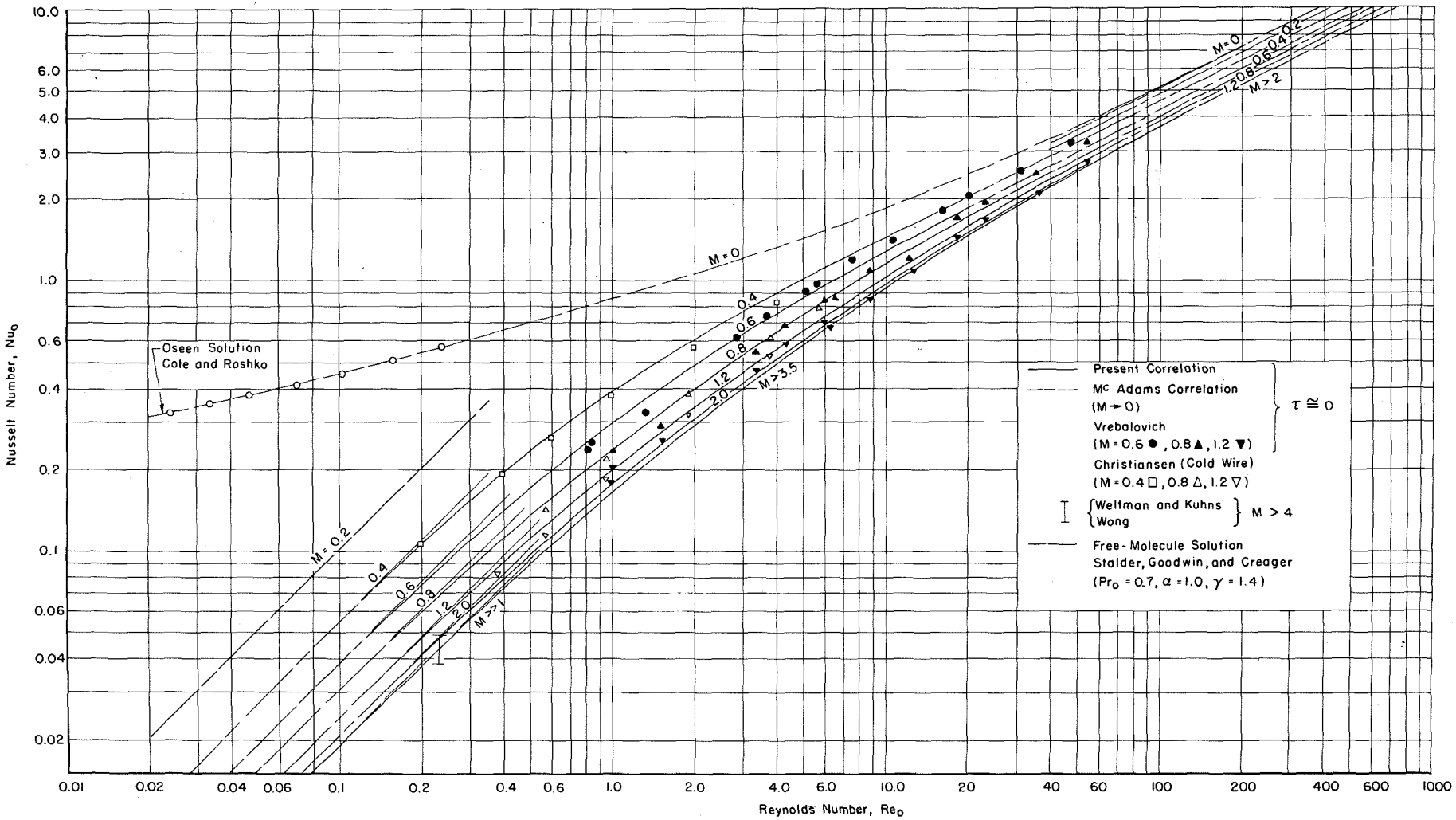

FIG. 7 - EMPIRICAL CORRELATION OF HOT-WIRE HEAT TRANSFER AT LOW REYNOLDS NUMBER

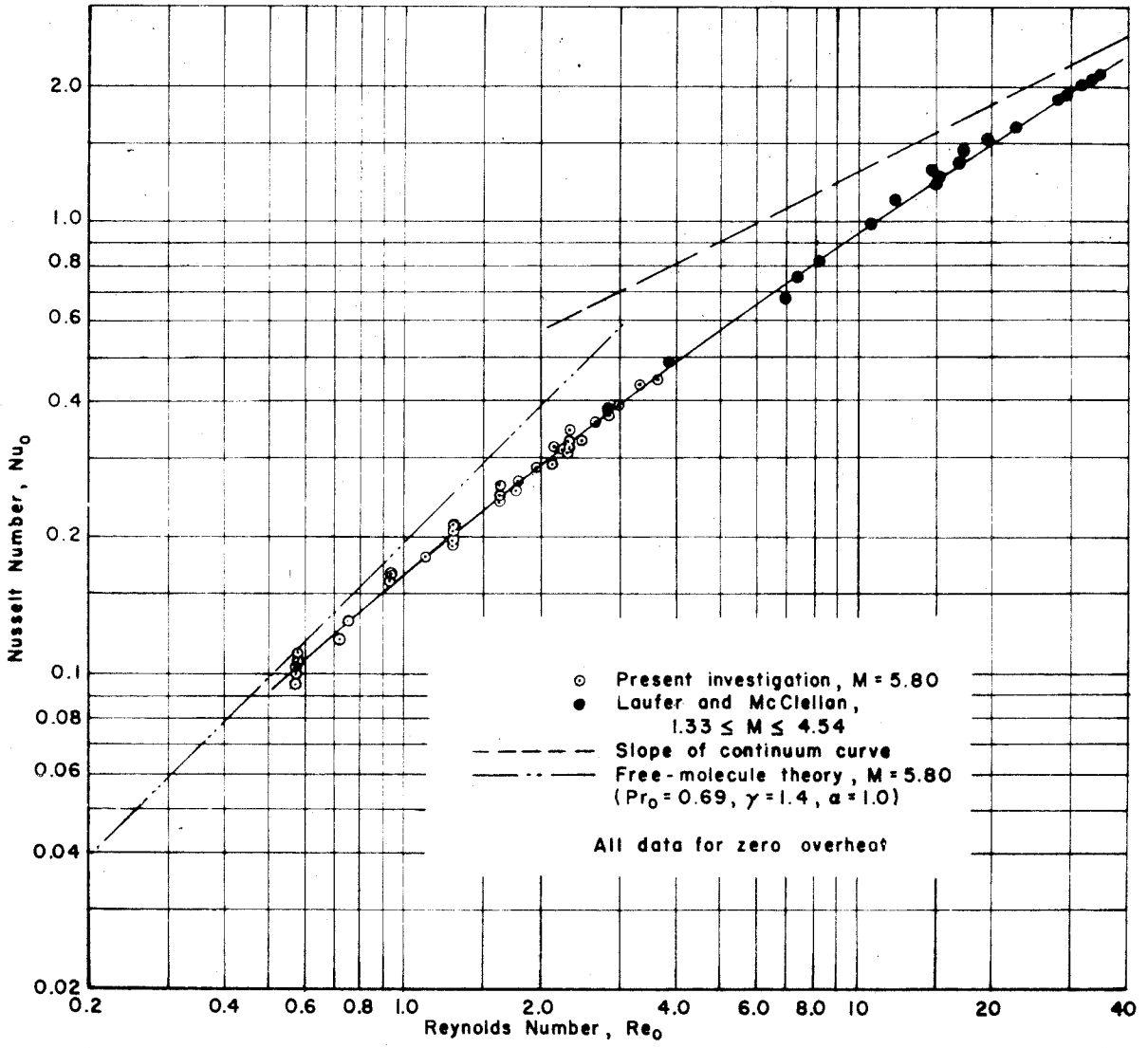

FIG. 8 NUSSELT NUMBER — REYNOLDS NUMBER RELATION FOR SUPERSONIC AND HYPERSONIC FLOW

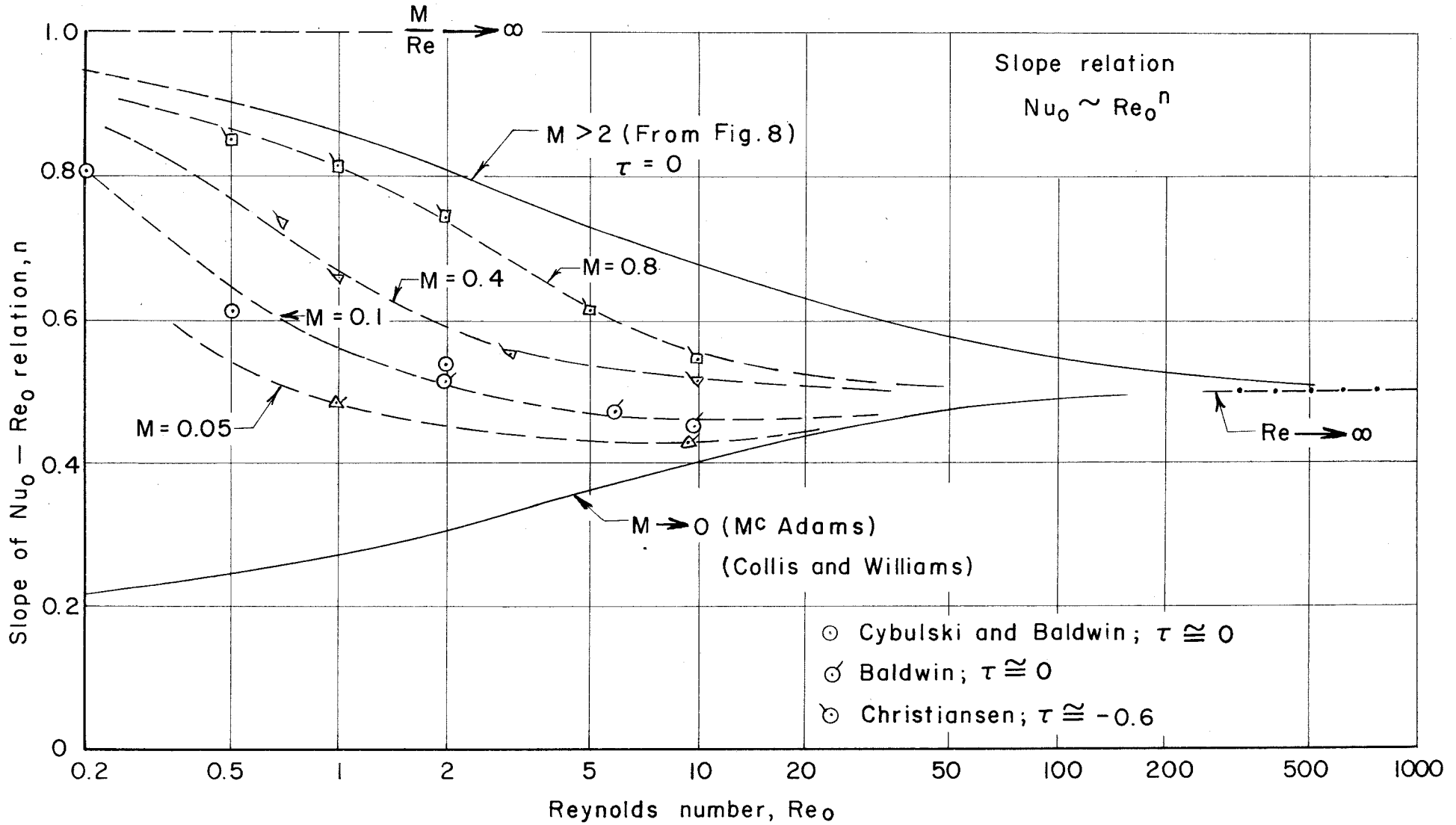

FIG. 9 – SLOPE OF NUSSELT NUMBER – REYNOLDS NUMBER RELATION AS A FUNCTION OF REYNOLDS NUMBER

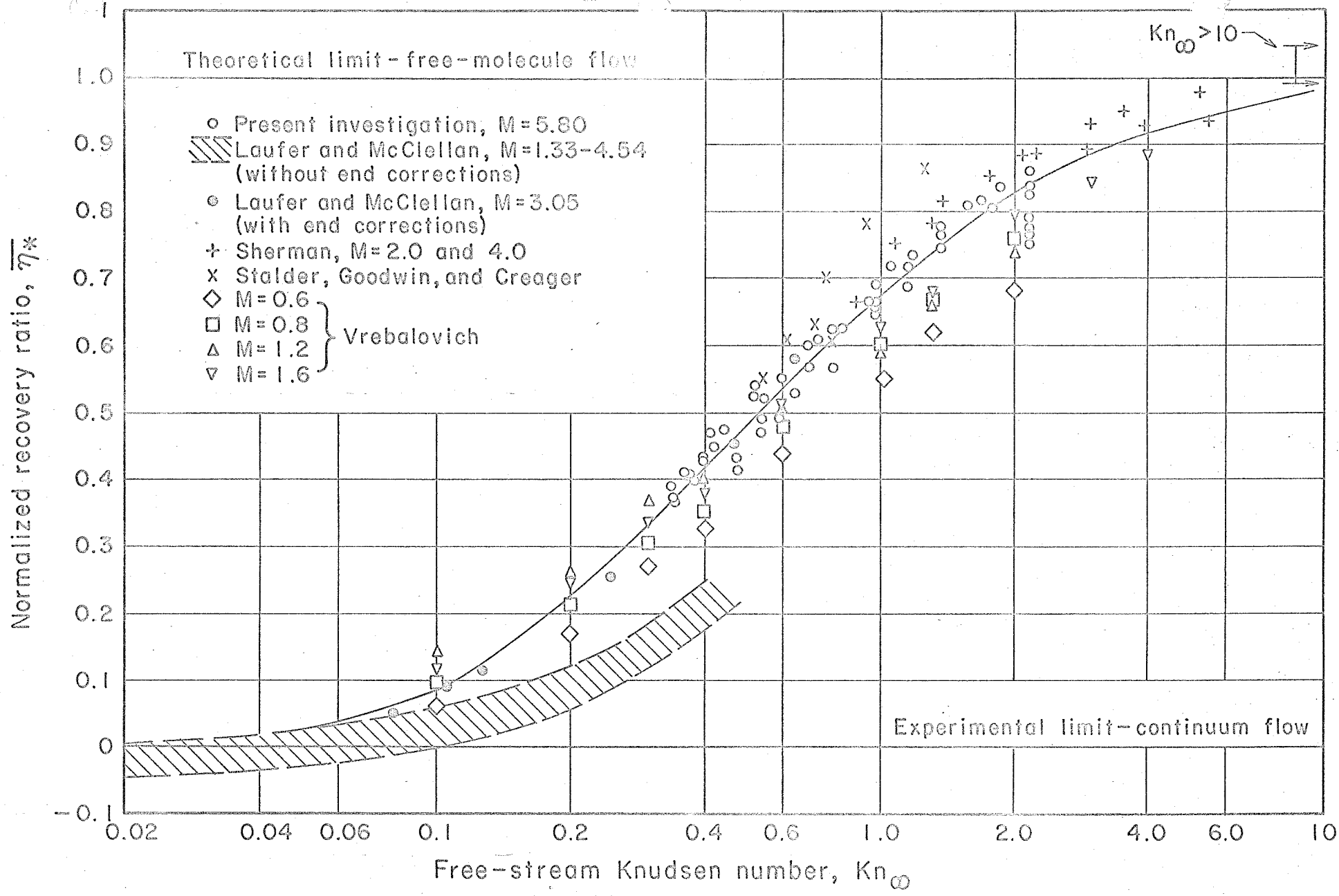

FIG. NORMALIZED VARIATION OF RECOVERY TEMPERATURE WITH KNUDSEN NUMBER

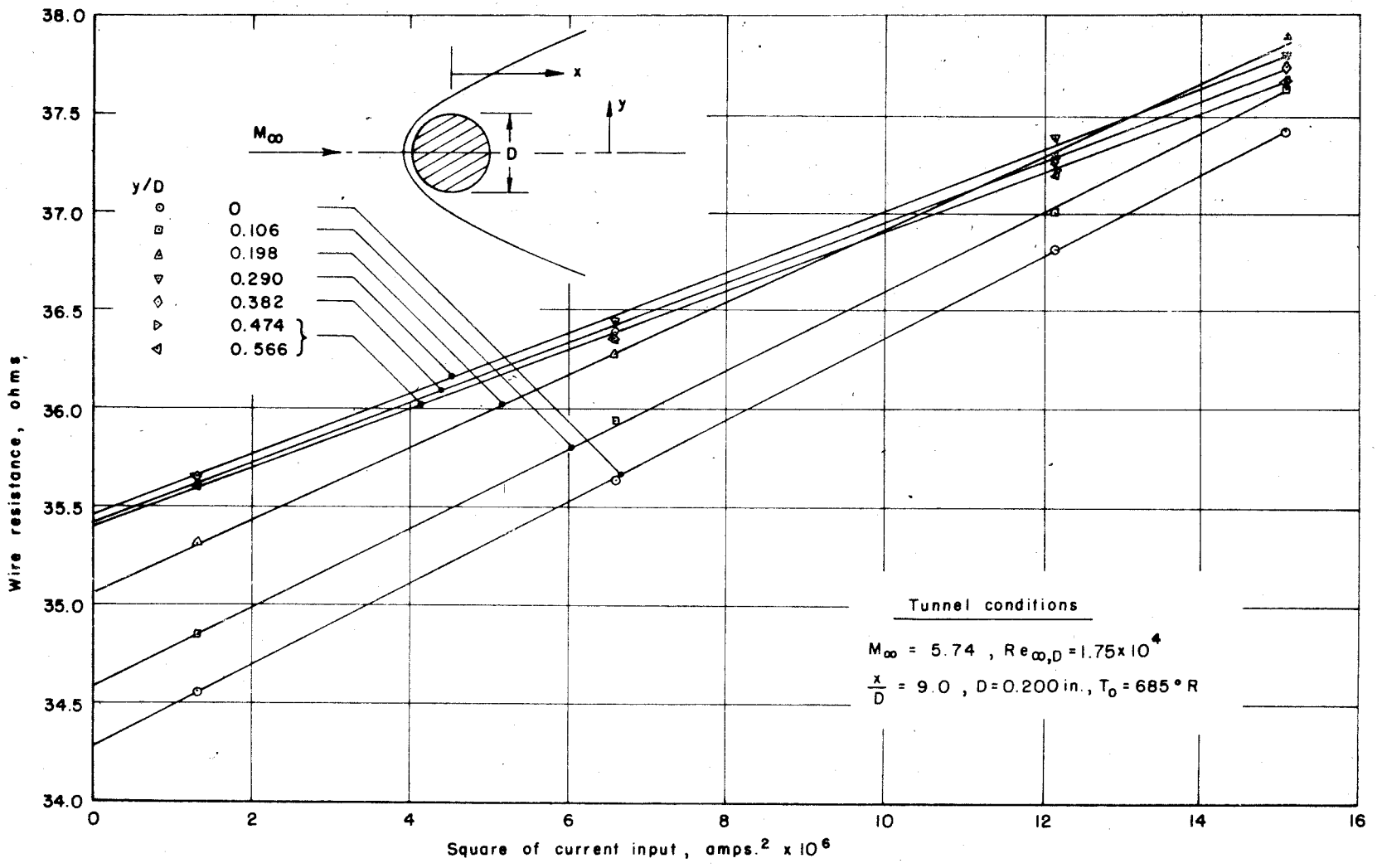

FIG. 11 - DATA OBTAINED FROM CYLINDER WAKE TRAVERSE

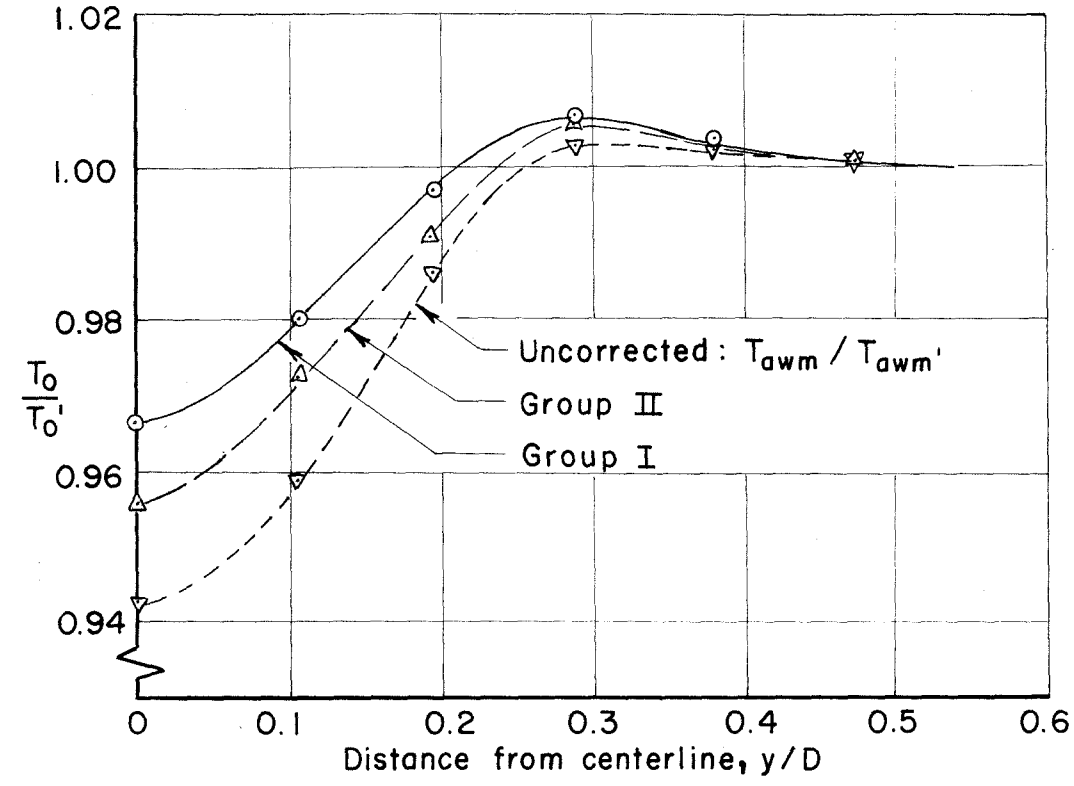

a) Temperature distribution

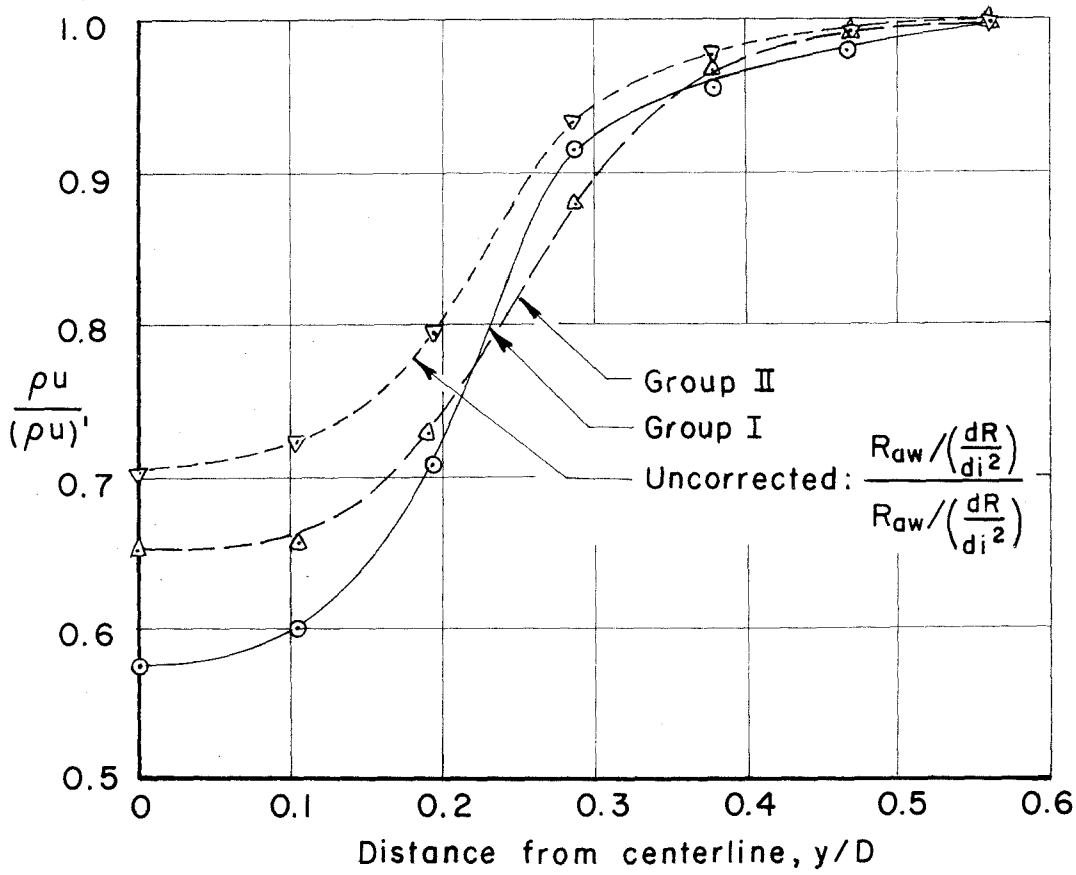

b) Mass flow distribution

FIG. 12 VARIATION OF FLOW QUANTITIES ACROSS THE CYLINDER WAKE

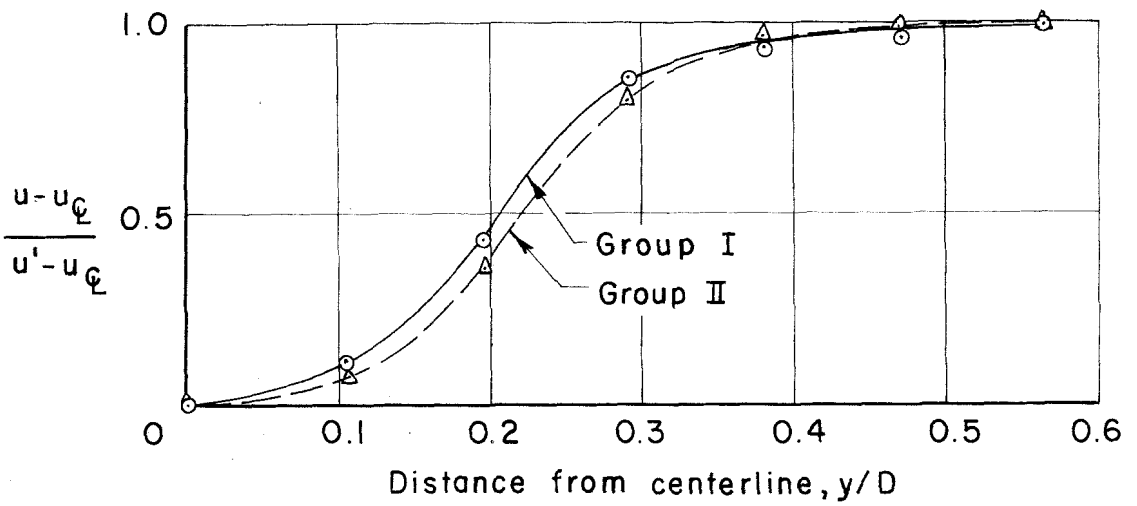

c) Velocity defect

FIG. 12, Cont'd.

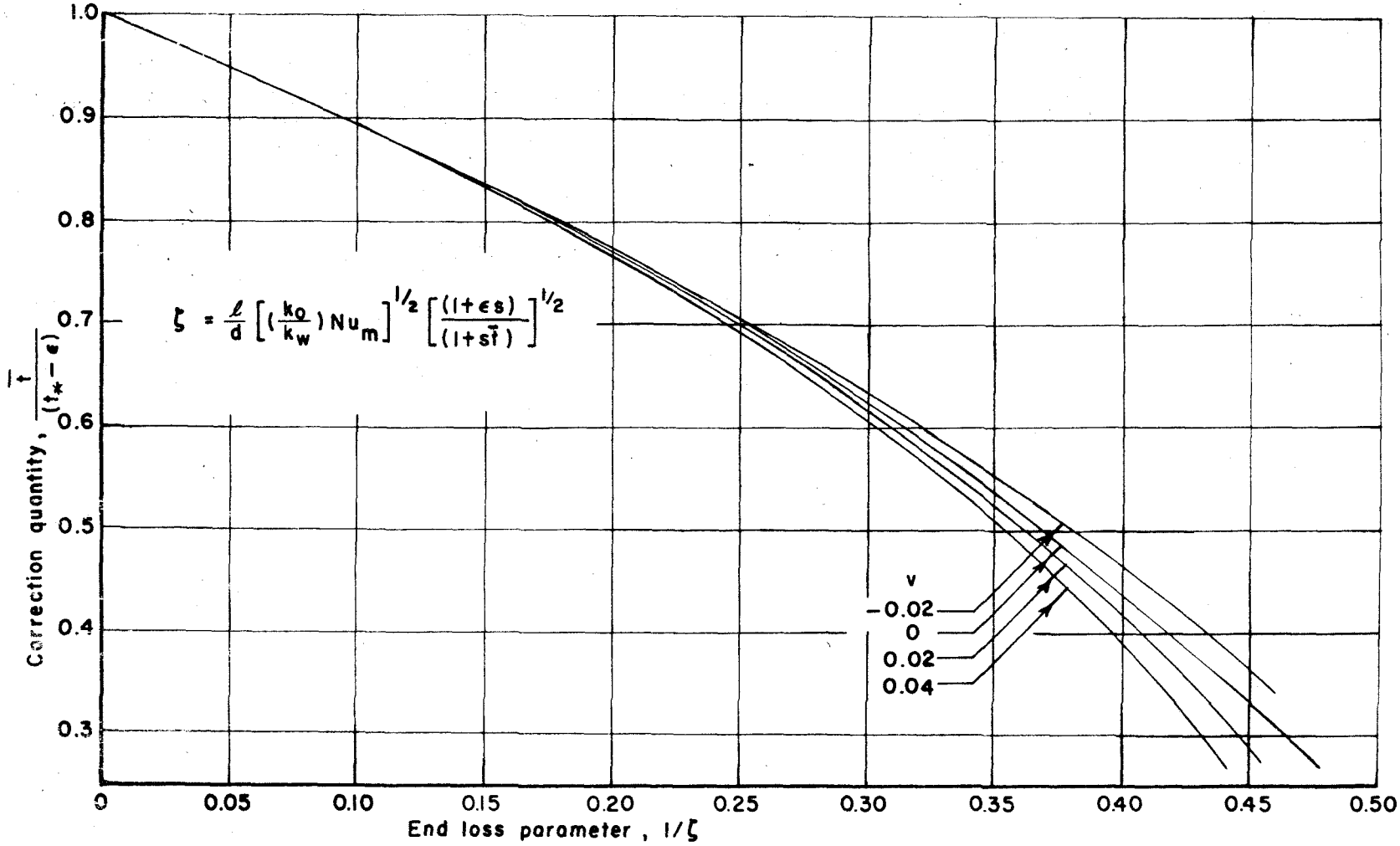

FIG. 13 END LOSS RELATIONS FOR NUSSELT NUMBER CORRECTION

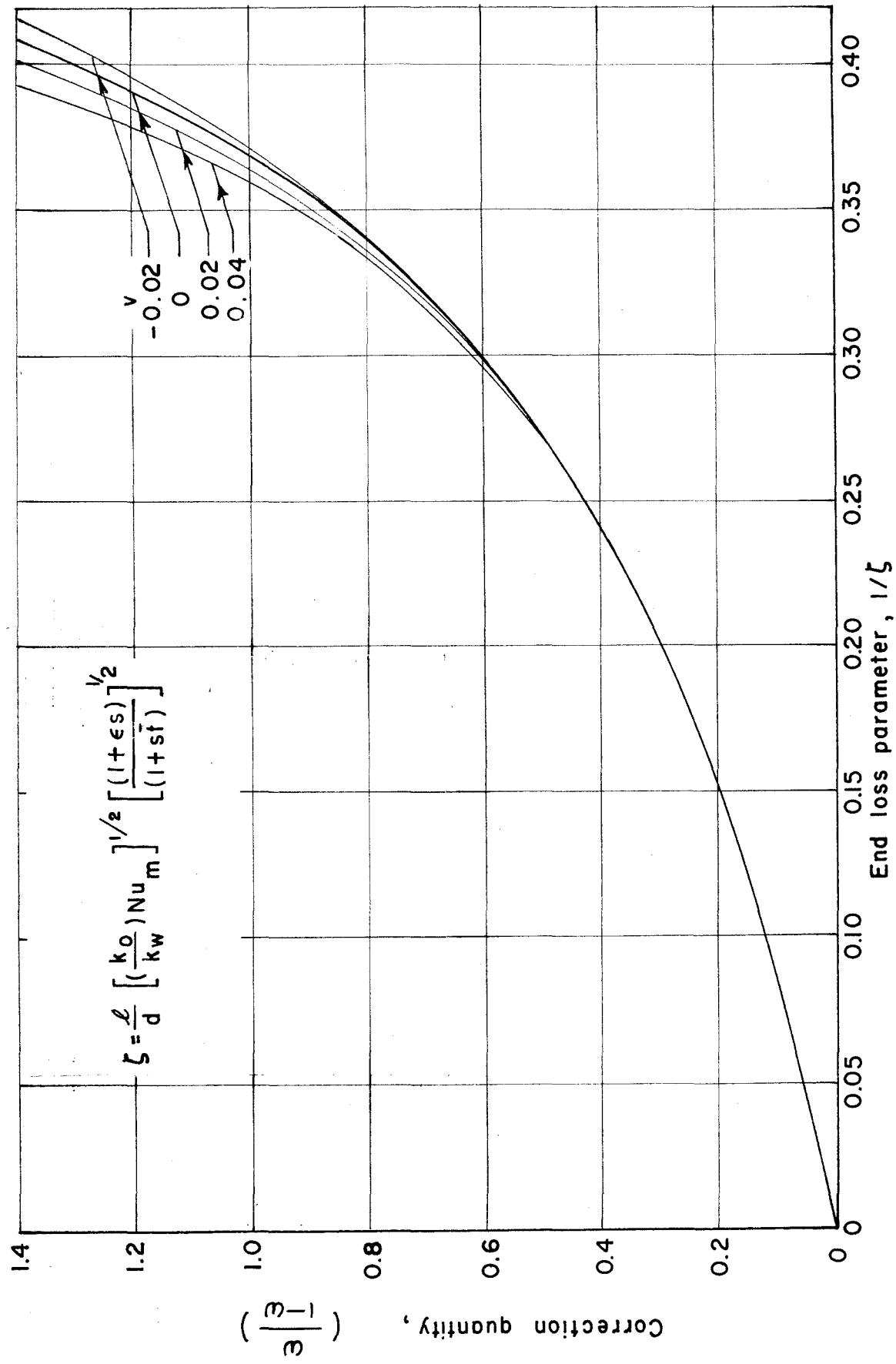

FIG. 14 END LOSS RELATIONS FOR RECOVERY TEMPERATURE CORRECTION

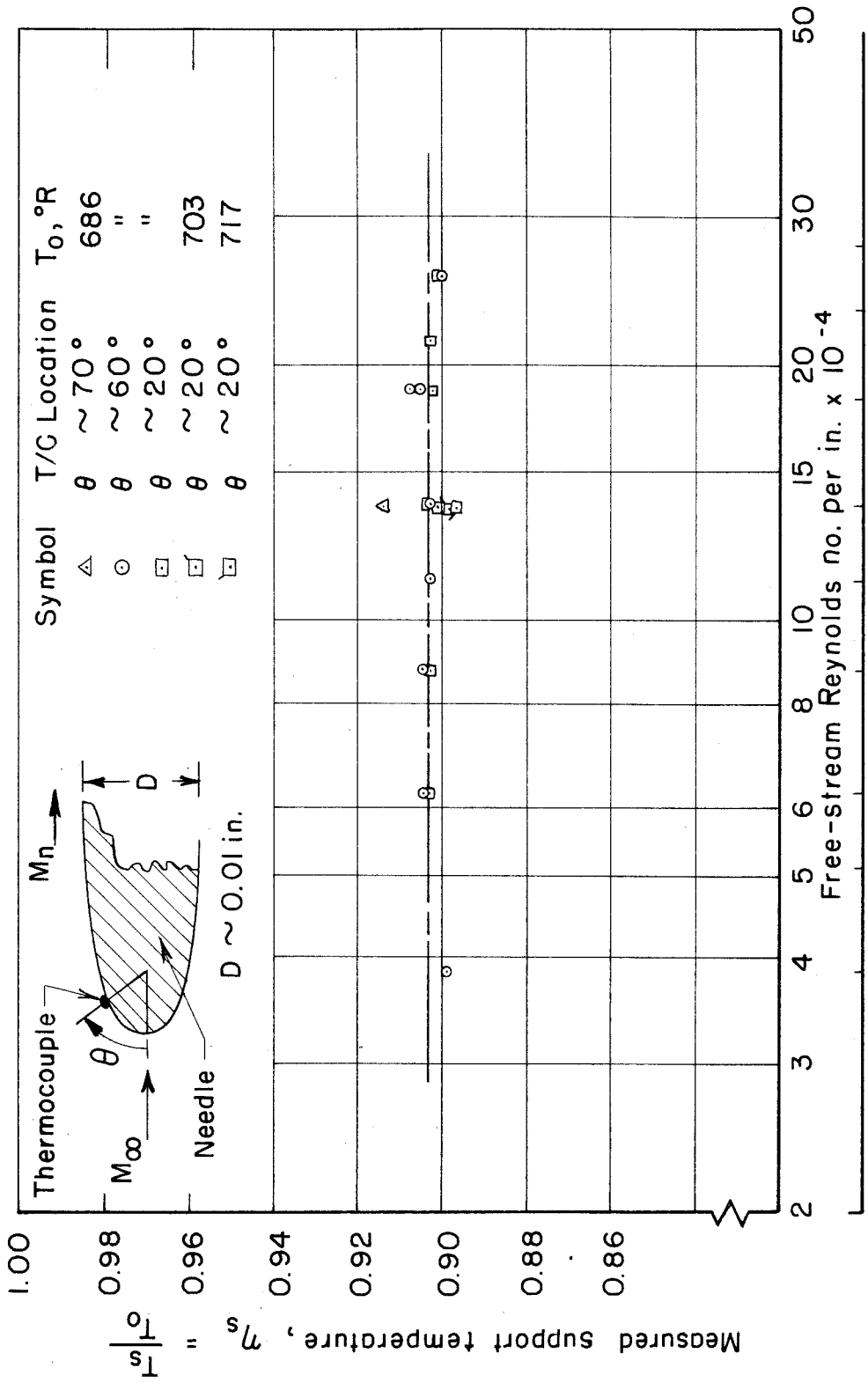

FIG. 15 WIRE SUPPORT TEMPERATURE AS A FUNCTION OF TUNNEL PRESSURE

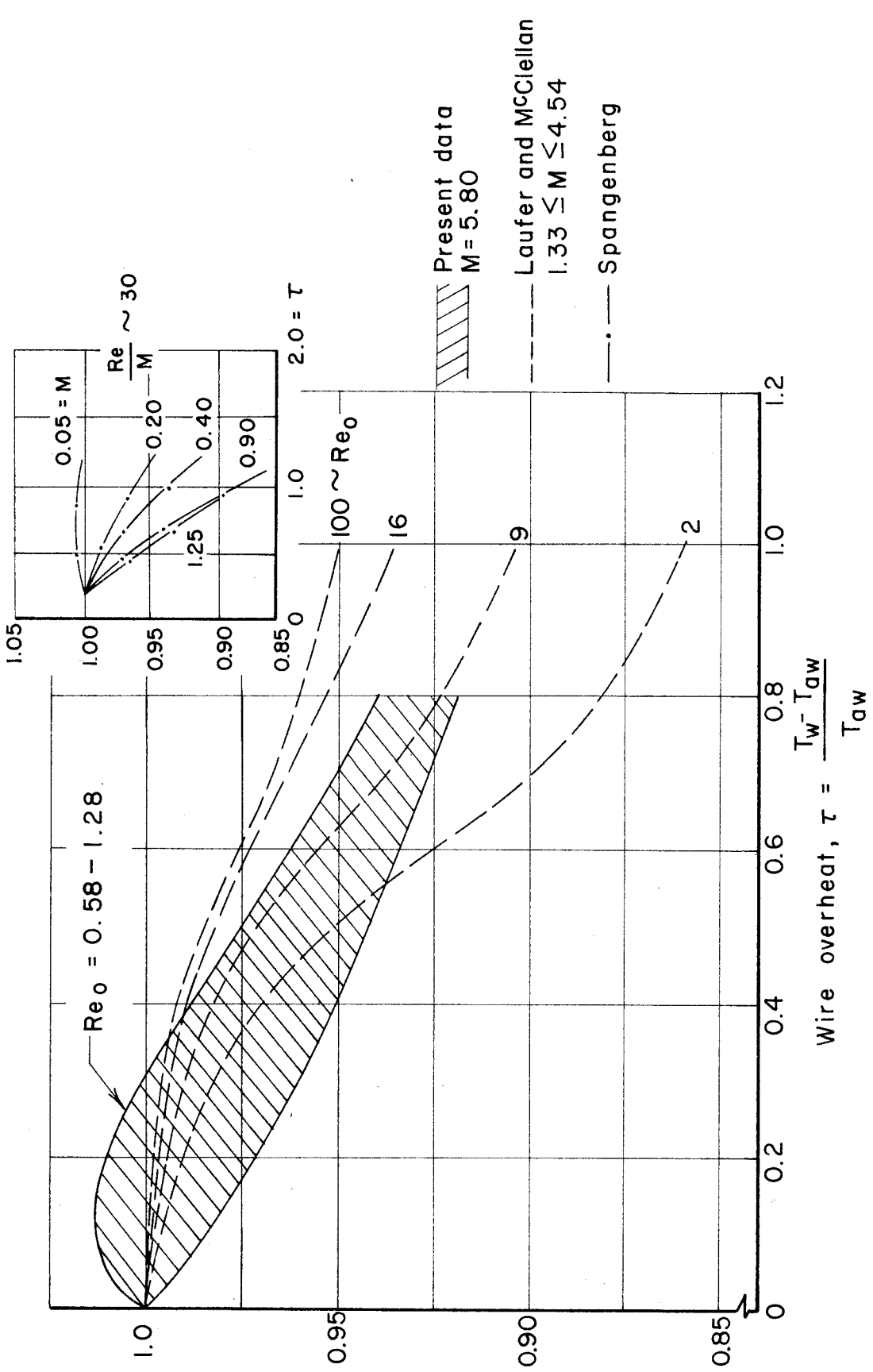

FIG. 16 – VARIATION OF NUSSELT NUMBER WITH OVERHEAT

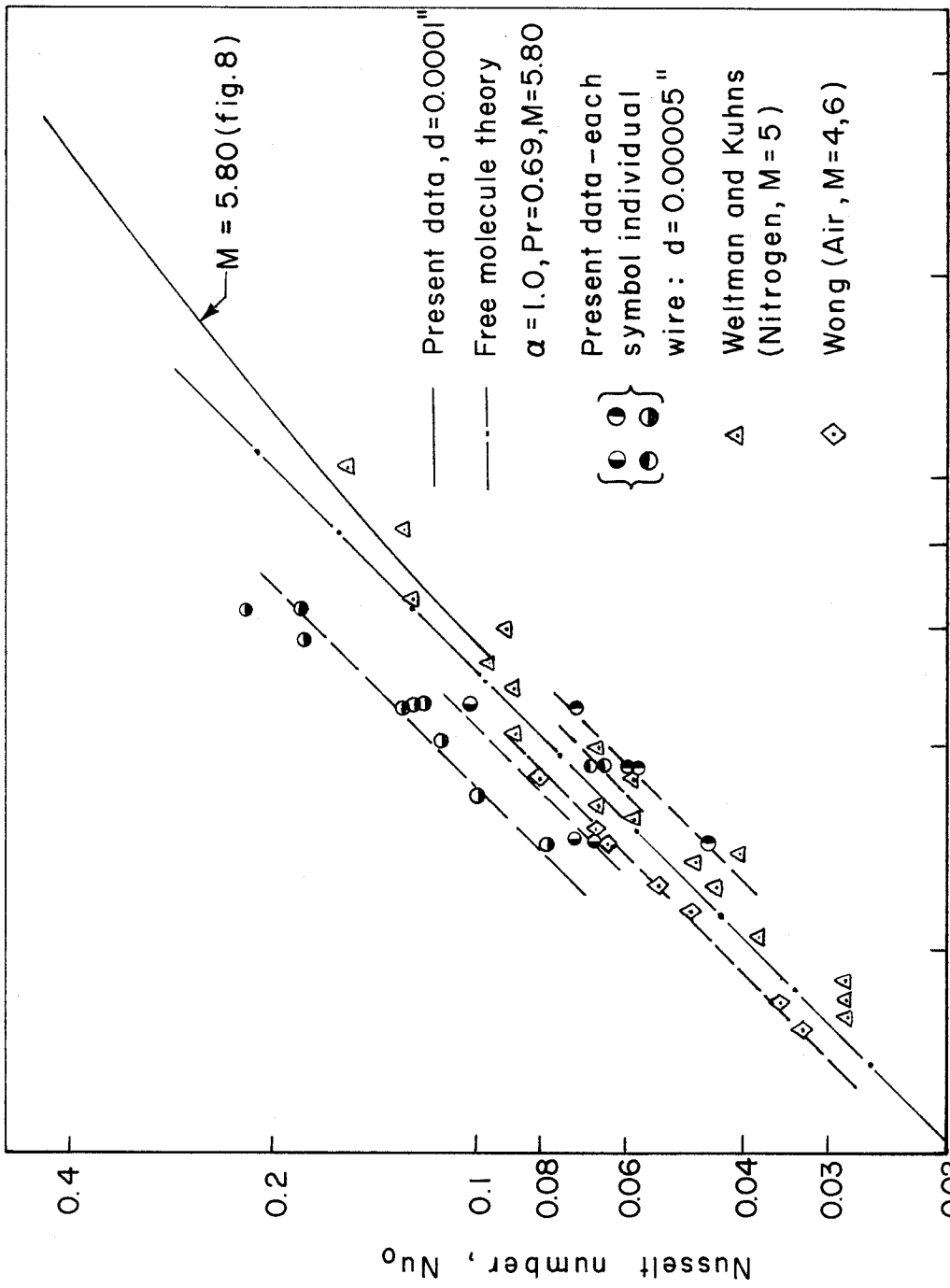

FIG. 17 NUSSELT NUMBER – REYNOLDS NUMBER RELATION APPROACHING FREE MOLECULE FLOW

MEASUREMENTS IN HIGHLY DISSIPATIVE REGIONS OF HYPERSONIC FLOWS

PART II. THE NEAR WAKE OF A BLUNT BODY AT HYPERSONIC SPEEDS

Thesis by

C. Forbes Dewey, Jr.

In Partial Fulfillment of the Requirements

For the Degree of

Doctor of Philosophy

California Institute of Technology

Pasadena, California

1963

ACKNOWLEDGMENTS

I am deeply indebted to Professor Lester Lees for his guidance and inspiration during my graduate career, and in particular for the support which he and Dr. Clark Millikan gave to the present investigation. My heartfelt thanks go to Dr. Toshi Kubota, who was always ready to offer his constructive advice; to Dr. A. Demetriades and other members of the GALCIT staff for enlightening discussions; to Mary Romig of the RAND Corporation for reviewing an early version of Section II. 2; to S. Roman, J. Van Dijk, G. Van Halewyn, and P. Baloga of the hypersonics group for their able assistance; to Truus van Harreveld for her conscientious and painstaking efforts in reducing the experimental data; and to C. Bartsch and R. Bartsch for fabricating models which should have been impossible.

This thesis is dedicated to my parents, whose untiring devotion has always been my greatest resource.

ABSTRACT

A theoretical model of the near wake is derived following the ideas of Chapman. This model is based on the postulates of mass conservation in the base flow region, thin viscous shear layers, and a recompression process which is independent of Reynolds number. The analysis, which includes the effects of initial shear layer thickness and base flow temperature, shows that the characteristics of the near wake (base pressure, shear layer angle, etc.) are independent of Reynolds number, and that the shear layer and initial wake thicknesses are proportional to $Re^{-\frac{1}{2}}$.

A series of experiments are presented which show that the postulate of thin shear layers is invalid for Reynolds numbers less than about 10^3. At higher Reynolds numbers, the theory is qualitatively incorrect if the Mach number M_e external to the shear layer is large. Detailed measurements with a steady-state hot-wire in the near wake of a two-dimensional circular cylinder indicate that the compression process at the neck is not isentropic, and that the maximum pressure rise occurs downstream of the stagnation point formed by the merging shear layers. Comparison between the experimental and theoretical results points out the importance of the base flow temperature and the initial shear layer profile in determining the observable characteristics of the near wake.

TABLE OF CONTENTS

TABLE OF CONTENTS (Cont'd)

LIST OF FIGURES

LIST OF FIGURES (Cont'd)

LIST OF SYMBOLS

The diagram and symbols given below define the nomenclature most frequently used in the text. Less common terms are explained as they appear.

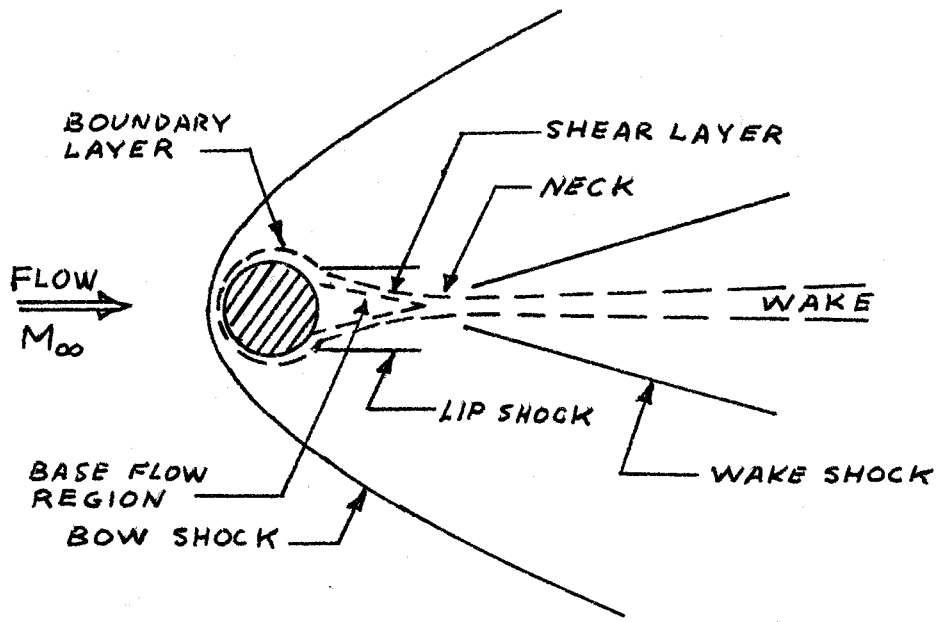

c_p	specific heat
d	hot-wire diameter
D	cylinder diameter
f	velocity ratio, (u/u_e)
h	convective heat transfer coefficient, $\frac{q}{T_w - T_{aw}}$
H	half-height of wedge; total enthalpy, $c_p T + u^2/2$
i	hot-wire current
k	air thermal conductivity
k_w	wire thermal conductivity
K_n	Knudsen number, $\sqrt{\pi\gamma/2}\ (M/Re_\infty)$

LIST OF SYMBOLS (Cont'd)

ℓ	hot-wire length; distance measured along shear layer
L	characteristic model length
M	Mach number
Nu_m	Nusselt number measured with finite length wire, $h_m d/k_0$
Nu_0	Nusselt number for infinite length wire, hd/k_0
p	static pressure in flow; model surface pressure
p_b	base pressure at model centerline
p_{t2}	total (stagnation) pressure behind a normal or oblique shock; pitot pressure behind a normal shock
Pr_0	Prandtl number $c_p \mu_0 / k_0$
q	heat transfer rate
R	wire resistance or resistance of thin-film gage
Re	Reynolds number $\rho u x/\mu$, where x is a characteristic distance
s	distance along dividing streamline from separation
T	temperature
u	local flow velocity
u_∞	free-stream velocity
x	distance in the streamwise direction from the centers of cylinders and spheres or the bases of cones and wedges
y	distance from model axis in transverse direction
α	accommodation coefficient
α_r	temperature-resistivity coefficient, $(R_w/R_r) \cong 1 + \alpha_r (T_w - T_r)$
γ	ratio of specific heats
δ	boundary layer or shear layer velocity thickness
δ^*	boundary layer or shear layer displacement thickness
η	non-dimensional temperature, T/T_0

LIST OF SYMBOLS (Cont'd)

θ	boundary layer or shear layer momentum thickness
θ_w	wedge angle
θ_s	angle between shear layer dividing streamline and the wake axis
θ_0	initial momentum thickness of the shear layer
λ	velocity function, $(1 - u_*/u_e)$
μ	viscosity
ν	kinematic viscosity, μ/ρ
ξ	parameter in shear layer analysis, $(\frac{s}{\theta_0})^2 \frac{1}{Re_{e,s}}$
ρ	density
τ	wire overheat, $(T_w - T_{aw})/T_{aw}$
ψ	stream function
Ψ	end loss correction factor

Subscripts

$( )_{aw}$	zero current
$( )_b$	evaluated in the base flow region
$( )_e$	quantity at outer edge of boundary layer or shear layer
$( )_m$	measured value
$( )_0$	evaluated at stagnation temperature
$( )_r$	evaluated at reference temperature T_r
$( )_*$	quantity along dividing streamline
$( )_\infty$	free-stream quantity
$( )_2$	static flow properties behind a normal or oblique shock
$( )_\text{¢}$	evaluated at wake centerline or axis of flow symmetry
$( )_B$	quantity evaluated along the body surface in the upstream attached flow region

LIST OF SYMBOLS (Cont'd)

$\bar{(\ )}$	mean value or normalized quantity; velocity or distance in the physical plane
$\tilde{(\ )}$	transformed variable
$(\ )'$	conditions at the edge of the wake downstream of the neck

I. INTRODUCTION

Among the many problems of modern and classical fluid mechanics, there are two which have aroused more interest and engendered more frustration than any others; these are turbulence and separation. The subject of this thesis--the near wake of a blunt body at hypersonic speeds--falls within the latter category, and throughout the text the problem will be approached as an example of laminar separation rather than a phenomenon unique to hypersonic flow.

The wake of a blunt body at low speeds is complicated by the existence of a time-dependent flow field. Roshko (1, 2)* found that at low speeds vortices develop behind the body in a periodic manner, the frequency of shedding being proportional to the free-stream velocity. This unsteadiness is also present in the investigations of Gorecki (3), Nash (4), Thomann (5), and Gowen and Perkins (6) at subsonic speeds. In the experiments cited above, the test body was two-dimensional, but similar results have been found for spheres in incompressible flow (7) and in subsonic flow (8, 9).

As the free-stream Mach number M_∞ is increased, a drastic change occurs in the structure of the base flow. For $M \gtrsim 1$ (the exact value varies with geometry and Reynolds number), the violent periodic shedding evidenced at lower speeds disappears and a steady supersonic flow pattern is established.

* Numbers in parentheses refer to references at the end of the text.

Figures 1 and 2, reproduced from the works of Thomann (5) and Nash (4), clearly indicate the dramatic change which occurs in the wake structure. A careful examination of these photographs will reveal a second important characteristic; at low supersonic Mach numbers and high Reynolds numbers, there is a definite "structure" to the wake immediately downstream of the neck*. The "graininess" is associated with small scale turbulent motion, and large "puffs" of turbulent fluid may be clearly identified (cf. Figure 1b). Similar phenomena are evident in the Schlieren photographs of spheres by Charters and Thomas (9) and of cones by Charters (10); two particularly graphic examples have been included in Figure 3.

Further increases in Mach number, at large body Reynolds numbers, produce no qualitative change in the near wake from the features shown in Figure 3.** This behavior is explained by the well-known "hypersonic freeze" or "Mach number independence principle" (11) which recognizes that the viscous and inviscid flow fields become independent of Mach number if the Mach number is sufficiently large. The governing parameter is $M_\infty \sin\beta$, where β is the angle between the free-stream direction and a tangent to the local body surface. Thus, the flow field about a blunt body will be "frozen" at a much lower value of free-stream Mach number than that which pertains to a slender body.

---

* Nomenclature for the various regions of the flow field is given in the List of Symbols

** Many body diameters downstream, the inviscid wake exhibits a static enthalpy profile which depends strongly on Mach number if $M_\infty >> 1$.

There is one additional feature of the near wake which must be discussed at this point. For large Reynolds numbers, the boundary layer along the body surface is turbulent, and the shear layer and wake are turbulent as well. Decreasing the Reynolds number at a fixed value of M_∞ will produce a laminar boundary layer on the body surface; as the boundary layer separates from the surface to become the shear layer, it will remain laminar if the Mach number M_e at its outer edge is greater than about 2.5. The two shear layers from opposite sides of the body then meet to form a laminar viscous wake which may persist for many body diameters in the downstream direction (References 12-14). Lees (15) has summarized the experimental and theoretical evidence for steady laminar regions of separation, and more detail on this question will be presented in a later section. The point to be made is that there exists an important class of separated flows for which the shear processes are laminar and time-independent.

It is the purpose of this thesis to examine the steady laminar near wakes of blunt two-dimensional bodies. The tools of this investigation are primarily experimental, although some momentum integral methods are used to discuss the development of the shear layer. First, a model of the base flow region is developed, generalizing certain features of the analysis introduced by Chapman (16). The effects of body Reynolds number, body temperature, and Mach number on the development of the shear are discussed, and the importance of the initial shear layer profile is demonstrated. Second, the results of the theoretical model are compared to base

pressure measurements on a transverse cylinder and two wedges. Next, the steady-state hot-wire is used to "map out" the near wake region of a transverse cylinder. Both heat loss and recovery temperature data are used to define the growth of the shear layer and the behavior of the flow in the reattachment region. Finally, a "goal post" technique for mapping streamlines is presented.

II. THEORETICAL CONSIDERATIONS

The purpose of this section is to examine the salient features of a laminar base flow region. A physical model of the flow is developed, following the ideas of Chapman (16). This model leads to scaling laws which show the effects of Mach number and Reynolds number on the base flow phenomena. A detailed treatment of the free shear layer is then given, and the results of some simple integral solutions are presented. Finally, a summary is made of the theoretical postulates which must be verified by experiment.

II.1. Physical Model of the Flow

Historically, the two most important contributions to a model of the near wake were: (1) a recognition of the fact that mass conservation requires all the fluid originally within the base flow region and entrained by the shear layer to be returned to the base region at the wake neck; and (2) a recognition of the dominant role of the shear layer mixing rate in determining the pressure rise required to satisfy this mass conservation condition. The mass conservation condition was first recognized by Chapman (16), and the role of the shear layer mixing process was originally expounded by Crocco and Lees (17).

The momentum integral method which Crocco and Lees used to study the shear layer mixing process provided a framework for studying the qualitative effects of Mach number, Reynolds number, and body shape on a wide variety of separated flow problems.

Several difficulties existed in applying this method, and these have been clarified only recently (18). The first successful quantitative prediction of base flow phenomena was given by Chapman for laminar flow (see References 19-21) and Korst, Page and Childs (22) for the case of a turbulent shear layer. Certain idealizations were made by these authors, and these will be discussed shortly; our present purposes will be served by a consideration of the two essential features mentioned above.

The sketch below defines the physical model which follows from the assumptions of mass conservation and momentum conservation along the dividing streamline. Under the influence of

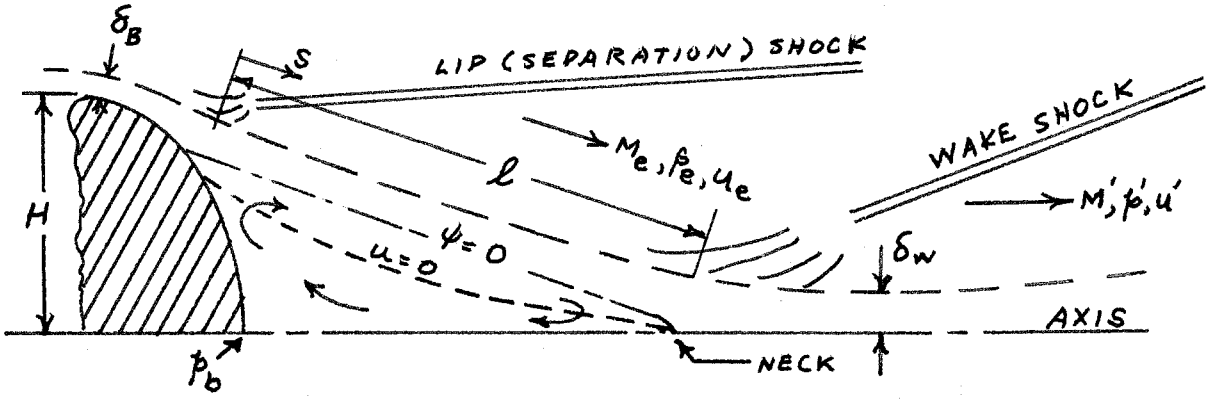

Sketch 1. Nomenclature for the near wake.

viscous and pressure forces, the boundary layer separates from the body to form a viscous mixing layer. This layer entrains mass from the inviscid region along its external surface (subscript e) and also along the lower boundary bordering the base flow region. As the shear layer grows, the velocity u_* and Mach number M_* along the streamline which was originally adjacent to the body

($\psi = 0$) increase because of momentum transfer. This streamline is called the "dividing streamline."

The path of the dividing streamline serves to define the geometry of the near wake. For two-dimensional flow, it is nearly a straight line of length ℓ (see Sketch 1), but in the axisymmetric case the shear layer is convex (e.g. Figure 3). If the separation point is fixed, then ℓ determines the angle between the shear layer and the axis, and consequently the quantities M_e, p_e, and u_e in the inviscid flow.

In order to conserve mass, all streamlines below $\psi = 0$ must be turned back into the base region by the compression process at the neck, and all particles following streamlines $\psi > 0$ will pass through the neck and flow downstream, although at a reduced velocity. Conservation of mass and momentum, therefore, specify the pressure rise $(p' - p_e)$ required to bring the dividing streamline to rest, and this pressure rise increases with an increasing deflection of the inviscid flow outside the shear layer.

This coupling between viscous mixing and flow geometry has a very simple interpretation. An analysis of the shear layer (Section II.3) shows that the Mach number ratio $M_*(\ell)/M_e$ at the neck is a monotonically increasing function of the parameter

$$\xi(\ell) = \left(\frac{\ell}{\theta_0}\right)^2 \frac{1}{Re_{e,\ell}} ,$$

where θ_0 is the initial momentum thickness of the shear layer. However, the value of M_* required by mass conservation decreases

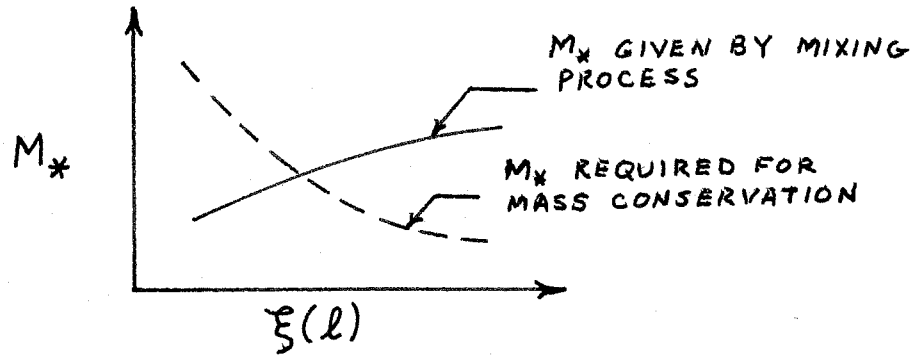

Sketch 2. Matching procedure for the neck region.

with increasing ℓ, because there is less pressure rise across the neck. Since ℓ increases with $\xi(\ell)$, there is a particular value of ξ for which the value of M_* required for mass conservation is equal to that given by the mixing process.

The importance of the initial momentum thickness is evident in this formulation. It is only in the case where $\theta_0 \to 0$ $(\xi \to \infty)$ that M_* becomes a function only of M_e and the base temperature T_b. If the Reynolds number $Re_{e,\ell} = (\rho_e u_e \ell/\mu_e)$ is large, then the shear layer is very thin. The readjustment regions in the vicinity of the separation point and the wake neck are only one or two shear layer thicknesses in extent*, and are small if $Re_{e,\ell}$ is very large. Then the shear layer should represent a relatively constant pressure surface, since the amount of flow entrained by the shear layer is not large and the dynamic pressure in the base region is small.

* This result is not obvious a priori, but may be inferred from the measurements presented in Section V.

Constant pressure mixing should therefore represent a good approximation to the actual shear layer process, a fact which greatly simplifies the analysis (Section II.3 and Appendix A). Chapman (19) obtained a limiting solution to the constant pressure mixing process for $\theta_0 \to 0$. The momentum equation reduces to that of Blasius with the boundary conditions $u \to u_e$ as $y \to \infty$, and $u \to 0$ as $y \to -\infty$, and possesses a similarity solution of the form

$$(u/u_e) = f\left(y\sqrt{\rho_e u_e/\mu_e s};\ M_e\right) .$$

In particular, he found (u_*/u_e) to be a constant, since $\xi(s) \to \infty$.

One important consideration is the distortion of the boundary layer profile as it leaves the body. Clearly, this process will be different for a "gradual" separation from a convex surface (such as a sphere or cylinder) and a "catastrophic" separation from a sharp corner (such as a cone or wedge). Separation from a sharp corner in supersonic flow involves a complex interaction between a strong Prandtl-Meyer expansion, a weak lip shock (e.g. Figure 3b), and the boundary layer, whereas a convex surface exhibits a single lip shock and a compression of the flow back toward the free-stream direction. One might therefore conjecture, as did Chapman (16) and Holder and Gadd (23), that for the case of a sharp separation the initial shear layer velocity profile will be more full and the initial mixing rate will be larger. If the initial shear layer momentum thickness θ_0 ($s = 0$) is not small, or more precisely (Section II.3) if

$$\left(\frac{\ell}{\theta_0}\right)^2 \frac{1}{Re_{e,\ell}} \lesssim 0(1) ,$$

then the velocity profile will differ significantly from Chapman's similar solution. In particular, the velocity u_*, the Mach number M_*, and the pressure rise (p'/p_e) will be less than the value obtained from the similarity analysis.

Three additional features of the supersonic near wake appear when a comparison is made between two-dimensional and axisymmetric bodies. Chapman (16, 20) applied the method of characteristics to the calculation of constant pressure surfaces downstream of a sharp circular base. He found that it is impossible for a steady axisymmetric inviscid flow to converge toward and intersect the axis in a pattern which will admit the existence of a wake shock; he reasoned that the action of viscosity will therefore be important in the neck region of an axisymmetric flow. For two-dimensional bases, this problem does not appear. Note that the characteristics calculation may proceed to very small distances from the axis if the Mach number is large.

The characteristics calculations (20) also revealed a second distinctive feature; a constant pressure axisymmetric surface which converges toward the axis is convex, whereas straight streamlines describe a constant pressure simple wave region in the corresponding two-dimensional problem. The curvature of the shear layers in Figure 3 is compatible with the constant pressure assumption. As the Mach number M_e increases, an axisymmetric constant pressure surface becomes less curved.

A third distinction arises between axisymmetric and two-dimensional flow if the shear layer thickness is allowed to remain

small but finite. In two-dimensional flow, the growth of the free shear layer is determined solely by the mixing rate between separation and the neck. In axisymmetric flow, the shear layer thickens considerably as the axis is approached, since the viscous wake which passes downstream must contain all of the mass which was originally in the boundary layer velocity thickness δ_B at separation. A crude estimate of the wake velocity half-thickness δ_w is then

$$\pi\delta_w^2 \gtrsim 2\pi H\delta_B$$

or

$$\left(\frac{\delta_w}{H}\right)^2 \gtrsim \left(\frac{\delta_B}{H}\right) .$$

If (δ_B/H) is 1/25, say, then (δ_w/H) will be about 1/5 which is not vanishingly small.

II.2. Scaling Laws for Blunt Bodies

Certain scaling laws may be derived very simply for the near wake of a two-dimensional body in supersonic flow. If the viscous shear processes are everywhere laminar and steady, and the shear layer thickness is small compared to the characteristic body dimension H, the important effects of Mach number, Reynolds number, base flow temperature, and body shape on the wake thickness δ_N, the zero streamline velocity u_*, and the base pressure $p_b \cong p_e$ may be explicitly determined.

For the sake of simplicity, consider the supersonic flow

of a perfect gas about a family of geometrically similar two-dimensional bodies which differ only in their characteristic dimension L (e.g. circular cylinders, 10° wedges, etc.). The body Reynolds number is assumed to be sufficiently small that all diffusion processes near the body are laminar, yet sufficiently large that viscous effects do not change the effective body shape. Then the inviscid flow about the body may, in principle, be calculated for any specified values of M_∞ and γ, and the inviscid field is independent of Reynolds number so long as the flow is attached to the body surface. A knowledge of the inviscid flow and the surface temperature allows the boundary layer profile and thickness to be determined at any point along the surface.

Of particular interest is the momentum thickness θ_0 of the shear layer at separation. This thickness may be symbolically expressed as

$$\frac{\theta_0}{L_B} = \frac{\kappa_1 \kappa_2}{\sqrt{Re_{B,L}}}$$

where

$$\kappa_1 = \kappa_1 \left(\overline{\beta}_B,\ M_\infty,\ \gamma,\ Pr,\ \frac{T_B}{T_0}\right)$$

= parameter relating the growth of the boundary layer in the transformed plane to the growth in the physical plane; it includes the numerical value of the displacement thickness in the transformed plane, and the effects of pressure gradients along the body are symbolically represented by $\overline{\beta}_B$,

$\kappa_2 = \kappa_2(M_e, M_B, \gamma)$

= parameter characterizing the changes in the boundary layer thickness and profile during the separation process; the compression/expansion details at separation depend on the Mach number M_B of the attached flow and the Mach number M_e of the separated flow,

and

$Re_{B,L} = \frac{\rho_B u_B L}{\mu_B}$, where ρ_B, u_B and μ_B are characteristic values of density, velocity, and viscosity external to the boundary layer along the body, and L is a characteristic body length.

The value of κ_2 and the total pressure loss (if any) of the inviscid flow at separation will be assumed constant for fixed values of M_e and M_B. (This should be a reasonable approximation in cases where the separation point is fixed by geometry, but must be reexamined if the separation point is allowed to vary with free-stream Reynolds number and the angle between the shear layer and free-stream direction is large.) The body temperature influences the momentum thickness θ_0 if $H_B = O(H_e)$.

This specification of the initial momentum thickness θ_0 entering the region of separation, when combined with a knowledge of the shear layer mixing rate and a description of the recompression process at the wake neck, is sufficient to define the complete flow field in the near wake. To describe the mixing and recompression regions, Chapman (21) made two assumptions. First,

he postulated that the dividing streamline $\psi = 0$ is brought to rest by an isentropic compression, so that the pressure rise across the neck is determined by

$$\frac{p'}{p_e} = \left(1 + \frac{\gamma - 1}{2} M_*^2\right)^{\frac{\gamma}{\gamma - 1}} \qquad (2)$$

where M_* is the local Mach number of the dividing streamline at the point where it begins the recompression process*. Second, he postulated that the velocity (and Mach number) of the dividing streamline could be determined by considering the constant pressure laminar mixing of a uniform stream and a fluid at rest. This implies that there is a negligible velocity in the base flow region, and that the shear layer thickness is negligible in comparison to the body dimension H and the distance to reattachment ℓ.

A Reynolds Number Independence Principle for Similar Bodies

The first two postulates given above, isentropic compression at the neck and constant pressure mixing in the shear layer, are the only ones which are essential to the argument. The further simplifications introduced by Chapman (21) to complete the problem (isoenergetic flow and $(\theta_0 / H) \to 0$) are not required. Toshi Kubota and I have investigated the constant pressure mixing problem using the Kármán momentum integral approach, and the details of this work

* Korst, Page, and Childs (22) proposed a model for turbulent flow in which the pressure rise is determined from oblique shock relations. The essential feature--that the zero streamline is brought to rest by pressure forces--is common to both models, and for this reason this condition is often called the "Chapman-Korst model."

are given in Appendix A. An equivalent numerical solution has been developed independently by Denison and Baum (25), and their results are in qualitative agreement with the present solution. In the present analysis it is found that the rate of growth of the laminar shear layer depends on the external Mach number M_e, the total enthalpy ratio (H_e/H_b) across the mixing region, and the local ratio of specific heats γ. If M_e, (H_e/H_b), and γ are fixed, the results show that the velocity u_* and Mach number M_* along the dividing streamline depend on the single parameter

$$\xi \equiv \left(\frac{s}{\theta_0}\right)^2 \frac{1}{Re_{e,s}} \tag{3}$$

where

$$Re_{e,s} = \frac{\rho_e u_e s}{\mu_e}$$

and

s = distance along the dividing streamline from the point of separation.

For $\xi \to 0$, $u_* \to 0$ and $M_* \to 0$ so that a negligible pressure rise is required to stagnate the dividing streamline; physically, this would correspond to the vanishingly small near wake of a thin plate. As $\xi \to \infty$, the original condition of Chapman $((\theta_0/H) \to 0)$ is realized so that u_* and M_* assume asymptotic values given by the appropriate similar solution of the free mixing problem. The results clearly indicate that an increase in the initial shear layer momentum thickness θ_0 (with $Re_{e,\ell}$ and ℓ fixed) acts to decrease M_* and increase the base pressure. Such predictions are in qualitative

agreement with experimental observation, and are quantitatively of the correct order of magnitude.

In applying the above theory to bodies at supersonic speeds, there is a subtle difference between (A) considering the effect of θ_0 on M_* with $Re_{e,\ell}$ fixed, and (B) considering the effect of Re_{∞,L_B} on M_* with ℓ and the body shape fixed (25).

Consider M_∞, Pr, γ, (T_B/T_0), and the body shape to be given. Then the inviscid flow is known and κ_1 appearing in Equation 1 is a constant for all values of L and $Re_{\infty,L}$. Assume that M_e is independent of Reynolds number and examine the consequences of this condition. If M_B, κ_2, and M_e are known, the pressure p_e ($p_e \cong p_b$) and the length ℓ of the shear layer are also determined. From Equation 1,

$$\frac{\theta_0}{L_B} = \frac{C}{\sqrt{Re_{B,L}}}$$

$$C = \kappa_1 \kappa_2 = \text{const.}$$

and combining this with (3) we have the important result

$$\xi(\ell) = \frac{1}{C^2} \left(\frac{\ell}{L}\right) \left(\frac{\rho_B u_B}{\rho_e u_e}\right) \left(\frac{\mu_e}{\mu_B}\right) . \qquad (4)$$

If we make the important assumption that the enthalpy H_b in the base region is independent of free-stream Reynolds number, then $\xi(\ell)$ is also independent of Reynolds number*. But if M_e is held constant

* If the viscosity is taken to vary as a power of the temperature, $\mu \sim T^\omega$, the viscosity term (μ_e/μ_B) is independent of the free-stream stagnation temperature only for $\omega = 1$. For $\omega \neq 1$, the succeeding arguments require the Reynolds number to vary with the stagnation temperature fixed.

and ξ is independent of $Re_{\infty,L}$, then M_* is also independent of $Re_{\infty,L}$ which was our original restriction, and the argument is therefore self-consistent.

With certain reservations, this result is applicable to axisymmetric bodies as well. In the axisymmetric case, a constant value of M_e implies a curved inviscid flow, so that the shear layer length ℓ should properly be defined as the curvilinear distance from separation to the neck along the zero streamline. To apply the present method of determining M_* with M_e and ℓ given, it must be postulated that the value of M_* for a converging axisymmetric flow differs from the result for two-dimensional flow by, at most, a constant; reference to the results of laminar boundary layer theory indicates that the shear layer must be everywhere small compared to its distance from the axis. Further, the compression process at the neck must be assumed to relieve the inviscid anomaly appearing near the axis in such a way that the flow above the zero streamline passes smoothly through this region. The assumption that the recompression region is small compared to the length ℓ of the shear layer may place severe restrictions on the allowed values of Reynolds number, since the axisymmetric shear layer thickens appreciably as it approaches the axis.

In summary, the original result of Chapman (21) which predicted that the base pressure and wake angle are independent of Reynolds number is now extended to the case of a finite initial

shear layer thickness. This may be termed a "Reynolds number independence principle for similar bodies," and is stated as follows:

> For any family of geometrically similar bodies experiencing purely laminar viscous flow, the base pressure and structure of the near wake are independent of the free-stream Reynolds number provided the inviscid flow, body temperature, and base flow temperature are also independent of Reynolds number.

One test, although not a crucial one, of the correctness of the arguments given above is to derive an expression for the wake "thickness" δ_w (see Sketch 1) immediately downstream of the neck. Since $\xi(\ell)$ is constant, the ratio $(\delta(\ell)/\delta_0)$ is also constant and the postulate of isentropic recompression demands that $(\delta_w/\delta(\ell))$ be a function only of (p_e/p') and M_e. At a fixed value of M_∞, therefore,

$$\frac{\delta_w}{L} \sim \frac{\delta_0}{L} \sim \frac{1}{\sqrt{Re_{B,L}}} \sim \frac{1}{\sqrt{Re_{\infty,L}}} \quad . \tag{5}$$

Figure 4, originally reported in Reference 26, shows that this conclusion is borne out for a circular cylinder in hypersonic flow. The pitot pressure measurements of McCarthy (27), diffusion profiles of Kingsland (28), and hot-wire data reported in Section V confirm these Schlieren results, although the wake "thickness" must be defined in a somewhat different manner for each method of observation.

Effect of Free-Stream Mach Number

According to the Mach number independence principle, the viscous and inviscid flow fields about a blunt body become independent of Mach number if the component of M_∞ normal to the body

surface is everywhere large. With regard to surface observables such as pressure and heat transfer, this result has been extensively verified; as a matter of interest, Part I of this thesis provides a typical example by showing that the heat transfer from a fine wire is independent of M_∞ for $M_\infty \gtrsim 3$. Since a circular cylinder is the primary model investigated in this experimental program, it is important to note that the cylinder surface pressure distributions measured by McCarthy (27), Tewfik and Geidt (29), Walter and Lange (30), and Gregorek and Kordan (31) show that the pressure distribution (p_B/p_{t2}) from the forward stagnation point to separation is identical for all values of $M_\infty \gtrsim 4.5$. The quantity p_{t2} is the stagnation pressure behind the leading edge shock wave, and for a cylinder this quantity is equal to the surface pressure at the stagnation point.

Throughout the range of Mach numbers and body shapes for which the Mach number independence principle applies, the appropriate Reynolds number and pressure are $Re_{0,L}=(\rho_\infty u_\infty L/\mu_0)$ and p_{t2}*. The fact that the base pressure p_b (M_∞) is independent of Reynolds number means that for blunt bodies at hypersonic speeds (p_b/p_{t2}) is independent of <u>both</u> the free-stream Mach number and Reynolds number. The measurements reported in Section IV show that this is very nearly true for a circular cylinder. Again, the restrictions of steady laminar flow and thin shear layers must be satisfied.

* The Reynolds number $Re_{2,L}=\rho_\infty u_\infty L/\mu_2$ appears frequently in correlations of heat transfer and skin friction results; at hypersonic speeds, $Re_{2,L}$ and $Re_{0,L}$ are very nearly equal. Several reasons for choosing the latter relation are given in Part I of this thesis.

II.3. The Free Shear Layer

The importance of the free shear layer in determining the characteristics of the near wake has already been indicated. What remains is to develop a quantitative method for predicting the Mach number M_* along the dividing streamline, and critically assess the limitations of the theory.

Several years ago, Chapman (16, 19) derived a solution for the self-similar laminar shear layer. Formally, this solution describes the constant pressure mixing of two parallel streams, where the initial thickness of the mixing layer is zero. This section is concerned with the application of momentum integral methods to the constant pressure mixing problem where the thickness of the initial shear layer is finite. More specifically, the problem is to determine the velocity, temperature, and mass flow profiles in the free shear layer when the parameter

$$\xi = \left(\frac{s}{\theta_0}\right)^2 \frac{1}{Re_{e,s}}$$

is not infinite.

The momentum integral method is only one of several alternative approaches to this problem. The Crocco-Lees (17) mixing theory and the numerical finite-difference scheme of Denison and Baum (25) are other examples. A fundamental similarity between all of the methods is that, once an initial profile at $s = 0$ and the boundary conditions (including H_b) have been specified, the solution

depends only on the independent variable ξ.*

A detailed exposition of the momentum integral formulation is given in Appendix A. In this treatment, the first step is to reduce the compressible problem to incompressible form by using the Howarth transformation and the mathematical simplifications $\mu \sim T$ and $Pr = 1$. The s-momentum and continuity equations are then uncoupled from the energy equation; their form is the same as for the incompressible constant pressure boundary layer:

$$\frac{\partial u}{\partial s} + \frac{\partial v}{\partial y} = 0 \tag{6}$$

$$u \frac{\partial u}{\partial s} + v \frac{\partial u}{\partial y} = \nu \frac{\partial^2 u}{\partial y^2} \ . \tag{7}$$

An initial velocity profile $u_0(y)$ is specified at $s = 0$, and the boundary conditions on the velocity are $u \to u_e$ at the outer edge of the shear layer and $u \to 0$ (monotonically) in the base flow region. The latter boundary condition is physically admissible only for shear layers whose thickness is very small compared to the dimensions of the base flow region. This approximation would certainly fail in the vicinity of the neck where the shear layers from opposite sides of the body meet.

It is found convenient to divide the shear layer into two regions (see Sketch 3 below), with Region I comprising all the streamlines $\psi \geq 0$ and Region II containing all the mass flux entrained by the shear layer from the base region. The velocity

* This statement is not true, of course, if transition occurs in the shear layer (17).

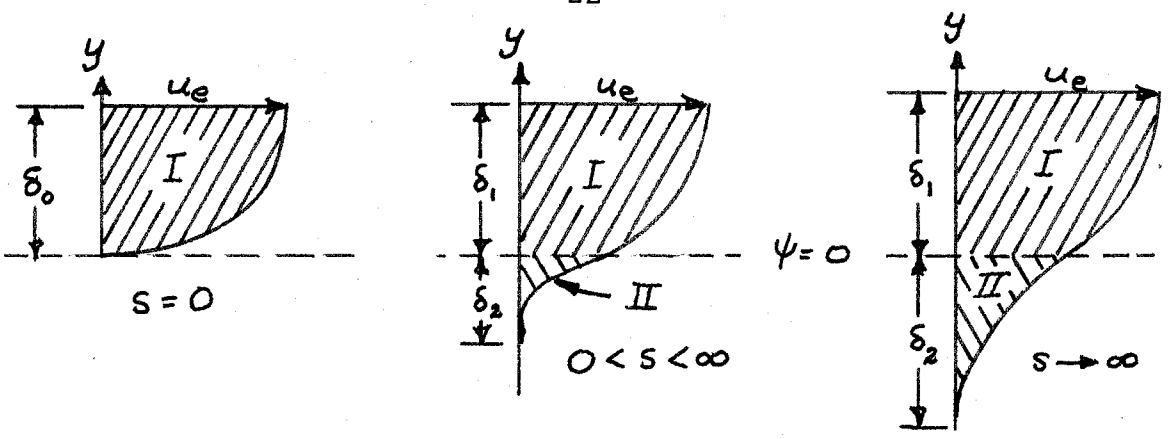

Sketch 3. Velocity profiles in the non-similar shear layer

profile in each part is represented by a simple analytic function $u(y;\delta_1,\delta_2,a_k)$ which contains a number of profile parameters $(a_k(s),\delta_1(s),\delta_2(s))$.

By multiplying the s-momentum equation by u^j $(j = 0, 1, \ldots)$ and integrating across the shear layer (making use of the continuity equation), a set of coupled ordinary differential equations is obtained which describe the variation of the velocity profile parameters (δ_1,δ_2,a_k) in the s-direction. Boundary conditions are also applied at the extremities of the shear layer, and matching conditions are imposed so that the velocity and certain of its higher derivatives are continuous at $y = 0$. The total number of moment equations, boundary conditions, and matching conditions must be equal to the total number of parameters appearing in the velocity profile. If the velocity profiles in Regions I and II are suitably chosen, the moment equations may be integrated in closed form.

Details of the calculation are given in Appendix A.

Figure 5 shows the resulting values of u_* as a function of the independent variable*, $\xi = (s/\theta_0)^2(Re_{e,s})^{-1}$. Curves are shown for:

(1) An initial Blasius profile, and numerical solution of the non-similar problem [Denison and Baum (25)].

(2) A quadratic profile, solution by the momentum integral method.

(3) An exponential profile, solution by the momentum integral method.

The three solutions are shown to be in good qualitative agreement, but they differ by as much as 0.15 in u_* at the same value of ξ. Even more disturbing is the fact that the values of ξ for a given u_* differ by as much as a factor of 6. For small values of u_*, the difference between the quadratic and exponential solutions may be explained by the fact that the value of $(\partial u/\partial y)$ at $y = 0$ is larger, and consequently the initial mixing rate is larger, for the exponential profile (see Equation A.42, Appendix A). The initial values of $(\partial u/\partial y)_{y=0}$ and final values of (u_*/u_e) for the quadratic and Blasius profiles are nearly equal, so that the difference between these two curves may be attributed to the method of solution.

Several general conclusions may be drawn from Figure 5. First, the value of u_* will be considerably less than that given by $\xi \to \infty$ in most physical situations. Second, the value of $u_*(\xi)$ is

---

* The velocity ratio u_*/u_e is independent of the base flow enthalpy H_b only if $\mu \sim T$. The Mach number M_* is a strong function of H_b, as will be demonstrated.

sensitive to the initial profile of the shear layer. And finally, the value of u_* (and consequently the base pressure, external Mach number M_e, and shear layer thickness) depend strongly on the details of the separation process if $\xi = O(1)$.

From these results, we may sketch the influence of the initial profile on $u_*(\xi)$. Consider three possible initial profiles as shown in Sketch 4 below. All are taken to have the same values

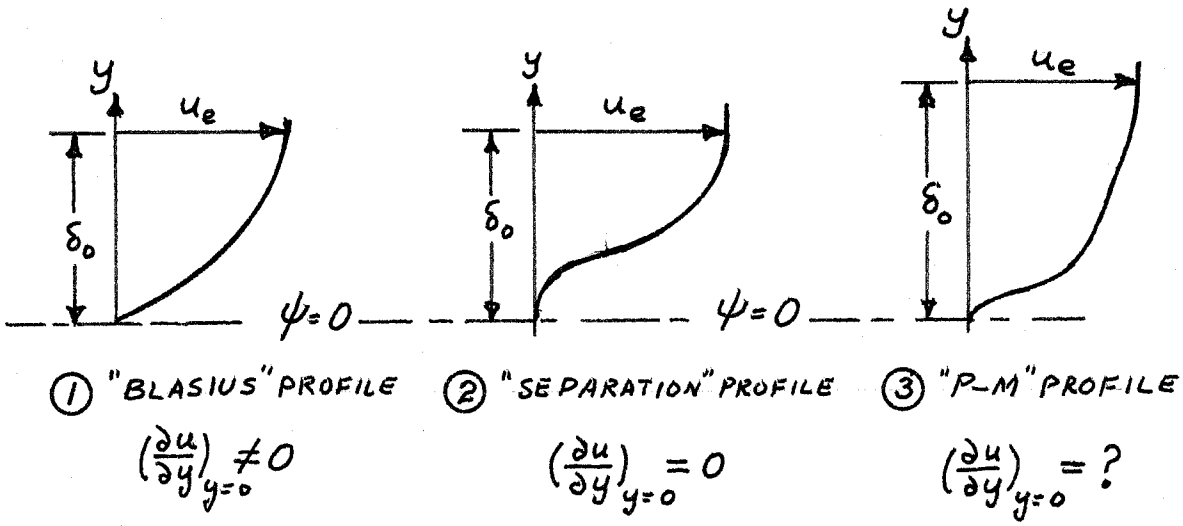

Sketch 4. Three possible shear layer initial profiles

of u_e and θ_0, but the details of the velocity distributions differ markedly. The "Blasius" profile ① may be regarded as a hypothetical separation in which no interaction between the inviscid flow and viscous flow has occurred. Profile ② is a representation of the velocity profile associated with a "gradual" separation in an adverse pressure gradient. The "P-M" profile ③ is typical of the "fat" velocity distribution which would result from a sharp corner separation which includes a Prandtl-Meyer

expansion fan; for the same value of θ_0, this profile will have a larger velocity thickness δ_0 than either (1) or (2).

Sketch 5 shows the conjectured behavior of $u_*(\xi)$ for the three profiles listed above. The "Blasius" profile will have a large value of u_* for small ξ because of the finite shear at the axis; initially, $u_* \sim s^{\frac{1}{2}}$ for the "smooth" separation, while $u_* \sim s^{1/3}$ for a Blasius profile. Soon the "P-M" value of u_* begins to grow "explosively" due to the high rates of shear in the lower portions of the profile. And finally, the spreading of the high vorticity in the outer portions of the "separation" profile will begin to be felt at the axis, and u_* will also grow rapidly for this case.

For large values of ξ, the three profiles approach the same asymptotic value of (u_*/u_e) (0.587 if Chapman's (19) result

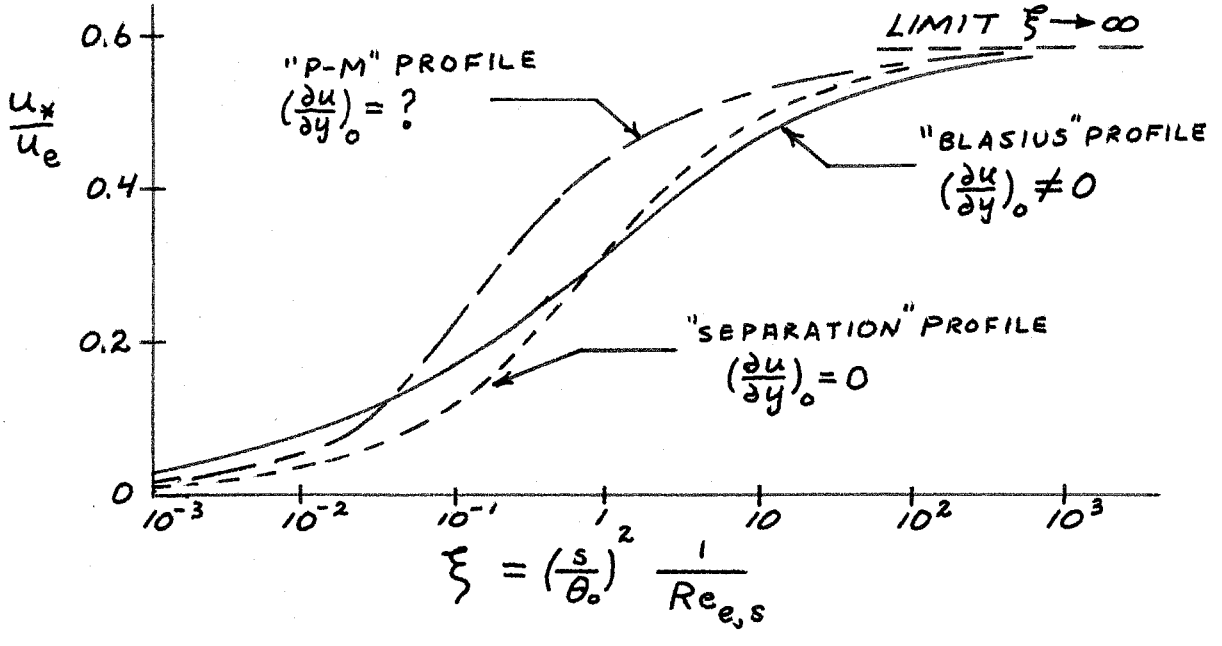

Sketch 5. Effect of the initial profile on the zero streamline velocity (schematic).

is used), although at a different rate. It should be emphasized that the coordinate ξ is based on the momentum thickness θ_0 after separation and not on the velocity thickness calculated for the attached boundary layer ahead of separation. Had this latter length been used, the "P-M" curve would have been displaced to the left and the "separation" curve to the right of their present positions relative to the "Blasius" result.

The growth rates shown in Sketch 5 explain the failure of solutions based on a "Blasius"-type profile to predict a value of u_* as large as that which is experimentally observed (see Sections IV and V). The discrepancy is particularly serious for sharp separations on cones and wedges, where the "P-M" profile is expected to apply. Since $\xi = O(1)$ for these bodies, a "P-M" initial profile would give a larger value of u_*, and consequently a lower base pressure and larger angle between the shear layer and the axis, than a "Blasius" distribution; this result would be in agreement with experimental observations.

In an unpublished investigation of the interaction between an attached boundary layer and an incident shock wave, B. L. Reeves* found a similar result. The high vorticity at the outer edge of a separation profile quickly diffuses to the zero streamline, and an "explosive" growth of the velocity u_* is observed. Lees and Hromas (32) have noted an "explosive" growth of the turbulent wake which is associated with the large gradients of static enthalpy

* Private communication

at the outer edge of the wake; this result is a rather interesting parallel to the growth phenomena shown by the laminar shear layer.

Referring to the results of Section II.2, it is now clear that the details of the separation process, as represented by κ_2, are important in determining the shear layer mixing rate. The assumption that κ_2 depends only on the gross features of the expansion/compression process [i.e. $\kappa_2 = \kappa_2(M_e, M_B, \gamma)$] is tenable only if the surface radius of curvature at separation is very much greater than, or very much less than, the attached boundary layer thickness. If the two are comparable and $\xi = O(1)$, the "Reynolds number independence principle" might be expected to fail. It is only in the extreme cases of $\xi \to 0$ [$(\theta_0/H) \to \infty$] and $\xi \to \infty$ [$(\theta_0/H) \to 0$] that the initial profile is not important.

The Mach number M_* and the pressure rise (p'/p_e) may be calculated once a solution to the energy equation is obtained. (See Sketch 2.) The assumptions leading to Equations 6 and 7 and the boundary condition $H(-\delta_2) = \text{constant}$ imply that the total enthalpy H is a linear function of u. Since $H = H_e$ at the outer edge of the shear layer, the total enthalpy H_* along the dividing streamline is a function only of u_* and the base flow enthalpy. Two extreme cases are considered: a "hot wall" case which corresponds to no heat transfer from the base flow region ($H = \text{constant} = H_e$); and a "cold wall" case where the temperature T_b in the base flow region is equal to the static temperature T_e at the outer edge of the shear layer.

Figures 6 and 7 show the computed values of M_* and (p'/p_e) for a quadratic velocity profile. Results are given for several Mach numbers M_e and the "hot wall" and "cold wall" boundary conditions. In Figure 6, the independent variable is based on θ_0 whereas in Figure 7 the shear layer velocity thickness $\overline{\delta}_0$ in physical coordinates is used. By using Equation 2 and Figures 6 and 7, M_* and (p'/p_e) may be obtained in either coordinate system. The utility of basing ξ on θ_0 is readily apparent; in Figure 6, the region of ξ which contains the growth of (M_*/M_e) is independent of Mach number, whereas if the independent variable is based on $\overline{\delta}_0$, as in Figure 7, there is a strong shift to lower values of the independent variable with increasing Mach number.

Strong cooling of the base region increases (M_*/M_e) and consequently increases the pressure rise (p'/p_e) which may be sustained at the neck. Denison and Baum (25) find a similar result for several specific body shapes. The effects of cooling become more pronounced with increasing Mach number. The stagnation temperature along the zero streamline, and hence the static temperature on the axis just downstream of the wake neck, is independent of ξ only in one case: adiabatic flow. In the limiting case considered by Chapman (19), $\xi \to \infty$ so that H_* must be equal to or greater than $(u_*/u_e) \times H_e$, which is $0.587\, H_e$ for $\xi \to \infty$. This fact was pointed out by Lees and Hromas (32). If, however, the base is highly cooled and $\xi = O(1)$, then both u_* and the total enthalpy H_* at the neck will be considerably less than their asymptotic values.

A word of caution should be extended lest the "cold wall" calculation be taken too seriously. In order that the total enthalpy across the shear layer be a linear function of velocity, it is necessary that the base flow enthalpy $H(-\delta_2)$ be constant. Now consider the physical problem posed by a highly cooled reentry vehicle with M_∞ very large. The body temperature will be a small fraction of the free-stream stagnation temperature, so that the boundary layer along the body will be highly cooled. As the boundary layer separates and entrains mass from the base flow region, the total amount of energy flux contained in the shear layer for $\psi < 0$ will be (approximately)*

$$(\text{Energy Flux})_{\psi<0} \cong \int_{-\bar{\delta}_2}^{0} \rho u H d\bar{y}$$

and this energy will be returned to the base flow region at the neck. In order that this region remain cool, the energy must be continually removed by heat transfer at the base of the body. Since heat transfer coefficients of surfaces within regions of separated flow are notoriously small (29, 34), it may be impossible to remove an amount of heat sufficient to keep the base region close to body temperature, and the axial enthalpy distribution may resemble that shown in Sketch 6. If $M_e >> 1$, then the mass flow ρu is very small below u_* because the static temperature is large and the density is low. Thus the total

* A more detailed energy balance for a separated region of the cavity-type is given by Chapman in Reference 33.

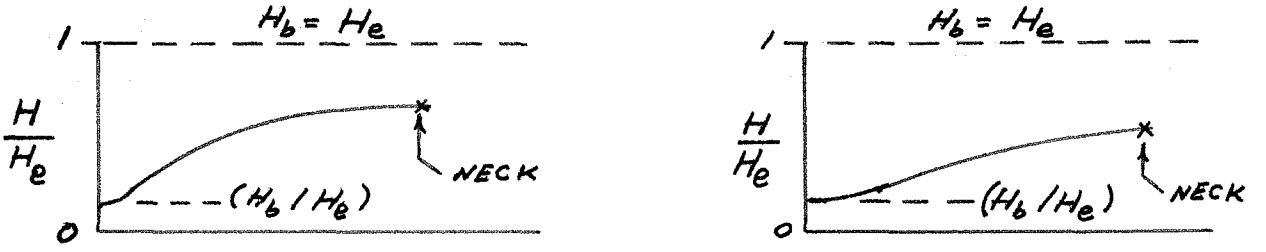

Case 1: $M_e \sim O(1)$ Case 2: $M_e >> 1$

Sketch 6. Axial enthalpy distribution in a "highly cooled" base flow region (schematic)

energy flux returned to the base will be less than an equivalent situation with $M_e = O(1)$. In either case, the solution of the energy equation will not be given by $H = A + Bu$, since the inner boundary condition on H varies with s. The value of M_*, and consequently the pressure rise (p'/p_e), may be significantly less than the result obtained assuming $H_b = H_B$.

A further difficulty arises in the case where H_B and H_b are much less than H_e. From the arguments given above, the axial variation of H_b is seen to depend on the rate of heat transfer at the base. But this heat transfer, and consequently the level of H_b and M_*, will vary with Reynolds number, so that some deviation from the "Reynolds number independence principle" should be expected for a highly cooled body.

In summary, this section has provided an insight into some of the details of the near wake by examining two simple momentum integral solutions to the non-similar constant pressure shear layer

mixing process. The qualitative and quantitative influences of base heat transfer and initial shear layer profile are indicated. The pressure rise (p'/p_e) across the recompression region is presented for several values of M_e, and arguments are advanced to show that a quadratic or other "Blasius-type" initial profile will predict values of (p'/p_e) which are smaller than are experimentally observed.

II.4. Results to be Verified by Experiment

The model of the near wake flow field developed in Sections II.1-II.3 rests on several assumptions which are strictly valid only in the limit of infinite Reynolds number (vanishingly small initial thickness). The following paragraphs summarize the assumptions and predicted observables which must be verified by experiment.

Assumptions to be Verified

(1) Isentropic recompression of the zero streamline. This is probably the most difficult postulate to examine directly by measurement. It is necessary to find the entropy, or equivalently (p/ρ^{γ}), along the dividing streamline both upstream and downstream of the neck. This experiment was not attempted, but an evaluation of the pressure gradients and shear layer profiles upstream and downstream of the neck provides a check on this postulate (Sections V.1 and V.2).

(2) Constant pressure in the mixing region. This assumption has been investigated at a Reynolds number sufficiently

low so that the regions of validity are clearly delineated (Section V.1).

(3) Negligible effect of flow within the base region on the development of the shear layer. A detailed mapping of the flow field behind a circular cylinder was obtained to indicate the applicability of this assumption (Section V.1).

(4) The path of the zero streamline is a straight line (two-dimensional flow) except in the regions very near separation and the neck. Its distance is well-defined, and it passes continuously from separation to a virtual stagnation point at the apex of the triangular base flow region. An attempt was made to define the zero streamline and the rear stagnation point using both "conventional" hot-wire measurements and a "goal-post" technique (Sections V.1 and V.2).

Predictions to be Verified

(1) Shear layer scaling laws

a) Wake thickness variation with Reynolds number (Section II.2)

b) Shear layer thickness as a function of Reynolds number (Section V.1)

(2) Reynolds number independence of base pressure for different geometrical families (Sections IV.1 and IV.2)

III. EXPERIMENTAL CONSIDERATIONS

The experiments were carried out in Leg #1 of the GALCIT hypersonic wind tunnel. The test section is 5" square, and contoured nozzle blocks produce a test section Mach number of 6. Because of sidewall boundary layer growth, the Mach number varies with free-stream Reynolds number as shown in Figure 8. The test rhombus of uniform flow is 3" wide and 15" long, with a static pressure uniformity better than ± 1.6% over any cross-section. Most of the data were obtained at a stagnation temperature of 275°F, this value being sufficient to avoid air liquefaction at all pressures encountered. The tunnel is capable of continuous operation at stagnation pressures between 1 and 8 atmospheres absolute; automatic regulators maintain a constant stagnation temperature within ± 2°F and a constant supply pressure within ± 0.07 psi over several hours. The limiting error in the flow uniformity and repeatability appeared to be the spanwise static pressure non-uniformity of ± 1.6%, which was caused by weak wavelets emanating from the sidewall access ports.

All data were obtained after the wind tunnel had been allowed to warm up for more than one hour, thus insuring that the nozzle blocks and other tunnel components had reached an equilibrium temperature. Temperatures of the pressure transducer, silicone manometer, and amplifier-recorder system were continuously monitored, and suitable calibrations employed to eliminate errors caused by temperature drift.

III. 1 Design and Calibration of Instruments

Pressure Instruments

Absolute pressure measurements were made with a U-tube micromanometer filled with Dow Corning DC 200 silicone oil and a Statham Model PA208-TC (0-5 psia) pressure transducer. The micromanometer was referenced to a pressure of 0.5μ Hg, as measured by a McLeod gauge, and incorporated an illuminated travelling eyepiece. The overall accuracy and repeatability of this manometer was about ± 3μ Hg. For the pressure transducer, operating in the range 0-60 mm Hg, the hysteresis and non-linearity was less than ± 0.06 mm Hg, as shown in the calibration of Figure 9*. This transducer is of the flush-diaphragm type, and a carefully constructed container with neoprene O-ring reduced the sampling volume to slightly less than 1/10 cc. This enclosure provided ample clearance for movement of the diaphragm while giving a rapid response time in the 10-60 mm Hg pressure range.

A part of the experimental program was the development of accurate pitot pressure measuring techniques which can be used to investigate separated flows. The final pitot probe design which resulted from this investigation is now described.

Pitot probes were manufactured from 0.028" dia. stainless steel tubing and pyrex. The stainless probe was flattened to an overall height of 0.0116", an overall width of 0.0408", and a wall thickness of about 0.001". The leading edge was squared off

* An initial hysteresis is present if the transducer has been exposed to pressures above 5 psia. Care was taken to keep the transducer pressure below 150 mm Hg during the complete test program.

normal to the probe axis. Round glass pitot probes were drawn from 6 mm O.D. x 4 mm I.D. pyrex tubing. By heating the glass to the softening point and deftly pulling it like a piece of taffy, tubes as small as 0.003" O.D. could be fabricated. All glass probes had a gradual taper of about 5° from the tip to a uniform section of 0.020"-0.025" O.D.. Reproductions of contour projector images for two of the probes are shown in Figure 10. The length of the glass tubing of each probe was 1.10". The delicate task of squaring off the end of each tube on a jeweler's lathe was handled by R. Bartsch of the GALCIT machine shop.

Hot-Wire Instruments

The hot-wire probes were designed to have a minimum cross-sectional area normal to the flow direction. They consisted of a small cone-cylinder-flare body, a thin streamlined strut, and two sewing needles to hold the wire. Three views of the probe are shown in Figure 11. The strut holding the needles was a "sandwich" of two 0.020" thick blades of hard brass shim stock joined with a thin layer of Stycast 2850GT cement. This bonding agent was chosen for its low thermal expansion coefficient (about $15 \times 10^{-6}/°C$) and high electrical resistivity (10^{13} ohm-cm at the tunnel operating temperature). The needles were soft-soldered to the brass blades, and a small bridge of Stycast 2850GT was placed half-way down the needles to increase their rigidity (see Figure 11).

The hot-wires were soft-soldered to the needles within 0.001" of the tips, and care was exercised to insure that the hot-wires were

normal to the flow direction. Pt-10% Rh Wollaston wire of 0.0001" diameter was used as the hot-wire material, and each wire was annealed and calibrated according to the procedures reported in Part I of this thesis. All wires were obtained from a single spool, and the mean resistivity coefficient was 1.657×10^{-3} °C^{-1} at 0°C.

A block diagram of the hot-wire circuit is shown in Sketch 7.

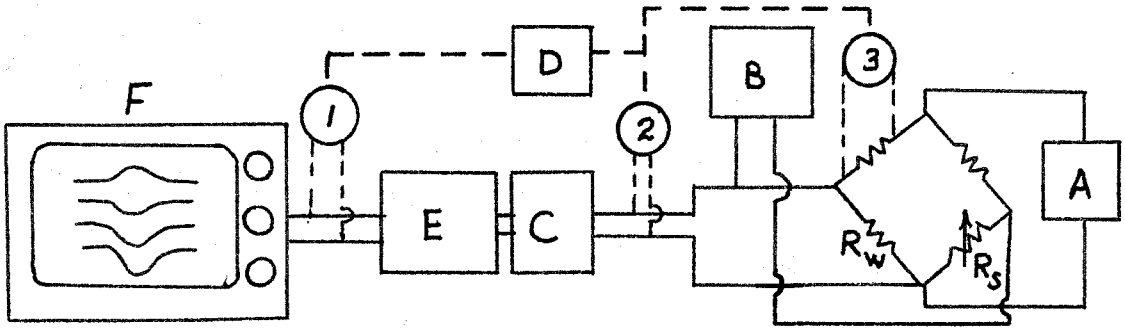

A. Oregon Electronics GP32-20 power supply with voltage divider and ballast resistors.

B. Leeds and Northrup 9834 Null Detector

C. Bucking voltage and calibration circuit

D. Kin-Tel 501B digital voltmeter

E. Sanborn 1500S amplifier

F. Moseley 2S X-Y recorder

Sketch 7. Block diagram of hot-wire circuit.

Absolute resistances R_w were measured to ± 0.01Ω using the bridge circuit and standard decade resistor R_s. The current through the hot-wire R_w was determined by measuring the voltage drop across a standard resistor in series with the hot-wire (input (3) to the digital voltmeter), and was accurate to ± 0.05%.

III.2 Wind Tunnel Models

All models were inserted into the tunnel through small lucite plugs mounted in a glass port. Pressure and thermocouple leads were brought out through the 0.250" dia. support shown in Sketch 8. The models consisted of circular cylinders and wedges which could

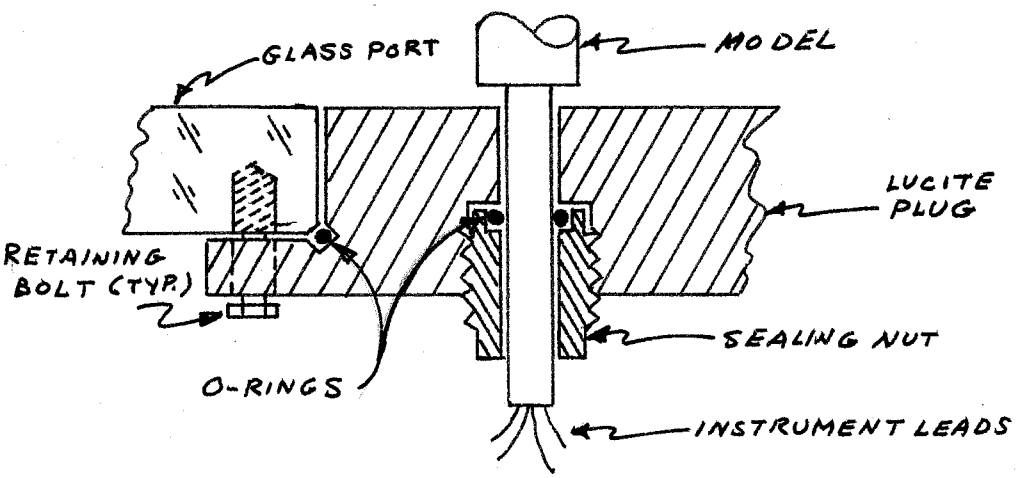

Sketch 8. Model support arrangement.

be rotated by turning the support strut.

Six circular cylinders were used in this investigation. Their characteristics are given in Table 1. The surface of each model was

Table 1. Circular Cylinder Models

Diameter	Details of Manufacture	Use
0.0838"	Three 0.009" dia. holes in line parallel to cylinder axis. 3" stainless steel center section	Surface and base pressure
0.1498"	Four 0.009" dia. holes. Brass	
0.300"	Five 0.009" dia. holes. Brass	
0.256"	Micarta with 0.007" nickel plating, I/C. Thermocouple	Surface Temperature
6 mm	6 mm O.D. x 4 mm I.D. pyrex, 0.010" x 1.00" Pt. strip	
0.238"	Ketos steel, 0.0005" bright nickel finish, with two 0.050" x 0.015" dia. goal posts 0.500" apart	Wake Survey

polished to 5 microinches mean roughness, and no pits or gouges were tolerated.

Table 2 gives the pertinent dimensions of the four wedges

Table 2. Wedge Models

Wedge Angle, $2\theta_B$	Base Height, 2H	Surface Pressure Taps
44° 49'	.1475"	No
44° 42'	.2810"	Yes
29° 12'	.1430"	No
30° 9'	.2989"	Yes

used in the base pressure experiments. The models were fabricated of Ketos steel, and the leading edges were less than 0.0005" thick. The trailing edges were of somewhat poorer quality, having a maximum radius of curvature of about 0.003". Two models had 0.015" dia. surface pressure taps on opposite sides of the wedge; these holes were connected to a small U-tube silicone manometer, and the angle of attack was set at 0° ± 1.5' by rotating the model until the two surface pressures were equal. The base pressure taps were 0.015" in diameter, and placed on the model centerline. For the smaller wedges, the angle of attack was set equal to zero by aligning the model with the centerline of the tunnel. The accuracy of this procedure was no better than ± 0.7°, but measurements at angles of attack up to 1.6° with the larger models showed less than 1% change in base pressure, and it was assumed that the error from this source was negligible.

III.3 Experimental Techniques

Base pressures were measured with the silicone U-tube micromanometer. Cylinder surface pressures were also obtained with the micromanometer, and the angle of rotation was determined by a mechanical counter having 5000 divisions for 360° rotation. The centerline for the cylinder base pressure and surface pressure studies was determined by symmetry; this procedure was highly satisfactory (see Section IV.2).

Hot-wire and pitot pressure surveys behind the 0.238" dia. cylinder were accomplished by mounting the probes on a traversing system capable of motion in the vertical and horizontal directions. Thus, "slices" could be taken at any streamwise station along the tunnel centerline. The vertical position of the probe was recorded by a mechanical counter. A leadscrew mechanically connected to the vertical actuator operated a Beckman Helipot as a voltage divider, producing an electrical signal proportional to vertical displacement. The wake centerline was determined by symmetry, and this procedure yielded a repeatability of about ± 0.001".

The axial position was determined with the aid of the two "goal-post" needles attached to the model. The tips of these needles, which extended 0.0501" ± 0.0002" above the model surface and were 0.5 inches apart, were rotated to the rear of the body and used as a "gunsight" to align the probe. By using a magnifier, the axial position could be consistently reset to ± 0.0015".

Figure 12 shows a sample of the raw data obtained with

the hot-wire probe. The x-axis of the plotter was connected to the helipot voltage divider and the y-axis input was the hot-wire signal. Each trace was taken at constant current. At the beginning of each trace, the wire resistance* was measured with the bridge circuit and the current determined by measuring the voltage drop across a standard resistor in series with the hot-wire. The bucking voltage circuit (see Sketch 7) was then adjusted to give a zero signal into the Moseley plotter, and this zero level was indicated by a horizontal mark. Therefore, as the wire traversed the wake, only the voltage difference

$$\Delta V = i\Delta R$$

was recorded. Standard impedance matching techniques reduced the systematic error in the determination of R_w to a negligible value. The bucking voltage circuit contained mercury cells and standard resistors for calibrating the hot-wire axis of the plotter, and the analog voltage for vertical position was calibrated by reading the mechanical counter at several positions of the vertical traverse system. Since the 0.0001" dia. hot-wire has a response time of 10^{-5}-10^{-6} sec., traces could be taken rapidly and continuously.

For the pitot pressure traces, the transducer output was fed into the Sanborn amplifier, and then to the Moseley plotter.

* A line resistance of less than 0.5 Ω was subtracted from all bridge readings. This line resistance was known to ± 0.002 Ω.

Calibration and data-taking procedures were similar to those employed with the hot-wire, except that the trace was not continuous. Because of the appreciable (1-50 sec.) time response of the probes, the record consisted of a series of discrete points across the wake. However, enough points were taken so that the interpolation between points introduced an error of less than 0.2% in the measured pressure. The Kin-Tel digital voltmeter was used to monitor the time response of the probes; each pressure was within 0.1% of its equilibrium value. The results of these surveys are shown in Figures 14, 15, and 16.

III.4 Experimental Corrections

Certain unavoidable systematic errors are present in the raw data obtained with hot-wires and pitot pressure probes. The most serious is the end loss error of the hot-wire, and the computation procedure for determining an appropriate correction for this effect is given in Appendices A and B of Part I of this thesis. Other systematic errors are smaller in magnitude, but are nonetheless important in interpreting the measurements.

Flow Interference Effects.

At the beginning of this investigation, serious attention was given to the effects of probe interference on the base flow field. The most sensitive measure of these interference effects was found to be the base pressure. For a circular cylinder at $M_\infty = 6$, the shear layer external Mach number M_e is about 3, so that a 1% change in base pressure corresponds to a 1.7% change in M_e.

Measurements were made of the base pressure as a function of probe position in the near wake, and these are shown in Figure 13. It may be seen that the hot-wire probe affected the base pressure by a maximum of 2% at $y/D = -0.4$, but the influence was less than 1% outside the region $-0.7 \leq y/D \leq -0.2$. ($y/D < 0$ means the probe was inserted completely across the wake.) For this reason, only hot-wire data for $y > 0$ were used in computation. The pitot probe presented little disturbance to the flow field, as shown by Figure 13. The pressure data were therefore read from the pitot trace for values of $y < 0$, since the probe was aligned with the flow in this region. No correction was applied to the magnitude of either the hot-wire or pressure data for these interference effects.

However, a more subtle influence of the probe interference did require correction. It was found that the pitot pressure probes consistently measured a smaller wake thickness than the hot-wire. This effect was caused by a "spreading" of the base flow region because of the presence of the hot-wire probe. The effect was not large, averaging 0.0035" on the radius. Because of the large gradients in the shear layer, it was necessary to correct for this shift by multiplying the y-coordinate of the pitot trace by a constant so that the lip shock positions measured with the pitot and hot-wire probes coincided. The numerical factor was unity for $x/D \leq 0.6$ and $x/D \geq 3.5$, and reached a maximum of 1.053 at $x/D = 1.50$. The numerical factor at a given x/D was repeatable within ±0.8% (i.e. ±0.0019") from pressure to pressure and from pitot probe to

pitot probe (Figures 14, 15 and 16 are shown without correction).

After correcting for this displacement, the pitot pressure and hot-wire data gave a consistent and complementary description of the flow field. Figure 17 reports the measured pitot pressure, hot-wire heat loss, and zero current wire resistance measured at $x/D = 0.80$. Equivalent sets of data were obtained at several downstream stations and at 4 different Reynolds numbers with similar results.

Pitot Pressure Corrections

There are four primary sources of systematic errors which must be considered when using pitot probes in low density shear flows. These are: (a) probe angularity with respect to the flow direction; (b) probe size and geometry with respect to the dimensions of the region investigated; (c) low Reynolds number corrections to the measured impact pressure; and (d) thermal transpiration. Although systematic investigations of these effects have been carried out separately*, few studies have been conducted where more than one pitot probe parameter has been varied under the same experimental conditions.

As a part of this investigation, the effects of pitot probe size, geometry, and angularity with respect to the flow direction were evaluated in situ by traversing the near wake of the 0.238" diameter cylinder with a variety of probes. The data are shown in

* See, for example, Sherman (35), Plan (36), Enkenhus (37), Matthews (38), Clayden (39), Bailey and Boylan (40), Bailey (41), Howard (42), and Arney and Bailey (43).

Figures 14, 15, and 16, and an interpretation of these results is given in Appendix B.

III.5 Data Reduction Procedures

Figure 12 is an example of the raw data obtained with the hot-wire. Twenty-three stations were selected in the region $0 \leq y/D \leq 0.9$, and at each station six values of the hot-wire resistance $R_w(i)$ were computed. For the small heating currents used in this investigation, R_w was a linear function of the Joulian heating i^2R_w. By plotting R_w as a function of i^2R_w, the slope $[dR/d(i^2R)]_{i=0}$ and the zero current intercept $R_{i=0}$ could be found. In order to determine the variation of $R_{i=0}$ across the shear layer with high precision, all readings were reduced relative to an interior reference station (say $y/D = 0.500$). The absolute values of $R_{i=0}$ and $[dR/d(i^2R)]_{i=0}$ are believed to be accurate to be accurate to $\pm 0.02\Omega$ (i.e. $\pm 0.06\%$) and $\pm 4\%$, respectively.

IV. BASE PRESSURE MEASUREMENTS AT HYPERSONIC SPEEDS

Base pressure measurements have a long history, dating back to the early experiments of the Prandtl School in Germany. Originally, these investigations were concerned with surface pressures as a measure of transition (the "critical Reynolds number" problem) and for investigating the behavior of a boundary layer near separation. In the 1940's and early 1950's, attention was again focused on the base pressure problem because of the sizeable (20-30%) contribution of base drag to the performance of supersonic wings and projectiles. From about 1955 to 1960, the emphasis swung back to a consideration of the separated flow aspects of the problem, and since 1960, the major impetus has been the connection between base pressures and the wakes of reentry vehicles. The interested reader may consult the reviews given by Goldstein (44), Chapman (20), Crocco and Lees (17), Korst, Page and Childs (22), Kavanau (45), Love (46), Holder and Gadd (23), Nash (4), and Kaufman et al. (47) which give a reasonably complete list of references on base flow and separation phenomena.

In this Section, base pressure and surface pressure measurements on wedges and circular cylinders are presented, and are interpreted using the near wake model described in Section II.

IV.1. Cylinder Base Pressures

The base pressure of a two-dimensional circular cylinder

at a free-stream Mach number of 6 is shown in Figure 18. It may be seen that the aspect ratio* required to render the ratio (p_b/p_{t2}) independent of cylinder diameter is on the order of 20, although the errors are not large for $AR \cong 10$.

According to the Mach number independence principle, the ratio (p_b/p_{t2}) should be independent of M_∞ if $M_\infty >> 1$. In Figure 19, the present experiments are compared to the results of Tewfik and Geidt (29), Walter and Lange (30), and Gregorek and Kordan (31) which cover the range $2.5 \leq M_\infty \leq 11$. It is apparent that the flow field at the rear of the cylinder is not independent of Mach number below $M_\infty \cong 4$. (The scatter of the data for $M_\infty > 4$ about the present measurements is attributed, in part, to aspect ratio effects.) At the higher Mach numbers, the base pressure ratio (p_b/p_{t2}) and, by inference, the structure of the near wake are functions only of the Reynolds number $Re_{0,D}$ and the body surface conditions.

The simplified model of the near wake presented in Section II predicts that the base pressure ratio (p_b/p_{t2}) is also independent of the Reynolds number $Re_{0,D}$. Although this is not exactly true, as indicated by Figure 18, it is certainly a good first approximation inasmuch as the base pressure changes by 30% over a 20-fold range of Reynolds numbers. An increase in base pressure with Reynolds number was also found by

* The aspect ratio is defined as the ratio of spanwise uniform flow to cylinder diameter, not the ratio based on tunnel dimensions and cylinder diameter.

Kavanau (36), who studied a blunt axisymmetric cone-cylinder model with a flat base at Mach numbers between 2 and 4. The fact that the present variation of base pressure with Reynolds number is small seems somewhat surprising, in view of the low Reynolds numbers $Re_{0,D}$. Even for a value $Re_{0,D} = 10^4$, the shear layer thickness is a significant fraction of the body diameter and many of the assumptions of the base flow model become questionable.

To compare the measured base pressures with the quantitative results of Appendix A, it is necessary to estimate the initial momentum thickness θ_0 after separation. This estimate requires (a) a knowledge of the momentum thickness θ_B on the body ahead of the separation point, and (b) a knowledge of the change in θ across the separation region. An estimate of θ_B may be obtained by the method of local similarity (48). Using Equation 4, the shear layer parameter $\xi(\ell)$ may be written

$$\xi(\ell) = \left(\frac{K_2}{2\tilde{Re}I_2^2}\right)\left(\frac{\ell}{L}\right)\left[\left(\frac{\rho_B u_B/\mu_B}{\rho_e u_e/\mu_e}\right)\left(\frac{\rho_B \mu_B}{\rho_w \mu_w}\right)\right]_{x=L} \tag{8}$$

where

$$\tilde{Re} = \frac{\left(\int_0^L \rho_w \mu_w u_B \, dx\right)_{\text{along body surface}}}{(\rho_w \mu_w u_B L)_{\text{at separation}}} \tag{9}$$

L = curvilinear distance along the body surface from the forward stagnation point to separation

x = distance measured along body surface

$( )_w$ = quantity evaluated at the local surface temperature and pressure

ρ_B, u_B, μ_B = local quantities evaluated at the edge of the boundary layer along the body

and κ_2 is the ratio (θ_0/θ_B) defined on page 13. The quantity I_2 is the momentum thickness integral across the boundary layer in the incompressible plane, and is a function of the local wall temperature and pressure gradient.

Using the cylinder surface pressure distribution measured by McCarthy (27), the value of $\tilde{Re}$ for a cylinder goes monotonically from the classical value of 1/2 at the stagnation point to about 7 at 120°. Similarly, the pressure gradient parameter β, as defined in Reference 48, goes monotonically from unity at the stagnation point to nearly 13 at 120°.

For the insulated cylinder considered here, the body temperature is equal to 0.95 of the stagnation temperature (see Appendix C). From an extrapolation of the numerical results of Beckwith and Cohen (49), the value of I_2 corresponding to $\beta = 13$ is 0.11. This result is a factor of four less than the classical Blasius value ($\beta = 0$) of 0.4696. Since $\xi \sim (I_2)^{-2}$, this reduction in I_2 means a difference of a factor of 16 in ξ for an insulated body. If the body is highly cooled, then I_2 is a weak function of the pressure gradient parameter, as suggested by Lees (50), and remains close to the Blasius value.

Table 3 presents the values of M_e, $p_e \equiv p_b$, and shear layer turning angle θ_w calculated for the exponential, quadratic and Blasius (numerical) solutions as discussed in Sections II.1 and II.3. These results were obtained assuming $\kappa_2 = 1$ and isentropic inviscid flow from the 90° point on the body through the

Table 3. Theoretical Predictions for an Insulated Circular Cylinder

	β	Exponential	Quadratic	Numerical	Chapman (21)
Base Pressure (p_b/p_{t2})	13	.039	.043	.046	.035
	0	.053	.058	.063	.035
Shear Layer Angle θ_w (Deg.)	13	10.7	9.4	8.5	12.3
	0	6.3	5.1	3.7	12.3
Mach Number M_e	13	2.77	2.71	2.66	2.84
	0	2.56	2.51	2.45	2.84

recompression region.

The influence of surface pressure gradient is readily apparent in Table 3. A comparison between the tabulated values and the experimental data of Figures 18 and 19 indicates that the results obtained using local similarity ($\beta = 13$) are in considerably better agreement with experiment than the values calculated by ignoring the pressure gradient term. The results obtained using Chapman's similarity solution for $\xi \to \infty$ are in much better agreement with experiment than the more realistic calculations which take the initial shear layer thickness into account.

The failure of the present theory to predict the correct base pressure for a cylinder is presumably caused by three primary effects. The first is the lack of an accurate description of the initial momentum thickness θ_0 because of the uncertainty in applying local similarity concepts to flows where the pressure gradient parameter β changes rapidly, and also because of the uncertainty surrounding the value of κ_2. Second, for the low Reynolds numbers shown in Figures 18 and 19, the shear layer is no longer thin, and

the assumptions of a constant pressure mixing process and negligible base flow are violated. And third, the pressure rise p'/p_e depends on Reynolds number, as shown by Reeves* and Rom (51). A decrease of base pressure with decreasing Reynolds number was first predicted by Crocco and Lees (17), although their arguments were somewhat different than those presented here.

IV.2 Cylinder Surface Pressures Near Separation.

Figure 20 presents the measured surface pressure distribution on a circular cylinder as a function of the Reynolds number $Re_{0,D}$. The pressure ratio (p/p_{t2}) should be independent of Mach number for $M_\infty \gtrsim 4$.

The data were obtained with two cylinders whose diameters were 0.150" and 0.300" (see Table 1, page 37). As shown by the dashed curve in Figure 18, the larger model was subject to small aspect ratio effects which tended to obscure the effects of Reynolds number on the surface pressures near separation. The pressure data for the 0.300" diameter cylinder were therefore multiplied by a constant so that the corrected base pressure was equal to the value shown by the solid line in Figure 18. The fact that the corrected surface pressures in the region of attached flow are independent of Reynolds number attests to the validity of this procedure.

The most striking feature of Figure 20 is the diminishing extent and finally the disappearance of the region of constant

* B. L. Reeves, private communication.

surface pressure with decreasing Reynolds number. The assumption of a constant pressure mixing region implies that the surface pressure aft of the separation region is a constant and equal to the value at the outer edge of the shear layer. Clearly, this assumption is invalid at the lowest Reynolds numbers shown in Figure 20. From the trends indicated in this figure, a large region of constant pressure would be anticipated for $Re_{0,D} \gtrsim 10^5$.

The second important result is that the separation point* moves aft with decreasing Reynolds number. The pressure rise Δp required to separate the boundary layer increases with decreasing Reynolds number, allowing the boundary layer to penetrate more and more deeply into the base region. At the lowest Reynolds numbers shown in Figure 18, the base flow must be complicated in the extreme!

The third and final item of importance in Figure 20 is the small pressure rise at the rear of the cylinder. This region of increased pressure extends about $\pm 15°$ on either side of the axis, suggesting a stagnation of the reverse flow in the base region. If the pressure plateau evidenced in the data for $Re_{0,D} = 7.89 \times 10^3$ is taken to be the true static pressure, and the pressure rise at the rear stagnation point is identified with the dynamic head of the reverse flow, then the Mach number of the reverse flow along the

* Both theoretical and experimental results indicate that the separation point is located very close to the surface pressure minimum. In this context, separation is defined as the point where the zero streamline leaves the body surface.

axis is 0.3.

IV.3 Wedge Base Pressures

In the preceding Section, the base pressure of a circular cylinder was found to vary by 30% over a factor of 20 in Reynolds number. As shown in Figures 21 and 22, the base pressure of a wedge is a strong function of Reynolds number.

The measured base pressures are normalized with respect to the stagnation pressure behind the leading edge shock wave, and the Reynolds number $Re_{2,L}$ is based on the velocity, density, and viscosity of the inviscid flow along the wedge surface. The characteristic length L was chosen to be the distance from the apex of the wedge to the separation point. A small (less than 10%) correction was made to the values of p_{t2} and $Re_{2,L}$ to account for hypersonic viscous interaction effects (Reference 48).

In addition to the strong variation of base pressure with Reynolds number, there are three systematic effects which must be explained. First, the free-stream Mach number varied with tunnel pressure level, as shown in Figure 8. The present normalization is an attempt to remove the dependence of the base pressure correlation on free-stream Mach number. Solid points are included on each curve to indicate a constant value $M_\infty = 6.04$; three such points were available for each model. The "tailing off" of the data for each model with decreasing Reynolds number is attributed to the small change in free-stream Mach number with tunnel pressure.

Second, the Mach number M_e along the shear layer of the base flow region is estimated to be between 6 and 8. The resulting static temperatures are below the condensation limit, and a possibility existed that the apparent Reynolds number effects were in reality caused by condensation. Tests at three separate stagnation temperatures, as indicated in Figures 21 and 22, showed that condensation effects were undetectable.

Third, the measured wedge base pressures were well below the free-stream pressure in the wind tunnel. To investigate the possibility of errors caused by a finite aspect ratio, small fences were placed in the base region of the 0.30" base height, 22 1/2° wedge. These inserts were triangular in shape, and were attached perpendicularly to the base just outside the tunnel wall boundary layers. If any significant cross-flow was present from the tunnel wall into the base region, these fences should have materially affected the base pressure. As shown in Figure 22, the difference between the base pressures with and without fences was only 3%. More importantly, the qualitative features of the base pressure-Reynolds number relation were not changed by these inserts.

The strong dependence of wedge base pressure on Reynolds number may be easily explained. The shear layer Mach number M_e is between 6 and 8, so that the pressure p_e, and consequently the base pressure p_b, are sensitive functions of the angle between the shear layer and the axis. Now according to Appendix A, the incompressible and compressible mixing problems are related

through the Howarth transformation (y is in the compressible plane, and $\bar{y}$ is the transformed variable)

$$y = \int_0^{\bar{y}} \frac{\rho_e}{\rho} \, d\bar{y} \, . \tag{10}$$

In the hypersonic shear layer, $(\rho_e/\rho) >> 1$ and the lower portion of the shear layer penetrates far into the interior of the base region. Typical mass flow profiles are shown in Sketch 9 for $M_e = 0$, 3.05, and 8.00 for a quadratic profile and isenthalpic flow. It is apparent

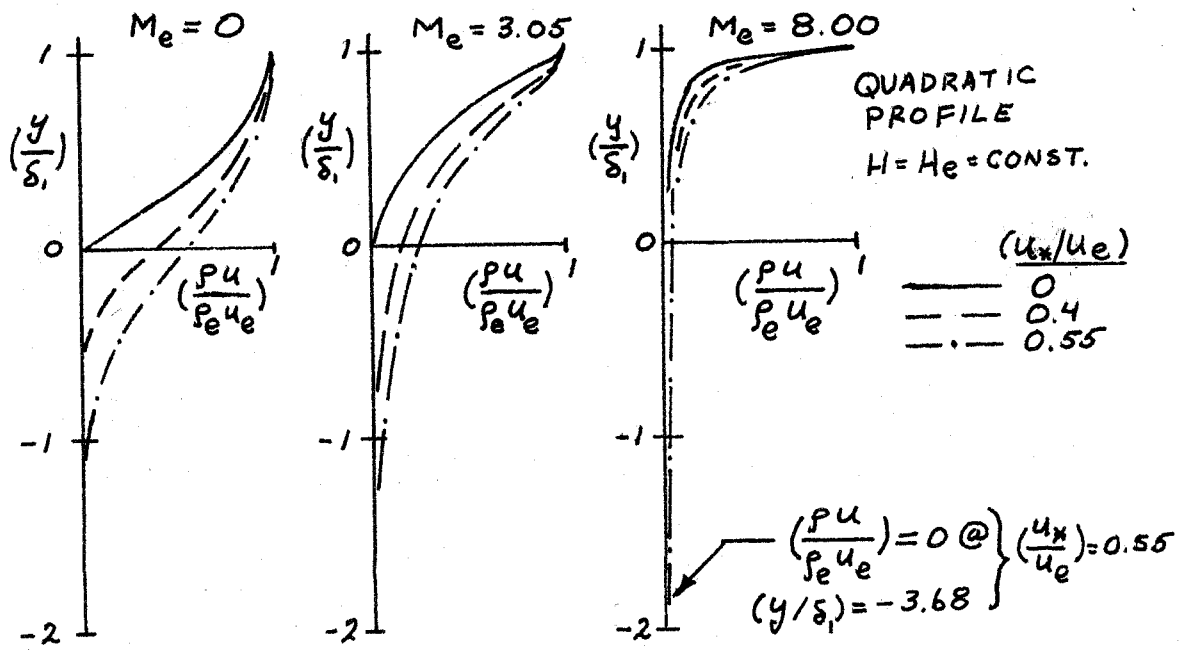

Sketch 9. Mass flow profiles in the shear layer.

that two hypersonic shear layers will interact strongly in the neck region, and the assumption that the shear layer thickness is small compared to the dimensions of the base flow region is violated. Since the shear layer thickness is proportional to $(Re_{2,L})^{-\frac{1}{2}}$, a

strong Reynolds number effect would be expected*. Preliminary hot-wire and pitot pressure surveys have confirmed that, in contrast to the cylinder shear layer profiles shown in Figure 17, there is a strong interaction between the two shear layers of a wedge.

Physically, the high Mach number layers may be pictured as "bouncing" off of each other as they approach the neck. This phenomenon gives rise to a displacement of the zero streamline away from the axis, and a decrease in the angle between the shear layer and the axis. This displacement increases with decreasing Reynolds number, and consequently the base pressure should increase with decreasing Reynolds number.

* The values of (p_b/p_{t2}) calculated using Chapman's model for $\theta_0 \to 0$ and isentropic recompression are 2.8×10^{-4} for a 15° wedge and 6.8×10^{-4} for a $22\frac{1}{2}°$ wedge.

V. DETAILED MEASUREMENTS IN THE NEAR WAKE OF A CYLINDER

This section presents the results of hot-wire heat loss and recovery temperature measurements in the near wake of a cylinder. The recovery temperature is used to describe the variation of shear layer thickness with Reynolds number at $x/D = 1.0$. A "map" of the near wake is obtained from hot-wire heat loss measurements; these results, which cover the first 5 diameters behind the cylinder, show the streamwise development of the shear layer, the extent of the compression process near the neck, and the evolution of the wake formed by the converging shear layers. Finally, a "goal post" technique for mapping streamlines is described.

V.1 Hot-Wire Profiles in the Near Wake Recovery Temperature Measurements

Figure 4 shows that the wake thickness δ_w obeys a laminar scaling law of the form

$$\frac{\delta_w}{D} \sim (Re_{\infty,D})^{-\frac{1}{2}} .$$

According to the theoretical model presented in Section II, the shear layer thickness should exhibit a similar dependence on Reynolds number.

To define the shear layer thickness, the hot-wire recovery temperature may be used. As shown in Part I of this thesis, the wire recovery temperature, or its equivalent wire resistance as $i \to 0$, is a measure of the local stagnation temperature of the flow.

Since the cylinder temperature is equal to 0.95 T_0, the viscous shear layer should consist of streamlines whose stagnation temperature is less than T_0*.

Figure 23 shows the results of 6 surveys across the near wake of a cylinder. The normalized resistance $R^* = (R-R_{LIP})/(R_{LIP}-R_{\text{¢}})$ at i = 0 has been used as a measure of the local stagnation temperature through the shear layer. R_{LIP} is the measured resistance at the inner edge of the lip shock emanating from the separation point. These data are uncorrected for end loss to the supports and represent measurements obtained from three individual hot-wires. The normalized resistance R* is essentially independent of both the end loss and the temperature-resistivity coefficient of the wire. This statement is proved by the coincidence of the solid and open inverted triangles. These points were obtained with two different wires operated at unit Reynolds numbers differing by a factor of two.

The data of Figure 23 indicate that the shear layer thickness increases with decreasing Reynolds number. A "maximum slope thickness" may be defined by the intersection of the tangent to the R* curve at its point of maximum slope with the values $R^* = 0$ and $R^* = 1$. For the five curves shown in the figure, the maximum slope thickness $\Delta(y/D)$ is proportional to $(Re_{\infty,D})^{-\frac{1}{2}}$

* A difficulty arises in this definition of the shear layer thickness. For Pr < 1, a laminar wake or shear layer may exhibit an overshoot in local stagnation temperature at its outer edge (see Section V, Part 1). For this reason, the maximum slope thickness is proposed as the correlating parameter.

within the scatter of the data, and this relation provides additional evidence supporting the scaling laws given in Section II.2.

It is apparent that the region of inviscid flow between the edge of the shear layer and the lip shock rapidly disappears as the Reynolds number decreases. For $Re_{\infty,D} = 0.765 \times 10^4$ ($Re_{0,D} = 1.04 \times 10^3$), a clear distinction can no longer be made between the shear layer and lip shock. At a value $Re_{\infty,D} = 6.18 \times 10^4$ ($Re_{0,D} = 8.01 \times 10^3$), the inviscid region is distinct.

The position of the lip shock is nearly independent of Reynolds number. Figure 23 indicates that the center* of the lip shock lies between $(y/D) = 0.44$ and $y/D = 0.48$ in the range $0.8 \times 10^4 \leq Re_{\infty,D} \leq 6 \times 10^4$. This corroborates the surface pressure measurements of Figure 20 which show the separation point to be a weak function of Reynolds number.

A minimum value of R* is associated with the zero velocity point in the shear layer profile. Consider the energy balance for a fine wire supported by two needles which are maintained at a temperature T_s, where T_s is less than the local stagnation temperature of the flow. As the wire current approaches zero, the remaining heat transfer mechanisms are (a) convection from the stream to the wire, (b) thermal conduction from the fluid to the wire, (c) radiation from the wire to the cold walls of the wind tunnel, and (d) solid body conduction from the wire to the supports.

* The weak lip "shock" is somewhat diffuse at these low Reynolds numbers. Its location was determined by the hot-wire heat loss profiles adjunct to these recovery temperature traces.

For these tests, radiation effects are unimportant so that a minimum in the wire resistance corresponds to a minimum in the convective heat transfer and a fortiori the point of zero velocity in the shear layer.

Figure 23 indicates that the zero velocity point at $x/D = 1.0$ is located at $y/D = 0.16$ and is independent of Reynolds number over the range investigated. This minimum is clearly evident in all traces except the one for $Re_{\infty,D} = 0.765 \times 10^4$. Furthermore, the temperature level below the zero velocity point rises rapidly to a constant value which is maintained near the axis. This behavior is evidence for a small core of low velocity reverse flow which eventually is brought to rest at the rear of the cylinder (see Section IV.2).

The interpretation of R* presented above is subject to some question since the hot-wire supports may disturb the reverse flow passing over the hot-wire. The magnitude of this disturbance is judged to be small because of the careful design of the hot-wire probe (see Figure 11). Furthermore, this interpretation leads to a clear picture of the reverse flow region which is consistent with the surface pressure measurements discussed in Section IV.2 and the heat loss measurements shown in Figure 24.

Heat Loss Measurements

The data presented thus far have provided an insight into the changes in the near wake associated with changes in Reynolds

number. Figure 24 presents a hot-wire "map" of the near wake of a cylinder at a Reynolds number $Re_{0,D} = 3.25 \times 10^3$. This low Reynolds number was chosen for two reasons: first, it was desired to map out the flow field under conditions where departures from the idealized model of Section II.2 would be readily apparent; and second, it was necessary to choose experimental conditions where the shear layer was thick enough to permit detailed investigation.

In Figure 24, profiles of the hot-wire heat loss $[dR/d(i^2R)]^{-1}$ are presented for the stations x/D = 0.44, 0.52, 0.60, 0.80, 1.00, 1.25, 1.50, 1.75, 2.00, 2.25, 2.50, 3.00, 3.50, 4.00, and 5.00. Each trace is plotted to the scale shown at the bottom of station x/D = 5. To aid in interpreting the data, the abscissa of each profile was placed so that the minimum value of $[dR/d(i^2R)]$ was located at the (x/D) station where the traverse was obtained. The minimum values are tabulated adjacent to the profile at (x/D) = 5. Recovery resistance profiles were also obtained at each station. These curves showed distinct off-axis minimums, similar to those shown in Figure 23, for x/D < 2. The locations of the minimums are shown as large circles in the (x/D)-(y/D) plane, and are connected by the line marked u = 0. This line is extended to that point on the trace of the body which marks the surface pressure minimum for this Reynolds number. As previously discussed, this point is the approximate location of separation.

In interpreting Figure 24, it is useful to consider the heat loss difference $\{[dR/d(i^2R)]^{-1} - [dR/d(i^2R)]^{-1}_{min}\}$ as being a measure of the local mass flow. This statement is not precisely true,

since the data are uncorrected for end losses and were obtained with several different wires. However, the mass-flow interpretation is qualitatively correct and provides a straightforward interpretation of the several features exhibited by the data.

As the boundary layer leaves the body surface to become the free shear layer, the velocity below the zero streamline is initially zero. The lower portion of the shear layer entrains mass from the base flow region, and the velocity u_* along the dividing streamline increases rapidly. Because of the curved bow shock wave, the inviscid flow outside the shear layer is highly rotational. The large inviscid gradients are evidenced by the slope of the heat loss profiles for $(y/D) > 0.5$*. The location of the lip shock is evidenced by a sharp "valley" in the heat loss data. The local minimum at the lip shock corresponds to the outer edge of this weak compression wave. Pitot pressure traces (see Figures 14-17) and Schlieren photographs have confirmed that this wave is not a sharp discontinuity but has a width of approximately 0.05 (y/D) (0.012"); additional hot-wire traces have indicated that this thickness decreases with increasing Reynolds number. The path of the lip shock is seen to be a straight line with a virtual origin at the outer edge of the boundary layer at the separation point; the lip shock meets and is

* The outer portions of the heat loss profiles at $(x/D) = 0.44$ and 0.52 were disturbed by the presence of a "goal post" wire (see Section V.2), and are shown as dotted lines. All other data were obtained without this disturbance.

swallowed up by the emerging wake shock at (x/D) = 3.00.

The lip shock and the shear layer are merged near separation. At (x/D) = 1.00, an inviscid region begins to appear between the two. For x/D > 1, the inviscid region is distinct and its extent is clearly evident in the heat loss data for (x/D) = 1.25.

A compression and turning of the flow is seen to begin at (x/D) = 1.50. The compression "hump" at the outer edge of the shear layer increases in magnitude and propagates outward as the neck region is approached. At (x/D) = 2.00, the two shear layers have merged. The compression process at the outer edge of the viscous region is essentially complete at (x/D) = 2.50. The compression region is initially diffuse (e.g. (x/D) = 2.00), but the steepness of the front increases in the streamwise direction. Beyond x/D = 3.00, the compression maintains the characteristic form of a wake shock.

A detailed examination of the profiles in the base flow region reveals several interesting features. From the requirement of mass conservation, the zero streamline and zero velocity line are required to form a wake "stagnation point" at the point of confluence of the two shear layers. From the trajectory of the u = 0 curve (which is not a streamline!), the wake stagnation point is found to be located between (x/D) = 1.75 and (x/D) = 2.00; it is tentatively placed at (x/D) = 1.90.

swallowed up by the emerging wake shock at (x/D) = 3.00.

The lip shock and the shear layer are merged near separation. At (x/D) = 1.00, an inviscid region begins to appear between the two. For x/D > 1, the inviscid region is distinct and its extent is clearly evident in the heat loss data for (x/D) = 1.25.

A compression and turning of the flow is seen to begin at (x/D) = 1.50. The compression "hump" at the outer edge of the shear layer increases in magnitude and propagates outward as the neck region is approached. At (x/D) = 2.00, the two shear layers have merged. The compression process at the outer edge of the viscous region is essentially complete at (x/D) = 2.50. The compression region is initially diffuse (e.g. (x/D) = 2.00), but the steepness of the front increases in the streamwise direction. Beyond x/D = 3.00, the compression maintains the characteristic form of a wake shock.

A detailed examination of the profiles in the base flow region reveals several interesting features. From the requirement of mass conservation, the zero streamline and zero velocity line are required to form a wake "stagnation point" at the point of confluence of the two shear layers. From the trajectory of the u = 0 curve (which is not a streamline!), the wake stagnation point is found to be located between (x/D) = 1.75 and (x/D) = 2.00; it is tentatively placed at (x/D) = 1.90.

T. Kubota* has examined the flow in the vicinity of this point using the full Navier-Stokes equations. He finds that both the zero streamline and zero velocity line must approach the axis vertically, and this fact has been utilized in drawing the u = 0 curve. A diagram of Kubota's result is shown in Sketch 10.

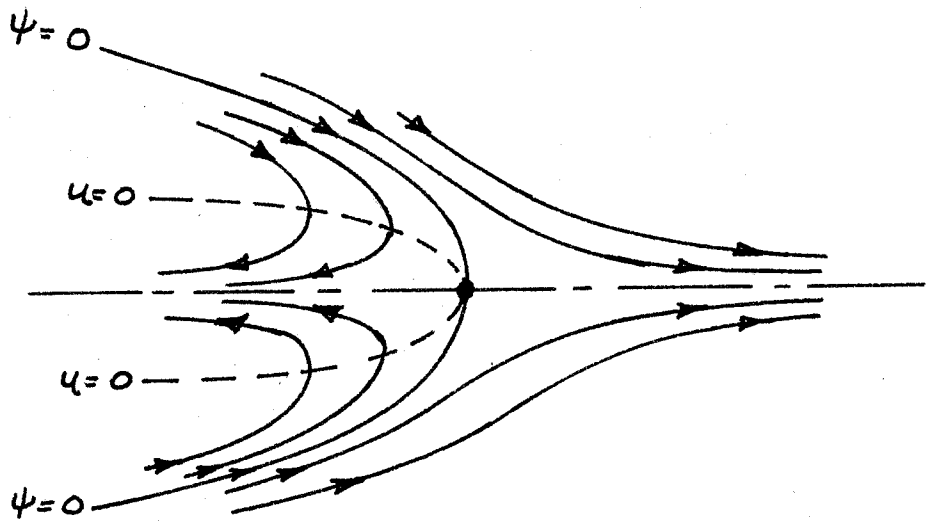

Sketch 10. The wake stagnation point (after T. Kubota).

The heat loss profiles exhibit a small increase below the zero velocity line. This behavior is attributed to the reverse flow in this region. The magnitude of this increase is very uncertain because end losses and thermal conduction comprise the bulk of the heat transfer below u = 0. As illustrated in Figures 14-17, the pitot pressure traces are completely incapable of picking up the reverse flow region. Traverses at higher Reynolds numbers,

* Private communication.

for which the end losses of the hot-wire were smaller, indicated that the reverse flow region is clearly marked by a small increase in the hot-wire heat loss. The location of the heat loss minimum coincides with the point of minimum wire temperature as expected.

According to the idealized model presented in Section II.2, the compression of the zero streamline at the neck is assumed to be isentropic, so that the pressure rises rapidly from p_e to p' across the neck. This model requires that the pressure rise is consummated in the immediate vicinity of the wake stagnation point. From the heat loss data of Figure 24, this assumption is seen to be incorrect. The minimum in the wake thickness occurs at approximately $(x/D) = 2.5$, while the wake stagnation point is located at $(x/D) = 1.9$. The action of significant viscous forces in the neck region is therefore indicated, at least for this low Reynolds number. Recent calculations by L. Lees* and B. Reeves have shown that the pressure rise at the neck requires several shear layer thicknesses to approach its downstream value, and the length of the recompression increases with increasing M_e.

To summarize the results obtained from the hot-wire heat loss measurements, as supported by recovery temperature and surface pressure studies, the following may be stated:

(1) At low Reynolds numbers, the penetration of the shear layer into the base flow region is extensive;

* Private communication.

(2) The neck compression region extends for several shear layer thicknesses upstream and downstream of the wake stagnation point;

(3) A distinct reverse flow exists in the interior of the base flow region;

(4) The inviscid region outside the shear layer becomes less distinct as the Reynolds number decreases. Below $Re_{0,D} \cong 10^3$, an inviscid flow between the shear layer and the lip shock can no longer be identified, and the base flow region contains large pressure gradients.

V.2 The "Goal Post" Technique for Mapping Streamlines

The 0.238" diameter cylinder used in the hot-wire heat loss investigation had two 0.009" diameter needles projecting 0.0501" from the surface and placed 0.500" apart along a common surface generator. The mounting arrangement, illustrated in Sketch 8, page 37, allowed the cylinder to be rotated about its axis and translated normal to the flow direction. For the heat loss and pitot pressure traverses, these two goal posts were rotated to the leeward side and translated to the tunnel wall.

A platinum wire 0.001" in diameter was soft-soldered between the two needles, forming a cross-bar between the two "goal posts." By rotating the cylinder, the wire could be placed at successive positions in the near wake flow field. Just as the parent cylinder leaves a characteristic wake in the uniform flow of the wind tunnel, the satellite wire leaves a wake in the parent

flow field. The wake of this goal post wire will follow a streamline of the parent flow; if the small wake does not spread rapidly, the trace of the streamline will be distinct.

Figure 25 shows the temperature wake of the goal post wire located outside the shear layer of the parent flow field. The three coordinates of this projection are (x/D), (y/D) and voltage of the hot-wire used to survey the hybrid flow field. The hot-wire was operated at a constant current of 1.000 ma, so the voltage was proportional to wire resistance which in turn was linearly related to the recovery temperature of the wire. The maximum "bucket" in the parent wake temperature profile is about 30°C, corresponding to a 3% change in the hot-wire resistance.

The wake of the goal post wire is very distinct in the first 3 diameters of the main base flow region. The small wake shocks produced by the goal post can be distinguished at (x/D) = 0.52. Even fine details such as the overshoot in total temperature at the outer edge of the goal post wake (since $Pr < 1$) may be recognized. The miniature wake eventually becomes absorbed by the main wake. This process begins, for this particular goal post position, at about (x/D) = 3; the small wake is barely discernible at (x/D) = 5.

Within certain limitations, this technique offers the possibility of mapping flow streamlines with great facility. The first requirement is that the drag of the goal post wire be small compared to the momentum defect of the near wake. For a cylinder or other blunt body, a large portion of the initial drag appears in

the inviscid flow, so that the momentum defect produced by the bow shock of the satellite body is added to the momentum defect of the main base flow region. In the present experiment, this produced a small but measurable translation of the main flow away from the side containing the disturbance. Second, the aspect ratio of the wire and the local Mach number of the flow approaching the goal post wire must be large. If these conditions are not satisfied, the gross perturbations produced by the supports will significantly change the profile of the main wake. Finally, the spreading of the wake must be small, so that a "single" streamline is identified. Otherwise, the existence of large gradients in the parent flow will make interpretation of the structure of the small wake very difficult (52).

REFERENCES

1. Roshko, A., "On the Development of Turbulent Wakes from Vortex Streets," NACA TN 2913 (1953).

2. Roshko, A., "On the Drag and Shedding Frequency of Two-Dimensional Bluff Bodies," NACA TN 3169 (1959).

3. Gorecki, J. P., "An Investigation of Temperature Fluctuations on Bluff Bodies," Ph.D. Thesis, Calif. Inst. Tech,, Pasadena (1960).

4. Nash, J. F., "A Review of Research on Two-Dimensional Base Flow," NPL Aero. Report 1006, A.R.C. 23,649, F.M. 3171 (March 1962).

5. Thomann, H., "Measurements of the Recovery Temperature in the Wake of a Cylinder and of a Wedge at Mach Numbers Between 0.5 and 3," FFA (Sweden) Report 84 (1959).

6. Gowen, F. E., and Perkins, E. W., "Drag of Circular Cylinders for a Wide Range of Reynolds Numbers and Mach Numbers," NACA TN 2960 (1953).

7. Margevy, R. H., and Bishop, R. L., "Wakes in Liquid-Liquid Systems," Phys. Fluids, 4, 800-805 (1961).

8. McMahon, Howard. Private communication to T. Kubota, September 19, 1960.

9. Charters, A. C., and Thomas, R. N., "The Aerodynamic Performance of Small Spheres from Subsonic to High Supersonic Velocities," J. Aero. Sci., 12, 468-476 (1945).

10. Charters, A. C., Private communication to L. Lees, 1956.

11. Hayes, W. D., and Probstein, R. F., "Hypersonic Flow Theory," Academic Press, New York, 1959.

12. Slattery, R. E., and Clay, W. G., "Experimental Measurement of Turbulent Transition, Motion, Statistics, and Gross Radial Growth Behind Hypervelocity Objects," Phys. Fluids 5, 849-855 (1962).

13. Demetriades, A., and Gold, H., "Transition to Turbulence in the Hypersonic Wake of Blunt-Bluff Bodies," ARS J. 32, 1420-1421. (1962).

14. Webb, W. H., Hromas, L., and Lees, L., "Hypersonic Wake Transition," AIAA Journal, 1, 719-721. (1963).

15. Lees, L., "Hypersonic Wakes and Trails," paper presented at the ARS. 17th Annual Meeting, November 1962, Los Angeles, Calif.

16. Chapman, Dean R., "Base Pressure at Supersonic Velocities," Ph.D. Thesis, California Institute of Technology, Pasadena (1948).

17. Crocco, L., and Lees, L., "A Mixing Theory for the Interaction Between Dissipative Flows and Nearly Isentropic Streams," J. Aero. Sci., 19, 649-676 (1952).

18. Glick, H. S., "Modified Crocco-Lees Mixing Theory for Supersonic Separated and Reattaching Flows," J. Aerospace Sci., 29, 1238-1249, 1259 (1962).

19. Chapman, Dean R., "Laminar Mixing of a Compressible Fluid," NACA Report 958 (1950).

20. Chapman, Dean R., "An Analysis of Base Pressure at Supersonic Velocities and Comparison with Experiment," NACA Report 1051 (1951).(Supersedes NACA TN 2137 (1950)).

21. Chapman, D. R., Kuehn, D. M., and Larson, H. K., "Investigation of Separated Flows in Supersonic and Subsonic Streams with Emphasis on the Effect of Transition," NACA Report 1356 (1958). (Supersedes NACA TM A55L14 (1956) and NACA TN 3869 (1957)).

22. Korst, H. H., Page, R. H., and Childs, M. E., "Compressible Two-Dimensional Jet Mixing at Constant Pressure," U. of Ill., M. E. Department Technical Note ME TN 392-1 (1954).

See also: Korst, H. H., "Comments on the Effect of Boundary Layer on Sonic Flow through an Abrupt Cross-Sectional Area Change," J. Aero. Sci., 21, 568-569 (1954).

23. Holder, D. W., and Gadd, G. E., "The Interaction between Shock Waves and Boundary Layers, and Its Relation to Base Pressure in Supersonic Flow," Proc. N.P.L. Int. Symp. on Boundary Layer Effects in Aerodynamics, Phil. Library, London (1957).

24. Meyer, R. E., "Note on a Hypersonic Tail-Shock Problem," RAND Memorandum RM-3148-PR, December 1962.

25. Denison, M. R., and Baum, E., "Compressible Free Shear Layer with Finite Initial Thickness," AIAA Journal 1, 342-349 (1963).

26. Dewey, C. F. Jr., GALCIT Hypersonic Research Project, Quarterly Status Report No. 22, January 1 to April 1, 1961.

27. McCarthy, J. F. Jr., "Hypersonic Wakes", GALCIT Hypersonic Research Project, Memorandum No. 67 (July 2, 1962). See also: McCarthy, J. F., Jr., and Kubota, T., "A Study of Wakes Behind a Circular Cylinder at M = 5.7," paper to be presented at the AIAA Summer Meeting, Los Angeles, June 17-20, 1963.

28. Kingsland, L. Jr., "Experimental Study of Helium and Argon Diffusion in the Wake of a Circular Cylinder at M = 5.8," GALCIT Hypersonic Research Project, Memorandum No. 60 (June 1, 1961).

29. Tewfik, O. K., and Geidt, W. H., "Heat Transfer, Recovery Factor, and Pressure Distributions Around a Cylinder Normal to a Supersonic Rarefied Air Stream: Part I - Experimental Data," U. of California (Berkeley) Technical Report HE-150-162 (January 30, 1959).

30. Walter, L. W., and Lange, A. H., "Surface Temperature and Pressure Distributions on a Circular Cylinder in Supersonic Cross-Flow," NAVORD Report 2854 (June 5, 1963).

31. Gregorek, G. M., and Kordan, K. D., "An Experimental Observation of the Mach- and Reynolds Number Independence of Cylinders in Hypersonic Flow," AIAA Journal, 1, 210-211 (1963).

32. Lees, L., and Hromas, L., "Turbulent Diffusion in the Wake of a Blunt-Nosed Body at Hypersonic Speeds," J. Aero/Space Sci., 29, 976-993 (1962).

33. Chapman, D. R., "A Theoretical Analysis of Heat Transfer in Regions of Separated Flow," NACA TN 3792 (October 1956).

34. Larson, H. K., "Heat Transfer in Separated Flows," J. Aero/Space Sci., 26, 731-738 (1959).

35. Sherman, F. S. "New Experiments on Impact-Pressure Interpretation in Supersonic and Subsonic Rarefied Air Streams," NACA TN 2995 (September 1953).

36. Plan, M., "Méthods D'Exploration Dynamique et Thermique et Étude de la Couche-Limite Laminare Compressible de la Plaque Plan," Publ. Sci. et Tech., Ministére de L'Air No. 331 (1957).

37. Enkenhus, K. R., "Pressure Probes at Very Low Density," UTIA Report No. 43 (January 1957).

38. Matthews, M. L., "An Experimental Investigation of Viscous Effects on Static and Impact Pressure Probes in Hypersonic Flow," GALCIT Memorandum No. 44 (June 2, 1958).

39. Clayden, W. A., "Preliminary Experiments on Pitot Pressure Interpretation of Small-Bore Square-Ended Probes in Low-Density Flow," Proc. 1st Int. Symp. on Rarefied Gas Dynamics, F. M. Devienne, Ed., pp. 32-37, Pergamon Press, N.Y. (1960).

40. Bailey, A. B., and Boylan, D. E., "Some Experiments on Impact-Pressure Probes in a Low-Density, Hypervelocity Flow," AEDC TN 61-161 (December 1961).

41. Bailey, A. B., "Further Experiments on Impact-Pressure Probes in a Low-Density, Hypervelocity Flow," AEDC TDR-62-208 (November 1962).

42. Howard, W. M., "The Effect of Temperature on Pressure Measured in a Hypersonic Wind Tunnel," J. Aero/Space Sci., 26, 764 (1959).

43. Arney, G. D., Jr., and Bailey, A. B., "An Investigation of the Equilibrium Pressure Along Unequally Heated Tubes," AEDC TDR-62-26 (Feb. 1962).

44. Goldstein, S., "Modern Developments in Fluid Dynamics," Vol. II, Oxford U. Press, London, 1938.

45. Kavanau, L. L., "Base Pressure Studies in Rarefied Supersonic Flows," J. Aero. Sci., 23, 193-207, 230 (1956).

46. Love, E. S., "Base Pressure at Supersonic Speeds on Two-Dimensional Airfoils and on Bodies of Revolution With and Without Fins having Turbulent Boundary Layers," NACA TN 3819 (1957).

47. Kaufmann, L. G. II, Hartofilis, S. A., Evans, W. J., Oman, R. A., Meckler, L. H., and Weiss, D., "A Review of Hypersonic Flow Separation and Control Characteristics," ASD TDR 62-168 (1962).

48. Dewey, C. F. Jr., "Use of Local Similarity Concepts in Hypersonic Viscous Interaction Problems," AIAA Journal, 1, 20-32 (1963).

49. Beckwith, I. E., and Cohen, N. B., "Application of Similar Solutions to Calculation of Laminar Heat Transfer on Bodies with Yaw and Large Pressure Gradient in High-Speed Flow," NASA TN D-625 (January 1961).

50. Lees, L., "Laminar Heat Transfer over Blunt-Nosed Bodies at Hypersonic Flight Speeds," Jet Propulsion, 26, 259-269 (1956).

51. Rom, J., "Theory for Supersonic, Two-Dimensional, Laminar, Base-Type Flows using the Crocco-Lees Mixing Concepts," J. Aero/Space Sci., 29, 963-965 (1962). See also Rom, J., and Victor, M., "Correlation of the Base-Pressure Behind a Two-Dimensional Backward-Facing Step in a Laminar Supersonic Flow," TAE (Israel) Report No. 23, December 1962.

52. Charwat, A. F., Dewey, C. F. Jr., Roos, J. N., and Hitz, J. A., "An Investigation of Separated Flows--Part II. Flow in the Cavity and Heat Transfer," J. Aerospace Sci., 28, 513-527 (1961).

53. Tani, I., "On Approximate Solution of the Laminar Boundary Layer Equations," J. Aero. Sci., 21, 487-504 (1954).

54. Carlson, W. O., "Heat Transfer in Laminar Separated and Wake Flow Regions," Proc. 1959 Heat Trans. and Fl. Mech. Inst., Stanford U. Press, Stanford, Calif., pp. 140-155.

55. Lees, L., and Reeves, B. L., "Some Remarks on Integral Moment Methods for Laminar Boundary Layers with Application to Separation and Reattachment," GALCIT Technical Report No. 1 (December 31, 1961).

56. Savage, S. B., "The Effect of Heat Transfer on Separation of Laminar Compressible Boundary Layers," GALCIT Technical Report No. 2 (June 1, 1962).

57. Kendall, J. M. Jr., "An Experimental Investigation of Leading Edge Shock Wave-Boundary Layer Interaction at Mach 5.8," J. Aero. Sci., 24, 47-56 (1957).

APPENDIX A

MOMENTUM INTEGRAL METHODS FOR THE LAMINAR FREE SHEAR LAYER

Momentum integral methods are very convenient for treating a wide variety of separated flow problems. Several examples have been reported in the literature (17,18,53,54,55) and further applications are being pursued (51,56). For the constant pressure mixing problem, the application is simple and direct, and leads to closed form solutions of the momentum equation. The results presented in this Appendix describe the development of a constant pressure laminar free mixing layer with a finite initial thickness.

Transformation to the Incompressible Problem

The continuity, momentum, and energy equations for a homogeneous laminar compressible shear layer are written (space and velocity variables in the compressible plane are barred)

$$\frac{\partial(\rho\bar{u})}{\partial\bar{s}} + \frac{\partial(\rho\bar{v})}{\partial\bar{y}} = 0 \tag{A.1}$$

$$\rho\bar{u}\,\frac{\partial\bar{u}}{\partial\bar{s}} + \rho\bar{v}\,\frac{\partial\bar{u}}{\partial\bar{y}} = \frac{2}{\partial\bar{y}}\left(\mu\,\frac{\partial\bar{u}}{\partial\bar{y}}\right) \tag{A.2}$$

$$\rho\bar{u}\,\frac{dH}{\partial\bar{s}} + \rho\bar{v}\,\frac{\partial H}{\partial\bar{y}} = \frac{\partial}{\partial\bar{y}}\left(\frac{\mu}{Pr}\,\frac{\partial H}{\partial\bar{y}}\right) - \frac{\partial}{\partial\bar{y}}\left[\mu\left(\frac{1}{Pr} - 1\right)\frac{\partial}{\partial\bar{y}}\left(\frac{\bar{u}^2}{2}\right)\right] \tag{A.3}$$

where the total enthalpy H is defined by

$$H = \int_0^T c_p\,dT + \frac{\bar{u}^2}{2} \tag{A.4}$$

and the usual boundary layer approximations have been made. The coordinate $\bar{s}$ is taken as the curvilinear distance along the path of the zero streamline, and $\bar{y}$ is measured normal to $\bar{s}$.

The Howarth transformation is used to reduce the problem to incompressible form (unbarred variables are in the transformed plane):

$$s = \bar{s} \quad , \quad y = \int_0^{\bar{y}} \frac{\rho}{\rho_e} d\bar{y} \quad . \tag{A.5}$$

Defining the stream function ψ in the usual manner, we have

$$\rho\bar{u} = \rho_e \frac{\partial\psi}{\partial\bar{y}} \qquad \rho\bar{v} = -\rho_e \frac{\partial\psi}{\partial\bar{s}} \tag{A.6}$$

$$u = \frac{\partial\psi}{\partial y} \qquad v = -\frac{\partial\psi}{\partial s} \tag{A.7}$$

which serves to define the transformed velocities u and v. By substituting A.6 into A.1, it may be seen that ψ automatically satisfies the continuity equation. The zero streamline $\psi = 0$ coincides with the origin of y.

To reduce the problem to its simplest elements, the approximations are made that the density-viscosity product $\rho\mu$ is constant and the Prandtl number Pr is unity. These simplifications are not essential, but reduce the mathematical labors required for solution. Using the definitions given by A.6 and A.7, the continuity, momentum, and energy equations in the transformed variables (s,y,u,v) are now identical to their incompressible form:

$$\frac{\partial u}{\partial s} + \frac{\partial v}{\partial y} = 0 \qquad (A.8)$$

$$u \frac{\partial u}{\partial s} + v \frac{\partial u}{\partial y} = \nu \frac{\partial^2 u}{\partial y^2} \qquad (A.9)$$

$$u \frac{\partial H}{\partial s} + v \frac{\partial H}{\partial y} = \nu \frac{\partial^2 H}{\partial y^2} \qquad (A.10)$$

where ν is the kinematic viscosity (μ_e/ρ_e). An examination of Equations A.9 and A.10 shows that the total enthalpy H is a linear function of u, and we may immediately write the solution

$$H = A + Bu \qquad (A.11)$$

A, B = constants

This solution is physically admissible only if the boundary conditions permit! The momentum equation A.9 and the continuity equation A.8 are now independent of the energy equation.

The Two-Layer Method

One method of solving A.8 and A.9 is to integrate the equations numerically, starting with an assumed velocity profile at $s = 0$. The calculation is continued until a similar profile corresponding to $s \to \infty$ is reached. This technique was used by Denison and Baum (25). The approximate solution adopted here is to represent the velocity profile by a simple analytic function containing several parameters which are allowed to vary with s. By multiplying the s-momentum equation by u^j ($j = 0, 1, 2, \ldots$) and integrating

across the shear layer (making use of the continuity equation), a set of coupled ordinary differential equations is obtained which describes the variation of the velocity profile parameters in the s-direction. Boundary conditions are also applied at the extremities of the shear layer. The total number of boundary conditions and moment equations must be equal to the number of parameters appearing in the velocity profile.

The shear layer is divided into two regions as shown in Sketch A.1. The velocity profile in each layer is assumed to be

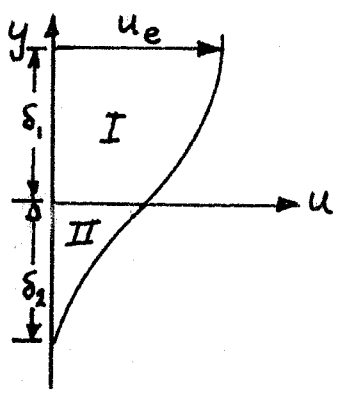

Region I: $y > 0$, $\eta = y/\delta_1$

Region II: $y < 0$, $\zeta = y/\delta_2$

$u(s) = u_*(s)$ along $\psi = y = 0$

Sketch A.1 Nomenclature for Two-Layer Method

of the form:

$$\text{Region I:}\quad \frac{u}{u_e} \equiv f = A_0 + e^{-\sigma\eta} \sum_{k=0}^{m} a_k \eta^k \tag{A.11}$$

$$\text{Region II:}\quad \frac{u}{u_e} \equiv g = B_0 + e^{\sigma\zeta} \sum_{k=0}^{n} b_k \zeta^k \tag{A.12}$$

and $\sigma = 0$ or 1 depending upon the type of representation which is desired. The number of terms (m,n) are chosen so that the

resulting profile will provide a "good approximation" for the physical problem being considered*. The profile parameters (A_0, a_k, B_0, b_k, δ_1, δ_2) are determined by the boundary conditions at the upper and lower extremities of the shear layer, the matching conditions at $y = 0$, and the moment equations. The possible boundary conditions are:

Outer Boundary

$\sigma = 0, \ \eta = 1$

$\sigma = 1, \ \eta \to \infty$

$$f = 1, \ f' = f'' = \ldots\ldots = 0 \qquad \text{(A.13)}$$

Inner Boundary

$\sigma = 0, \ \zeta = -1$

$\sigma = 1, \ \zeta \to -\infty$

$$g = 0, \ g' = g'' = \ldots\ldots = 0 \qquad \text{(A.14)}$$

By demanding continuity of the velocity and its derivatives at $y = 0$, one obtains the following:

* One difficulty with the momentum integral method is that the number of terms taken to represent the velocity profile is arbitrary. In this case, there are two criteria which aid in this choice: (a) the assumed profile must correspond closely to the specified initial profile as $s \to 0$; and (b) the final similar profile for $s \to \infty$ must agree well with the exact solution obtained by Chapman (19). Because of its simplicity, the free shear layer problem represents an excellent test case for the moment method, since various combinations of profile parameters, boundary conditions and moment equations may be used without undue algebraic complication. Such an exhaustive examination, however, is extraneous to this investigation.

Matching Conditions

$$\left(\frac{d^r f}{d\eta^r}\right)_0 = \left(\frac{\delta_1}{\delta_2}\right)^r \left(\frac{d^r g}{d\zeta^r}\right)_0 , \quad r = 0,1,2.. \tag{A.15}$$

The moment equations are defined by

$$M_j(+) = \int_0^{\text{Upper Limit}} u^j \left[u \frac{\partial u}{\partial s} + v \frac{\partial u}{\partial y} - \nu \frac{\partial^2 u}{\partial y^2}\right] dy = 0 \tag{A.16}$$

$$M_j(-) = \int_{\text{Lower Limit}}^0 u^j \left[u \frac{\partial u}{\partial s} + v \frac{\partial u}{\partial y} - \nu \frac{\partial^2 u}{\partial y^2}\right] dy = 0 . \tag{A.17}$$

The upper and lower limits of integration are $\pm \infty$ for $\sigma = 1$ (exponential profiles), and $(+\delta_1, -\delta_2)$ for $\sigma = 0$ (polymonial profiles).

Definition of the Integral Thicknesses

The integral thicknesses in the incompressible plane are defined separately for each region of the shear layer. For the exponential profiles ($\sigma = 1$), they are:

Displacement Thickness

$$\delta_1^* = \int_0^\infty \left(1 - \frac{u}{u_e}\right) dy = \delta_1 \int_0^\infty (1-f)\, d\eta \tag{A.18}$$

$$\delta_2^* = \int_{-\infty}^0 \left(1 - \frac{u}{u_e}\right) dy = \delta_2 \int_{-\infty}^0 (1-g)\, d\zeta \tag{A.19}$$

Momentum Thickness

$$\theta_1 = \int_0^\infty \frac{u}{u_e}\left(1 - \frac{u}{u_e}\right) dy = \delta_1 \int_0^\infty f(1-f)\, d\eta \tag{A.20}$$

$$\theta_2 = \int_{-\infty}^0 \frac{u}{u_e}\left(1 - \frac{u}{u_e}\right) dy = \delta_2 \int_{-\infty}^0 g(1-g)\, d\zeta . \tag{A.21}$$

The polynomial profiles are similarly defined, with the upper and lower limits of integration being replaced by δ_1 and $-\delta_2$ respectively. Higher order integral thicknesses may be defined as required; the number of integral thicknesses used increases with the order of the moment equations (the value of $j = 0,1,\ldots$).

Solution for a Quadratic Profile

A very simple example of this method is a quadratic profile. Let $\sigma = 0$, $m = n = 2$, so that the eight unknowns are* (a_0, $a_1, a_2, b_0, b_1, b_2, \delta_1, \delta_2$). Invoking the boundary conditions

$$\begin{aligned} &\eta = 1: \quad f = 1, \; f' = 0 \\ &\zeta = -1: \quad g = 0, \; g' = 0 \end{aligned} \tag{A.22}$$

and the matching conditions $r = (0,1)$,

$$f(0) = g(0); \; \left(\frac{\partial f}{\partial \eta}\right)_0 = \frac{\delta_1}{\delta_2}\left(\frac{\partial g}{\partial \zeta}\right)_0 \tag{A.23}$$

leaves two constants to be determined. Using the moment equations $M_0(+)$ and $M_0(-)$, we find the equations

$$\frac{d}{ds}\left[\delta_1 \int_0^1 f(1-f)d\eta\right] = \frac{\nu}{\delta_1 u_e}\left(\frac{\partial f}{\partial \eta}\right)_{\eta=0} \tag{A.24}$$

$$\frac{d}{ds}\left[\delta_2 \int_{-1}^0 g^2 \, d\zeta\right] = \frac{\nu}{\delta_2 u_e}\left(\frac{\partial g}{\partial \zeta}\right)_{\zeta=0} \tag{A.25}$$

Define the initial thickness δ_0 and the quantities λ and δ by

* The constant terms a_0 and b_0 are redefined to include A_0 and B_0.

$$\lambda \equiv 1 - f(0) = 1 - g(0); \quad \lambda(s = 0) = 1$$

$$\delta \equiv \delta_1 + \delta_2 \; ; \; \delta(s = 0) = \delta_1(s = 0) \equiv \delta_0 \; . \tag{A.26}$$

Then the quadratic profile satisfying (A.22) and (A.23) is

$$f = 1 - \lambda (1 - \eta)^2$$

$$g = (1 - \lambda) (1 + \zeta)^2 \tag{A.27}$$

and the corresponding moment equations are

$$\frac{d}{ds} \left[\delta \lambda^2 \left(\frac{1}{3} - \frac{1}{5} \lambda\right)\right] = \frac{2\nu}{u_e \delta} \tag{A.28}$$

$$\frac{d}{ds} \left[\delta (1 - \lambda)^3\right] = \frac{10\nu}{u_e \delta} \; . \tag{A.29}$$

Equations A.28 and A.29 possess the solution

$$\left(\frac{s}{\delta_0}\right)^2 \frac{1}{Re_{e,s}} = \frac{1}{5} \frac{(1 - \lambda)^3}{(3 - 9\lambda + 4\lambda^2)^2} - \frac{1}{55} \frac{(\lambda+3)(1-\lambda)}{(3 - 9\lambda + 4\lambda^2)}$$

$$+ \frac{4}{55\sqrt{33}} \left[\log \left| \frac{8\lambda - 9 + \sqrt{33}}{8\lambda - 9 - \sqrt{33}} \right| + \log \left(\frac{\sqrt{33} + 1}{\sqrt{33} - 1}\right)\right] \tag{A.30}$$

which has the asymptotic form

$$\lim_{s \to \infty} \lambda = 0.406 \text{ or } \lim_{s \to \infty} u_* = 0.594 \, u_e \; . \tag{A.31}$$

This result, $(u_*/u_e) = 0.594$, is extremely close to the exact value of 0.587 found by Chapman (19). The initial profile must be a quadratic with $\lambda = 1$, since

$$\lambda = \frac{\delta_1}{\delta_1 + \delta_2}$$

and δ_2 is zero at $s = 0$. A more powerful solution would be one in which two or more free parameters are available to specify the initial profile; the important effect of the initial profile on the rate of growth of u_* would then be immediately apparent.

Solution for an Exponential Profile

The exponential profiles ($\sigma = 1$) provide a particularly simple system of matching relations. Because of the fact that all derivatives of u approach zero at $\pm \infty$, the constants (a_k, b_k) are determined only by the matching conditions at $y = 0$ and the moment equations $M_j(\pm)$. Also, the integral thicknesses appear in a simple form; for example, it is easy to show that*

$$\theta_1 \equiv \delta_1 I_1 = \delta_1 \left\{ - \sum_{k=0}^{m} a_k \Gamma(k+1) - \sum_{k=0}^{m} \sum_{j=0}^{m} a_k a_j \left(\frac{1}{2}\right)^{j+k+1} \times \right.$$

$$\left. \times \Gamma(j+k+1) \right\} \qquad (A.32)$$

and that part of θ_2 which appears in the $M_0(-)$ equation is

$$I_2 = \int_{-\infty}^{0} g^2 \, d\zeta = \sum_{k=0}^{n} \sum_{j=0}^{n} (-1)^{k+j} \left(\frac{1}{2}\right)^{k+j+1} \Gamma(k+j+1) b_k b_j \qquad (A.33)$$

Higher order thicknesses are also readily obtained.

The derivatives of u may be easily calculated; since $A_0 = 1$ and $B_0 = 0$, we have

* The Gamma function is $\Gamma(n) = (n-1)!$ for n = integer.

$$\underline{r = 0} \quad 1 + a_0 = b_0 = u_*$$

$$\underline{r = 1} \quad b_1 = - u_* + \left(\frac{\delta_2}{\delta_1}\right)(1-u_* + a_1)$$

$$\underline{r = 2} \quad b_2 = \left(\frac{\delta_2}{\delta_1}\right)^2 \left(- \frac{1}{2} + \frac{u_*}{2} - a_1 + a_2\right) + \frac{u_*}{2} - \left(\frac{\delta_2}{\delta_1}\right)(1 - u_* + a_1)$$

$$\underline{r = 3} \quad b_3 = \left(\frac{\delta_2}{\delta_1}\right)^3 \left(a_3 - a_2 + \frac{1}{2} a_1 - \frac{u_*}{6} + \frac{1}{6}\right) - \left(\frac{\delta_2}{\delta_1}\right)^2 \left(a_2 - a_1 + \frac{u_*}{2} - \frac{1}{2}\right) + \left(\frac{\delta_2}{\delta_1}\right)\left(\frac{1}{2} a_1 - \frac{1}{2} u_* + \frac{1}{2}\right) - \frac{1}{6} u_* \, .$$

The fact that these relations between δ_1, δ_2, a_k, and b_k appear at $y = 0$ allows the asymptotic value of u_* to be immediately obtained. Setting $m = 0$ in A.32,

$$I_1 = \lambda - \frac{\lambda^2}{2} \; ; \; I_2 = \frac{1}{2}(1 - \lambda)^2 \tag{A.33}$$

and from $M_0(+)$ and $M_0(-)$, using A.32 and A.33,

$$\frac{d}{ds}[\delta_1 I_1] = \frac{\nu}{u_e \delta_1} \left(\frac{\partial f}{\partial \eta}\right)_0 \tag{A.34}$$

$$\frac{d}{ds}[\delta_2 I_2] = \frac{\nu}{u_e \delta_2} \left(\frac{\partial g}{\partial \zeta}\right)_0 \tag{A.35}$$

or

$$I_1 = \frac{\delta_2}{\delta_1} I_2 + \frac{\delta_0}{\delta_1} I_1(0)$$
$$I_1(0) = I_1 \, (u_* = x = 0) = \frac{1}{2} \tag{A.36}$$

Setting the matching conditions r = (0,1), we immediately obtain $a_1 = b_1 = 0$ and

$$\frac{\delta_1+\delta_2}{\delta_0} = \frac{\delta}{\delta_0} = -\frac{1}{(1-3\lambda+\lambda^2)} \tag{A.37}$$

which shows that the asymptotic value of u_* is 0.618. This is in poorer agreement with Chapman's result of 0.587 than the value of u_* given by the quadratic solution.

After a little algebra, the simultaneous solution of Equations A.34 and A.35 is found to be

$$\left(\frac{s}{\delta_0}\right)^2 \frac{1}{Re_{e,s}} = \frac{3}{20} + \frac{(4\lambda-1)}{20X} + \frac{\lambda(1-\lambda)}{4X^2}$$

$$+ \frac{3}{10\sqrt{5}} \left[\log\left|\frac{2\lambda-3+\sqrt{5}}{2\lambda-3-\sqrt{5}}\right| + \log\left|\frac{1+\sqrt{5}}{1-\sqrt{5}}\right|\right] \tag{A.38}$$

$$X = 1 - 3\lambda + \lambda^2$$

and the similarity form for the shear layer thickness is

$$\lim_{s\to\infty} \frac{\delta}{x}\sqrt{Re_{e,s}} = 4.10 . \tag{A.39}$$

This solution also contains a single profile parameter λ, so that the initial profile is constrained to be ($\eta > 0$)

$$\lim_{s\to 0} \frac{u}{u_e} = 1 - e^{-\eta} . \tag{A.40}$$

Transformation to the Compressible Plane and Comparison with Numerical Solutions

The initial momentum thicknesses in the incompressible and physical coordinates are identical in form, viz.

$$\overline{\theta_0} = \int_0^\infty \frac{\rho\bar{u}}{\rho_e \bar{u}_e} \left(1 - \frac{\bar{u}}{u_e}\right) d\bar{y} = \int_0^\infty \frac{u}{u_e}\left(1 - \frac{u}{u_e}\right) dy = \theta_0 \quad . \qquad (A.41)$$

It is for this reason that the momentum thickness appears to be the "proper" length scale of the initial profile. By using A.27 in A.41, and setting $\lambda = 1$, the quadratic profile is found to give $\theta_0 = \frac{2}{15}\delta_0$. For the simple exponential profile, Eqs. (A.40) and (A.41) show that $\theta_0 = \frac{1}{2}\delta_0$. The unbarred form of θ_0 will be used in subsequent discussion.

For the solution of Denison and Baum (25), an equivalent value of θ_0 must be defined. In their nomenclature (all quantities in the physical plane)

$$s^* \equiv F_w^2 \int_0^s \rho_e u_e \mu_e ds$$

where $F_w \equiv \dfrac{f_w''}{\sqrt{2S_b}}$, f_w'' = constant of the initial profile and proportional to the initial shear at the axis.

and $S_b = \left(\int_0^{\text{separation}} \rho_e u_e \mu_e dx\right)$ along body surface.

We may define an equivalent displacement thickness

$$\theta_0 = \left(\int_0^\infty \frac{\rho u}{\rho_e u_e}\left(1 - \frac{u}{u_e}\right) dy\right)_{s=0}$$

$$= \frac{\sqrt{2S_b}}{\rho_e u_e} \left(\int_0^\infty \frac{u}{u_e}\left(1 - \frac{u}{u_e}\right) d\eta\right)_{s=0}$$

where

$$\eta = \frac{\rho_e u_e}{\sqrt{2\tilde{\xi}}} \int_0^y \frac{\rho}{\rho_e} dy$$

$$\tilde{\xi} = \int_0^s \rho_e u_e \mu_e ds \ .$$

Now for a Blasius initial profile,

$$\int_0^\infty \frac{u}{u_e} \left(1 - \frac{u}{u_e}\right) d\eta = f''_w$$

so that

$$s^* = \left[\left(\frac{s}{\theta_0}\right)^2 \frac{1}{Re_{e,s}}\right] f''_w \ \tilde{Re}$$

$$\tilde{Re} = \left(\frac{\int_0^s \rho_e u_e \mu_e ds}{\rho_e u_e \mu_e s}\right) \text{along shear layer}$$

$\equiv 1$ for uniform constant pressure mixing.

Taking $f''_w = 0.4696$ for the Blasius solution,

$$s^* = 0.04863 \left[\left(\frac{s}{\theta_0}\right)^2 \frac{1}{Re_{e,s}}\right] \ . \qquad \text{(A.41)}$$

The variation of the mixing velocity u_* with the "proper" distance variable,

$$\xi \equiv \left[\left(\frac{s}{\theta_0}\right)^2 \frac{1}{Re_{e,s}}\right] \ ,$$

is shown in Figure 5. The quadratic, exponential, and Blasius results are seen to be in qualitative agreement, although the magnitude of u_* differs at a given value of ξ. Since each of the solutions involves only one free profile parameter*, it may not be stated with certainty whether the difference between the numerical solution and

* In principle, a numerical solution could be obtained for any initial velocity profile.

the moment method results are produced by the differences in the initial profile or the differences in the method of calculation.

However, near $\xi = 0$, the situation is quite clear. Each initial profile is linear near $y = 0$, so that the initial shear $(\frac{\partial u}{\partial y})_{y, s=0}$ determines the early variation of $u_*(\xi)$. These shear rates are expressed in normalized terms as

$$\underline{\text{Blasius solution:}} \quad (\frac{\partial f}{\partial \tilde{y}})_{\tilde{y}, s=0} = 0.2205$$

$$\underline{\text{Quadratic solution:}} \quad (\frac{\partial f}{\partial \tilde{y}})_{\tilde{y}, s=0} = 0.2667 \qquad \text{(A.42)}$$

$$\underline{\text{Exponential solution:}} \quad (\frac{\partial f}{\partial \tilde{y}})_{\tilde{y}, s=0} = 0.5$$

where the definitions of f and $\tilde{y}$ are

$$f = \frac{u}{u_e}, \quad \tilde{y} = \frac{1}{\theta_0} \int_0^{\bar{y}} \frac{\rho}{\rho_e} d\bar{y} \qquad \text{(A.43)}$$

and $\bar{y}$ is the distance normal to the zero streamline in the physical plane.

From Equation (A.42), it is obvious that the initial growth of $u_*(\xi)$ will be more rapid if the initial profile is an exponential than if it is quadratic, and this supposition is borne out by Figure 5. The difference between the initial shear $(df/d\tilde{y})$ of a Blasius profile and a quadratic is small; hence the difference between the values of $u_*(\xi)$ for small ξ calculated by Denison and Baum (25) and the values found from the quadratic solution are attributed to the

approximate nature of the momentum integral method. Considering the simplicity of the momentum integral method, the agreement is very good.

Effects of Heat Transfer and Calculations of M_*

A determination of the Mach number $M_* = (u_*/\sqrt{\gamma R T_*})$ requires solution of the energy equation A.3. In transforming A.3 to A.10, it was assumed that $\rho\mu$ = const. and Pr = 1 so that

$$H = A + Bu \ . \tag{A.11}$$

For purposes of illustration, we will consider only the solution obtained for the quadratic profile. Then using $\eta = y/\delta_1 = \frac{\delta_2}{\delta_1}\zeta$ as the normal coordinate,

$$0 \leqslant \eta \leqslant 1 \qquad \frac{u}{u_e} = 1 - (1-u_*)\,(1 - \eta)^2 \tag{A.44}$$

$$-\frac{\delta_2}{\delta_1} \leqslant \eta < 0 \qquad \frac{u}{u_e} = u_* \left(1 + \frac{\delta_1}{\delta_2}\eta\right)^2 \tag{A.45}$$

Consider first the case where the temperature in the base flow region ($u \to 0$) is equal to the total temperature of the inviscid flow (this will be called the "insulated wall" case). Then $H = H_e$ through the shear layer and

$$\frac{T}{T_e} = 1 + \frac{\gamma-1}{2} M_e^2 \left[1 - \left(\frac{u}{u_e}\right)^2\right] \ . \tag{A.46}$$

The physical distance $\bar{y}$ may be written as a function of the transformed distance y:

$$\bar{y} = \int_0^y \left(\frac{T}{T_e}\right) dy \ . \tag{A.47}$$

By combining equations A.44 - A.47 and integrating, the following relations are obtained:

$$\underline{0 \leq \eta \leq 1} \qquad \frac{\bar{y}}{\bar{\delta}_1} = \left(\frac{\delta_1}{\bar{\delta}_1}\right)\left[\eta + \frac{\gamma-1}{2} M_e^2 \left\{\frac{2}{3}\lambda\left[1 - (1-\eta)^3\right]\right.\right.$$

$$\left.\left. - \frac{\lambda^2}{5}\left[1 - (1-\eta)^5\right]\right\}\right] \tag{A.48}$$

$$\underline{-\frac{\delta_2}{\delta_1} \leq \eta < 0} \qquad \frac{\bar{y}}{\bar{\delta}_1} = \left(\frac{\delta_1}{\bar{\delta}_1}\right)\left[\eta\left(1 + \frac{\gamma-1}{2} M_e^2\right) - \frac{1}{5}\left(\frac{1-\lambda}{\lambda}\right)\left(\frac{\gamma-1}{2}\right)M_e^2(1-\lambda)^2 \times\right.$$

$$\left.\times\left\{\left(1 + \frac{\lambda}{1-\lambda}\eta\right)^5 - 1\right\}\right] \tag{A.49}$$

$$\left(\frac{\bar{\delta}_1}{\delta_1}\right) = 1 + \frac{\gamma-1}{2} M_e^2 \left(\frac{2}{3}\lambda - \frac{1}{5}\lambda^2\right) \tag{A.50}$$

and $\lambda = (1 - u_*)$.

If the fluid in the base flow region is very cold, then M_* will be large. For purposes of illustration, consider the base temperature to be equal to the static temperature T_e of the external flow (this will be called the "cold wall" case). Then the equations corresponding to A.46, A.48 - A.50 are

$$\frac{T}{T_e} = 1 + \frac{\gamma-1}{2} M_e^2 \left[\left(\frac{u}{u_e}\right) - \left(\frac{u}{u_e}\right)^2\right] \tag{A.51}$$

$0 \leq \eta \leq 1$ $\quad \left(\frac{\bar{y}}{\bar{\delta}_1}\right) = \left(\frac{\bar{\delta}_1}{\bar{\delta}_1}\right)\left[\eta + \frac{\gamma-1}{2} M_e^2 \left\{\left[1-(1-\eta)^3\right] \frac{\lambda}{3}\right.\right.$

$$\left.\left. - \left[1-(1-\eta)^5\right] \frac{\lambda^2}{5} \right\}\right] \tag{A.52}$$

$-\frac{\delta_2}{\delta_1} \leq \eta < 0$ $\quad \left(\frac{\bar{y}}{\bar{\delta}_1}\right) = \left(\frac{\bar{\delta}_1}{\bar{\delta}_1}\right)\left[\eta-(1-\lambda)\left(\frac{1-\lambda}{\lambda}\right)\left(\frac{\gamma-1}{2}\right) M_e^2 \left\{\frac{1}{3}\left[1\right.\right.\right.$

$$\left.\left.\left. - (1 + \frac{\lambda}{1-\lambda}\eta)^3\right] - \frac{1}{5}(1-\lambda)\left[1 - \right.\right.\right.$$

$$\left.\left.\left.(1 + \frac{\lambda}{1-\lambda}\eta)^5\right]\right\}\right] \tag{A.53}$$

$$\left(\frac{\bar{\delta}_1}{\delta_1}\right) = 1 + \frac{\gamma-1}{2} M_e^2 \left(\frac{1}{3}\lambda - \frac{1}{5}\lambda^2\right) . \tag{A.54}$$

The Mach number $M_*(\xi)$ may be calculated from Eqs. A.30, A.46, and A.51. The results are shown in Figure 6 and discussed in Section II.3. Mass flow and velocity profiles obtained from Equations A.30, A.44 - A.46, and A.48 - A.54 are discussed in Section V.1.

APPENDIX B

THE USE OF PITOT PRESSURE PROBES IN THE NEAR WAKE OF A BLUNT BODY

The effect of pitot probe geometry, size, and angle with respect to the flow direction were investigated in situ by making a series of traverses across the near wake of the 0.238" diameter cylinder.

The effects of probe size and geometry are illustrated in Figure 14. The streamline direction at the outer edge of the shear layer is about 12.5° for (x/D) = 1.00. Therefore, all four probes were aligned within ±5° of the flow direction at the outer edge of the shear layer. The Mach number M_e is about 3.0, and the unit Reynolds number Re'_e based on undisturbed flow quantities is about 1.2×10^4 per in., giving a range of probe Reynolds numbers based on vertical height between 90 and 210. From the data summarized by Enkenhus (37), the viscous correction should be less than 1% at the outer edge of the shear layer. Similarly, the pitot probe angle correction (27) should be less than 1/2%, and the velocity gradient correction (following Plan (36)) should be identically equal to zero (since the pitot pressure goes through a local maximum and the width of the "uniform" flow is only slightly smaller than the largest probe). Since all the corrections* are less than 1%, the small deviation of ±0.7% between the four curves is a measure of the repeatability of the measurements.

The data shown were obtained with the probes inserted completely across the wake, and the centerline was defined as being

*Using the relations of Arney and Bailey (43), the thermal transpiration effect was less than 1% for all the measurements presented here.

half-way between the pressure "valleys" produced by the lip shocks from opposite sides of the cylinder. The similarity of the four curves indicates that the shear layer thickness defined by each probe was identical. The magnitude of the pressure at the "valley" of the lip shock varied by 5% between the smallest and largest tubes, but was identical for the 0.012×0.044" stainless steel probe and the 0.012" diameter glass probe. Similarly, in the region of forward flow ($y \geq 0.03$"), these two probes measured identical values of the pitot pressure. It may be inferred from these results that the effects of geometry on the measured pitot pressure in the free shear layer (for a given transverse probe height) are negligible.

In the region $y \geq 0.11$", the smallest measured pitot pressure is associated with the smallest probe, indicating a "displacement" in the direction of increasing velocity. This behavior is in qualitative agreement with the results obtained by Plan (36) in a flat-plate boundary layer, although the present displacement is considerably smaller than he obtained. The 0.0075" dia. glass probe gave the highest pressure in the forward flow region of the shear layer; this is attributed to viscous effects which override displacement effects in this region. The local probe Reynolds number at $y = 0.06$" is $Re_d \simeq 14\text{-}20$ for the smallest probe, and the Mach number is near unity. The magnitude of the observed pressure increase is about equal to the value found by Sherman (35) in subsonic-transonic flow.

Figures 15 and 16 illustrate the effect of probe angularity on the measured pitot pressure. The data for $x/D = 2.00$ are difficult to interpret because of the large changes in flow direction at this

station. The angle of the streamline at y = 0.055" is estimated to be 4-6°. This angle results in a larger measured pitot pressure for the probe which is aligned with the axis. In Figure 16, the wake flow between the two shock waves is nearly parallel to the axis. The maximum pressure is again measured by the probe aligned with the axis. In the plateau region outside the shear layer, the pressure measured by the 17.4° angle probe is 3.0% below that of the aligned probe, in agreement with the measurements made by McCarthy (27) in a uniform flow.

In comparing these results with the previous systematic investigations of Plan (36), Kendall (57), and others, several important results appear. First, in contrast to measurements made on a flat plate, there is no distinct advantage in using round pitot probes. All probes measured the same shear layer thickness and shock location, and the displacement and angle-of-attack errors were independent of geometry. Second, the viscous correction for rectangular and round probes is found to be equal (within the present experimental scatter) for probe Reynolds numbers between 20 and 150. And third, the present data and that of Claydon (39) and others indicate that displacement effects are small (less than 1.5%) if the ratio of the probe diameter to the shear layer thickness* is less than about 0.5. This means that a free shear layer or wake is much less sensitive to probe size than an attached boundary layer of equal thickness.

* An analysis of several sources of data shows that the appropriate thickness is defined by the intersection of a tangent to the maximum slope of the measured pitot pressure profile with the constant pressure lines marking the axis of symmetry and the outer edge of the shear layer.

APPENDIX C

SURFACE TEMPERATURE DISTRIBUTION ON AN INSULATED CYLINDER

During the course of this investigation, several cylindrical models were built to determine the changes in surface temperature distribution introduced by different model materials. The results of the measurements for two cylinders are compared with the data of Tewfik and Geidt (29) and Walter and Lange (30) in Figure 26. The dimensions of the cylinders are given in Table 1, page 36.

Surface temperatures were obtained by rotating the cylinder about its axis; the procedure was identical to that described on page 36 for the surface pressure studies. The temperature of the nickel-plated micarta model was obtained from an iron-constantan thermocouple imbedded in the nickel plating and polished flush with the surface. The thermocouple wires were 0.001" in diameter. For the glass model, a sputtered thin-film platinum resistance gauge was used for the temperature measurement; the gauge was 1" long, 0.040" wide, and about 5 microns thick. The resistance-temperature relation of the gauge was determined in the hot-wire calibration oven.

Figure 26 shows that the surface temperature of a cylinder becomes more uniform as the thermal conductivity of the model increases. The data appear to approach the recovery temperature ratio $(T/T_0) = 0.95$ with increasing thermal conductivity of the model. This value is the recovery temperature which has been measured for a hot-wire in high Reynolds number, high Mach number flows (see Part I of this thesis).

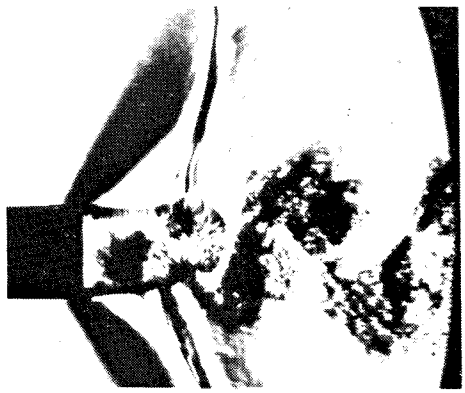

(a) M = 0.925

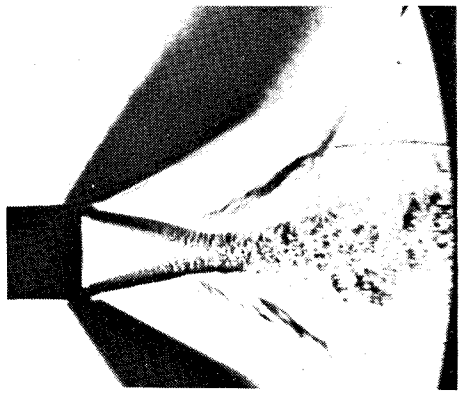

(b) M = 1.00

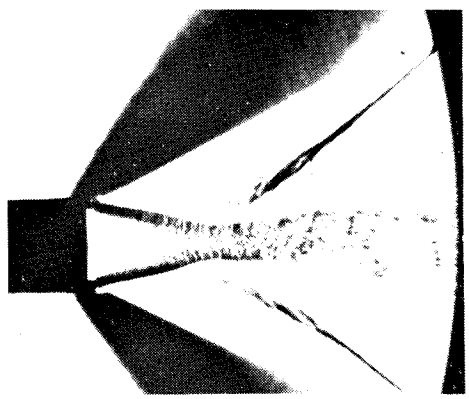

(c) M = 1.05

FIG. 1 BASE FLOW BEHIND A SLENDER TWO-DIMENSIONAL BODY AT TRANSONIC SPEEDS (after Nash).

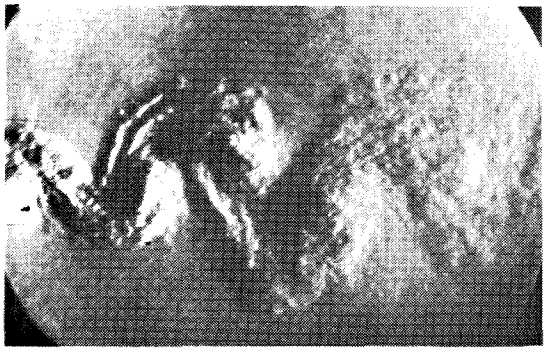

(a) M = 0.56

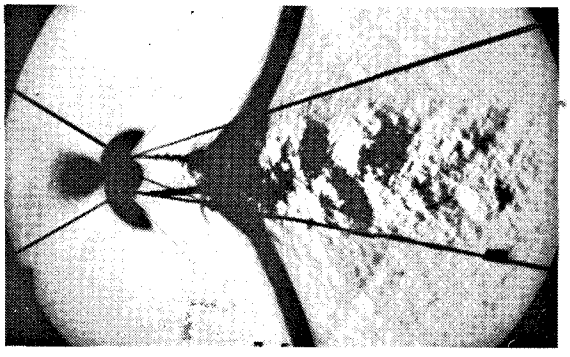

(b) M = 0.95

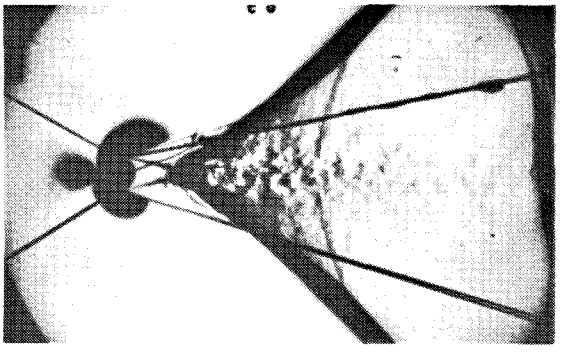

(c) M = 1.16

FIG. 2 BASE FLOW BEHIND A CYLINDER AT TRANSONIC SPEEDS (after Thomann).

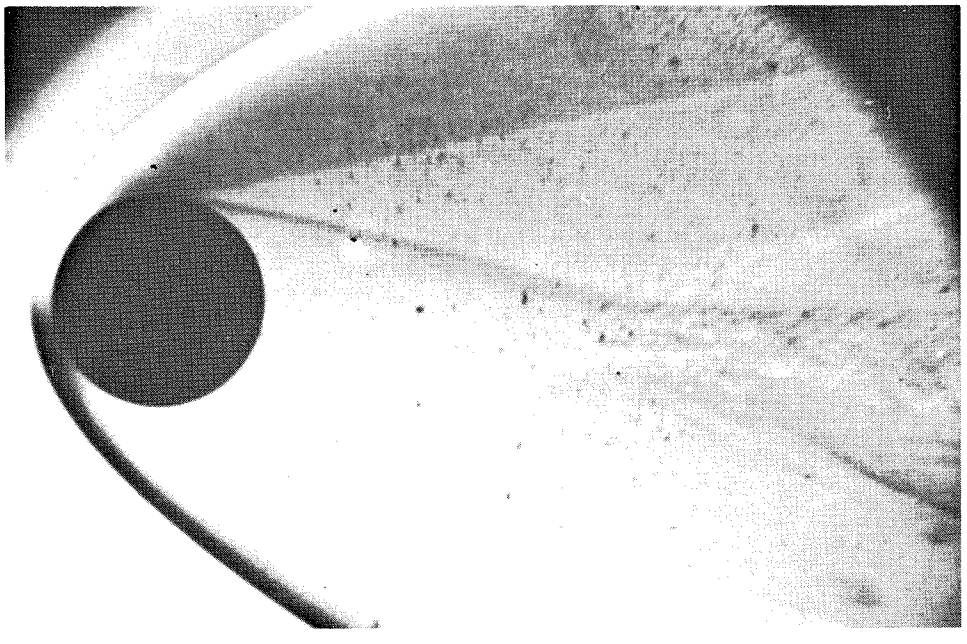

(a) Sphere, $M_\infty = 3.11$

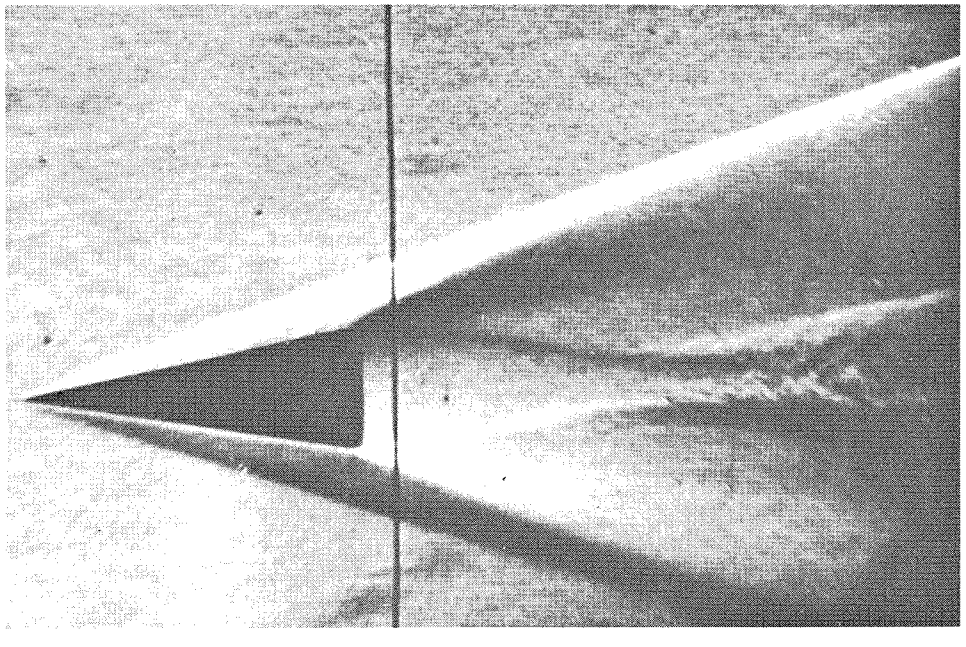

(b) 10° Half-angle cone, $M_\infty = 3.75$

FIG. 3 THE NEAR WAKE OF AXISYMMETRIC BODIES AT SUPERSONIC SPEEDS (After Charters(10))

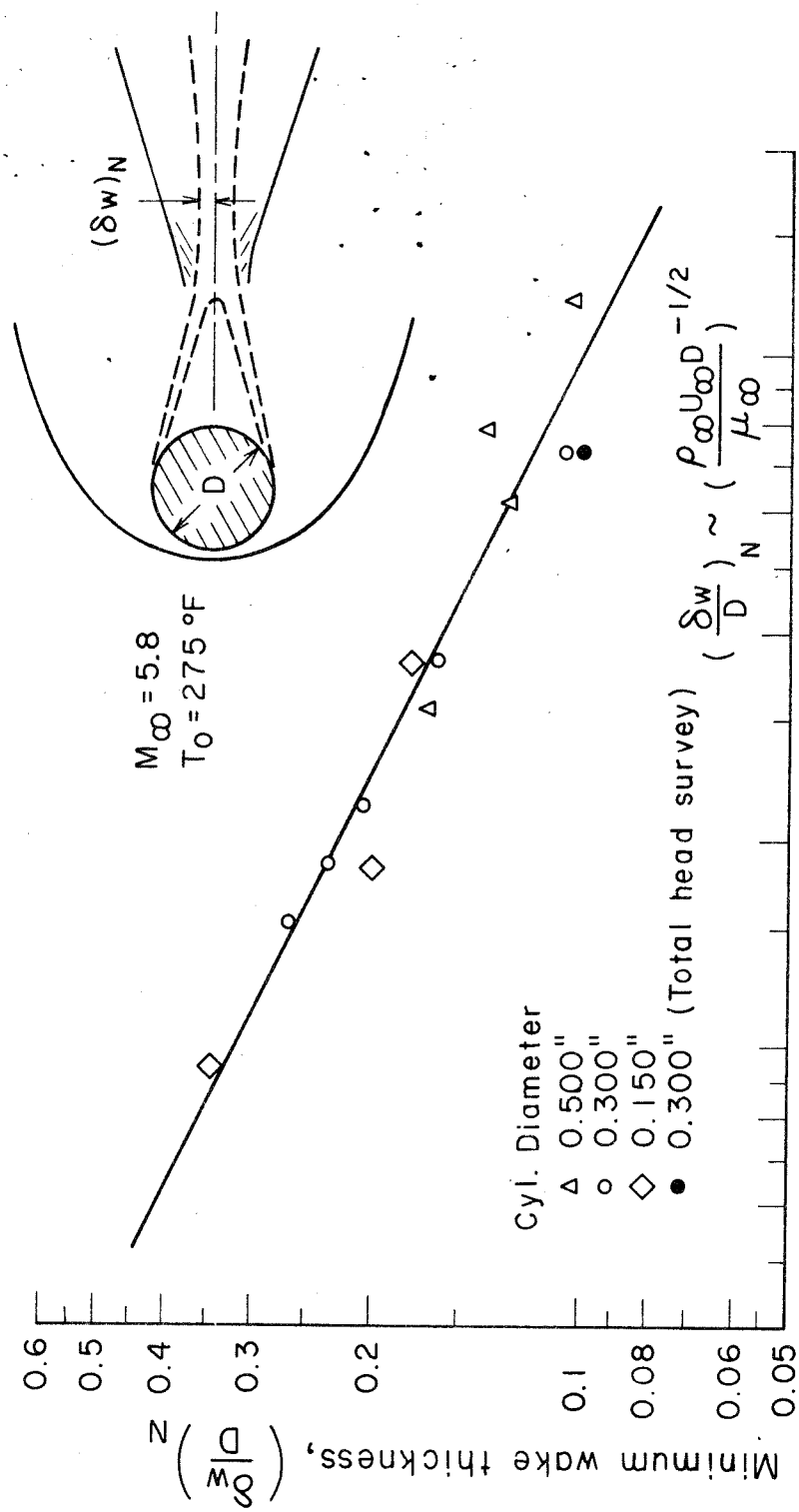

FIG. 4 INITIAL WAKE THICKNESS FROM SCHLIEREN OBSERVATION

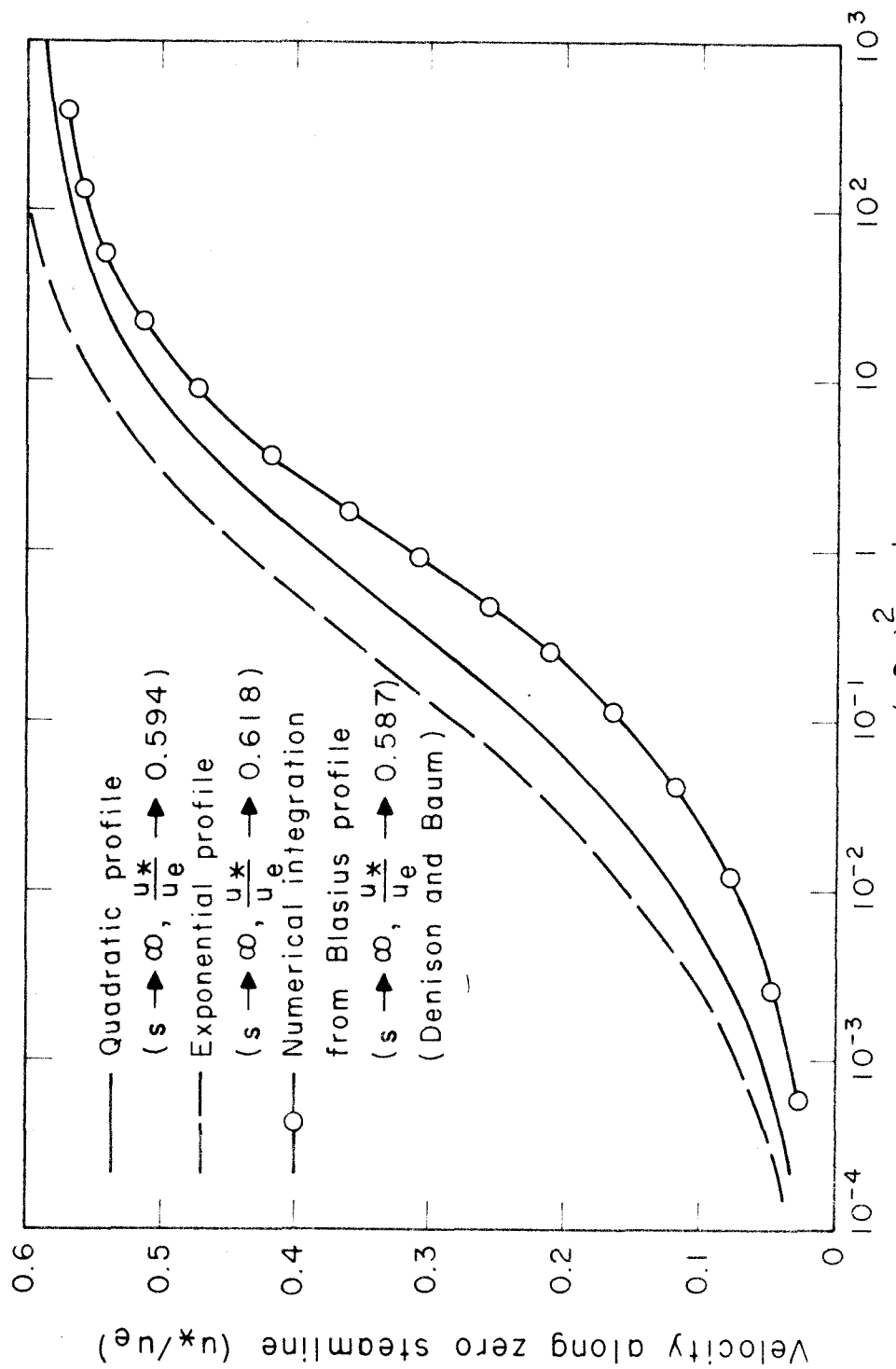

FIG. 5 EFFECT OF SHEAR LAYER PROFILE ON VELOCITY ALONG ZERO STREAMLINE

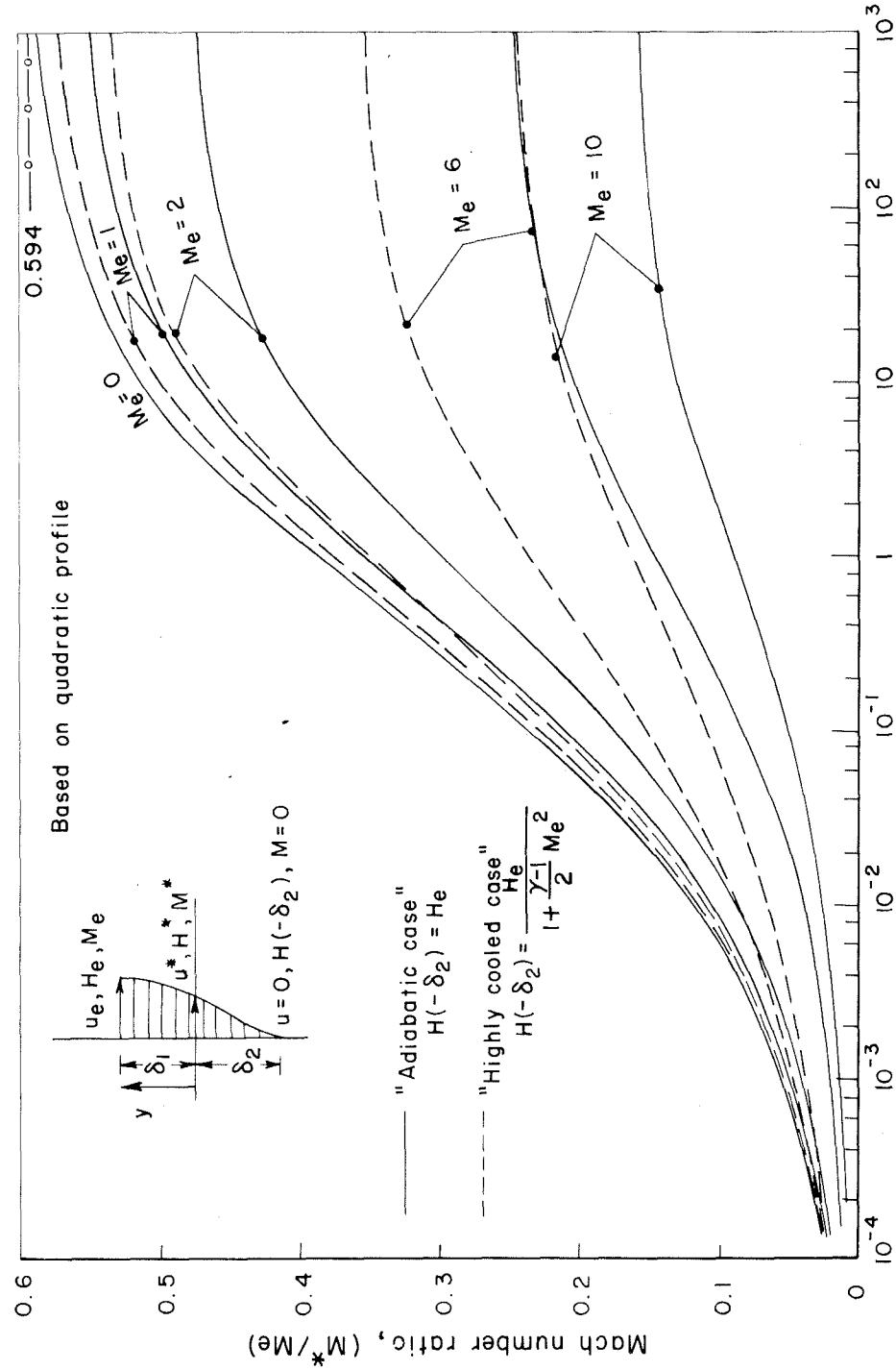

FIG.6 EFFECT OF EXTERNAL MACH NUMBER AND INTERNAL COOLING ON M_*

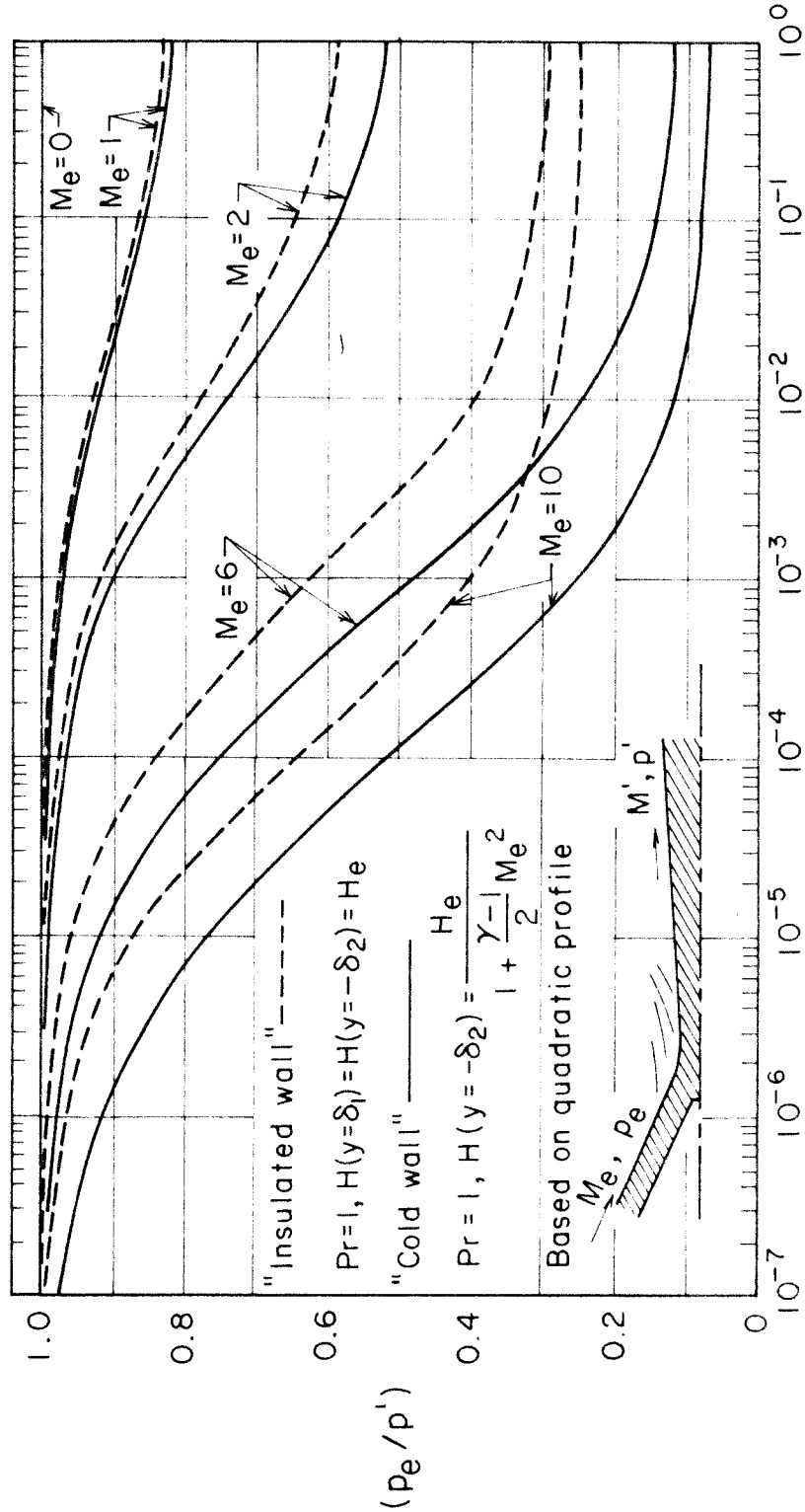

FIG. 7 PRESSURE RATIO ACROSS THE RECOMPRESSION REGION

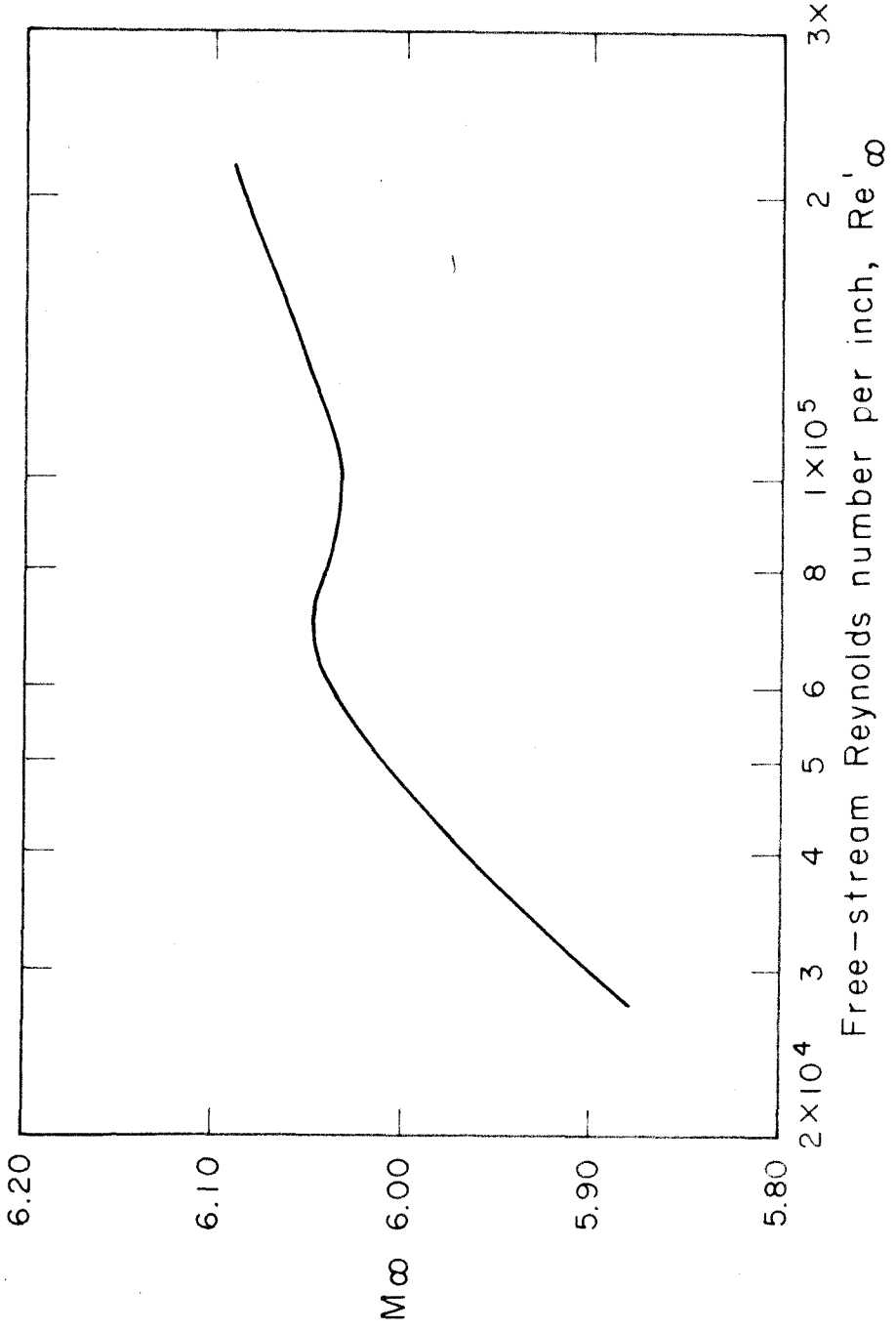

FIG. 8 VARIATION OF FREE-STREAM MACH NUMBER WITH STAGNATION PRESSURE

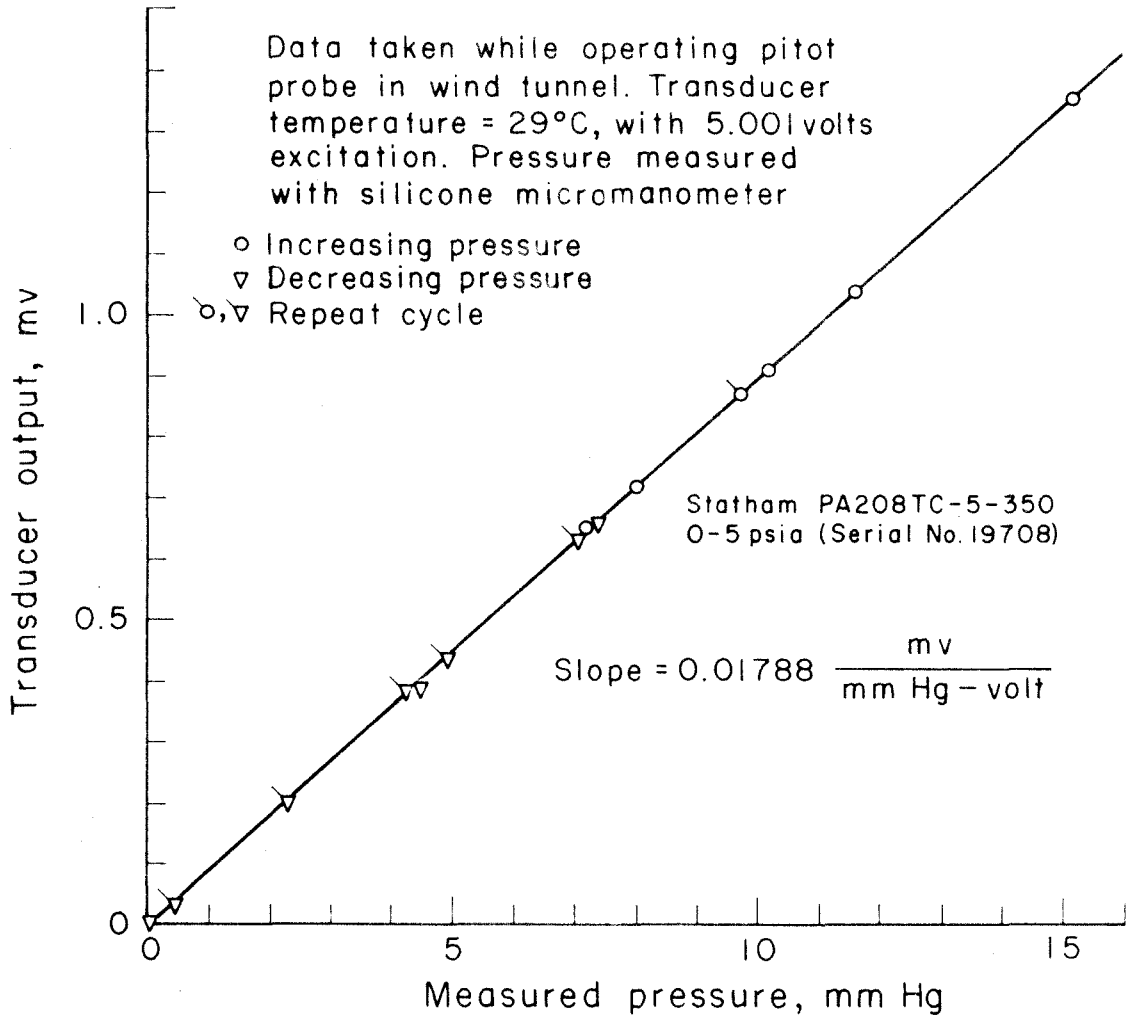

FIG. 9 CALIBRATION OF ABSOLUTE PRESSURE TRANSDUCER

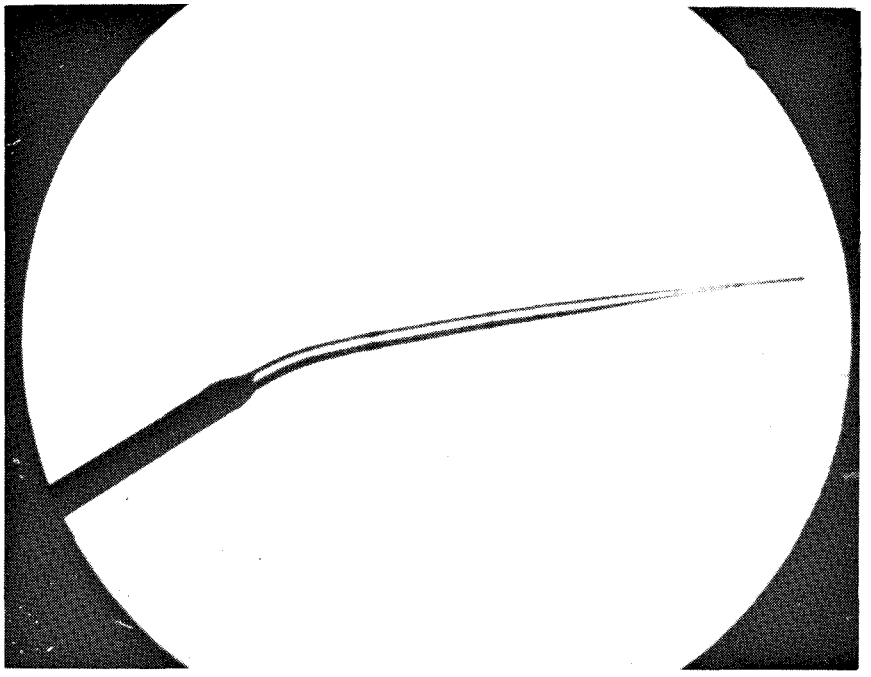

(a) O.D. = 0.0075", I. D. = 0.0040", $\measuredangle$ = 8.3°

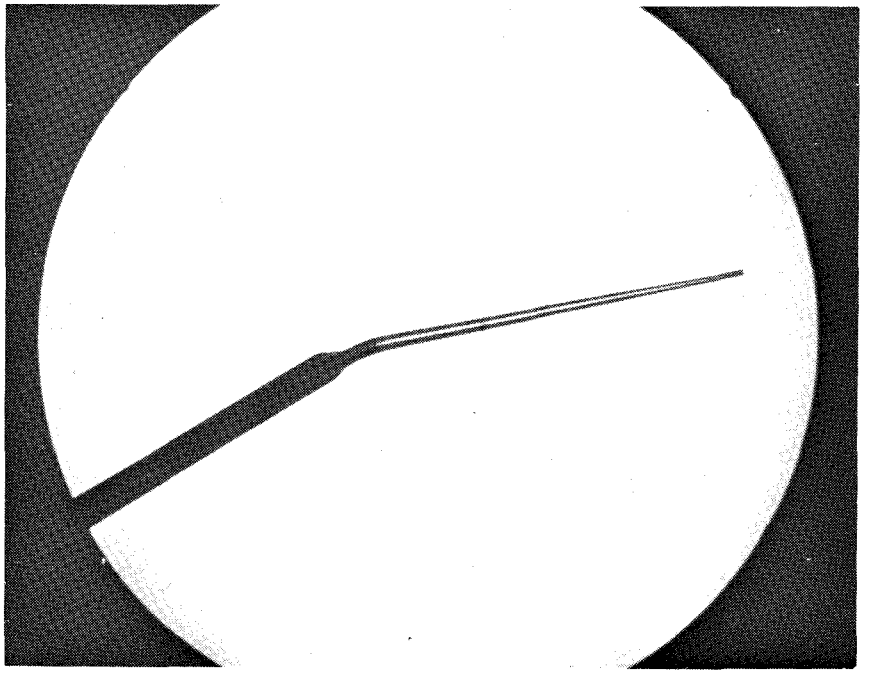

(b) O. D. = 0.0120", I. D. = 0.0075", $\measuredangle$ = 12.0°

FIG. 10 GLASS PITOT PROBES FOR USE IN SHEAR LAYER SURVEYS

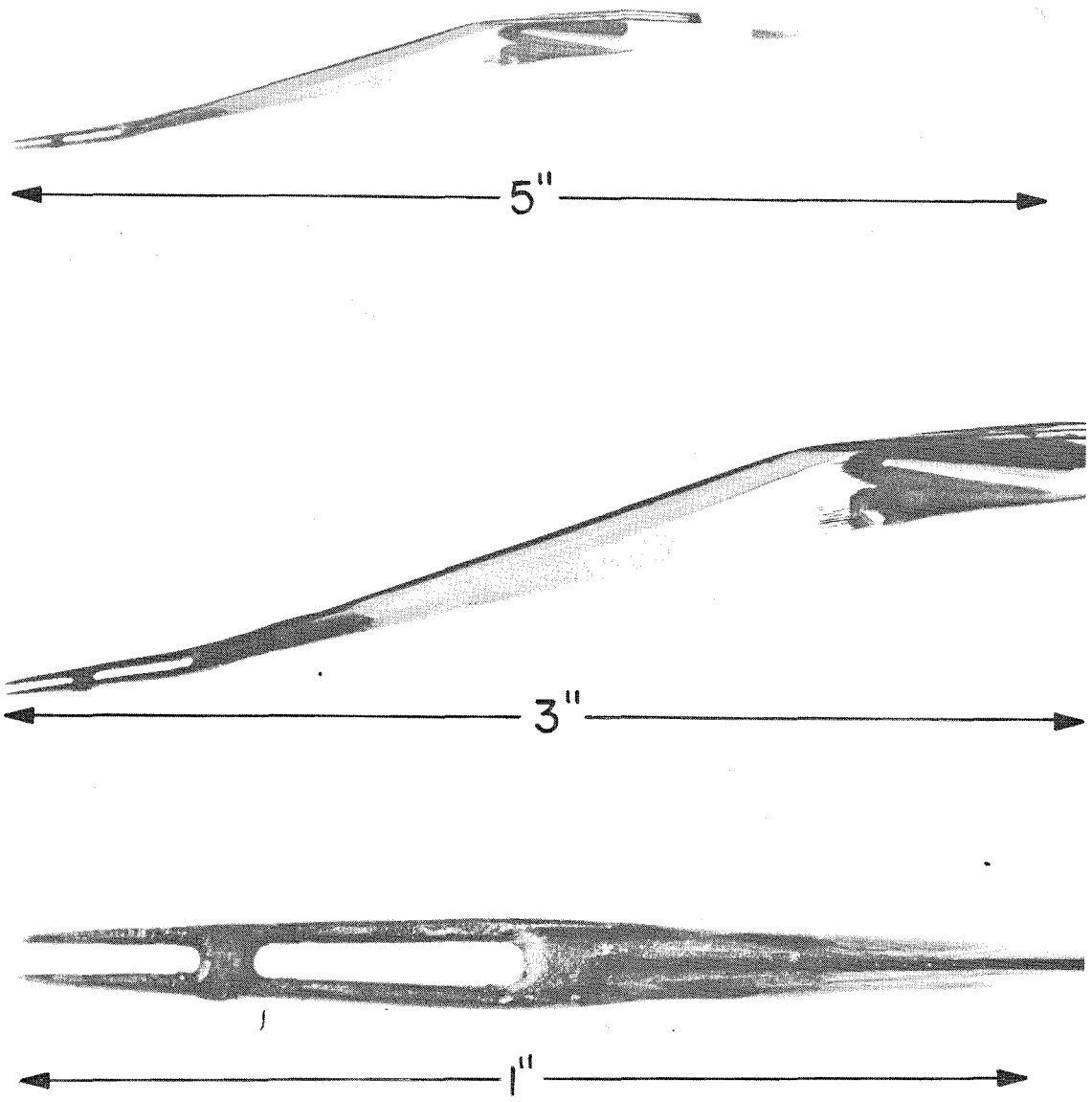

FIG. 11 THREE VIEWS OF THE HOT-WIRE PROBE

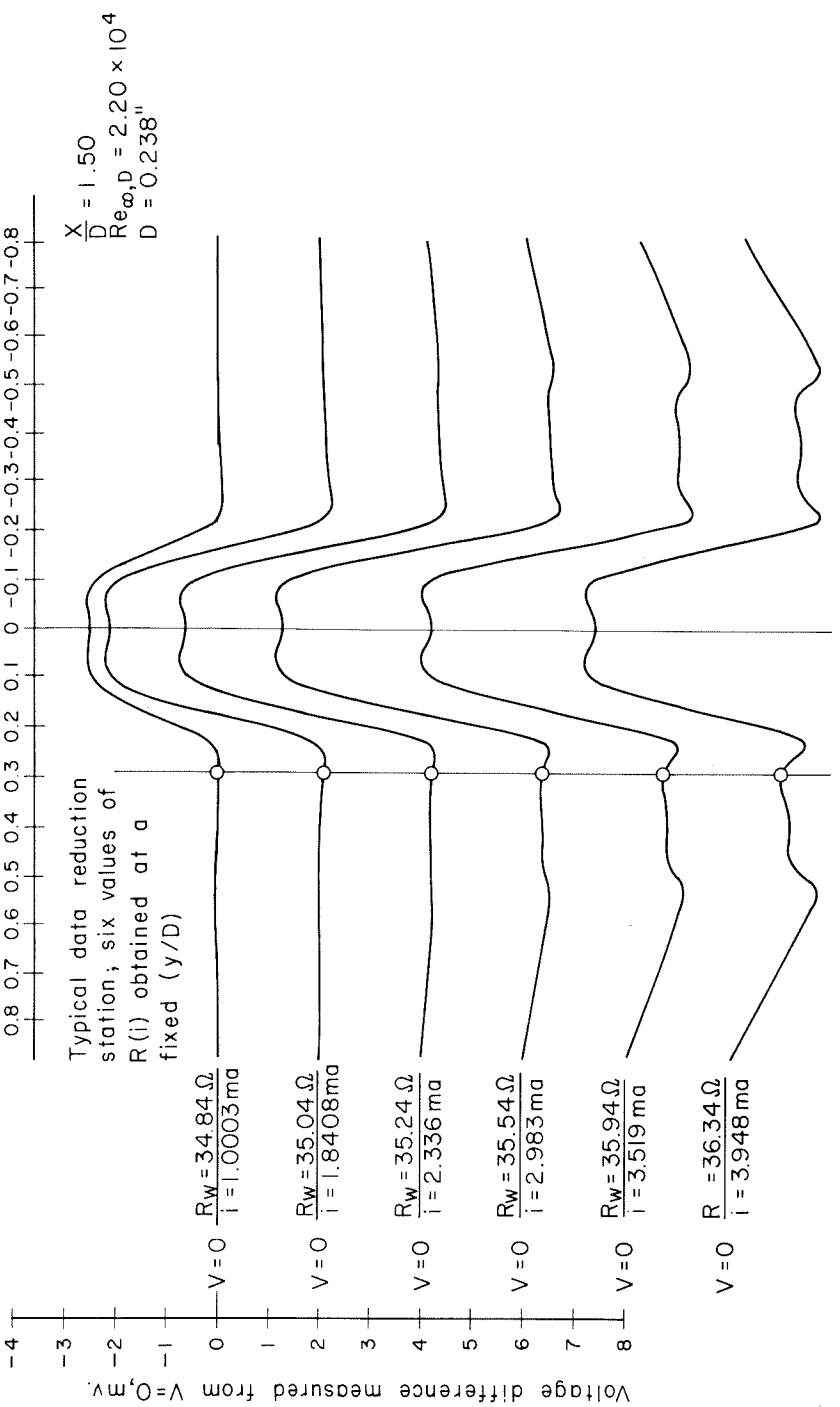

FIG. 12 RAW DATA OBTAINED FROM A HOT-WIRE IN THE NEAR WAKE OF A CYLINDER

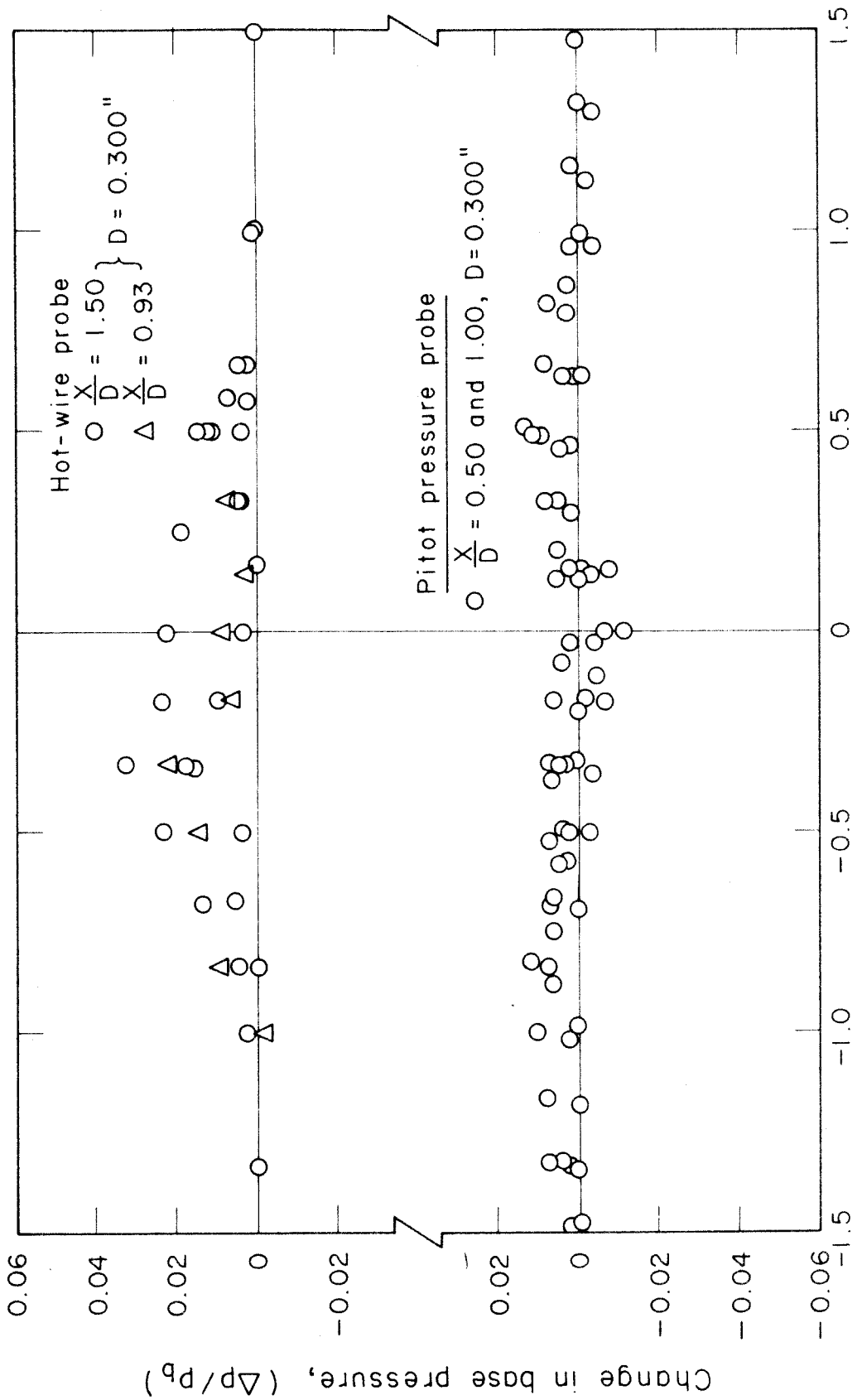

FIG.13 PROBE INTERFERENCE EFFECTS

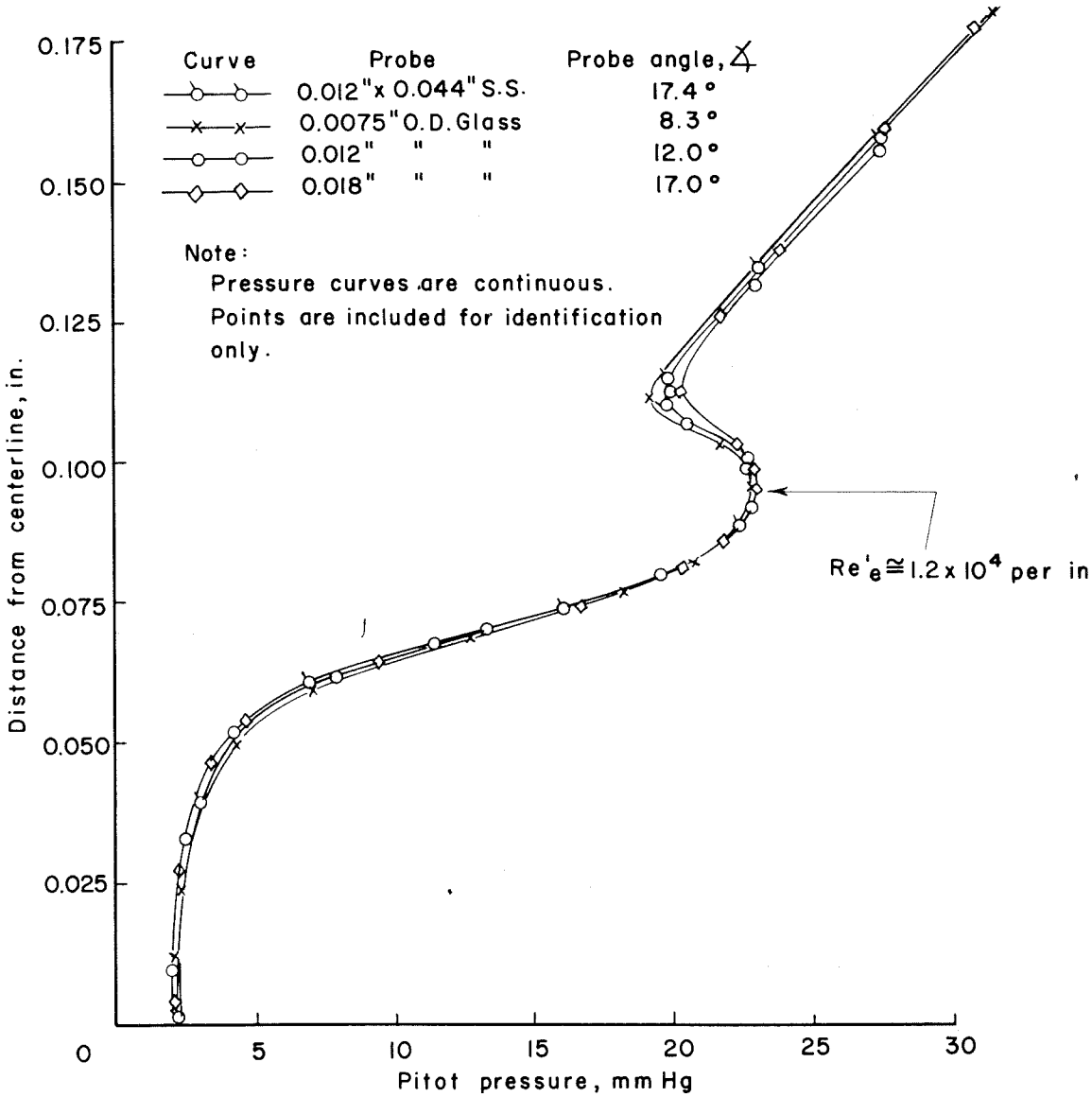

FIG. 14 EFFECT OF PITOT PROBE ANGLE AND WIDTH ON MEASURED PITOT PRESSURE, X/D = 1.00

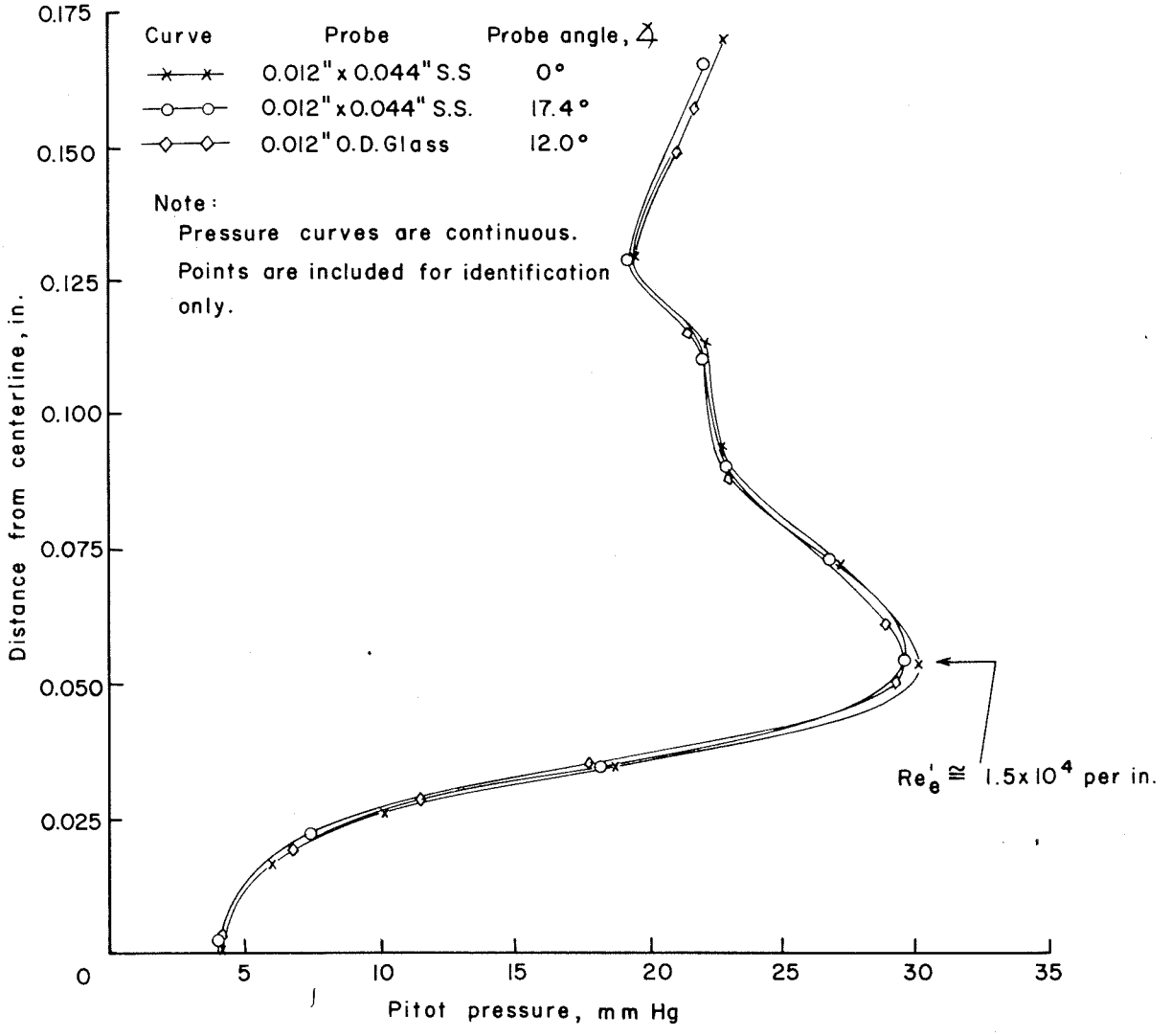

FIG. 15 EFFECT OF PITOT PROBE ANGLE AND WIDTH ON MEASURED PITOT PRESSURE, X/D = 2.00

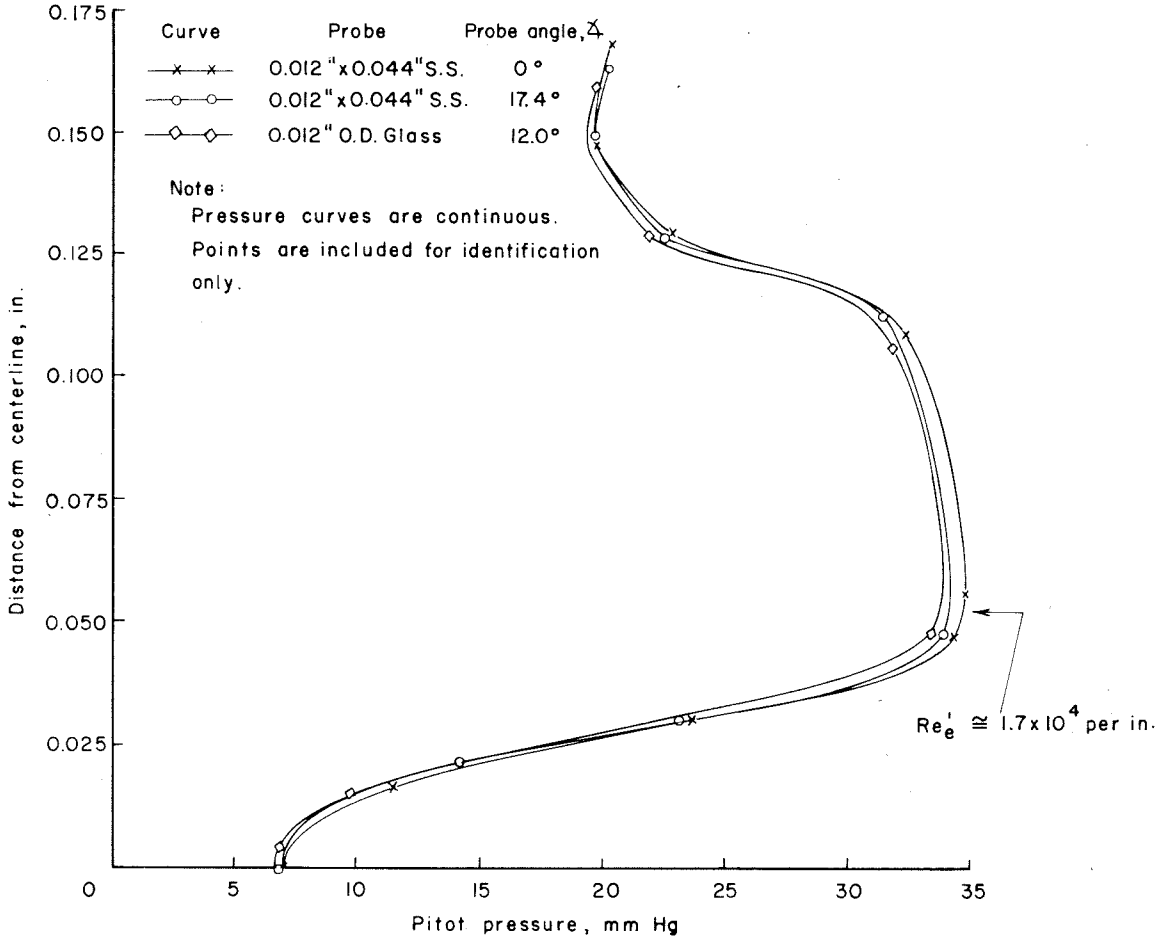

FIG. 16 EFFECT OF PITOT PROBE ANGLE AND WIDTH ON MEASURED PITOT PRESSURE, X/D = 3.00

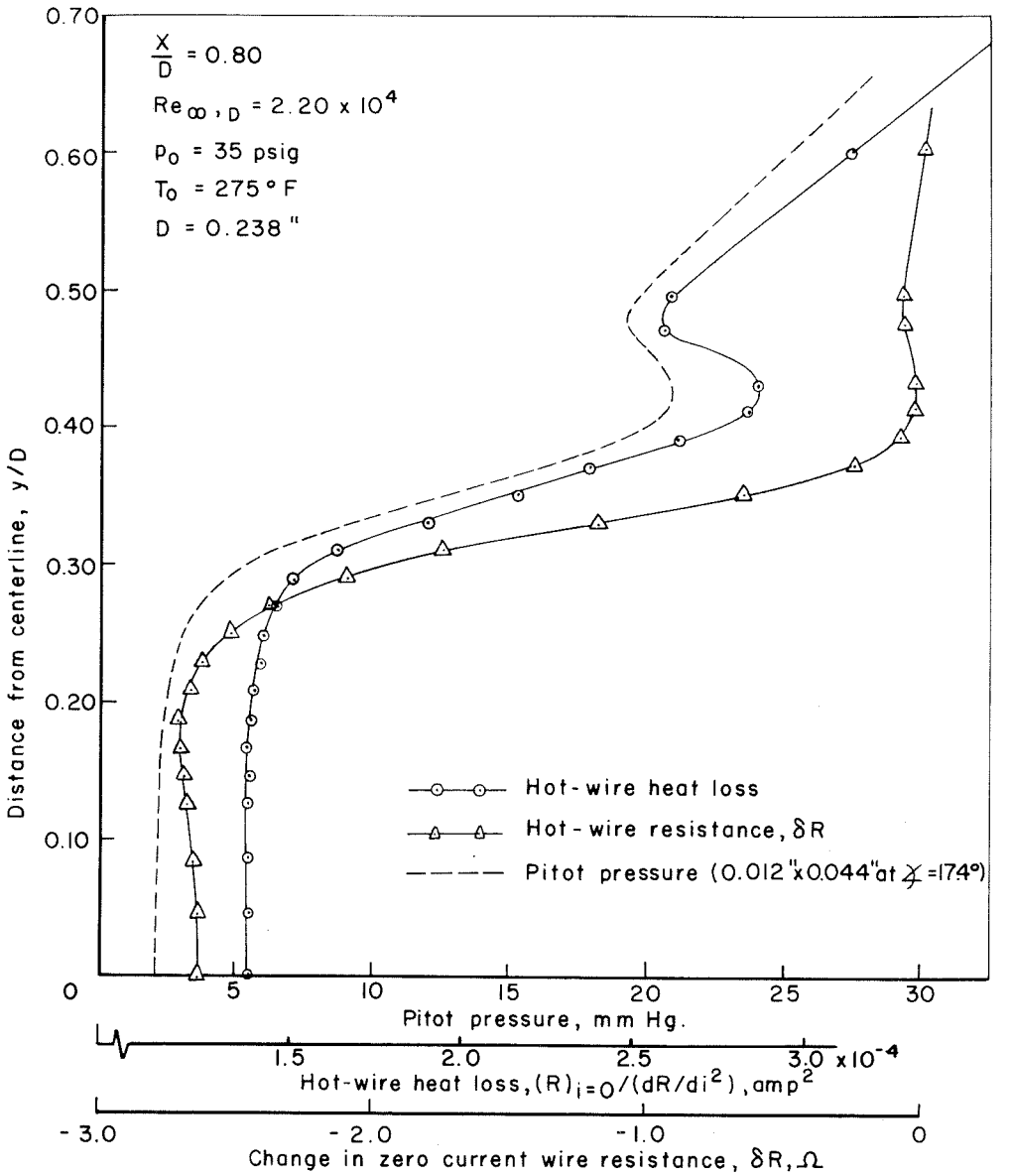

FIG. 17 COMPARISON BETWEEN MEASURED HOT-WIRE AND PITOT PRESSURE PROFILES

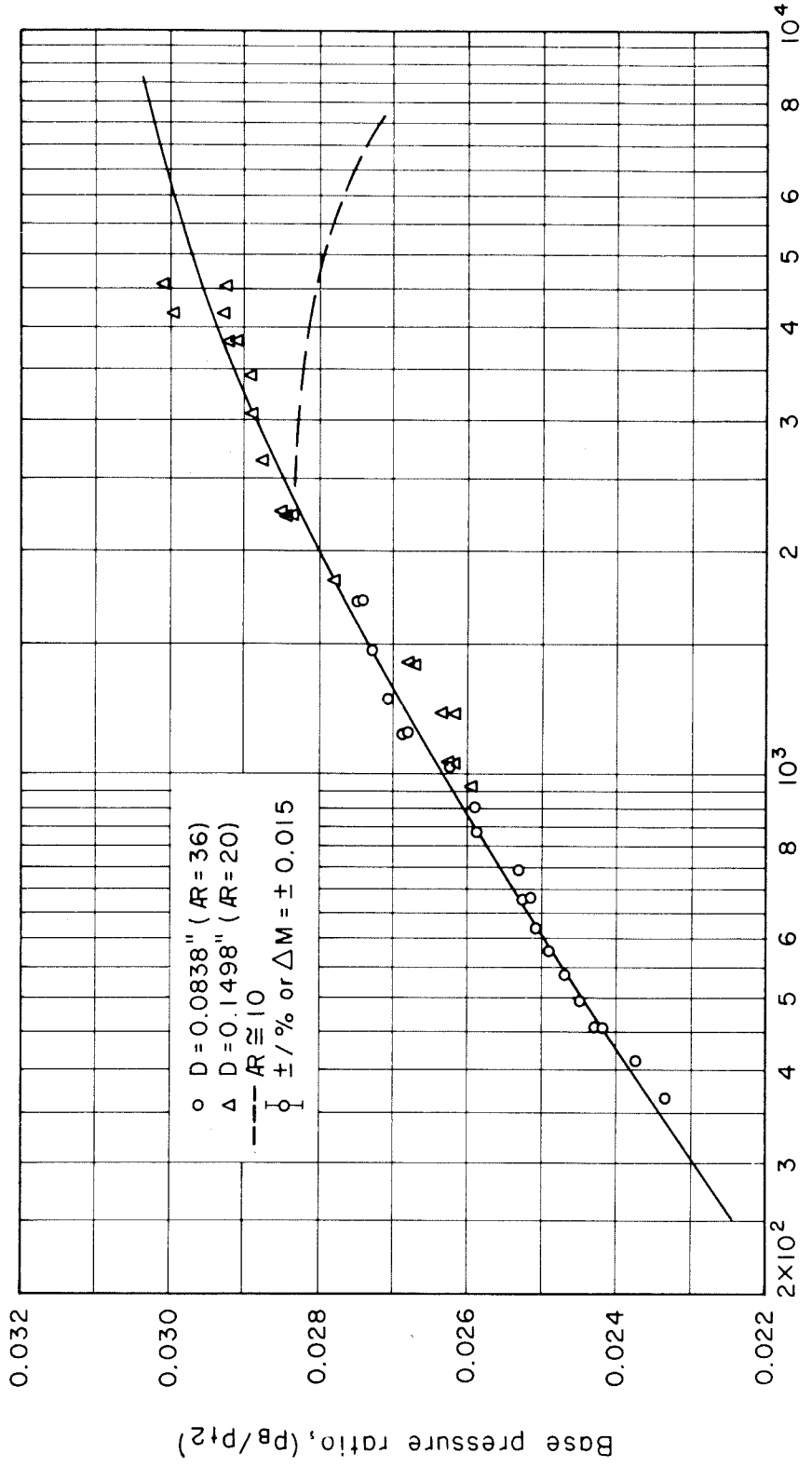

FIG. 18 VARIATION OF CYLINDER BASE PRESSURE WITH REYNOLDS NUMBER

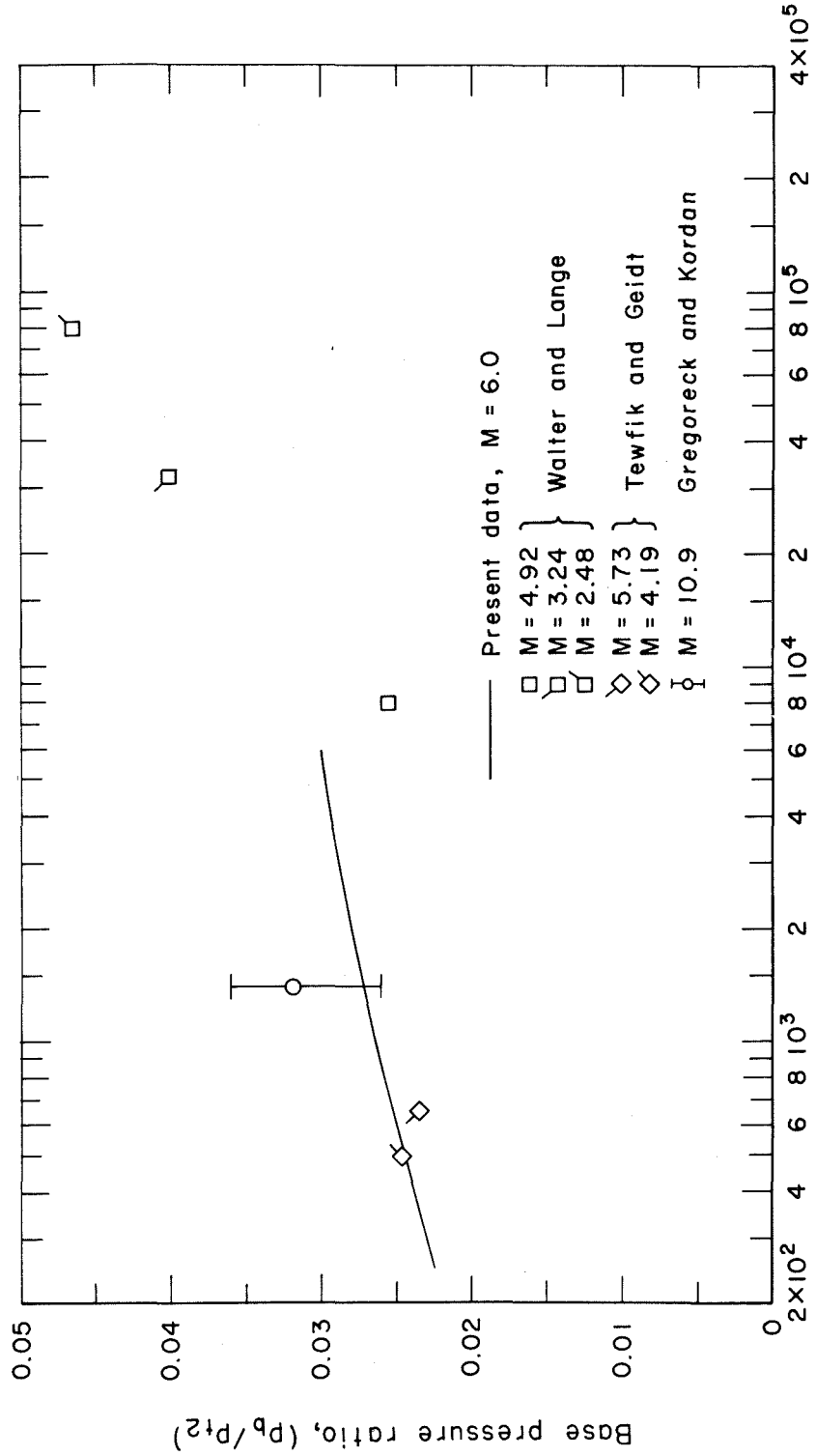

FIG.19 CORRELATION OF CYLINDER BASE PRESSURES IN SUPERSONIC AND HYPERSONIC FLOW

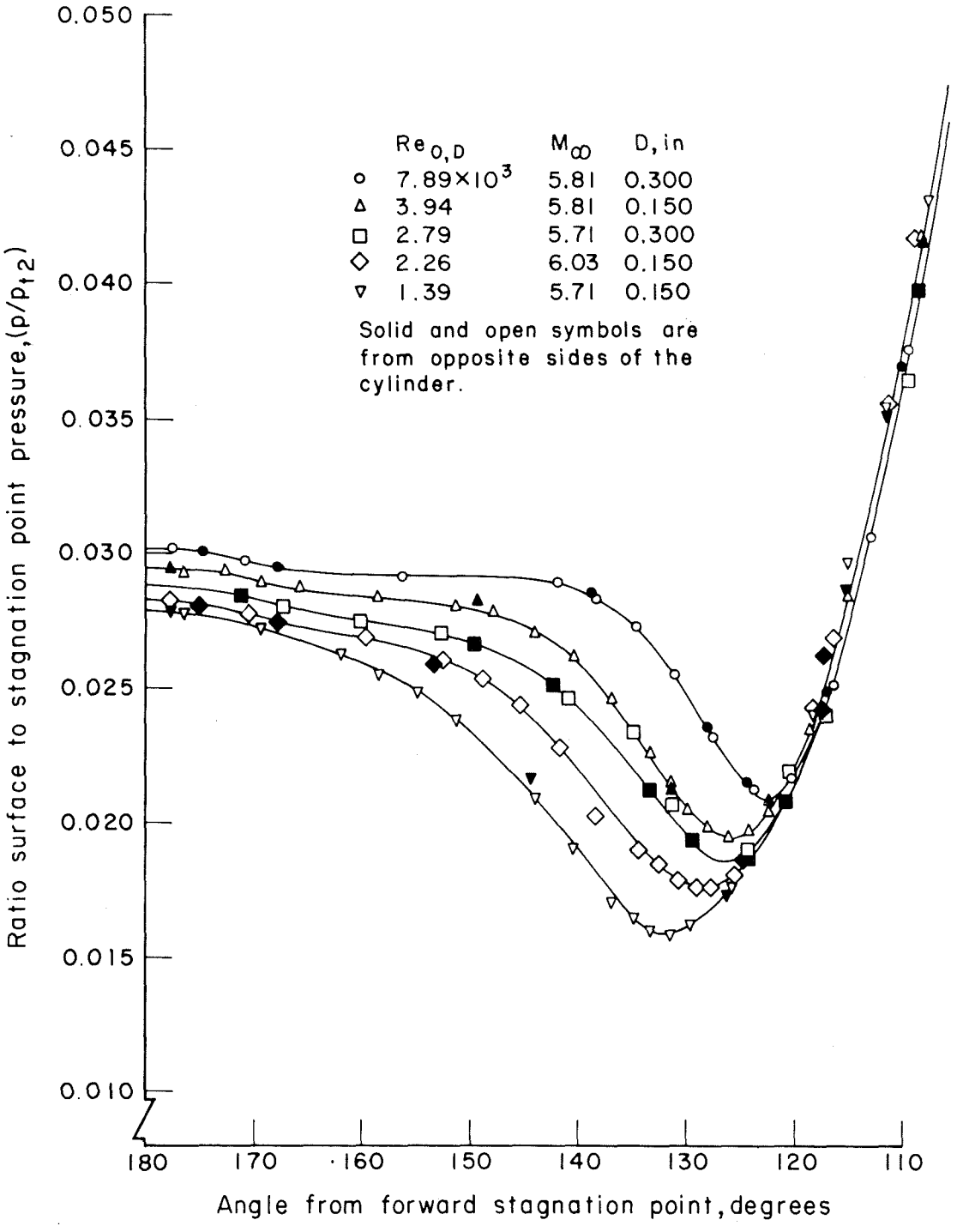

FIG. 20 SURFACE PRESSURE IN THE REGION OF SEPARATION

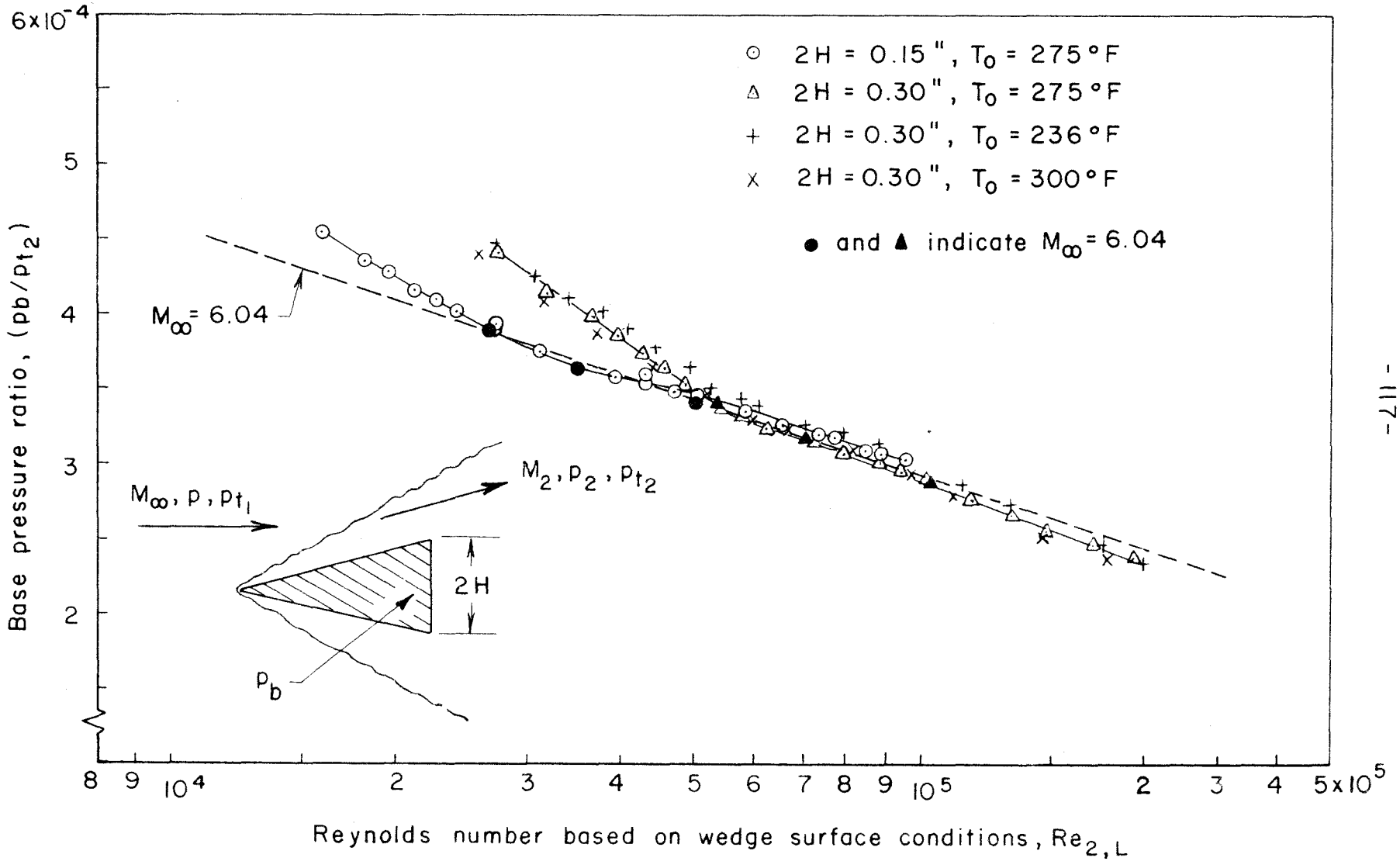

FIG. 21 BASE PRESSURE FOR A 15° HALF - ANGLE WEDGE

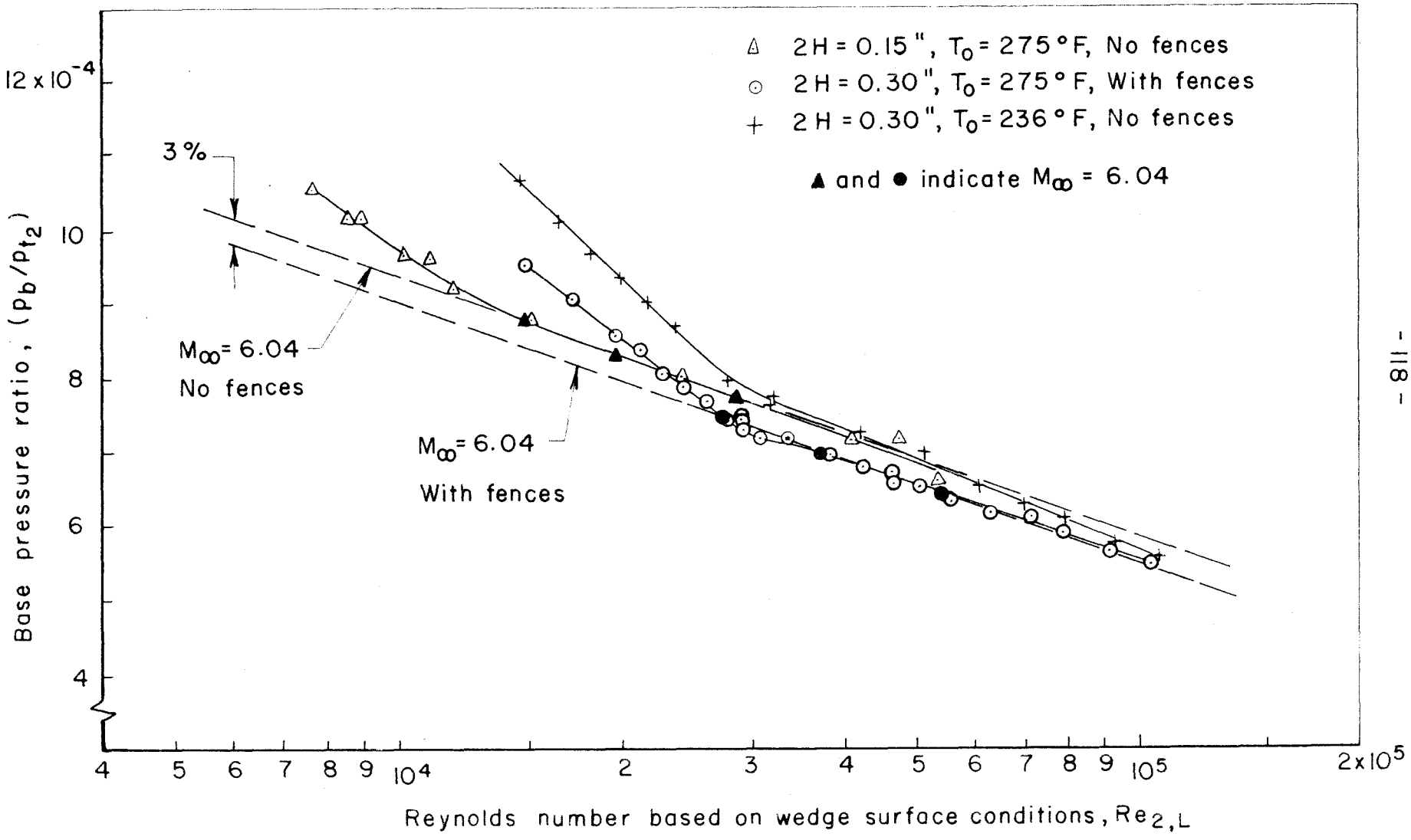

FIG. 22 BASE PRESSURE FOR A 22.5° HALF-ANGLE WEDGE

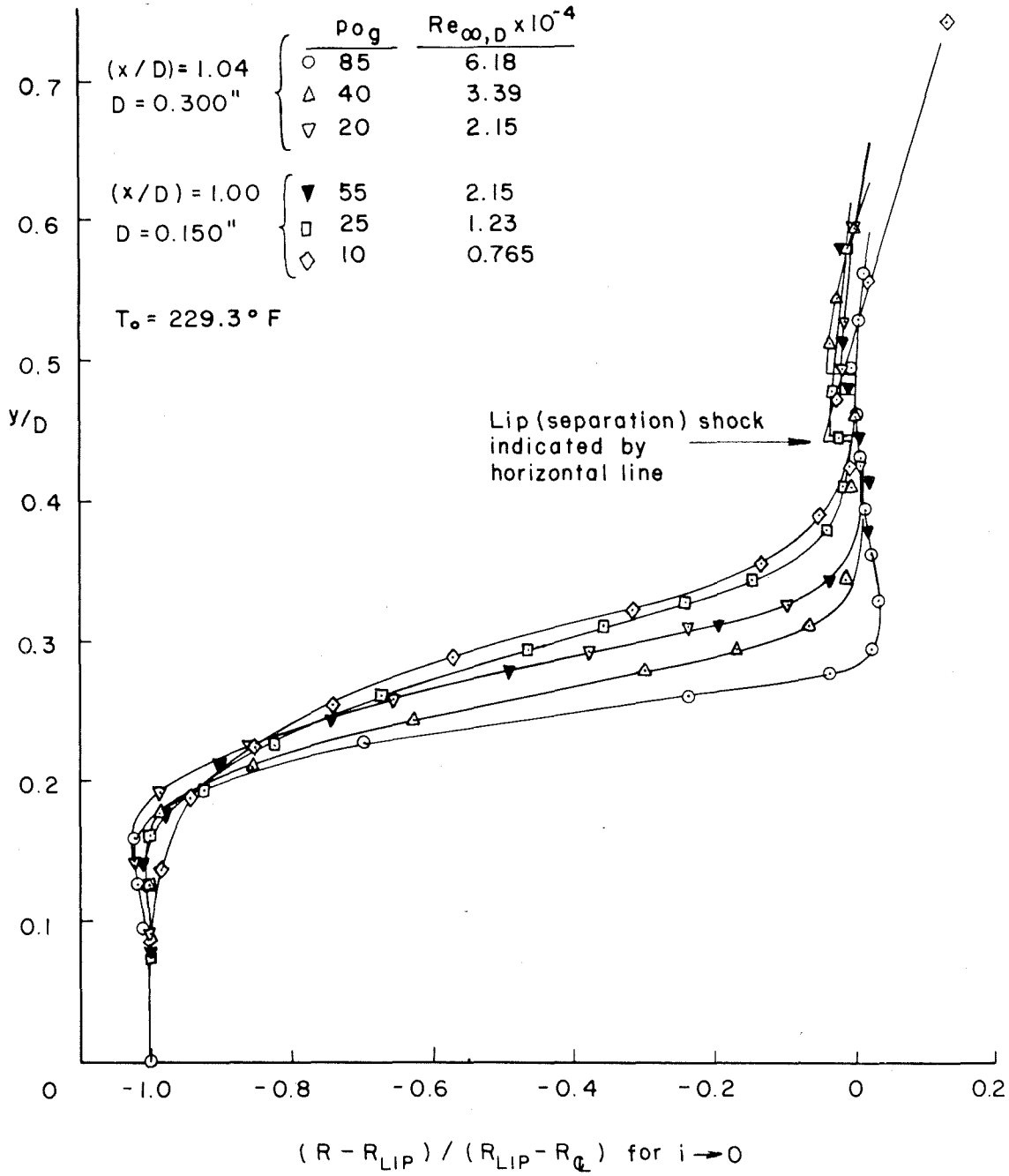

FIG.23 EFFECT OF REYNOLDS NUMBER ON SHEAR LAYER THICKNESS

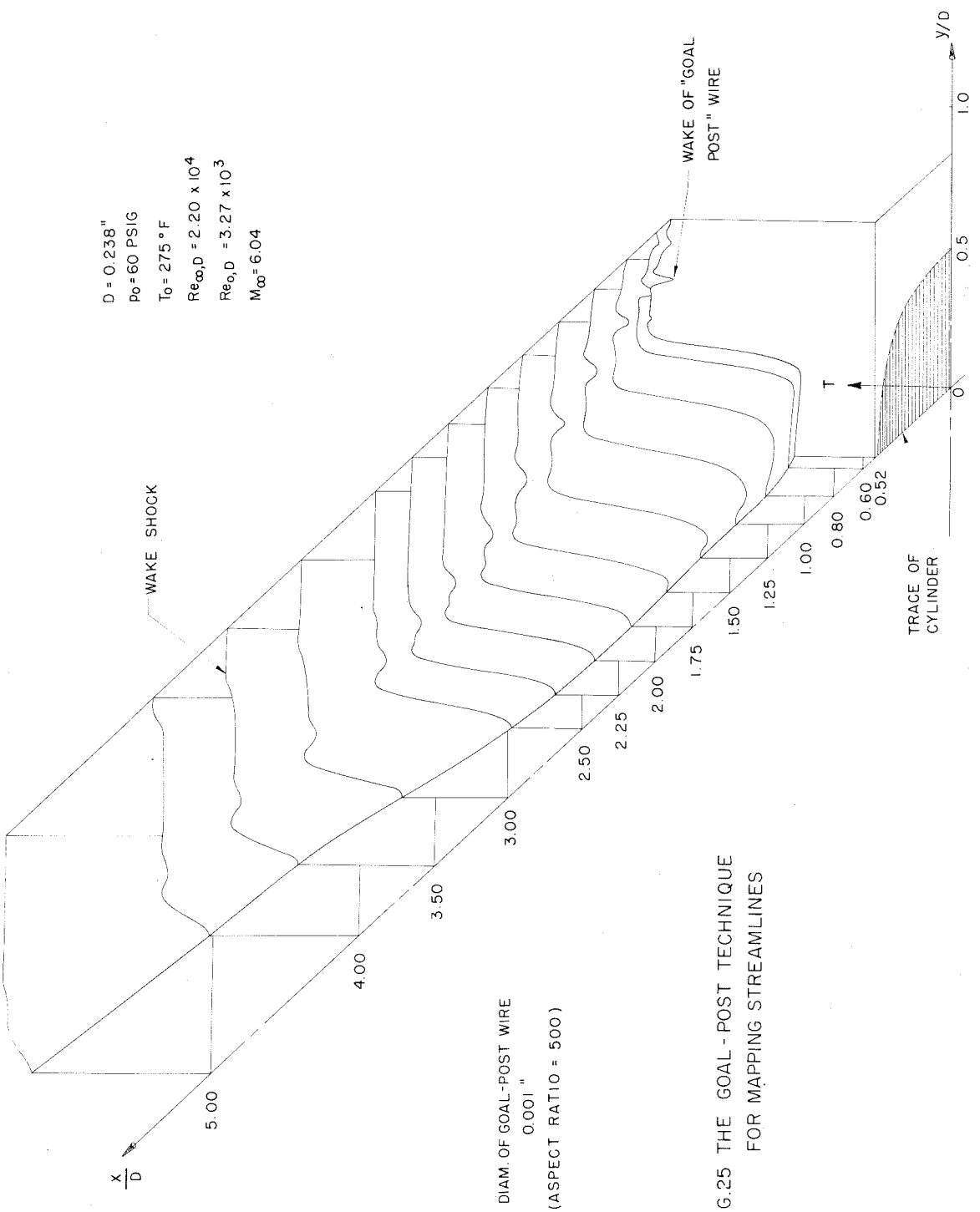

FIG.25 THE GOAL-POST TECHNIQUE FOR MAPPING STREAMLINES

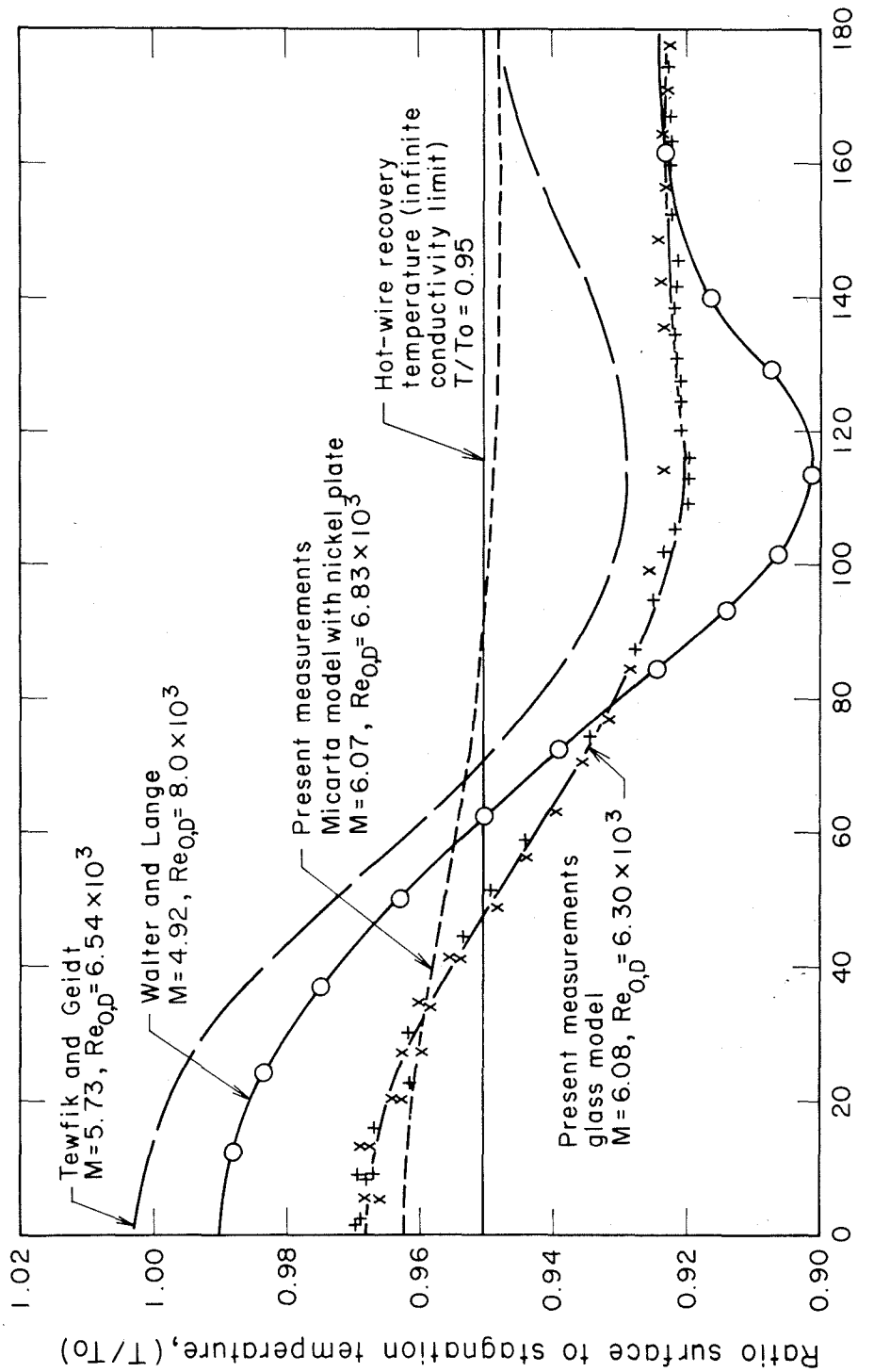

FIG.26 SURFACE TEMPERATURE DISTRIBUTION ON AN UNCOOLED CYLINDER